UNIVERSITY OF CALIFORNIA

Santa Barbara

Kinetics and Thermodynamics of Molten Silicate Attack on Thermal and Environmental Barrier Coatings

A dissertation submitted in partial satisfaction of the requirements for the degree

Doctor of Philosophy

in

Materials

by

Collin Scott Holgate

Committee in charge:

Professor Carlos G. Levi, Chair

Professor Anton Van der Ven

Professor Ram Seshadri

Professor Frederic Gibou

December 2021

The dissertation of Collin Scott Holgate is approved.

Anton Van der Ven

Ram Seshadri

Frederic Gibou

Carlos G. Levi, Committee Chair

September 2021

Kinetics and Thermodynamics of Molten Silicate Attack on

Thermal and Environmental Barrier Coatings

By

Collin Scott Holgate

ACKNOWLEDGEMENTS

The six years of my PhD—not all of which were what I think a sane person would call "enjoyable"—are something I will cherish for the rest of my time. I have had the incredible fortune of working alongside and making friends with extraordinarily bright and kind people. They made the body of science presented here possible, either directly by shaping me as a scientist or indirectly by shaping me as a human and making this time something to cherish.

The person with the most impact for me as a scientist is, by far, my advisor, Professor Carlos Levi. His scientific rigor and emphasis on understanding complex mechanisms has made me, and the resulting work presented herein, stronger and more complete. I am grateful for all the work he did behind the scenes to keep my funding through the Office of Naval Research (and for David Schifler at ONR for his continued belief in UCSB's work). Not once did I have to worry about funding, and I recognize that is not the case for many graduate students. Thank you, Carlos, for passing on your wisdom, for letting me travel to share the work, and for giving me space to think, stumble, and grow.

My committee members, Professors Anton Van der Ven, Ram Seshadri, and Frederic Gibou were also fantastic resources throughout my PhD. I am grateful for their insight and for challenging my ideas—the resulting research was stronger for it. Finally, I owe a significant debt of gratitude to Professor Frank Zok for welcoming me into his group. The lessons learned on executing and writing scientific results enhanced the quality of this scientific work. The sense of community in his group made doing the work a much happier experience.

Two fantastic mentors shaped my start in graduate school. David Poerschke was solely responsible for my training in the Materials Processing Lab. Through his generous donation of time, I learned a lot on how to do experiments and how to think about them. Even today, David will make time to answer my questions. I'm so grateful to have crossed paths with you. Then, at the end of my second year, I moved across the country for a summer internship at GE Global Research where I worked with Don Lipkin. Thank you, Don, for giving me the freedom to explore a fun project and always including as an equal on the team. I learned a lot from our conversations, whether in the lab or in a kayak going down the Mohawk River.

My lab mates throughout the years were also invaluable to my training as a scientist. Chandra Macauley welcomed me into the group so kindly and made my first day on campus so much less overwhelming than it could have been. Kaylan Wessels was an amazing source of advice and wisdom, both early on and throughout the rest of my PhD. Colin Stewart, Stefan Heinze, and Rebecca Reitz were there to answer the stupid questions that come up in everyday research life and helped get me through every major examination; I'm so grateful for all your help and to have gotten to spend so much time with you. The post docs, David Poerschke, Wes Jackson, Daesung Park, Najeb Abdul-Jabbar, Brad Lutz, Sarah Miller, and Ravit Silverstein were all great resources to learn from. I enjoyed our conversations immensely because of your unique perspectives. Finally, and certainly not least, Tom Drtina and Mayela Aldaz were my support system from the start of it all. Thank you so much for going through this journey with me. I'm grateful for all that I've learned from you, but, more than anything else, I'm grateful for how wonderful you both are and for the time I got to share with you.

The help of staff scientists on campus made carrying out the science much easier. Without Gareth Seward the concentration profiles that make up the basis of this work would not be possible. He has the perfect mix of scientific rigor and pragmatism—he is also just fun to work with. Thank you for making the hours and hours on the EPMA enjoyable. The Materials Microscopy Facility was also a critical part of this research. Thank you, Mark Cornish, Stephan Krämer, Aidan Taylor, and Claire Chisholm for making it easy to walk up to an electron microscope and collect data. Deryck Stave and Pete Maxwell kept the Materials Processing Lab running flawlessly. It is immensely difficult to imagine the lab without them, but I know my time here would have been so much more frustrating. Thank you for all the work you do to keep equipment online and for always helping us.

My interns YiLing Yang and Rodrigo Rodriguez helped substantially with the work presented in Chapters 5 and 7. Jonathan Nguyen and Benedikt Reiplinger also worked hard on projects that never quite took off but that made me a better scientist. I enjoyed working with you all more than I think you'll ever know—our time will always be a highlight of my graduate school experience. Thank you for all your hard work and for pushing me to be better.

* * *

Research isn't always enjoyable. Experiments can fail, then fail and fail again. In the scientific "dark times" my friends provided so much light.

My roommates throughout the years define my time in Santa Barbara most of all. Thank you, Tristin, for taking me on a theater adventure—I enjoyed experiencing something so different from science. Thank you, Ben Bales and Lukas Dresel, for making home life infinitely more enjoyable. Our weekly Los Agaves and game nights (being detectives in Phoenix Wright), various phone calls with actual detectives (Where did Lukas go? 2018), foam airplane making (crashing and fixing), and ice skating are some of my favorite memories. Finally, thank you Avery Samuel, Fabian Fleischer, and Bryan Josloff for being my quarantine/work-from-home buddies and for making our house feel like a home.

Mayela Aldaz and Andrés Carrete are the closest thing possible to my "chosen family" in Santa Barbara. Thank you for opening your house to me during holidays away from home, for checking in, for offering a shoulder to cry on, and being there to share the good times. Your kindness is unparalleled, and it will forever inspire me. Thank you, Will Summers and Andy Ericks, for offering not only your scientific insight but your wonderful friendship. The memories of our trips—watching elephant seals, the great restaurant tour of San Diego, or almost running out of battery in a brand-new Tesla—still make me laugh at their shear ridiculousness. I appreciate both how deep and how shallow our conversations can be. Joe Wendorf, Carolina Frey, Leah Mills, Neal Brodnik, Toby Francis, and Avery Samuel were my D&D buddies; thank you for exploring the make-believe with me and thank you Joe for organizing everything. I explored fancy food and California wines with Amanda Ruschel, Liam Dow, Lauren Poole, Virginia Collier, and Victoria Christensen, the Social Chair. Thank you all for the fun days or nights out, our conversations, and your friendship. Victoria deserves a special thanks—our sanity lunches and walks helped me more than you know. Thank you for listening and pushing when appropriate—those pushes helped finish this dissertation. I am deeply grateful that you all decided to come to UCSB.

I've also been very fortunate to meet many wonderful people outside the Materials Department, mostly connected—one way or another—to the UCSB computer security lab: Lukas Dresel, Sharon

Levy, Fabio Gritti, Chris Salls, Chani Jindal, Nicole and Lauren Moghaddas, Shannon Wang, Fabian Fleischer, and Nicola Ruaro. Becoming friends with you is the clearest transition point where Santa Barbara started to feel like home. Thank you for pulling me out of my bedroom or lab to explore Santa Barbara and the national parks in California, for our Tahoe trips, and for the SB Summer of Fun. And thank you for regularly making me smile so much that my jaw begins to hurt.

A few friendships predating graduate school also helped keep me sane. My brother, Galen, has become such a good friend. He moved to California around the same time as me, and I have been so grateful to have him close. Thank you for our hours-at-a-time conversations, for sharing your work/life philosophy, and for listening to—and challenging—mine. Connie Dong first taught me to go beyond coursework or research in school—something that has brought me much joy through ΤΒΠ and later Beyond Academia. Thank you for our GRE study sessions, being my University of Minnesota visit buddy, and for being a great person. Matthew Stetler and Chad Reed, Homeowner, have been close friends since elementary school—they have both shaped me in ways that are probably impossible for me to know. Thank you both for being anchors throughout my time away from Minnesota, especially Chad whom I have talked to nearly every day of graduate school. There have been numerous challenges the last six years, but loneliness was rarely one. Thank you for sharing all of the good days and bad days, listening to my rants, and for calling me out when I deserved it.

On the topic of challenges, graduate school has been a time of technical learning and emotional healing/growth made possible by UCSB's excellent mental health coverage. I am grateful for "the powers that be" that have made this possible, for CAPS, Ryan S., and, most of all, José R. Thank you for helping me process feelings of imposture syndrome, heartbreak, anxiety, and apathy healthily.

Finally, I want to thank my family who delivered me here. My path to graduate school was not predestined or guaranteed. It was a road built through the wilderness and paved with the bricks of their sacrifices and hard work to provide for me. I feel especially grateful because I know it wasn't easy. Thank you for your light touch and letting me discover which direction to build the road.

There are a few family members I especially want to thank. While my interest in science did not fully crystallize until high school, I believe my aunt Zardoya planted the seed much earlier. Our chemistry experiments and crystals-in-a-jar wound up shockingly close to my PhD research, which may be more than just a coincidence. More importantly though, she has supported me with love far beyond expectation for my whole life. Likewise, my stepparents, Dave and Lisa, have been wonderful additions to my life. Thank you for all the love and support you've so generously shared—especially because you never "had to". You are amazing people and I feel like I hit the jackpot. My dad, Scott, has taught me the power of transformation and how to create something for yourself through hard work. I am so grateful for our time together and your support—especially through my years in university when I was so narrowly focused on a singular thing. Finally, I want to thank my mom, Teri, who is most responsible for the road delivering me to UCSB. Words will never fully capture the depth of my gratitude. Your sheer force of might prevented us from falling off a proverbial cliff. It kept me in good schools with fantastic and inspiring teachers; it allowed me to keep my friendships that I cherish to this day; and it taught me how to appreciate the simple things in life and "enough". Thank you from the bottom of my heart.

VITA OF COLLIN SCOTT HOLGATE

EDUCATION

PhD	**University of California, Santa Barbara**, Materials GPA: 4.0/4.0	2015-2021
BS	**University of Minnesota**, Materials Science and Engineering Minored in Chemistry GPA: 3.82/4.0	2010-2015

PUBLICATIONS

Journal Publications

E Zoghlin, J Schmehr, **CS Holgate**, R Dally, Y Lie, G Laurita, and SD Wilson, "Evaluating the Effects of Structural Disorder on the Magnetic Properties of $Nd_2Zr_2O_7$," *Phys. Rev. Mater.*, **5**, 8, 084403, (2021).

CS Holgate, Y Yang, and CG Levi, "Reactive crystallization in HfO_2 exposed to molten silicates," *J. Eur. Ceram. Soc.*, **41**, 11, 5686–5695, (2021).

CS Holgate, GGE Seward, AR Ericks, DL Poerschke, and CG Levi, "Dissolution and diffusion kinetics of yttria-stabilized zirconia into molten silicates," *J. Eur. Ceram. Soc.*, **41**, 3, 1984–1994, (2021).

BA Williams, ND Trejo, A Wu, **CS Holgate**, LF Francis, and ES Aydil, "Copper–Zinc–Tin–Sulfide Thin Films via Annealing of Ultrasonic Spray Deposited Nanocrystal Coatings," *ACS Appl. Mater. Interfaces*, **9**, 22, 18865–18871, (2017).

BA Williams, MA Smeaton, **CS Holgate**, ND Trejo, LF Francis, and ES Aydil, "Intense pulsed light annealing of copper zinc tin sulfide nanocrystal coatings," *J. Vac. Sci. Technol A*, **34**, 5, 051204, (2016).

BA Williams, A Mahajan, MA Smeaton, **CS Holgate**, ES Aydil, and LF Francis, "Formation of copper zinc tin sulfide thin films from colloidal nanocrystal dispersions via aerosol-jet printing and compaction," *ACS Appl. Mater. Interfaces*, **7**, 21, 11526–11535, (2015).

Journal Papers in Preparation

CS Holgate, R Rodriguez, SM Miller, E Godbole, DL Poerschke, and CG Levi, "Phase stability of yttrium iron and yttrium iron-aluminum garnets," *In preparation.*

ORAL PRESENTATIONS

CS Holgate, Y Yang, DL Poerschke, and CG Levi, "Dissolution kinetics of thermal barrier oxides in molten silicates," ICACC, Daytona Beach, FL, January 2020.

CS Holgate, DL Poerschke, and CG Levi, "Dissolution and diffusion of thermal barrier oxides in molten silicates," ICACC, Daytona Beach, FL, January 2019.

CS Holgate, DL Poerschke, and CG Levi, "Kinetics of thermal barrier oxide interactions with molten silicates," ICACC, Daytona Beach, FL, January 2017.

RESEARCH EXPERIENCE

Graduate Research Assistant 2015-Present
University of California, Santa Barbara
Advisor: Professor Carlos G. Levi

- Developed a mechanistic understanding of thermal and environmental barrier coating degradation by molten silicates.
- Quantified the dissolution and diffusion kinetics of oxides into molten silicates.
- Modeled coating-melt interactions leveraging determined kinetics and finite element models.
- Developed thermodynamic database for reactive crystallization by collaborating with another university and industry partners.

Graduate Fellow Intern June-September 2017
General Electric Global Research Center, Niskayuna, NY
Supervisor: Dr. Don Lipkin

- Provided an initial investigation for a TRL-1 project in a metallic system.
- Collaborated with a diverse set of engineers and scientists in a fast-paced team setting.

Undergraduate Research Assistant May 2013 to August 2015
University of Minnesota
Advisor: Professor Lorraine Francis

- Independently investigated the ultrasonic spray coating of colloidal nanocrystalline dispersions by leveraging synthesis, experimental design, and analysis skills.
- Optimized processing parameters to produce a dense coating, which resulted in publication.

TEACHING EXPERIENCE

Instructor, School for Scientific Thought Oct. 2018 to Nov. 2018
University of California, Santa Barbara
Course title: Understanding our material world, from atoms to catastrophe

- Created and delivered a curriculum to introduce the concept of materials science to high school students with a range of science education backgrounds (grades 9–12).
- Developed hands-on activities for the students to reinforce concepts.
- Actively sought feedback, improving the course week-to-week.

Teaching Assistant, Manufacturing and Materials March 2016 to June 2016
University of California, Santa Barbara
Instructor: Professor Carlos G. Levi

- Organized sections for additional course assistance and graded assignments.

Course Development Assistant May 2015 to August 2015
University of Minnesota
Supervisor: Professor Lorraine Francis

- Developed new laboratory experiments for a senior-level processing course.

PROFESSIONAL SERVICE

Beyond Academia Conference, University of California, Santa Barbara 2018–2020
Role: Chair (2019–2020), Logistics Co-chair (2018–2019)

- Planned and conducted regular meetings of sub-committees in programming, logistics, finance, and marketing. Oversaw the progress in each committee and assisted when needed.
- Executed planning and development of an event with a hard deadline.
- Coordinated with conference venues and catering services to ensure smooth operation for the ~200 attendees.

Intern Supervisor and Mentor, University of California, Santa Barbara 2018–Present
Role: Supervisor to five undergraduate- or masters-level research assistants (up to two concurrent).

- Trained new research assistants on materials science laboratory techniques, including sample preparation, characterization, and analysis.
- Mentored research assistants on professional development, assisting with graduate school applications or with internship applications.
- Routinely taught assistants about concepts in materials science using communication skills.

Tau Beta Pi, University of Minnesota 2014–2015
Role: Communications Officer

ABSTRACT

Kinetics and Thermodynamics of Molten Silicate Attack on

Thermal and Environmental Barrier Coatings

Collin Scott Holgate

Enhancing the efficiency of gas turbine engines requires higher operation temperatures and the materials capable of surviving the increasingly challenging environment. Ceramic barrier coatings, with carefully engineered microstructures, protect the structural components within the hottest sections of the engine. However, these coatings are susceptible to damage mechanisms arises from the ingestion of siliceous debris, which can melt and deposit on the coating's surface. Thermomechanical strains develop that are either mitigated or exacerbated by the thermochemical interactions between the coating and the melt. This work investigates these thermochemical interactions and their pertinent kinetics and thermodynamics.

Dense compacts or single crystalline pieces of barrier coating oxides were placed into a semi-infinite 1D diffusion couple geometry with one of two synthetic silicate melts at 1200–1400 °C. Concentration profiles within the melt were obtained and fit to partial differential equations quantitatively describing the coating dissolution rate into the melt and diffusivities therein. Cation diffusivities were most affected by the melt composition, whereas the ratio of rare-earth (RE^{3+}) oxides to ZrO_2 or HfO_2 most strongly affected the initial detachment rate of barrier oxides into the melt. Ultimately, the dissolution kinetics were sufficiently slow to delay melt saturation and the nucleation of reprecipitated or reaction phases that limit coating degradation. This delay was worse for barrier oxides with low concentration of RE^{3+} elements. Finite element models—using the gathered kinetic

data but applied to small length scales relevant for real coatings—suggest this delay will be controlled primarily by the initial interface detachment rate in practice.

After the initial dissolution transient period, the crystallization of reprecipitated and reaction phases was investigated qualitatively using electron microscopy and chemical analysis techniques. The presence of only a small amount of RE^{3+} oxide in the dissolving material (e.g., 7%) kinetically hindered the crystallization of reaction products—even those based on Zr^{4+} or Hf^{4+}—favoring instead reprecipitated phases, deviating from the expected thermodynamic response predicted by CALPHAD databases. Conversely, those barrier oxides free of RE^{3+} (e.g., HfO_2) more readily crystallized reaction products such as $(Zr,Hf)SiO_4$, or $Ca_2HfSi_4O_{12}$; those containing a substantial amount of RE^{3+} (e.g., $Gd_2Zr_2O_7$) rapidly crystallized a RE-apatite, nominally $Ca_2RE_8(SiO_4)_6O_2$.

Finally, the thermodynamics of Y-Al-Fe-garnet formation, i.e., the solid-solubility limits of substitutional cations Ca^{2+}, Mg^{2+}, Fe^{2+}, and Si^{4+}, their crystallographic site preference, and the competition between garnet and other phases was investigated. Long duration heat treatments afforded equilibrated samples, for which the phase assemblage was analyzed using X-ray diffraction, electron microscopy, and standardized chemical analysis techniques. A key factor in the stability of garnet was the Fe:Al ratio of the system. Indeed, increasing the Fe:Al ratio of the as-synthesized powder significantly increased the Ca^{2+} and Si^{4+} solubility and the quantity of garnet present, with a concomitant decrease to the quantity of other important reaction phases such as apatite.

This dissertation advances the understanding of thermochemical interactions between protective barrier coatings and molten silicates, which is critical to design robust coatings. The quantitative kinetic data and thermodynamic information enables computational approaches to coating design.

TABLE OF CONTENTS

CHAPTER 1. INTRODUCTION

Aerospace gas turbine engines have afforded an unprecedented world connectivity. Some ~4.5 billion passengers boarded a commercial flight for business or pleasure in 2019 [1]. This value is reflected in the economic figures. The commercial aerospace industry had a revenue of approximately $612 billion on passenger travel, with an additional $100 billion from cargo in 2019. Yet, this comes at a significant carbon cost: 96 billion gallons of jet fuel burned and 914 million tons of CO_2 emitted in 2019. With the projected demand for passenger air travel doubling over the next 20 years [2] and significant electrification of air travel unlikely within that time frame, the market demand for increased efficiency of gas turbine engines is unabated.

Gas turbine engines can be made more efficient by increasing their operation temperatures, but the temperature is persistently limited by the materials within. Thus, significant effort over decades has sought to discover and design novel materials, microstructures, and architectures capable of higher temperature operation than the previous generation. The interest of this dissertation lies in the hot turbine section of the engine, where the most extreme thermo-mechanical conditions are experienced. Materials development in this section has evolved in two major directions, depicted schematically in Fig. 1.1. The first and more established approach uses nickel-based superalloys for the critical structural components. The airfoils are typically cast as single crystals to enhance their creep performance, but gas temperatures typically exceed the melting point of the superalloy requiring active cooling of the components through internal passages and transpiration holes [3]. Thermal barrier coatings (TBCs) typically based on yttria-stabilized zirconia (YSZ), are commonly used to thermally-protect the superalloy [4,5]. These ceramic coatings have a significantly lower

thermal conductivity than the metallic substrate and provide a large temperature gradient through the thickness of the coating, ~0.5-1 K/μm [6]. Their columnar microstructure affords strain tolerance under thermal cycling, resulting from the mismatched coefficients of thermal expansion (CTE) with the underlying superalloy.

The second route is more recent and involves replacing the superalloy with a ceramic matrix composite (CMC) wherein both the matrix and fibers are derived from SiC; the latter is both lighter weight and capable of higher temperatures than modern nickel-based superalloys [7,8]. However, SiC oxidizes and volatilizes when exposed to high temperature/pressure/velocity flowing water vapor as typical of the combustion environment. Thus, a ceramic environmental barrier coating (EBC) is employed to act as a volatilization barrier [7,9]. The EBC material must be closely matched thermally to SiC to minimize stresses that can lead to cracking upon thermal cycling, compromising the hermeticity of the coating. In both routes, then, the integrity of the structural component relies on a protective coating—the latter are subject to their own challenges and failures when the engine operation temperature, and hence the thermal excursion during cycling, is continually increased.

The degradation of thermal and environmental barrier coatings (T/EBCs) by molten silicates represents a major barrier to increasing the operation temperatures [10,11]. These melts, collectively known as CMAS for their primary constituents (CaO, MgO, $AlO_{1.5}$, SiO_2) form in the hot gas path from siliceous debris ingested with the intake air. The molten silicates dissolve the T/EBC oxides, which modify the melt composition and often trigger the crystallization of new or modified phases. The effect of these reactions depends on the type of coating and the characteristics of the products. For TBCs the primary goal is to minimize melt penetration into the coating's open porosity which

enables strain tolerance. This requires rapid dissolution of the TBC and crystallization of reaction products, particularly stable phases that consume a substantial fraction of the melt constituents. The preeminent example is the Ca+rare-earth oxi-apatite [10]. Conversely, EBCs typically react with the melt, creating products that are less optimally matched to the SiC CMC thereby increasing the driving force for cracking and delamination of the coating. In sum, the thermochemical interaction with CMAS induces thermomechanically driven failure mechanisms that limit the life of the entire system. The search for novel T/EBCs that withstand CMAS degradation while maintaining the other requisite properties for the coatings (e.g., phase stability, low thermal conductivity, acceptable toughness, CTE, stability in combustion environments, etc.) is still ongoing and of critical importance.

The development of next-generation T/EBCs requires a deep understanding of how the coatings react with CMAS to minimize the thermomechanical impact of the latter. Simultaneously, the complexity and size of the relevant composition space—silicate melts can contain any combination of 3–6 oxides and the coatings are produced from another group of 6–8 relevant oxides—precludes a solution approach through experiments alone. Instead, a more fundamental understanding of the mechanisms, thermodynamics, and kinetics of coating-melt interactions must be developed. The insight would guide the development of coupled models, via an Integrated Computational Materials Engineering (ICME) approach, capable of predicting the thermochemical and thermomechanical performance of candidate coating materials to a menu of possible silicate melts [10]. While a significant body of research, outlined in the subsequent chapter, has established the phenomenology of CMAS-T/EBC interactions, there remains a paucity of fundamental understanding needed to

guide coating design, especially of the mechanisms and associated kinetics. That need motivates the present dissertation. The work that follows will advance the fundamental understanding of *(i)* the kinetics, including how quickly T/EBC oxides dissolve into and diffuse within silicate melts; *(ii)* the mechanisms, including how crystallization develops the reaction microstructures and how systems approach equilibrium via non-equilibrium pathways; *(iii)* how the kinetics and mechanisms would be expected to manifest on coating relevant length scales; and *(iv)* the thermodynamics of the garnet phase, an important reaction product.

To accomplish that goal, the dissertation is organized as follows. Chapter 2 will provide relevant literature background and concepts to motivate the present studies. The experimental and quantification methods are detailed in Chapter 3.

A 1D diffusion couple geometry was employed with short-duration experiments to study the dissolution of barrier oxides (BOs) into molten silicates and the diffusion of BO cations therein, which is presented in Chapter 4. These rates will be quantified, via concentration profiles, for the first time. The kinetic response of multiple BOs is compared.

Chapter 5 investigates the microstructural development of the interaction/reaction zones once crystallization has begun. The observed microstructures will be framed by the expected response from relevant thermodynamics, i.e., deviations from the thermodynamically predicted crystallization pathway will be noted. The deviations will be framed in the context of the dissolution mechanism from Chapter 4. Furthermore, the response of different barrier oxides will be contrasted leveraging the kinetic insight gathered by Chapter 4.

The quantified dissolution and diffusion rates will be applied to finite element models on coating-relevant length scales in Chapter 6. The models provide insight for materials selection. Other implications for coating design will be discussed therein.

The focus shifts to a study of the thermodynamics of iron and iron/aluminum-based garnets, an important but poorly understood reaction product, in Chapter 7. The work will enhance existing CALPHAD thermodynamic databases relevant for coating design.

Finally, conclusions, outlook, and recommendations for future work are presented in Chapter 8.

1.1. Figures

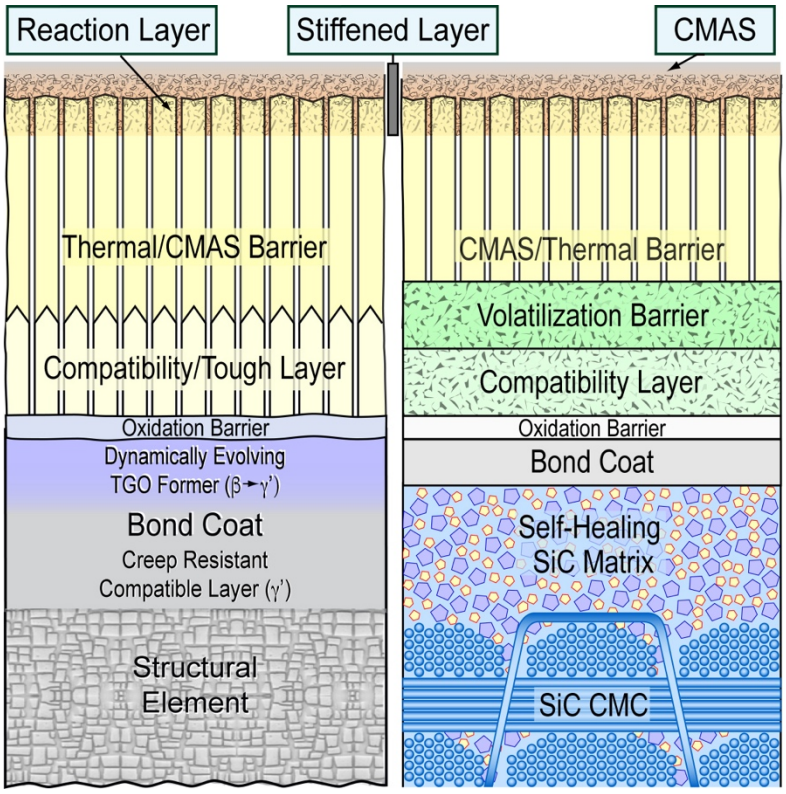

Fig. 1.1: Schematics of protective coatings employed in gas turbine engines. Both thermal barrier coatings (TBCs, left) and environmental barrier coatings (EBCs, right) employ a bond coat to afford oxidation resistance to the underlying structural component. The TBC provides a temperature drop through thickness, limiting the surface temperature of the metallic superalloy. The EBC instead provides a volatilization barrier, protecting the underlying SiC structural component from water vapor. Both coatings are susceptible to failure when exposed to ingested siliceous debris (CMAS).

CHAPTER 2. BACKGROUND

The technical problem, as outlined in the introduction, is multi-faceted and includes the interaction of complex engineered systems with ingested debris. This chapter will provide a general background of gas turbine engines; the protective coatings they employ and their necessary properties; as well as the nature of siliceous debris and its mechanisms of coating degradation. This background builds up to the key mechanism: reactive crystallization—the crystallization of new solid phases containing elements from both the ingested debris and from the protective coating. The formation of such phases (a thermochemical process) can be either beneficial or deleterious to the thermomechanical response of the system. Furthermore, the thermochemical process is complicated—it involves the coupled thermodynamics of 5–8 component systems with the kinetics of coating dissolution, diffusion, nucleation, and growth.

The remainder of the chapter will provide background and summarize key prior studies on reactive crystallization and its constituent processes. The goal is to understand reactive crystallization via an ICME-based approach, as alluded in the introduction, which demands a fundamental understanding of the underlying kinetic and thermodynamic processes. The key points that will be summarized include dissolution mechanism of solid oxides into molten silicates, cation diffusion within molten silicates, the efforts to understand the relevant thermodynamics by building CALPHAD (CAlculation of PHAse Diagrams) databases, and the relevant reactive crystallization phases.

2.1. Gas turbine engines

Gas turbine engines are used to provide thrust for aircraft, generate electricity on land, or propel ships at sea. Despite their diverse applications, the operating principle of these engines are identical: use continuous combustion to rotate a shaft. A schematic of a turbofan engine—used in commercial passenger aviation—is shown in Fig. 2.1. There are three key stages. First, air ingested into the engine core gets compressed by a series of stationary and rotating airfoils. Second, the compressed air, now optimized for ignition, enters the combustion chamber where it is mixed with fuel and ignited. This greatly increases the gas temperature and pressure, accelerating it to the entrance of the third stage: the turbine section. This consists of a series of airfoils, similar to the compressor stage, with alternating stationary guide vanes and rotating turbine blades; the latter attached to the central axis of the engine. The turbine section is responsible for extracting energy from the hot gas flowing through it, driving a rotating shaft that spins the compressor stage and the large fan at the front of the engine. After converting most of its energy, the gas is exhausted providing a portion of additional thrust.

The ubiquity of gas turbine engines and their reliance on combustion has motivated, and continues to motivate, a significant effort to increase their efficiency. As suggested by the Carnot and Brayton Cycles (which apply to heat engines and gas turbines, respectively) increased efficiency is obtained by hotter combustion gases [12]. An appropriate rule of thumb is a 1% efficiency increase per ~30 °C [13]. Simultaneously, higher temperatures burden key components of the engine, e.g., the turbine airfoils, create new degradation mechanisms, and exacerbate existing ones. Thus, increasing engine efficiency demands new materials and architectures tolerant of the increased demand. This is

generally true throughout the entire engine, but the turbine section is uniquely demanding—it experiences extreme temperature from the combustion gasses and the rotating components must simultaneously withstand high centrifugal stresses.

Materials within the hot turbine section have incrementally improved for decades enabling higher operation temperatures, Fig. 2.2 [7,13–15]. The base material of the turbine section components are metallic Ni-based superalloys. These have exceptional high-temperature strength and creep-resistance afforded by a two-phase γ-γ' microstructure [13]. The creep-resistance has been improved significantly through three primary development avenues: alloy composition improvements, processing improvements culminating in casting the components as single crystalline (eliminating grain-boundary driven creep mechanisms), and by introducing internal and surface film cooling to the blades (reducing the alloy temperature for a given gas temperature). Thermal protective systems, shown schematically in Fig. 2.3(a), provide additional temperature resistance beyond that intrinsic to the superalloy. Immediately adjacent to the superalloy is the bond coat. This aluminum-rich metallic coating forms a thin, dense thermally grown oxide (TGO), imparting oxidation protection to the superalloy. The hottest sections (e.g., the first stage turbine immediately after the combustor) employ an additional ceramic topcoat ~150–300 μm thick for aircraft engines or up to ~1 mm thick for power generation; this low thermal conductivity ceramic affords a significant temperature decrease through-thickness and completes the thermal barrier coating (TBC) system. This system—a single crystalline superalloy equipped with air cooling and a TBC—represents the current day in the established aircraft turbine section materials.

2.1.1. Thermal barrier coatings

A TBC must exhibit multiple critical, and often competing, properties to be effective and survive the conditions of gas turbine engines. In reality, no perfect coating material exists; acceptable tradeoffs are obtained through careful materials selection and processing to enhance or diminish traits. The key property is a low thermal conductivity (κ) to maximize the temperature decrease through the coating's thickness (minimizing the superalloy's surface temperature for any given gas temperature). The coating must be phase stable, resistant to volatilization in high temperature water vapor, and thermochemically compatible with the TGO layer (alumina in current technology); failure to meet either criterion will result in stress development at temperature or during thermal cycling of the engine, ultimately leading to coating failure. The oxides of zirconium and hafnium most readily meet these critical properties but are also poorly thermally matched to superalloys. The practical solution is to produce a TBC with a segmented (or porous) microstructure, which offers both some microstructural control over the effective κ through thickness and affords an in-plane compliance and tolerance to thermal mismatch strains with the superalloy. However, it is imperative that the ceramic have a reasonably high sintering resistance to maintain this microstructure. In addition, increasing the coating porosity degrades its erosion resistance; therefore, the TBC material should possess a high toughness to counteract this effect and to afford additional resistance to thermal mismatch stresses.

The necessary porous microstructures are typically produced using one of two disparate methods: atmospheric plasma spray (APS) or electron beam physical vapor deposition (EB-PVD). In APS, a fine ceramic feedstock powder is fed into a plasma jet, which melts the powder and accelerates it

towards the desired metallic part [16–18]. The coating is then built up "splat-by-splat" up to the desired thickness. The resulting mesostructure, Fig. 2.4(a), contains porous inter-splat regions, which primarily run parallel to the substrate and act to reduce the effective κ for the coating; some strain tolerance is afforded by microcracks in the coating. The advantages of APS lie in its ease of processing and its substantial reduction in κ. Plasma torches fit readily to six-axis robotic arms enabling large parts with complex geometries to be coated, all under atmospheric conditions. The technique allows for thick coatings to be applied, reaching up to 1 mm for electricit generation and industrial power applications [19].

Conversely, coatings produced by EB-PVD are substantially more expensive to produce. In this technique, a ceramic source ingot is heated with an electron beam under a partial vacuum; a melt pool is created on top of the ingot from which the material can be evaporated. The vapor deposits on the desired part, which is rotated throughout the deposition process to afford the desired microstructure: single crystalline columns separated by a thin (typically <1 μm wide) intercolumnar "gaps", Fig. 2.4(b). The columns themselves feature an additional "feathery" porosity that lowers κ, but less effectively than in APS coatings. The primary advantage of EB-PVD coatings is significantly enhanced strain tolerance due to the vertically aligned porosity. Ultimately, the microstructural benefits of EB-PVD motivates their application in the high-pressure turbine blades and vanes of aero engines, despite increased cost and lower throughput. APS coatings are then used for the remainder of the necessary locations, including in the combustion liners, shrouds, and in lower temperature locations of the turbine section. (Power generation gas turbines often rely exclusively on APS coatings as their part size precludes deposition using EB-PVD.) While this dissertation investigates neither

APS or EB-PVD coatings directly (see Chapter 3), discussion will extend primarily considering the microstructure of EB-PVD coatings.

The requisite properties and processability of the top coat (hereafter "TBC") are met by tetragonal zirconia partially stabilized with 7–8 wt% yttria (7YSZ, ~7.6–8.8 mol% $YO_{1.5}$), the industry standard for the past ~40 years [4,15]. The thermal conductivity of bulk 7YSZ (~2.5 W/mK [20]) is approximately an order of magnitude lower than that of superalloys [3,13] and can be further improved by the porous structures of TBCs; coatings produced by EB-PVD achieve $\kappa \approx 1.5$ W/mK and those produced by APS achieve $\kappa \approx 1.15$ W/mK. While ceramics with lower bulk κ exist, these values for 7YSZ are acceptable given its additional thermomechanical benefits. For example, 7YSZ has a relatively high CTE for refractory ceramics (~11 ppm/K, [21]) reducing the thermal mismatch strains with the high CTE superalloy substrate (~13–17 ppm/K, [3,22]). The still significant thermal mismatch strains are further mitigated by the segmented or microcracked microstructure of actual coatings. Here too 7YSZ has an advantage: its constituent oxides, ZrO_2 and $YO_{1.5}$, have similar vapor pressures affording compositionally uniform deposition and ease of processing by EB-PVD [23]. The resulting columnar microstructures reduce the effective transverse elastic modulus from ~200 GPa to ~40 GPa [24–26] thereby reducing stored elastic energy by 80%. The final component to the success of 7YSZ is its high intrinsic toughness, ~35–50 J/m2, which is on the order of the stored energy on thermal cycling [27–30]. This toughness has been attributed to ferroelastic switching, wherein the application of a stress (e.g., at a crack tip) reorients the tetragonal domains such that a compressive residual stress applies at the crack tip [30]. Other toughening mechanisms, e.g., crack bridging, can also be implemented in coating microstructures to further enhance the

toughness; for example, dense vertically cracked APS coatings have exhibited effective toughness as high as 350 J/m^2 [29].

There are three relevant phases for YSZ: monoclinic (*m*), tetragonal (*t*), and cubic (*c*). The relevant phase boundaries are shown in Fig. 2.5 for the ZrO_2-rich portion of the ZrO_2-$YO_{1.5}$ phase diagram. 7YSZ nominally exists in the two-phase *t*+*c* region at peak engine temperatures and the *m*+*c* region below ~1000 °C. The *t* to *m* transformation is disruptive with an approximately 4% volume expansion—repeated thermal cycling through this transformation must be avoided for long-term coating durability [15]. Zirconia can be fully stabilized in the cubic phase by adding high concentrations of $YO_{1.5}$ (e.g., ~20%), but cubic YSZ is much less tough than 7YSZ for coating applications [30]. Thus, the successful implementation of YSZ-based TBCs is due to the ability to create a tough, metastable tetragonal phase that is non-transformable on cooling, designated *t'*, which can be generated by either APS or EB-PVD.[a] The relevant composition range for *t'* is bounded by the T_0 curves (representing the temperatures where two phases have equivalent Gibbs free energy). The YSZ must contain sufficient $YO_{1.5}$ (~6%) to avoid crossing the T_0(t/m) curve on cooling, but not so much as to cross the T_0(c/t) curve at the target operation temperature. Traditionally, compositions with lower $YO_{1.5}$ are targeted because they exhibit higher tetragonality and toughness—thus the preeminent use of 7YSZ is established.

As engine gas temperatures have continued to increase, 7YSZ coatings have experienced intrinsic and extrinsic failure mechanisms that severely limit coating lifetime [31]. At temperatures exceeding

[a] In EB-PVD, the *t'* phase grows directly from the vapor. In APS, conversely, the phase forms from the transformation of the melt-crystallized cubic (c) phase upon cooling beneath the T_0(c/t) curve.

~1200 °C there is a sufficient thermodynamic driving force and kinetics for the metastable *t'* phase to transform to the equilibrium *t*+*c* two phase mixture [32–34]. The resulting *t* phase would undergo the deleterious monoclinic transformation upon cooling and drive cracking. Sintering has also been observed in 7YSZ coatings operated at high temperature, which compromises the in-plane strain tolerance of the coating and enhances thermal conductivity through thickness [35]. Extrinsically, 7YSZ coatings are also severely degraded by siliceous debris ingested with the intake air [10,31,36,37]. (This point will be elaborated in a later section.) Therefore, there is a need for novel TBC chemistries (and possibly architectures) to meet the temperature demands of next-generation engines. The search is complicated by requisite properties of a candidate TBC material—the material must show enhanced phase stability, toughness, sintering resistance, and molten silicate resistance, all while maintaining a low thermal conductivity and stability in flowing water vapor to fulfill its primary role.

2.1.2. Environmental barrier coatings

An alternative solution to the temperature limits of superalloys and TBCs has been developed in recent years, which involves replacing the superalloy with a ceramic matrix composite (CMC) [7,8,38]. These CMCs offer substantially higher temperature capabilities compared to superalloys while simultaneously having approximately one-third of the mass density. The state-of-the-art CMC comprises silicon carbide (SiC) fibers embedded in a SiC matrix. The key innovation is the thin boron nitride (BN) coating applied to the fibers, which deflects matrix cracks along fiber interfaces rather than propagating through the fiber. The net effect is a damage tolerant failure mechanism and high toughness despite the fully ceramic nature of the component. However, SiC is not stable in the combustion environment; it reacts with oxygen to produce a would-be passivating

SiO_2 scale, but the latter subsequently reacts with water vapor to form volatile silicon oxi-hydroxide species. The combined reactions ultimately recess the part at an aggressive rate, on the order of 1 μm/h in the conditions of gas turbine engines [9,39]. Thus, CMCs are prime reliant on an environmental barrier coating (EBC). This is achieved in two parts: a Si bond coat to form a thermally grown SiO_2 oxide (serving as an oxygen barrier and compatibility layer) and an oxide ceramic topcoat (serving as a water vapor barrier). Like TBCs, the EBC bond coat remains an active area of research (e.g., Ref. [40]); however, this dissertation will focus only on the ceramic top coat. For simplicity, the latter will hereafter be referred to as "EBC".

The purpose of EBCs controls the necessary properties for the coating; like TBCs, these properties are often competing and no perfect single EBC material has been discovered. The EBC must be dense and free of vertical cracks to hermetically seal the SiO_2 from water vapor. This imposes the key constraint on EBC materials: the coating must be closely matched thermally to the SiC substrate to preclude crack formation on thermal cycling. The low CTE of SiC (~4–5 ppm/K) severely limits EBC materials selection to a subset of crystalline phases, mostly silicates. However, silicate EBCs are themselves susceptible to volatilization in water vapor—the material must therefore have a low silica activity (e.g., <0.1)[b] to survive for target lifetimes in the 5,000–20,000 of hours. It must also be phase stable throughout the operation temperature range, and it must be thermochemically compatible with the TGO (SiO_2).

Early research on EBC materials focused on mullite ($Al_6Si_2O_{13}$) and barium–strontium aluminosilicate (BSAS), but these materials were ruled out due to issues with volatility and

[b] The rate of volatilization is linearly proportional to the silica activity [41].

compatibility with SiO_2, respectively. The current state-of-the-art EBCs are rare-earth silicates, which include a disilicate ($RE_2Si_2O_7$) and monosilicate (RE_2SiO_5). In particular, the ytterbium silicates (RE=Yb) are arguably the most likely to be put into service; these are phase stable up to melting (~1920 °C, [42]), avoiding the many polymorphic transformations observed in other RE silicates [43], thermochemically compatible up to ~1750 °C [42], and are more cost efficient than other phase stable REs (e.g., Lu, Sc).[c] The disilicates (DS) are favored for their closer CTE match to SiC (e.g., ~4 for YbDS) [44]. But, they exhibit a larger silica activity of ~0.1 [41,42], which would limit coating lifetime and therefore increase the engine service frequency. Conversely, the monosilicates show a larger CTE (~7 ppm/K for YbMS) but exceptionally low silica activities (~0.01) [41,42,45]. The envisaged approach[d] uses a bilayer EBC, e.g., Fig. 2.3(b), coated by careful plasma spray of heated substrates [46]. The primary layer is YDS/YbDS deposited immediately upon the Si bond coat; YbMS is deposited as a thin layer (minimizing the thermal mismatch stresses) atop the YDS/YbDS to provide additional water vapor resistance. However, novel EBC materials are still being sought to further decrease the silica activity (ideally being silica-free), ensure compatibility with future bond coats (the melting point of Si currently limits the operation temperature of current EBCs), and improve the resistance of the coatings to molten silicates, which will be elaborated further.

[c] The yttrium silicates are widely studied in the academic literature. While these are not phase stable, their transformations are sufficiently sluggish to enable study for fundamental investigations.

[d] CMCs and their protective EBCs began limited operation in commercial aviation in 2016 in the CFM International LEAP engine. The EBC system employed is not yet public information.

2.2. Molten silicate degradation of coatings

Aerospace engines will unavoidably encounter airborne siliceous debris during normal operation conditions. At low temperatures (e.g., cruise conditions) this debris threatens erosion, clogging of cooling channels, or loss of power [47,48]. However, at elevated temperatures (e.g., take-off conditions and next-generation temperature targets) the debris can melt and significantly degrade the protective TBCs or EBCs, including ultimate loss of coating. This section first provides background on the siliceous debris, then establishes the mechanisms of coating degradation and mitigation strategies for TBCs and EBCs. For both coating types, coating failure is fundamentally thermomechanical in nature, but the thermochemical response of the coating to the molten siliceous debris dictates the severity of the damage.

2.2.1. Siliceous debris is ubiquitous

Siliceous debris is ubiquitous, and its chemistry is diverse. However, the oxides of calcium, magnesium, iron, aluminum, and silicon make up the vast majority (~90%) of the Earth's upper mantle [49] and have therefore been vastly investigated both in the materials science and geological literatures. Within the context of the gas turbine literature, mixtures of these oxides are generically known as CMAS and generally come from three sources: *(i)* sand and dust, e.g., from deserts; *(ii)* volcanic ash; and *(iii)* fly ash, e.g., from fossil or biomass fuel [10]. The CMAS source affects the general composition trends as summarized in Fig. 2.6 [31]. The two most relevant types of siliceous debris are arguably sand and ash. Sands consist primarily of CaO and SiO_2, with minor additions of MgO, $AlO_{1.5}$, and FeO_x. Volcanic ashes tend to be SiO_2-rich and typically have more FeO_x than other sources. Ultimately, however, the composition of ingested debris often represents an assortment of

multiple sources due to atmospheric mixing (outside of highly localized exposures like a volcanic ash plume). Both the local concentration and composition (i.e., the ratios of the primary constituents) of what is ingested evolves constantly.

One must distinguish between the composition of the bulk deposit, and the composition of the liquid it can form at a given temperature. Ultimately, the *composition* of the liquid in contact with the barrier coatings is all-important. It controls one side of the thermochemical response in reactive crystallization (or lack thereof), as explored in previous sections, and determines the relevant melt properties at the temperature of interest. The latter includes its viscosity (a manifestation of the melt's structure), its tendency to vitrify or crystallize (and the relevant temperatures for each), and the CTE of the glass or crystalline product(s) it forms. These properties are important to understand in the context of coating degradation. For example, melt viscosity will directly affect the infiltration kinetics into TBC porosity; likewise, the CTE of the vitrified melt (or crystallized phases) will directly affect the thermal mismatch stresses placed on EBCs. A holistic approach is needed to address the problem of CMAS-induced coating degradation.

This first requires an understanding of the liquid composition ranges. The relevant phase equilibria for combinations of CaO-MgO-FeO_x-$AlO_{1.5}$-SiO_2 have been thoroughly investigated in the literature, and thermodynamic databases have been developed to predict phase stability at relevant temperatures [50–52]. Isothermal sections of the CaO-$AlO_{1.5}$-SiO_2 phase diagram are presented in Fig. 2.7 at (a) 1300 °C and (b) 1500 °C [10]; these temperatures represent target temperatures for TBC and EBC systems, respectively. The single-phase liquid region (dark shaded) makes up only a small portion of the phase diagram at 1300 °C but the extent of the phase diagram that contains any

liquid in equilibrium (light shaded) is substantially larger. The shape of the liquid field suggests a narrow range of $AlO_{1.5}$ concentrations will be relevant, but the Ca:Si ratio of CAS melts may vary significantly. However, minor (e.g., 10 mol%) MgO and/or FeO_x additions evolve the shape and size of the single-phase liquid region, e.g., Fig. 2.7(c) at 1300 °C. The primary effect is a "widening" of the liquid field with respect to the concentration of $AlO_{1.5}$; a secondary effect from MgO additions is the crystallization of melilite and spinel which suppress CaO-rich liquids. By 1500 °C, almost all ingested CAS deposit would at least be partially molten, and the single-phase liquid field expands substantially. The implication is that molten CMAS exposures will become more frequent and their chemistries more diverse as engine temperatures increase.

2.2.2. TBC degradation by molten silicates

The TBC's reliance on porosity (either from APS or EB-PVD) introduces their susceptibility to damage by molten silicates. When inevitably ingested into the engine, siliceous debris can melt, readily wet the TBC and infiltrate its porosity (driven by capillarity), solidify,[e] and significantly stiffen the effective in-plane modulus of the coating. For example, the in-plane modulus for a pristine 7YSZ coating (~40 GPa) increases to ~170–185 if fully infiltrated, approaching the 200 GPa modulus of bulk 7YSZ [24]. The result is a buildup of elastic strain energy on cooling and, if the energy surpasses the critical energy release rate, a driving force for coating delamination [26,31,53]. (The molten silicate can also react with the alumina TGO or cause creep cavitation of the bond coat [31].) The full mechanics solutions have been worked out as a function of molten silicate penetration

[e] Molten silicates can solidify—either by crystallization or vitrification—by two routes. First, engine cooling (e.g., the plane transitioning from take-off into cruise). Second, by the melt penetrating far enough into the TBC's imposed thermal gradient that the temperature is no longer above the solidus.

under temperature gradients by Jackson et al. [24] building on past works [53–55]. The key result for this dissertation is that the driving force for delamination (energy release rate, G) increases non-linearly with the silicate melt penetration depth, as shown in Fig. 2.8 [24]. The implication is that minimal damage is done if the penetration is prevented or arrested near the coating surface.

Unfortunately, silicate melts can have low viscosity at the temperatures of interest resulting in rapid infiltration rates. This is illustrated in the insets of Fig. 2.7(a,b), which plots isopleths of melt viscosity throughout the liquid phase field at 1300 °C and 1500 °C; calculated infiltration times for an isothermal 150 μm EB-PVD TBC are presented for each isopleth. Melt viscosities span orders of magnitude (~10^{-6}–10^{4} Pa·s at 1500 °C) resulting in a concomitantly large variation in isothermal infiltration times, from less than 1 s to 1 h. (The actual infiltration times under a thermal gradient would be slower due to temperature dependent viscosities, but one would still expect a similarly large range resulting from relatively modest composition ranges.)

The current TBC, 7YSZ, is inadequate when exposed to molten silicates because it does not possess a mechanism to arrest the infiltration. Both ZrO_2 and $YO_{1.5}$ are soluble in CMAS melts; thus, the initial response involves the CMAS simultaneously dissolving the *t'*-7YSZ coating and infiltrating the coating's open porosity. The high ZrO_2 concentration in 7YSZ leads to Zr^{4+} saturation in the melt and a yttria-depleted, *t*-zirconia phase (*t* in Fig. 2.5) reprecipitates thereafter [37,56]. The latter is harmful for three reasons. First, it provides a mechanism for continued coating dissolution, i.e., dissolution does not cease upon ZrO_2 melt saturation. In practice this often results in large interaction zones consisting of reprecipitated t-zirconia and CMAS (e.g., Ref. [56]). Second, the t-zirconia contains insufficient yttria to avoid the tetragonal to monoclinic transformation on cooling

(Fig. 2.5) [56,57]. The associated volume expansion can stress the infiltrated coating, particularly if the reprecipitated material grows epitaxially on the parent structure [56]. Third, the dissolution of 7YSZ *increases* the volume of melt, which is not adequately counterbalanced by the reprecipitated phase [58].

Therefore, 7YSZ coatings depend on intrinsic crystallization—the formation of crystalline phase(s) containing only melt constituents, e.g., those found in Fig. 2.7—to consume the melt and arrest penetration. This is an inherently unreliable mechanism because it relies on undercooling the melt. The thermal gradient through the TBC's thickness means the melt will cool as it infiltrates the coating; but silicate melts tend to be good glass formers. In practice, infiltration is rapid, which affords rapid cooling rates, poor intrinsic crystallization, and significant penetration of even supercooled liquids [10,24,59]. Melts with high FeO_x content have been observed to crystallize more readily, due to an expanded menu of crystalline phases and an evidently enhanced driving force for crystallization. However, the variability of melt compositions, Fig. 2.6, demands a melt agnostic solution. Furthermore, intrinsic crystallization will become precluded altogether as target surface temperature increase and keep the CMAS above the solidus.

Instead, the solution approach for TBCs has involved finding novel coating chemistries that, when exposed to CMAS, promote the rapid formation of crystalline *reactive* phases, i.e., phases that contain both melt and TBC constituents. Like intrinsic crystallization phases, reactive phases contain melt constituents and therefore act to consume the melt and block infiltration channels; but the nucleation of reactive phases can be triggered by TBC dissolution well above the liquidus of the CMAS. This affords a more "active" mitigation strategy known colloquially as *reactive crystallization*.

For the mechanism to be successful, however, the nucleation and growth must occur on a timescale competitive with the rate of melt infiltration, the growth morphology must be favorable to block infiltration channels, and the reactive phase must efficiently crystallize a large volume of melt per volume of TBC dissolved (i.e., have a high V_{crys}:V_{TBC}).

The prototypical example of this mechanism was first observed in the interaction of EB-PVD gadolinium zirconate ($Gd_2Zr_2O_7$, GZO), a candidate TBC material with improved phase stability, κ, and sintering resistance, with a $C_{33}M_9A_{13}S_{45}$[f] melt by Krämer et al. [60], shown in Fig. 2.9 [31]. Like 7YSZ, GZO dissolved into and locally saturated the $C_{33}M_9A_{13}S_{45}$ melt at dissolution fronts; excess ZrO_2 crystallized as a Gd-depleted zirconia phase (fluorite/cubic with 13–24% $GdO_{1.5}$). But the key difference is that GZO contains substantially more RE^{3+} than 7YSZ and enables RE-based reactive phases to form. In this case the excess $GdO_{1.5}$ reacted with CaO and SiO_2 to form a Gd-oxyapatite silicate phase, Fig. 2.9(b,c), with a nominal composition of $Ca_2Gd_8(SiO_4)_6O_2$ [60]. The latter rapidly nucleated (e.g., within ~30 s in Fig. 2.9c), grew as needle-like grains, and had a favorable *Vcrys*:*VTBC*, all helping to seal infiltration channels. In sum, the GZO coating successfully limited infiltration to <30 μm from the coating surface even under more demanding isothermal conditions. Similar performance has been observed in exposures of APS GZO coatings [61], and the EB-PVD material has shown success in actual engine tests [31] although little information is publicly available.

From a CMAS mitigation standpoint, the ideal TBC would maximize apatite formation. All RE zirconates across the lanthanide row, e.g., La^{3+} [62], Nd^{3+} [63], Gd^{3+} [60], Sm^{3+} [64], Yb^{3+} [65], and

[f] CMAS concentrations are expressed in mole percent of the oxide formulae based on a single cation, using the first letter of the oxide, i.e., C=CaO, M=MgO, F=FeO_x, A=$AlO_{1.5}$ and S=SiO_2.

Y^{3+} [58] are apatite formers. However, not all the REs crystallize the same quantity of apatite because dissolved RE can be captured by other (less useful) phases [10,66]. The primary concern is the reprecipitated zirconia phase, which can capture a significant portion of the dissolved RE (e.g., up to 60–80% for Yb^{3+} [66]). A systematic investigation by Poerschke et al. has shown larger RE cations (e.g., La^{3+}) exhibit the best behavior here: their reprecipitated phase contains minimal RE^{3+} (e.g., <6% for La^{3+}), leaving most of it to form apatite [66]. In addition, the large RE cations do not crystallize other RE-silicate reactive phases with less favorable kinetics, like silicocarnotite and garnet [58].

To summarize, the CMAS mitigation strategy for TBCs relies on the rapid crystallization of reactive phases, primarily apatite, to block infiltration channels and minimize in-plane stiffening of the coating. This mechanism is best achieved with $Gd_2Zr_2O_7$ or $La_2Zr_2O_7$ at target temperatures of 1300 °C. Both candidate TBCs minimize the amount of RE captured in the not useful reprecipitated zirconia thereby maximizing apatite formation. However, these materials have their own challenges. Most significantly, the RE zirconates show lower toughness [67] (leaving them vulnerable to erosion or delamination from partially infiltrated coatings), are not thermochemically compatible with an alumina TGO [68], and can be challenging to deposit (especially for La^{3+} [69]). Furthermore, RE zirconates may be less viable at higher temperatures (≥1400 °C); decreasing melt viscosities will accelerate infiltration rates, and more RE is captured in the reprecipitated phase [10]. No single material to-date satisfies all the property requirements of TBCs necessary for higher temperature operation. Thus, the search for novel TBC materials and processing methods—including bilayer approaches, e.g., 7YSZ/GZO [70], to address the toughness and compatibility issues of pure GZO—is still ongoing and motivates further research.

2.2.3. EBC degradation by molten silicates

CMC component lifetime is limited by EBC loss. This loss occurs slowly by exposure to water vapor (for silicate based EBCs), but the coatings are also significantly degraded by CMAS melts. There are two pertinent mechanisms that often act simultaneously—both reduce the EBCs thickness and its efficacy as a diffusion barrier. First, EBCs are directly consumed (i.e., dissolved) by CMAS melts. The amount of consumption can be extensive, including full consumption in as little as tens to hundreds of hours [10,71–73], especially for Ca-rich melts. Second, coating dissolution leads to the formation of reactive phases—most typically and importantly apatite—that are poorly thermally matched to the SiC components [74–76]. Large in-plane tensile stresses develop in the deposit and reaction layers, which impose a driving force for cracking in the nominally dense EBC [10,77]. The channel cracks provide rapid diffusion pathways for water vapor and oxygen and can link with others to cause local coating spallation [10,78]. The severity of damage (i.e., the likelihood for cracking) increases as the CTE mismatch between SiC and the reaction layer or residual melt increases, and as the thickness of those layers increase.

Both the RE disilicates and monosilicates react with most CMAS to form apatite by unique mechanisms. The disilicates react to form apatite via:

$$4RE_2Si_2O_7 + 2CaO\ (melt) \rightarrow Ca_2RE_8(SiO_4)_6O_2 + 2SiO_2\ (melt)$$

Thus, an equimolar exchange of CaO for SiO_2 occurs, resulting only in a minor change to the melt volume. In this sense, the reaction will continue until equilibrium is reached between the melt and the coating (i.e., when further dissolution would be limited by the saturation limit of the disilicate, which may reprecipitate on cooling). The latter occurs when the SiO_2 concentration in the melt is

sufficiently enriched (and the CaO sufficiently depleted per the reaction). The monosilicates react with CaO and SiO_2 in the melt to form apatite via:

$$4RE_2SiO_5 + 2CaO\,(melt) + 2SiO_2(melt) \rightarrow Ca_2RE_8(SiO_4)_6O_2$$

Thus, the reaction acts to consume the melt, like apatite formation in TBCs but less efficient because two-thirds of the SiO_2 captured in the apatite is from the EBC. Melts with low Ca:Si ratios will also form the disilicate via:

$$RE_2SiO_5 + SiO_2\,(melt) \rightarrow RE_2Si_2O_7$$

Thus, the RE-monosilicates react with CMAS to form apatite and RE-disilicate. The reactions will continue until the entirety of the melt is consumed if the system is taken to equilibrium.[g] The minor melt oxides, MgO, $AlO_{1.5}$, and FeO_x, will primarily crystallize as intrinsic phases (e.g., melilite, anorthite, and spinel).

Summers et al. have systematically investigated the consumption and reaction of yttrium disilicate and monosilicate (YDS and YMS) to a diverse range of molten silicates by leveraging computational thermodynamic databases and carefully designed experiments [79,80]. Thermodynamic equilibrium calculations suggest that the amount of YDS recession is significantly sensitive to the starting Ca:Si ratio of the melt, Fig. 2.10(a). Melts with high CaO concentrations consume more YDS and yield more apatite before reaching equilibrium; conversely, CaO-lean melts generally avoid forming apatite altogether and experience minimal recession. Complementary experiments were using three representative CMAS compositions (Ca:Si of 0.14, 0.33, or 0.72) largely validated the recession

[g] Note that residual CaO and SiO_2 may still exist when reaction ceases. The key point is that enough CaO and SiO_2 have been removed that the liquid is no longer thermodynamically stable.

distances predicted by the thermodynamic calculations, Fig. 2.10(c); the implication is YDS reacted until equilibrium was reached. Notably, increasing the temperature of the experiments had little effect on the recession depth but did decrease the time necessary to obtain equilibrium.

Conversely, equivalent calculations on YMS suggest its recession is *much less sensitive* to the melt composition. Regardless of the initial Ca:Si ratio, the reaction ceases within a narrow range of YMS consumption, Fig. 2.10(b), after the Ca:Si ratio of the melt decreases below ~0.2. This was attributed to the fact that YMS and most silicate melts are not thermodynamically stable in contact with one another—reaching equilibrium necessitates entire consumption of either the melt or the YMS coating. The predicted amount of YMS dissolution, about 2.5 times the initial deposit thickness, was subsequently larger than that predicted for YDS (0.25–1.5). However, the experimentally observed recession depths in YMS were significantly lower than expected, Fig. 2.10(c), indicating YMS did not reach equilibrium. Instead, dissolution was kinetically constrained by the formation of a dense and mostly hermetic apatite layer Fig. 2.10(d). The net result was the experimental recession depth of YMS was either comparable to or better than YDS. The experiments also showed YMS recession experimentally varied with the melt Ca:Si ratio, with more extensive recession observed for Ca-rich melts, Fig. 2.10(c). The initial melt composition, therefore, primarily controls the reactivity of both monosilicate and disilicate EBCs.

In practice, both YMS and YDS can react extensively with molten silicates, and the Ca:Si ratio of the melt is the dominant factor determining the extent of reaction. In theory, the dense nature of EBCs means the coating response will be dominated more by thermodynamics than kinetics, but the latter clearly plays a role in YMS recession and reaction. Even still, the relatively large recession depths of

both YMS and YDS under CaO-rich melts are likely troublesome for application. This motivates the search for novel EBC chemistries. Two routes for the ideal EBC are envisioned: one seeks to maximize the melt reactivity to fully crystallize the melt with minimal coating dissolution; the other seeks to minimize reactivity either by increasing the thermodynamic stability of the coating or finding a system which forms a dense, shielding layer to slow the kinetics. Another proposed solution involves the application of a segmented CMAS barrier (e.g., EB-PVD GZO) on top of the EBC, which would act as a CMAS barrier. Regardless, all approaches will require an understanding of how the coating oxides react with the relevant range of CMAS compositions, including the relevant thermodynamics and kinetics.

2.2.4. Summary of coating degradation

In summary, both TBCs and EBCs can react with molten silicates to form new crystalline phases that contain oxides originally from the melt and coating. This reactive crystallization is all-important—its details (the thermodynamics and kinetics) dictate the elicited thermomechanical response of the coating. In the case of TBCs, the reactive phase must form quickly and efficiently solidify the melt to arrest the latter's penetration into the TBC; thus, the coating must elicit a favorable thermodynamic response and the crystallization kinetics must compete with the infiltration kinetics. In EBCs, reactive crystallization is mostly deleterious. It consumes the coating, and the phases that crystallize impose a thermal mismatch stress, which leads to loss of coating. The interaction is primarily driven by the thermodynamics, but kinetic effects can become important in the case of crystallization that affords a shielding layer.

The solution approach must therefore understand how coating oxides reactively crystallize with the entire composition range of CMAS that could possibly be ingested into the engine and melt. The relevant composition spaces are large, including a 4–6 component melt in contact with RE-zirconates, hafnates, and silicates. Furthermore, the thermochemical interaction is intimately dependent on temperature (which may vary temporally or spatially), and the reaction kinetics depend on the coating microstructure. (The thermomechanical response will also depend on the thermophysical properties of the as processed coating, not necessarily those of the bulk material.) Ultimately, the problem of CMAS-induced coating degradation is too complex to solve by experimental iteration alone.

2.3. Envisaged solution approach

An efficient solution approach is envisioned in the development of coupled computational models capable of assessing the durability of coatings exposed to molten silicates [10]. The framework, depicted in Fig. 2.11 [10], includes descriptions for the system design (the coating microstructure, properties, and service conditions), the coating-melt interactions (the thermodynamics and kinetics of reactive and non-reactive crystallization), and the subsequent thermomechanical response. When fully implemented, the framework could be used to identify promising coating systems after extensive virtual tests varying the CMAS composition and dosage, temperature, duration, etc. The most promising candidates could then be validated with minimal experiments. It would also benefit the interpretation of ex-situ service hardware. Parts of the framework have been developed—particularly in models for melt properties, thermomechanics, and thermodynamic databases—but additional model development work is needed, which this dissertation will partially address.

The best example of the framework in action is found in modeling EBC materials because of the dominant role of thermodynamics in their degradation. This was recently demonstrated by Summers et al. [77] for model YDS coatings of arbitrary thickness with appropriate material properties (CTE, elastic modulus, and toughness). A CMAS deposit of arbitrary composition and thickness was applied to the model coating and the expected extent of consumption and reaction products was estimated using the ThermoCalc and the TCOX6 thermodynamic database [81]. The latter includes descriptions for $YO_{1.5}$ in CMAS and is reasonably well optimized around apatite formation, the primary product in YDS exposures [79]. (Additional background on the thermodynamic databases and their strengths and weaknesses will be provided in a subsequent section.) The thermophysical properties of all layers and phases after reaction were applied from experimental measurements (e.g., CTE of apatite) or estimated from models (e.g., the CTE of CMAS glass from the Fluegal model [82]). Altogether, the energy release rates upon cooling some ΔT were calculated [83,84], the fracture behavior was predicted [85], and coating loss maps could be generated throughout CMAS composition space. The work by Summers et al. [77] clearly demonstrates the power of the ICME framework, but additional fundamental work is needed to refine the results and extend the method to other EBC chemistries. For example, YMS dissolution is kinetically constrained by a nearly hermetic apatite layer such that thermodynamic calculations may not accurately predict the amount of YMS consumption (Fig. 2.10c, [71,80]). In other cases, the formation of garnet was poorly predicted [80] or the EBC cations may be missing from the thermodynamic databases altogether (e.g., Yb^{3+}).

The degradation of TBCs is an inherently kinetic process and, therefore, the framework must be capable of modeling the relevant subprocesses. Ultimately, the competition between infiltration and crystallization rates directly controls the extent of coating damage.[h] Infiltration models have been explored in the literature with reasonable success [56,86], but both require an accurate estimation of the melt viscosity as a function of temperature. While multiple viscosity models for molten silicates have been developed, their predictions warrant some discussion. The empirical viscosity model by Giordano et al. [87] was calibrated using experimental viscosity measurements of geologically relevant silicate melts. All CMAS elements relevant for gas turbine applications are described but the speciation of iron oxide (i.e., the mixture of FeO and $FeO_{1.5}$) is not considered.[i] However, the paucity of experimental viscosity measurements on simple, synthetic melts limits its accuracy when applied to CMAS. Despite this, the model is freely available and is the most widely used in the TBC/EBC literature for estimations of melt viscosity. (Another empirical model developed by Fluegal [88] was calibrated on synthetic, technically relevant melts, e.g., borosilicates and E-glass, and is therefore not readily applicable to the CMAS found in gas turbines, but has been shown to give reasonable predictions in some cases [89].) An altogether different approach is found in the FactSage viscosity model [51], which relates the melt structure to the viscosity using its own thermodynamic database. This unique feature allows it to predict the ratio of FeO:$FeO_{1.5}$ at a given set of conditions and is therefore more applicable to the iron-containing melts. In practice, no single viscosity model is the

[h] The mechanics solutions to predict TBC damage are well established in the literature [24,53–55]. This has been incorporated into a computational package, LayerSlayer [83,84], which is readily integrated into the envisioned ICME framework.

[i] The model also describes other oxides arguably less relevant for gas turbine applications. Examples include: NaO2, KO2, P2O5, and MnO.

best across all composition space. The few existing comparative studies have suggested the Giordano model applies well to CaO-rich melts but poorly to SiO_2-rich melts [89–91], which are better fit to the FactSage model. Nevertheless, the existing viscosity and infiltration models allow one to readily estimate the infiltration times throughout all relevant liquid compositions that may come into contact with a TBC, e.g., Fig. 2.7(a,b) insets. Unfortunately, models to predict any aspect of the crystallization kinetics—including its subprocesses as elaborated later—are absent from the literature. This represents the critical knowledge gap for implementing the ICME framework to predict actual penetration depths.

Two outstanding knowledge gaps emerge in the ICME framework that will be addressed, in part, by this dissertation—both seek to enhance our understanding of reactive crystallization. First, the kinetic processes that prelude reactive crystallization, namely dissolution and diffusion, are not well understood. This gap precludes applying the modeling framework (Fig. 2.11) to TBCs where the kinetics of reactive crystallization is critical to compete with melt infiltration and limits application to some EBC materials. Second, the thermodynamic databases must be improved to better capture the formation of garnet, a reactive crystallization phase with large solid solubility ranges. This phase is particularly important to understand for EBCs; garnet has a large CTE mismatch with SiC and is more likely to form for small RE cations (e.g., Y^{3+} and Yb^{3+}) used extensively by EBCs. But the phase is often not adequately predicted, e.g., garnet was observed experimentally in YMS studies by Summers et al. [80] but was not predicted thermodynamically. The remainder of the chapter will provide additional background on these gaps.

2.4. Kinetics of reactive crystallization

Reactive crystallization is a complex phenomenon with multiple kinetic steps, each with the potential to limit the overall rate. The final steps involve the actual crystallization. Here the nucleation and growth rates of different phases may vary because of their crystal structure and the complexity of the polyhedral network they form. However, nucleation cannot occur until the melt is saturated in the relevant coating cation(s). The time before melt saturation represents a "transient period" wherein, for example, a TBC could be infiltrated with no possibility of arrest. Therefore, the kinetic processes that control this transient period are critical to understand.

The buildup of reactive cation(s) in the ensuing boundary layer toward saturation is mediated by the balance of the rate atoms are detached from the dissolving material and the rate of diffusional dissipation into the bulk melt. Three possibilities emerge, which are depicted in Fig. 2.12. If diffusion is very slow compared to the rate at which atoms are detached into the melt, Fig. 2.12(a), the concentration at the interface almost immediately reaches saturation and Fickian diffusion is recovered in the melt. This mechanism would afford rapid nucleation but likely limit further dissolution locally. Fig. 2.12(b) represents the opposite scenario: diffusion is very rapid relative to detachment rate. In this case, little concentration gradient exists through the melt, but the concentration builds as more dissolution occurs; as the entire melt becomes saturated at roughly the same time, nucleation could be immediately followed by growth. The third case, Fig. 2.12(c) represents a combination, where both diffusion and detachment occur at roughly equivalent rates. The result involves both a distinguishable concentration build up at the interface and concentration profiles throughout the melt. In this case nucleation would be delayed until the interface is saturated,

and growth would be further limited after that. Thus, the balance in detachment and diffusion rates have a direct impact on the transient period and on the nucleation and growth of reactive crystallization—despite this importance, these phenomena have not been significantly studied in the relevant literature.

2.4.1. Dissolution into silicate melts

Dissolution of TBC-relevant cations and materials was recently investigated by Chellah et al. [63,92] and Perrudin et al. [93,94], but with a methodology that arguably precludes fundamental insight. Their methodology involved creating powder mixtures of RE oxides and a calcium aluminosilicate, fusing the mixtures at the experimental temperature for 2–4 minutes (including two crushing stages), then exposing for longer durations (5–90 min). The RE concentration in the melt was measured ~10 μm away from nucleated phases or intact RE oxide particles. The results clearly show the concentration at this single point increases with time towards a plateau, but without a full concentration profile the dissolution mechanism cannot be ascertained. In essence, it is unclear if the observed increasing concentration was a result of slow detachment, slow diffusion, or both. Furthermore, the lengthy fusing duration at the experimental temperature and subsequent crushing introduces external disturbance to the dissolution process. The mixed powder nature of the experiment also creates issues with the analysis. First, it leaves the concentration in the melt susceptible to quench effects, observed throughout the geochemical literature (e.g., Ref. [95]). Second, it provides a more complex geometry—the dissolution occurs in 3D and powders are not uniformly mixed. Ultimately, the geometry can be useful to qualitatively investigate reactive crystallization (e.g., Ref. [10]), but it is inappropriate to understand or quantify kinetic processes.

Instead, some insight can be gained from the geochemical community, who have studied mineral dissolution into silicate melts and have developed crystal dissolution and diffusion models to quantify the processes. Here, simple 1D crystal-melt diffusion couples are set up with semi-infinite geometries. Concentration profiles are collected for multiple experimental durations; these enable cation diffusivities to be quantified and the dissolution mechanism to be identified. The dissolution of most minerals into silicate melts follows Fig. 2.12(a), i.e., the interface melt saturates in ~0.1–100 s and dissolution becomes rate-limited by diffusion into the bulk melt following a $t^{1/2}$ dependence [95–98]. However, quartz dissolution represents a notable exception to the above; it shows mixed control by detachment and diffusion following Fig. 2.12(c) [99]. This is not a result of an enhanced diffusion rate (the diffusivity of $(SiO_4)^{4-}$ is lower than most other cations [100]). The implication is that atoms are detached from the quartz crystal slower than most minerals.

Minerals with stronger bonds detach, and therefore dissolve, slower. Researchers have successfully applied the product of cation and anion charge involved in the actual bond breakage, $Z^+ \cdot Z^-$, a simple metric of bond strength, to predict the dissolution mechanism into water [98]. A similar type of dependence is expected to apply during dissolution by silicate melts. For example, the crystal structure of olivine, $(Mg,Fe)_2SiO_4$, consists of isolated $(SiO_4)^{4-}$ anion tetrahedra surrounded by Mg^{2+} and Fe^{2+} cations; its dissolution into silicate melts can occur primarily via the breaking of Fe-O and Mg-O bonds ($Z^+ \cdot Z^- = 4$) rather than Si-O bonds ($Z^+ \cdot Z^- = 8$). The resulting dissolution rate is very fast, following Fig. 2.12(a), where the interface melt is estimated to saturate in under 120 s [97]. Conversely, Si-O bonds must be broken in the dissolution of quartz—the result is slower dissolution, with a mechanism of Fig. 2.12(c) [99]. However, this remains primarily a phenomenological

observation; few experiments use the same melt composition, making it difficult to deconvolute the effect of the mineral composition alone.

The melt composition also affects the melt structure, its viscosity, and how quickly it can dissolve minerals or barrier coating oxides. In general, dissolution is faster in melts with lower viscosities. For most minerals—those with diffusion-limited dissolution mechanisms following Fig. 2.12(a)—this is a direct consequence of faster cation diffusion in lower viscosity melts. (These diffusional effects will be explored further in a subsequent section.) For minerals totally or initially limited by the rate of detachment, i.e., following Fig. 2.12(b,c), the enhanced detachment rates are most likely a result of greater site availability in low viscosity melts. The latter contain a significant proportion of non-bridging oxygens, enabling faster structural rearrangement of the melt to accept atoms when detached from the dissolving material. The detachment rate is also affected by the relative activities of components in the dissolving material and in the melt. For example, the detachment rate of quartz was observed to be heavily dependent on the silica activity of the melt [99]. This effect will likely be secondary for most TBCs—ingested siliceous debris will contain trace amounts of elements like Zr and rare-earths. Conversely, such an effect would be very important for the dissolution kinetics of RE-silicate EBCs.

2.4.2. Diffusion within silicate melts

Diffusion within silicate melts has been widely studied in the geological community—including the quantification of cations relevant to thermal and environmental barrier coatings—and was most recently summarized in 2010 by Zhang et al. [100]. Unfortunately, the available data is rarely transferrable to the geometry and conditions of gas turbines [101,102]. The problem of dissolution

and diffusion relevant to this dissertation immediately imposes a multicomponent diffusion problem. A full description would, therefore, require the full diffusion matrix to be experimentally determined, which is complex and expensive—an n component system contains $(n\text{-}1)^2$ unknowns to solve, requiring at least $(n\text{-}1)$ different diffusion couples carefully chosen to probe the appropriate unknowns [103]. This has led many to instead quantify an effective binary diffusion coefficient (EBDC), which treats the diffusion of component i as that due to only its own concentration gradient [101,102,104]. (This assumption represents treating all other components as a single component, i.e., all off-diagonal terms in the diffusion matrix are ignored.) The approximation results in some sensitivity to the experimental details, like the matrix composition and direction of all concentration gradients [101], but these arguably represent a small price especially when the diffusing species are not initially present in the melt. The available data helps to identify key trends with respect to temperature, diffusing species, and melt composition.

Within a particular melt, the effect of temperature on diffusivity is the best constrained. The relationship is famously described by the Arrhenius equation,[j] namely:

$$D = D_o \exp\left(-\frac{Q}{RT}\right)$$

where Do is a pre-exponential factor representing the jump attempt frequency for a diffusing atom (correlated with bond breaking), and Q is the activation energy representing an energy barrier (often correlated to melt rearrangement to make room for the diffusing atom) [100,104]. In general, the Arrhenius equation accurately fits diffusion data within silicate melts for large temperature ranges,

[j] Other effects, such as that of pressure and dissolved water content, can also be couched by an Arrhenius equation [101] but those are less relevant for this dissertation.

indicating no substantial change to the diffusion mechanism with temperature. Non-Arrhenius behavior is observed surrounding the glass transition temperature (T_g), but this is expected to be of minimal consequence for gas turbine applications—the much lower diffusivities in glasses effectively freeze the kinetics at $T<T_g$.

A cation's ionic field strength[k] (IFS) is a useful tool to qualitatively predict diffusivity trends of multiple cations in a particular melt. A list of IFS for some relevant cations is presented in Table 2.1. Cations with larger IFS typically diffuse slower—a rough diffusivity sequence applicable to most silicate melts is Zr≈Hf≈Si<RE≈Y<Ca≈Mg [100]. Within this sequence, the RE element diffusivities vary by a factor of ~1.6x across the lanthanide row (Y^{3+} can be placed with Ho^{3+} as their ionic radii are nearly identical); the trend is nicely linear with Eu as the only exception (it can exist in a divalent state, greatly decreasing its IFS and increasing its diffusivity). The important implication of the diffusivity sequence is that different constituents of a TBC or EBC may diffuse at different rates during dissolution, which could either benefit or hurt reactive crystallization depending on the active dissolution mechanism. Under a dissolution mechanism such as Fig. 2.12(c), this would cause the coating cations to build up at the interface at different rates. For example, $Gd_2Zr_2O_7$ contains equal amounts of Zr^{4+} and Gd^{3+}, but the latter would build up slower due to its faster diffusivity—this would delay apatite nucleation, thereby allowing more melt penetration into the TBC. Conversely, dissolution in Fig. 2.12(a) is rate-limited purely by diffusion—a faster Gd^{3+} diffusivity affords rapid dissolution and saturation throughout the channel.

[k] The IFS has been defined multiple ways, but always includes some variant of the cation valence divided by its size. This dissertation will use $IFS=Z/(R_c+R_a)^2$, where Z is the charge, R_c and R_a are the cation and anion radii, respectively, with the appropriate coordination number [105].

Correlating diffusivities to melt composition is arguably more important but has been much more difficult to constrain. Previous attempts at quantitatively predictive models, e.g., Mungall [106], have largely failed; while some success is seen in the limit of large diffusivities, the model typically underpredicts diffusivities, up to three orders of magnitude. Ultimately, it is not yet clear what compositional parameters most impact diffusion within the melt and their mechanism of doing so [100]. However, some general trends emerge considering the melt viscosity [100,104]. Small and monovalent (or neutral) species diffuse fastest in high viscosity melts; the latter have high ionic porosities, allowing the small atoms to readily diffuse between gaps in the silicate melt structure. Conversely, large or multivalent cations (those typically relevant to barrier coatings) diffuse fastest in low viscosity melts. These have more non-bridging oxygens (are less polymerized) that enable faster structural rearrangement; this affords the melt some flexibility to "make room" for the large diffusing cations, which would otherwise not fit in the ionic porosity of the silicate structures, and aids in bond breaking for multivalent cations [100].

For few species, the Eyring equation [107,108], an empirical relationship wherein diffusivity is proportional to the inverse melt viscosity, offers a mechanism to predict diffusivity for arbitrary melt compositions. Based on reaction rate theory, it can be derived as:

$$D = \frac{kT}{\eta l} \tag{2.1}$$

where η is the melt viscosity and l represents the diffusion jump distance. The latter is often treated as a fitting parameter between experimental measurements of D and η but has been found to correlate well with physical length scales, e.g., ionic radii, bond lengths, or polyhedra size. The applicability of

the Eyring equation is limited to cases where the mechanism of diffusion is equivalent to that of viscous flow—i.e., the breaking of network forming bonds. Therefore, the diffusion of Si^{4+} and O^{2-} are readily predicted by the Eyring equation (in anhydrous melts[l]) [100,104]. In addition, the diffusivity of Zr^{4+}, a noted network former in most silicate melts [110], has been well fit by the Eyring equation by works in the literature [111–113]. Thus, it may be possible to estimate diffusivities of barrier oxide cations Zr^{4+} and Si^{4+} within an arbitrary melt composition provided the viscosity is available or could be accurately estimated with viscosity models. However, the sensitivities of EBDC to their experimental conditions means that such correlations would have to be established under the dissolution-diffusion conditions. It remains unclear whether the Eyring equation could be used to predict the diffusivities of a RE cation, arguably the more important cation in reactive crystallization. The RE oxides act as intermediate oxides in aluminosilicate melts [114,115]—whether they serve as a network former or modifier depends on the composition of the melt and is not well studied in the literature.

2.5. Thermodynamic considerations

A full ICME-based assessment of coating degradation requires knowledge of the relevant thermodynamics that drive system evolution. This section will first provide background on the key reactive crystallization phases for this dissertation. Then, some background will be provided on the relevant thermodynamics (focusing on phase diagrams and single equilibrium studies on higher order systems) and a computational thermodynamic database. (The latter is the key constituent of the

[l] Molecular water significantly enhances oxygen diffusion rates in hydrous silicate melts. The diffusion mechanism is decoupled from that of viscous flow, and the Eyring equation no longer applies to O^{2-} diffusivities [109].

envisioned ICME-based approach, as demonstrated by Summers et al. [77,79] for YDS.) The attention will then turn to provide background on some relevant phases for this dissertation.

2.5.1. Key phases in CMAS-TBC/EBC interactions

A summary of the relevant phases, their names, and compositions is provided in Table 2.2.

Apatite

Apatite is arguably the most important reactive phase in barrier oxide interactions with molten silicates. The phase has a nominal composition of $Ca_2RE_8(SiO_4)_6O_2$ according to the general formula $M^I_4M^{II}_6(SiO_4)_6O_x$, where M^I and M^{II} are cation sites. The crystal structure of apatite, Fig. 2.13(a), is hexagonal (space group $P6_3/m$) with isolated $(SiO_4)^{4-}$ tetrahedra; the two cation channels run along the c-axis [116–118]. The four M^I sites are nine-fold coordinated, containing Ca^{2+} and RE^{3+}. The additional RE^{3+} cations occupy the seven-fold coordinated M^{II} sites. This structure, an orthosilicate, affords rapid crystallization kinetics due to the isolated $(SiO_4)^{4-}$ tetrahedra, which do not require melt rearrangement to connect in complicated structures (e.g., rings or sheets).

In theory, the apatite structure allows a substantial amount of substitution mediated by cation or O^- anion vacancies, Fig. 2.13(b). The nominal, defect-free, composition, $Ca_2RE_8(SiO_4)_6O_2$ with Ca:RE≈1/4, can vary from $RE_{9.33}(SiO_4)_6O_2$ to $Ca_4RE_6(SiO_4)_6O$ ($0 \leq$ Ca:RE $\leq 2/3$) by the addition of cation or anion vacancies. (Larger Ca:RE ratios are favored for arresting infiltration into TBCs) In practice, however, only a small subset of this range appears to be available. Within the pseudo-ternary $(Gd/Y)O_{1.5}$-CaO-SiO_2 equilibria, most of the RE-rich theoretical stability range is available, but less than half the Ca-rich range is available (e.g., $Ca_{2.75}RE_{7.25}(SiO_4)_6O_{1.875}$) [119,120]. But the

composition range appears to become even more constrained in higher-order C(MF)AS+TBC systems. First, apatite appears to nucleate with the nominal composition regardless of the melt composition or the TBC/EBC composition [10,60]. The apatite composition can then evolve in longer duration experiments to be Ca-lean (e.g., [121]) or Ca-rich (e.g., [58]); in practice, however, these vacancies appear to carry a significant energy penalty with them. For example, equilibrium experiments with Si-rich melts and $(Y/Gd)O_{1.5}$ mixtures formed apatite with the defect free composition [58]. Furthermore, CaO-rich apatites typically form from melts during the dissolution of a RE-zirconate or hafnate and not from RE disilicates or monosilicates, Fig. 2.13(c); rather than incorporating vacancies to maintain charge neutrality, the apatite becomes Ca-rich by equimolar substitutions of Ca^{2+} and $(Zr/Hf)^{4+}$, up to ~3–7 cation percent [58]. The implication is that anion vacancies less favorable than the joint substitution of Ca^{2+} and Zr^{4+} in the full CMAS system. In practice, apatite formation from a CMAS melt requires a critical CaO concentration in the initial deposit to form, consistent with findings in the literature [79,80].

Garnet

Garnet is a RE-based reaction product, which exhibits a large range of solid solubility and is generally thermodynamically stable for small RE cations (e.g., Y^{3+} and Yb^{3+}). Its crystal structure contains three cation sites, with stoichiometry of $A_3B_2T_3O_{12}$, each of which can contain multiple elements simultaneously. Generally, the dodecahedral A-site can contain Y^{3+}, Ca^{2+}, Mg^{2+}, and Fe^{2+}; the octahedral B-site can contain Mg^{2+}, Fe^{3+}, and Al^{3+}; and the tetrahedral T-site can contain Si^{4+}, Fe^{3+}, and Al^{3+}. The critical constraint is that the crystal structure—a cubic orthosilicate—does not readily accept oxygen or cation vacancies. The implication is the garnet formula must charge balance, with

the sum of cation charge being 24; this constrains the valid substitutions, e.g., incorporation of Ca^{2+} in the A-site requires equimolar Si^{4+} in the T-site. Full occupation of a single element in a cation site defines the "end-member" garnet compositions. The RE end-members, e.g., yttrium aluminum garnet (YAG, $Y_3Al_5O_{12}$) and yttrium iron garnet (YIG, $Y_3Fe_5O_{12}$), are stable at ambient pressures [122,123], but the silicate end-members (e.g., grossular, $Ca_3Al_2Si_3O_{12}$) are unstable. Therefore, Ca^{2+}, Mg^{2+}, Fe^{2+}, and Si^{4+} experience a finite solubility in garnets formed in reactive crystallization between RE-containing coatings and CMAS melts. Still, garnet is highly efficient at crystallizing the melt; it contains at least 1.67 CMAS cations for each RE cation, which is further enhanced depending on the Ca^{2+}, Mg^{2+}, and Si^{4+} solubilities. (This can be compared to apatite, whose defect-free composition captures 1 CMAS cation for each RE cation.)

Like apatite, garnet formation in practice is sensitive to the barrier coating composition and the CMAS composition. First, the coating must contain high enough quantities of RE^{3+} [58] (although the exact amount depends on the solubility of CMAS cations as previously mentioned). For example, Gomez Chavez et al. observed garnet formation in CMAS exposures to EB-PVD yttrium zirconate coatings containing greater than ~50 $YO_{1.5}$, but the phase was absent from a coating with ~43% $YO_{1.5}$ [124]. Garnet is more frequently observed in CMAS melts with relatively high concentrations of Mg^{2+}, Al^{3+}, and Fe^{3+} [58,80,125,126], with Al^{3+} and Fe^{3+} being suggested as key stabilizers [125,127]. This sensitivity intuitively makes sense considering Mg^{2+}, Al^{3+}, and Fe^{3+} are found in relatively few reactive crystallization phases compared to Ca^{2+} and Si^{4+}; for example, melts rich in Ca^{2+} and Si^{4+} can form apatite, zircon, or Zr/RE-cyclosilicates in addition. Ultimately, the competition between garnet formation another reactive or intrinsic phases is poorly understood. Its thermodynamics are

complicated by its large solid solubility ranges and the phase does not often appear in academic studies. Godbole et al. [127] recently investigated the thermodynamics of YAG-CMAS mixtures systematically. The thermodynamics of iron-containing garnets is the subject of Chapter 7—additional background on the study and on garnet will be discussed therein.

Cyclosilicates

The two cyclosilicate phases—$Ca_2ZrSi_4O_{12}$[m] and $Ca_3RE_2Si_6O_{18}$ with disparate structures consisting of rings of 4 and 3 $(SiO_4)^{4-}$ polyhedral, respectively [128,129]—feature similar formation conditions and kinetics. Both phases require a significant amount of the relevant coating cation in the dissolving oxide; for example, both phases were observed to form in the dissolution of $Nd_2Zr_2O_7$ but ZrO_2–24 mol% $NdO_{1.5}$ did not form the Nd-cyclosilicate [92]. Both the Zr- and RE-cyclosilicate are stable at 1400°C in the CaO-SiO_2-($GdO_{1.5}$/$YO_{1.5}$/ZrO_2) phase diagrams [119,120,130]; however, the addition of alumina appears to significantly destabilize the phase at high temperature. Instead, in the higher order coating-C(MF)AS system, cyclosilicates are generally observed at lower temperatures (<1250°C), are rarely observed at 1300°C, and appear to be unstable at 1400°C [58,62,63,92–94].

Both cyclosilicates also show relatively sluggish crystallization kinetics [92–94], presumably due to the silicate rings within the crystal structure [128,129]. Small RE cations appear to crystallize RE-cyclosilicate faster than large RE cations [94]. (Even still, however, the phase is consistently slower than apatite. For example, experiments by Perrudin et al. [94] showed crystallization and redissolution of a metastable apatite before forming RE-cyclosilicate, despite the latter being the only

[m] In theory, a Hf-cyclosilicate, $Ca_2HfSi_4O_{12}$, should also be stable. The phase has not been observed in the barrier coating-CMAS literature to the author's knowledge.

thermodynamically stable reactive phase.) While some experiments indicate Zr-cyclosilicates form faster than zircon [92], there is a general paucity of observations of both phases simultaneously. The implication is that while cyclosilicates are very effective at crystallizing CaO and SiO_2 from the melt, they may not form quickly enough to arrest melt penetration in TBCs.

Zircon

The most frequently observed Zr-based reactive phase is zircon, nominally $ZrSiO_4$. It is a tetragonal orthosilicate, insisting of chains of SiO_4 tetrahedra, which share edges with ZrO_8 dodecahedra along the c-axis [131]. Unlike apatite, the crystal structure does not contain ionic O^{2-} sites (i.e., all oxygen is bonded to Zr^{4+} or Si^{4+}), which largely precludes oxygen vacancies and restricts solid solubility. That said, zircon has been observed with small (e.g., 1–3%) $REO_{1.5}$ concentrations, which are hypothesized to be stabilized via oxygen protonation [58,132]. In theory, zircon formation would be good for arresting melt penetration—it converts an equimolar amount of melt per mole TBC dissolved and leaves almost all the RE available for further apatite formation. In practice, there are four factors with zircon that prevent it from effectively mitigating infiltration. First, much of the available Zr^{4+} is often captured by reprecipitated zirconia, reducing the quantity of zircon formed substantially. Second, the phase has slow crystallization kinetics (e.g., nucleation has been observed after 30 min in a study by Chellah et al. [63,92]). Third, zircon often grows atop the dissolving coating oxides thereby slowing dissolution substantially [58,63]. Fourth, its formation is largely dependent on the melt and coating composition; the melt must contain enough SiO_2, and the movement to RE-rich zirconates (to promote apatite formation) further reduces the Zr activity, reducing the driving force for zircon.

It is worth noting, however, that a similar crystal hafnon, $HfSiO_4$ can form from hafnia-based coatings [133]. The phase is poorly understood in the literature in the context of CMAS-coating interaction (e.g., formation conditions, temperature stability, and solubility of other cations). But the elevated phase stability of hafnia relative to zirconia [134] enables phase-stable pure hafnia coatings and may be of interest for EBC applications. In contrast to TBCs, the dissolution shielding property of a hafnon reactive layer would be beneficial for EBCs to limit coating consumption.

2.5.2. Phase diagrams and higher-order equilibria

Previous studies have investigated the thermodynamic equilibrium of some systems relevant for this dissertation. Pseudo-ternary phase diagrams relevant to molten silicates have been investigated [135–139]; for example, CaO-$AlO_{1.5}$-SiO_2 [135] and MgO-$AlO_{1.5}$-SiO_2 [136] afford an excellent understanding of the melting behavior and the relevant intrinsic phases prior to barrier coating dissolution. Further efforts have developed pseudo-ternary phase diagrams that include oxides relevant to barrier coatings; diagrams for $YO_{1.5}$-$AlO_{1.5}$-SiO_2 [122], $YO_{1.5}$-ZrO_2-$AlO_{1.5}$ [140,141], and $(Y/Gd)O_{1.5}$-ZrO_2-SiO_2 [142] provide valuable information for coating systems containing $YO_{1.5}$ and ZrO_2 (e.g., 7YSZ TBCs) and help to constrain the phase equilibria between important Y-aluminate, Y-silicate, and Zr-silicate phases. Likewise, $(Y/Gd)O_{1.5}$-CaO-SiO_2 [119,120] phase equilibria provides important information on the apatite phase and its solid solution range.

To supplement the fundamental knowledge afforded by pseudo-ternary phase diagrams, Poerschke et al. [58] investigated the thermodynamics of select higher-order quinary/senary mixtures of relevant TBC oxides (ZrO_2, 7YSZ, $Gd_2Zr_2O_7$, $Y_4Zr_3O_{12}$, $YO_{1.5}$, and $GdO_{1.5}$) with four C(M)AS melts with varying Ca:Si ratios. The study indicated the thermodynamics of reactive crystallization

are strongly influenced by the Ca:Si ratio of the melt, the RE:Zr ratio of the coating oxide, and the identity of the RE (i.e., Y^{3+} or Gd^{3+}). Apatite and zircon were the primary reactive crystallization products, especially for Gd^{3+}-containing samples. Y^{3+} was present in higher quantities in the reprecipitated phase, generally reducing its availability for reactive phases. In addition, Y^{3+} was more likely to partition into other Y-based reactive phases like yttrium disilicate, garnet, and silicocarnotite.

The utility of such pseudo-ternary phase diagrams and equilibrium experiments lies in the computational thermodynamic databases that can be constructed and optimized from them. A well-calibrated and diverse database can predict the thermodynamic response of higher order TBC/EBC-CMAS reactions where the composition space becomes prohibitively large to probe experimentally. The Thermo-Calc Software Metal Oxide Solutions Database (TCOX) [50] represents the state-of-the-art here; it contains thermodynamic descriptions for CMAS with additions of Zr^{4+}, Y^{3+}, and Gd^{3+}.[n] Phase equilibria with are generally well predicted by the database, particularly with respect to apatite formation. However, many improvements are desirable. First, the lack of additional RE oxides precludes computational investigations into other candidate coating compositions—a critical exclusion. The RE species has a large impact on which reactive phases form and their quantities [58,143]. These differences can be phenomenologically captured using Gd^{3+} and Y^{3+} representing small and large cations, respectively, but they will not accurately predict phase fractions or compositions for other RE. A second improvement would be the inclusion of Hf^{4+} to the database.

[n] La^{3+} is partially described but primarily in the context of other barrier oxides (e.g., La-Gd-Y-Zr-O) such that La-derived reactive phases are poorly estimated.

Hafnia-based coatings have been of increasing interest as the cation shares many properties with Zr^{4+} but is phase stable to higher temperatures [144]. Third, the database does not properly represent Y-based garnets (e.g., garnet formation from YMS dissolution [80]), despite the well-studied nature of Y^{3+} in the database. As garnet competes for similar melt cations as apatite (i.e., Y^{3+}, Ca^{2+}, and Si^{4+}), it is critical that this phase is accurately modeled in the database.

2.6. Problem statement and scope of research

This dissertation will address two critical gaps for implementing the ICME-based approach to coating design described in Fig. 2.11. First, little is known about the kinetics of barrier coating-melt interactions, particularly quantitatively, which is important to understand in the context of TBCs. The work that follows will leverage semi-infinite, 1-D diffusion couples. These identify the active dissolution mechanisms and enable quantification of the barrier oxide dissolution rate into the melt and the cation diffusion rates therein via fitting measured concentration profiles to dissolution and diffusion models. The early stages of reactive crystallization will also be investigated and compared to the expected equilibrium pathways to develop a better understanding of the reactive phases, which are susceptible to kinetic suppression. Electron microscopy techniques serve as the primary tool—microstructural evolution is studied using SEM and TEM, while quantitative chemical analysis is obtained with an electron microprobe (EPMA) equipped with wavelength-dispersive X-ray spectroscopy. Finite element models will be leveraged to provide context to the obtained kinetic data; namely how dissolution and diffusion manifest on coating-relevant length scales and how these processes compete with the rate of melt infiltration.

Second, yttrium-based garnets are poorly modeled in the current thermodynamic databases due to a dearth of systematic studies into their stability within CMAS melts. The core issue is a consequence of garnet's large solid solubility, which remains poorly defined. To address this gap, multiple samples in the Y-CMAS system will be synthesized and homogenized at 1400 °C; specifically, bulk sample compositions were chosen to assess the extent of Ca^{2+}, Mg^{2+}, Fe^{2+}, and Si^{4+} solubility and site partitioning preferences. The study leverages SEM, XRD, and EPMA for phase identification and chemical analysis of all phases (with particular focus on garnet).

2.7. Figures and tables

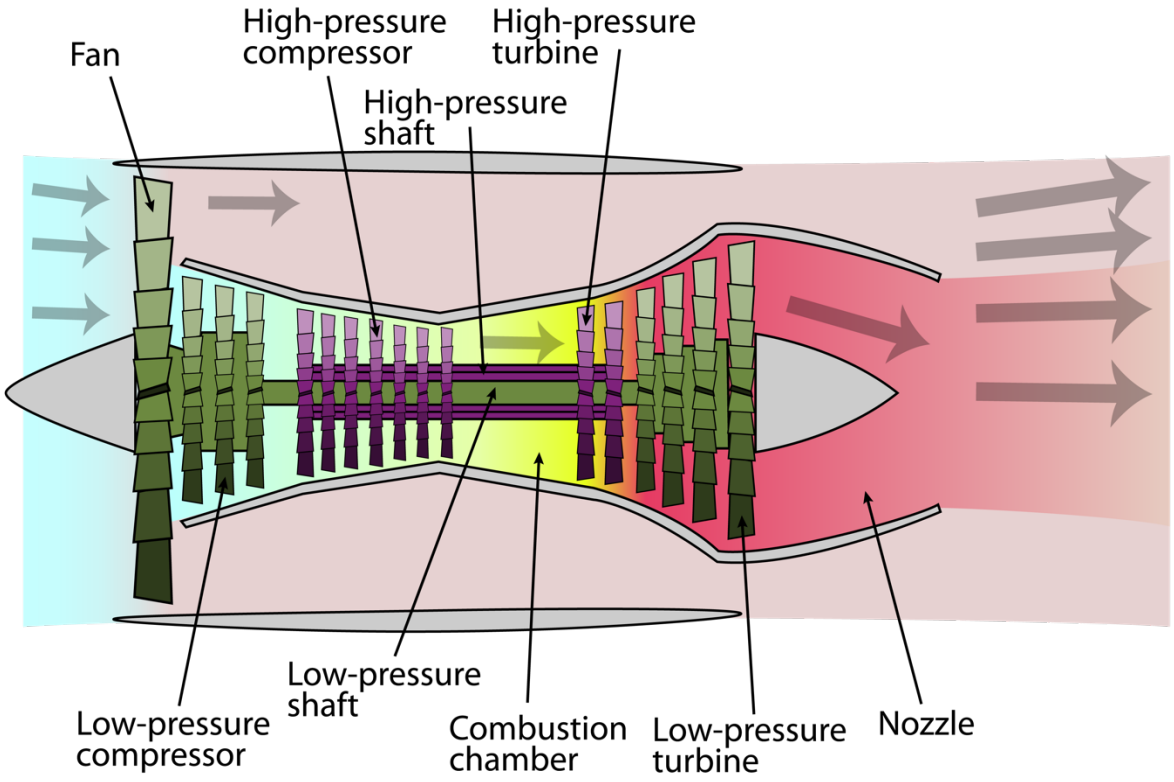

Fig. 2.1: Simplified schematic of a turbofan, a type of gas turbine engine. Air entering the engine core is first compressed, then ignited in the combustion chamber, before flowing through the turbine section. The latter drives the necessary rotation for the fan and the compressor stages. Schematic adapted from K. Aainsqatsi under the Creative Commons Attribution 2.5 Generic [145].

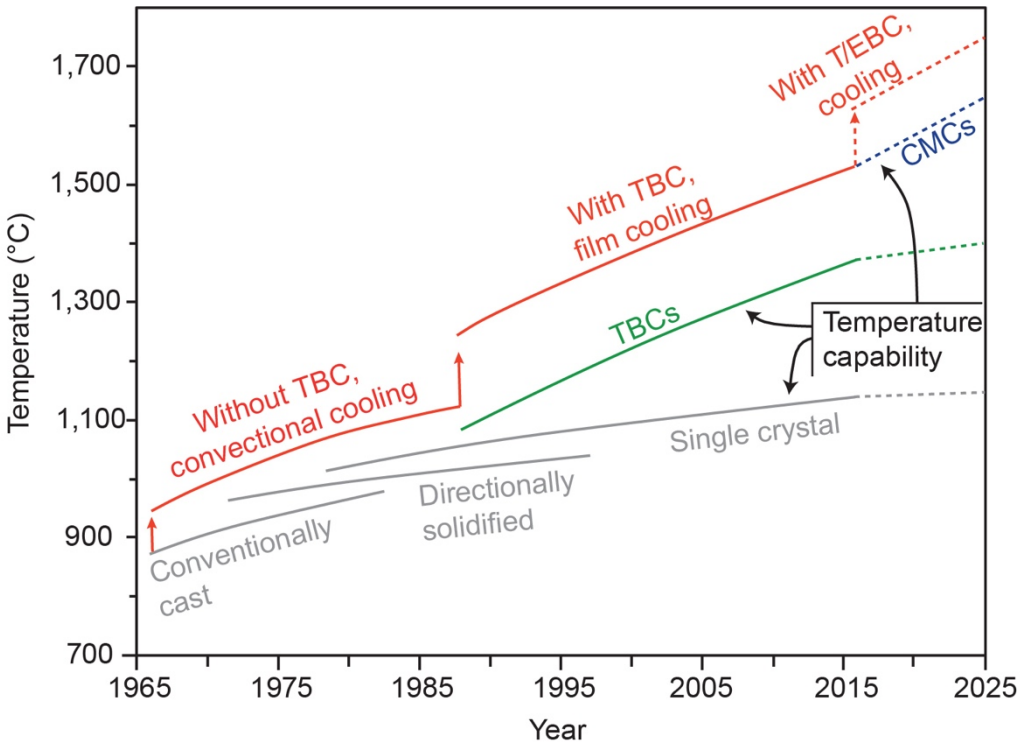

Fig. 2.2: Continued materials and processing developments have improved the temperature capability of superalloys (grey) and thermal barrier coatings (TBCs, green) over decades. The addition of film cooling enabled a further increase to the gas temperatures (red), which now exceed the temperature capabilities of the components. Further temperature increases could be realized by the implementation of Ceramic Matrix Composites (CMCs, blue) and their protective environmental barrier coatings (EBCs). Figure adapted from [7]

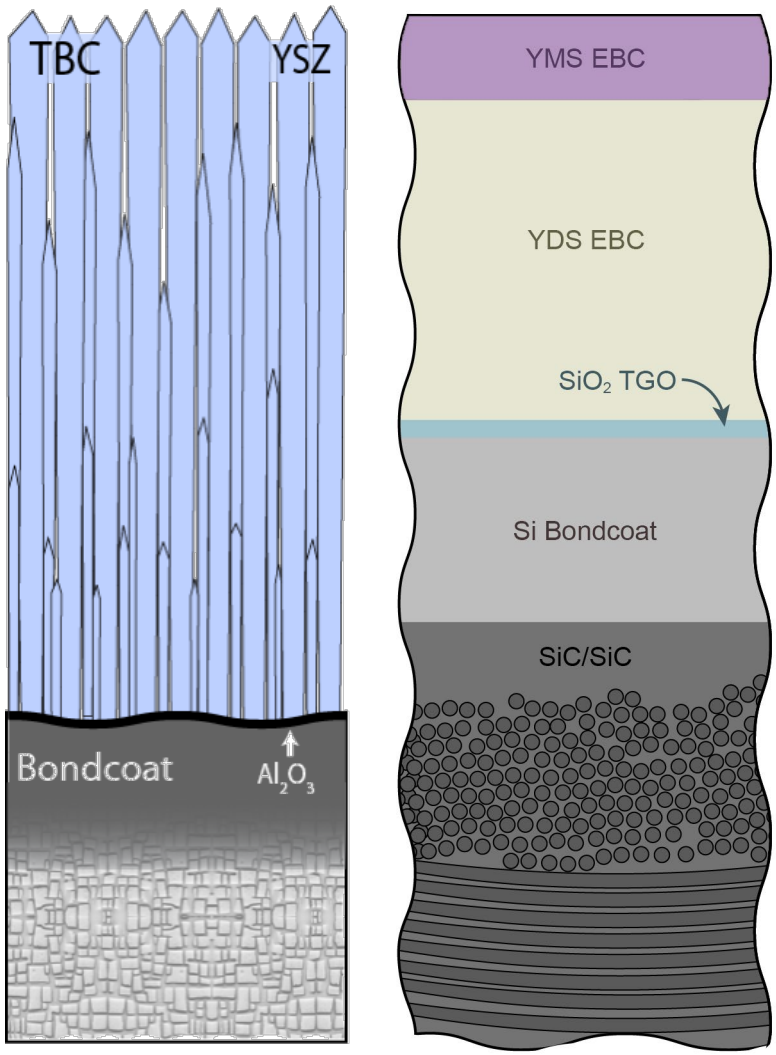

Fig. 2.3: Representative schematics showing the components of thermal barrier coatings (TBCs, left) and environmental barrier coatings (EBCs, right). Both coating architectures employ a metallic bondcoat, which provides oxidation resistance to the superalloy or SiC/SiC CMC. The TBC ceramic topcoat (e.g., yttria-stabilized zirconia, YSZ) features a columnar microstructure, providing in-plane compliance to the coating. Conversely, the EBC ceramic topcoat (e.g., yttrium disilicate, YDS, and yttrium monosilicate, YMS) must be dense to provide a hermetic seal against water vapor attack. Schematics courtesy of David Poerschke and William Summers.

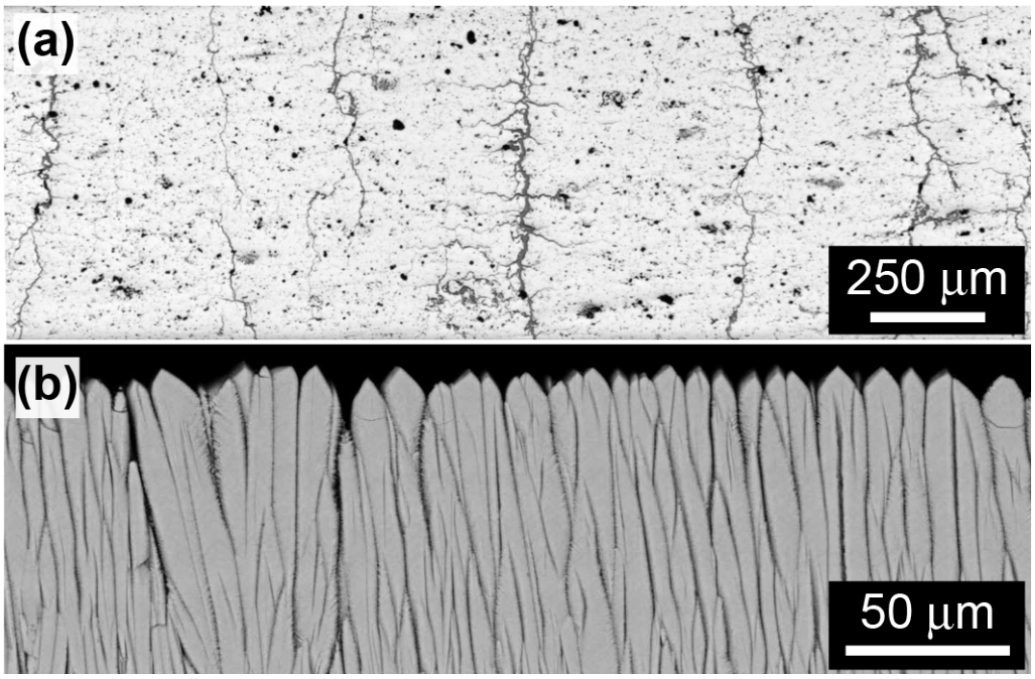

Fig. 2.4: Representative thermal barrier coating microstructures deposited by (a) air plasma spray (courtesy of Erin Donohue) and (b) electron-beam physical vapor deposition (courtesy of Elisa Zaleski).

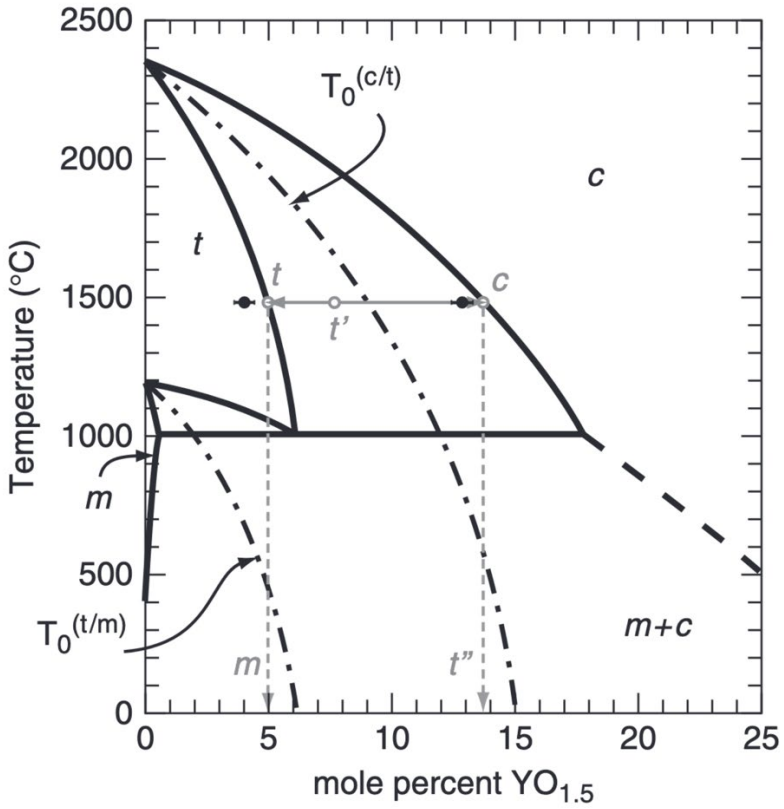

Fig. 2.5: Zr-rich portion of the ZrO_2-$YO_{1.5}$ pseudo-binary phase diagram, including T_0 curves for the monoclinic-tetragonal transformation and the tetragonal-cubic transformation. Most YSZ-based TBCs use the *t'* composition, with ~7–8% $YO_{1.5}$. Because the composition stays between the two T_0 curves throughout the entire operational temperature range, it is non-transformable on cooling. Figure reproduced from [16], with permission.

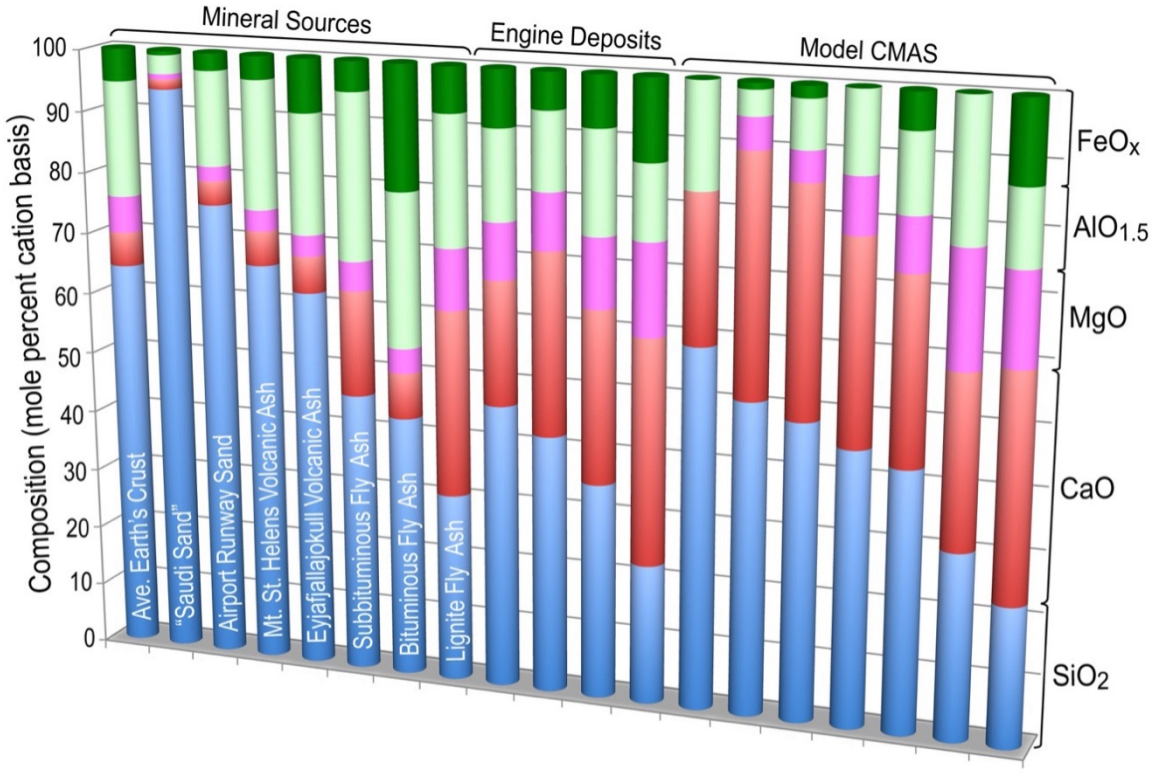

Fig. 2.6: The composition of siliceous debris shows significant variability within and between classes, shown above for the major constituents SiO_2, CaO, $AlO_{1.5}$, MgO, and FeO_x. The composition of engine deposits (measured ex-situ from flight hardware) are also shown, along with model compositions used to study silicate debris induced degradation. Figure from Levi et al. [11], with permission.

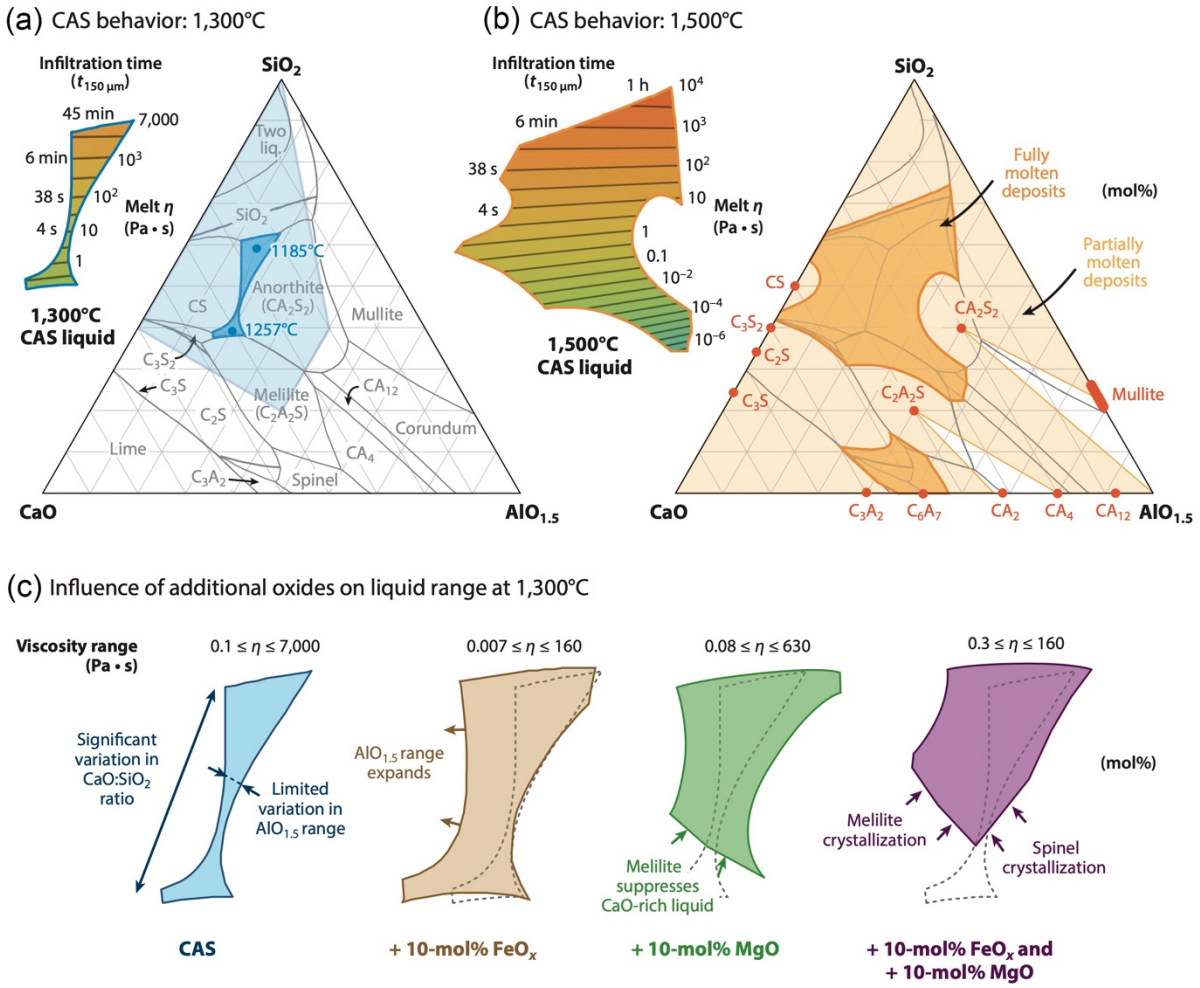

Fig. 2.7: Calculated liquidous projections (a,b) for the CaO-$AlO_{1.5}$-SiO_2 pseudo-ternary system [51,52]. Light-shaded and dark-shaded regions denote portions of the phase diagram that are partially molten or fully molten, respectively, at (a) 1300 °C and (b) 1500 °C. The calculated liquid viscosity [87] is shown throughout composition space in the insets. The liquid phase field evolves upon small additions of iron and/or magnesium oxides (c), which generally decrease the melt viscosity. The results indicate that a significant portion of ingested siliceous debris will be at least partially molten at 1300 °C and that the problem of molten silicate degradation will be largely unavoidable by 1500 °C. Figure from Poerschke et al. [10], with permission.

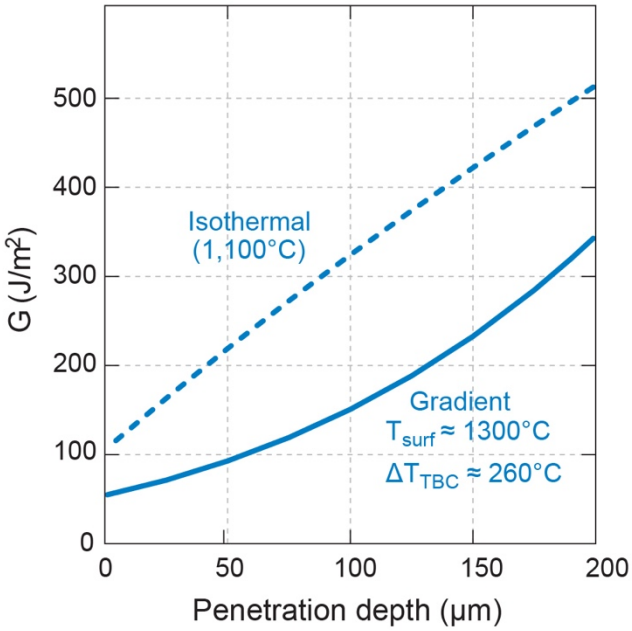

Fig. 2.8: Calculated elastic energy release rate (G) for melt-infiltrated thermal barrier coatings (TBCs). Isothermal conditions (unrealistic in-engine but often used experimentally) are more damaging than the equivalent penetration depth under a thermal gradient. Importantly, *G* scales non-linearly with the penetration depth. Figure adapted from [10].

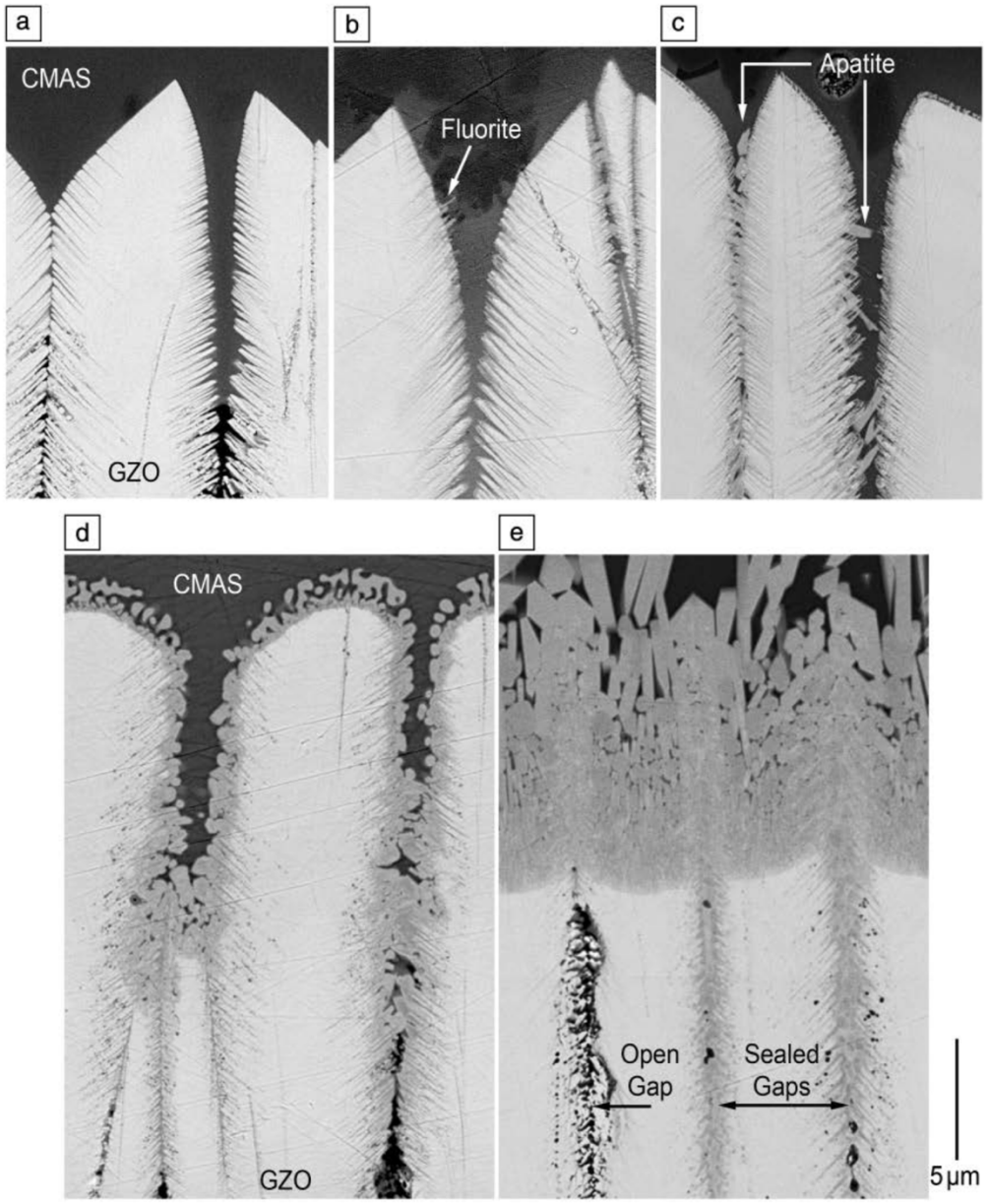

Fig. 2.9: Example of reactive crystallization in an $Gd_2Zr_2O_7$ EB-PVD coating exposed to an initially amorphous $C_{33}M_9A_{13}S_{45}$ composition heated to 1150 °C for (a) 10 s, (b) 20 s, and (c)30 s and subsequently quenched. Fluorite reprecipitates (b) first, which is followed by apatite shortly after (c). Images in (d,e) represent initially crystalline $C_{33}M_9A_{13}S_{45}$ heated to (d) ~1250 °C for 4 min and (e) 1300 °C for 4 h. Reactive crystallization occurs rapidly, acting to seal the intercolumnar gaps and prevent further penetration. Figure from Levi et al. [31],with permission.

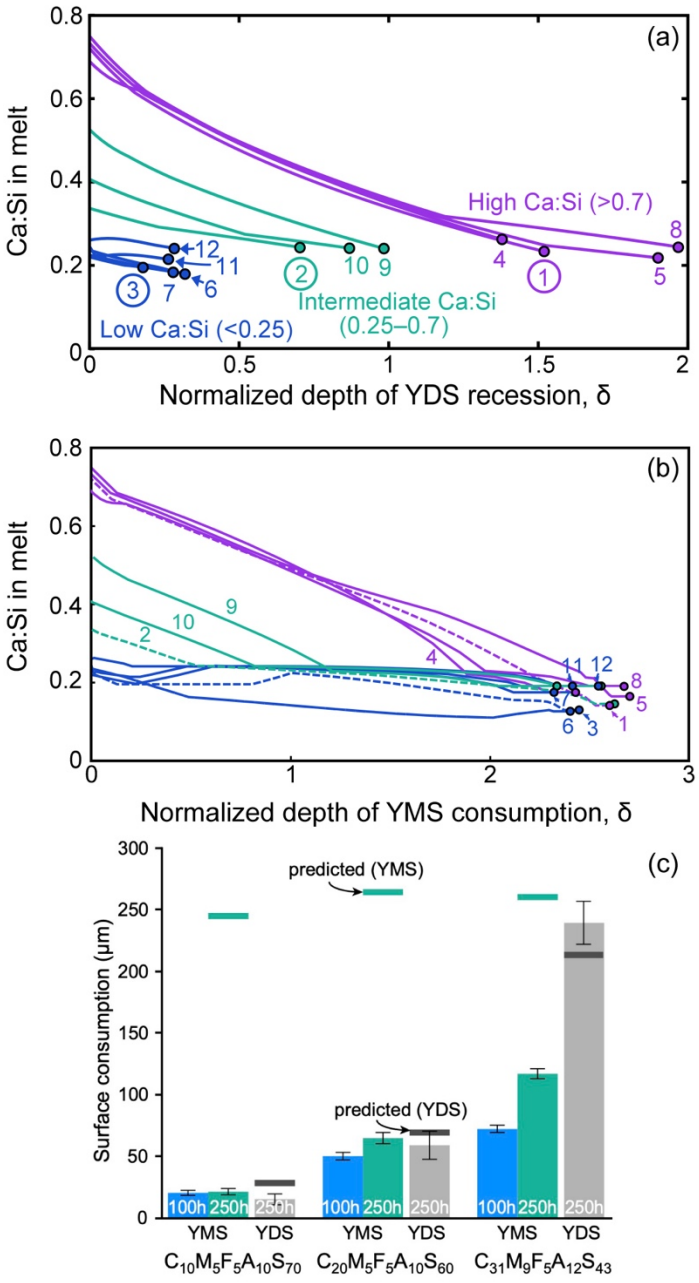

Fig. 2.10: In theory, EBCs will be dissolved by CMAS melts until thermodynamic equilibrium is reached or either the melt or coating is consumed. More yttrium disilicate (a) must be dissolved to reach equilibrium for Ca-rich melts. Conversely, yttrium monosilicate (b) is unstable in contact with silicate melts; the amount of coating dissolution necessary to crystallize the initial melt is largely insensitive to the Ca:Si ratio of the latter. Experiments (c) on YDS are largely consistent with the expected results from thermodynamics but YMS consumption becomes kinetically constrained by the formation of hermetic layers of apatite (d). Figure adapted from Summers et al. [79,80], with permission.

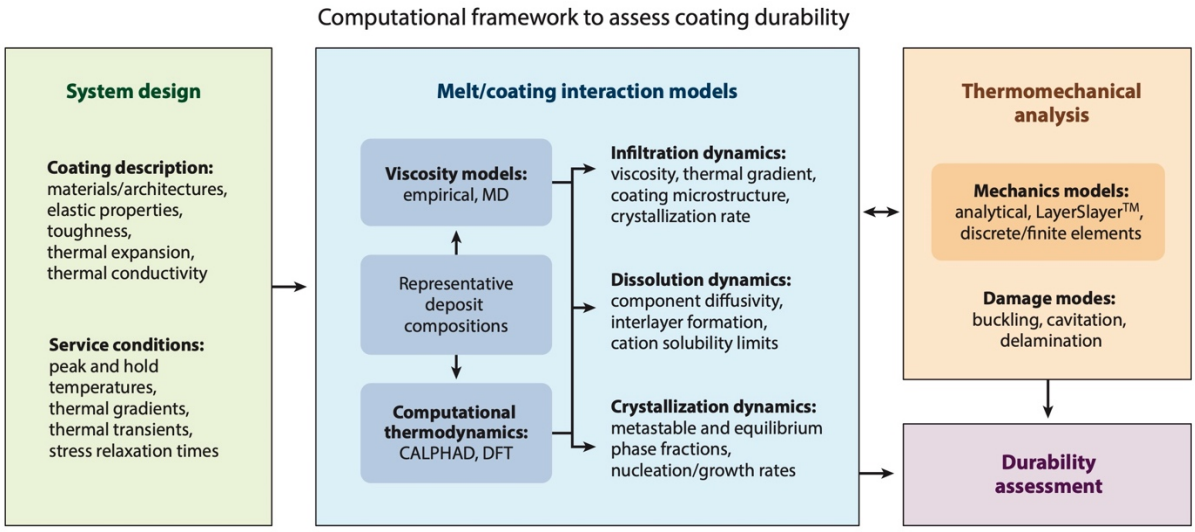

Fig. 2.11: The envisioned computational framework to assess coating durability includes models for system design (green), melt/coating interactions (blue), and the subsequent thermomechanical response (orange). Multiple components of this integrated model have been developed (e.g., models for coating properties, melt viscosity, and thermomechanics). However, some components (e.g., thermodynamic models) need further work to improve accuracy, whereas other components (e.g., kinetic models) are altogether absent. Figure from Poerschke et al. [10], with permission.

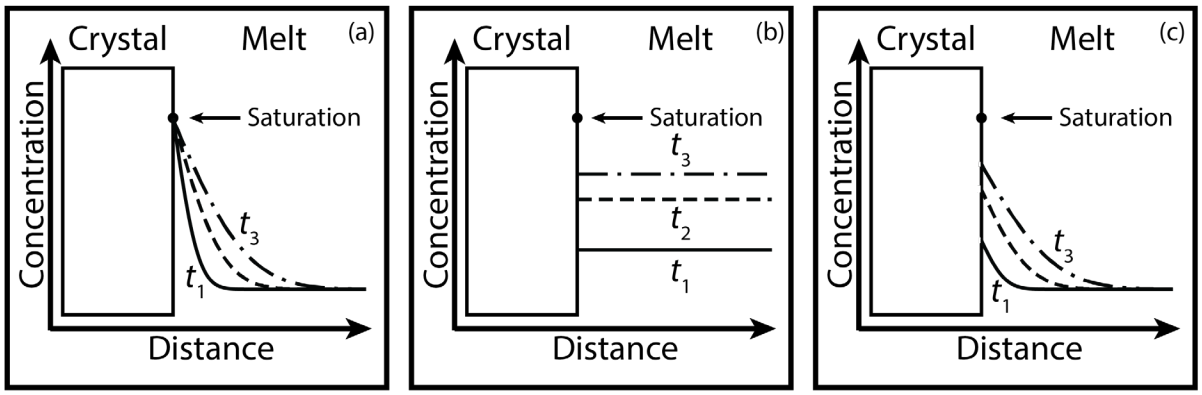

Fig. 2.12: Crystal dissolution and diffusion can occur by one of three mechanisms depending on the relative rate of interface detachment (u_o) and diffusion (D). (a) Rapid interface saturation occurs when $u_o >> D$ and concentration profiles in the melt are captured by standard Fickian diffusion; dissolution in this regime is rate-limited by diffusion away from the crystal-melt interface. (b) Conversely, flat concentration profiles in the melt are obtained in $u_o << D$; the crystal dissolution rate in this regime decreases as the concentration approaches saturation. (c) If neither process dominates (i.e., if $u_o \approx D$) concentration gradients occur in the melt with the concentration at the crystal-melt interface approaching saturation with time; the time-varying dissolution rate in this regime depends on both u_o and D.

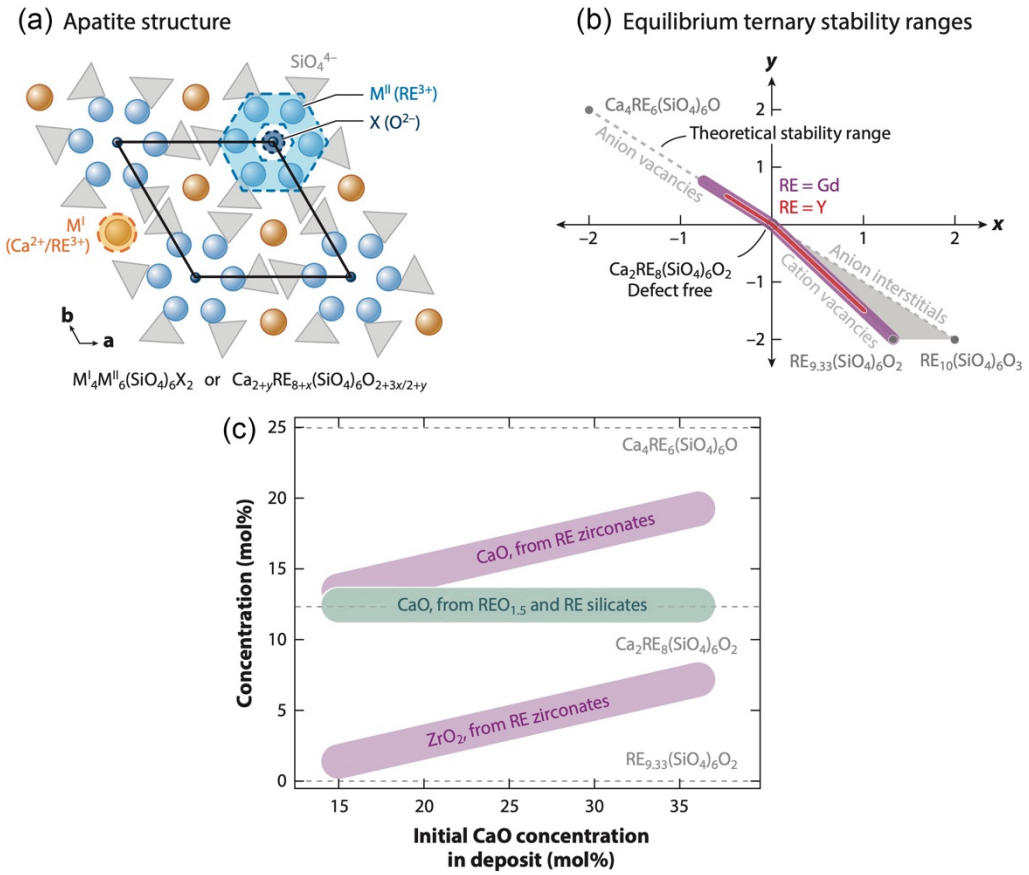

Fig. 2.13: The crystal structure of apatite (a) features two cation sites, M^I and M^{II}, with substitution allowed in the M^I site. This solid solubility observed in ternary CaO-$REO_{1.5}$-SiO_2 systems (b) is stabilized with cation or anion vacancies in the apatite structure, but the theoretical stability range is not stable in practice. In higher-order systems (those relevant to CMAS-coating interactions) the stability of vacancies appears to be further reduced such that apatite with the defect-free composition is strongly favored. However, substitution (c) of CaO for $REO_{1.5}$ can occur with concomitant substitution of ZrO_2 or HfO_2 to charge balance. Figure adapted from Poerschke et al [10], with permission.

Table 2.1: Ionic field strength of relevant cations in silicate melts. Calculated using $IFS \equiv Z/(r_c+r_a)^2$ where Z is the cation charge, r_c is the cation radius, and r_a is the radius of O^{2-} (1.4 Å).

Cation	**Assumed Coordination Number**	**Radius (Å)** [146]	**Ionic Field Strength**
Ca^{2+}	6	1.0	0.35
Mg^{2+}	6	0.72	0.44
Al^{3+}	4	0.39	0.94
Si^{4+}	4	0.26	1.45
Zr^{4+}	6	0.72	0.89
Hf^{4+}	6	0.71	0.90
Y^{3+}	6	0.90	0.57
Gd^{3+}	6	0.94	0.55

Table 2.2: A summary of relevant phases, organized by category, including their abbreviation used throughout the dissertation and a representative formula.

Type	Phase Name	Abbreviation	Nominal Formula*
Reactive Crystallization	Apatite	Ap	$(Ca,RE)_4(RE,M)_6(SiO_4)_6O_2$
	Garnet	G	$(RE,Ca,Mg,Fe^{2+})_3(Mg,Al,Fe^{3+})_2(Si,Al,Fe^{3+})_3O_{12}$
	M-Cyclosilicate	M-Cy	$Ca_2MSi_4O_{12}$
	RE-Cyclosilicate	RE-Cy	$Ca_3RE_2Si_6O_{18}$
	Zircon/Hafnon	ZS/HS	$MSiO_4$
	Silicocarnotite	SC	$Ca_3RE_2Si_3O_{12}$
Reprecipitation	Monoclinic	m	$(M,RE,Ca)O_{1.x}$
	Tetragonal	t	$(M,RE,Ca)O_{1.x}$
	Cubic (Fluorite)	c/F	$(M,RE,Ca)O_{1.x}$
Intrinsic Crystallization	Spinel	Sp	$(Mg,Fe^{2+})(Al,Fe^{3+})O_7$
	Olivine	Ol	$(Mg,Fe^{2+})_2SiO_4$
	Anorthite	An	$CaAl_2Si_2O_8$
	Melilite	Mel	$Ca_2(Al,Mg)(Al,Si)SiO_7$

* RE = Rare-earth (e.g., Y^{3+}, Gd^{3+}, etc.). M = Zr^{4+}, Hf^{4+}

CHAPTER 3. EXPERIMENTAL METHODS

The overarching goal of this research—to quantify the kinetics of barrier oxide (BO) interactions with molten silicates and investigate the development of new crystalline phases—demands a simplified experimental geometry from which the requisite information can be obtained. Actual thermal or environmental barrier coatings feature complex geometries and engineered (TBCs) or unintended (EBCs) porosity. To avoid these complications dense bodies of thermal or environmental barrier oxides (hereafter barrier oxides, BOs) suitable to study in a 1D, semi-infinite diffusion couple geometry shown schematically in Fig. 3.1, were acquired or produced. This chapter will discuss *(i)* the relevant materials studied and their production; *(ii)* the 1D diffusion couple geometry leveraged for all experiments and the relevant furnace procedures; *(iii)* the characterization of the diffusion couples; *(iv)* the quantification of the ensuing concentration profiles in the melt, which afforded the determination of dissolution rates of the BOs into the molten silicates and the diffusion rate of the relevant species therein.

3.1 Starting materials

3.1.1 Barrier oxides

The experimental geometry, shown in Fig. 3.1, required dense pieces of BO approximately 2.8 mm x 2.8 mm squares, which were produced following the methodology summarized in Fig. 3.2. In all cases, the desired square pieces were cut from larger plates or cylindrical pellets using a high-speed diamond blade saw. Representative micrographs of the starting polycrystalline BOs are shown in Fig. 3.3.

Samples of yttria-stabilized zirconia (YSZ) were procured from external sources. Polycrystalline YSZ (hereafter 7YSZ) was obtained as ribbons approximately 100 mm x 13 mm x 1.5 mm in size (Ceramic Technologies Inc., Houston, TX). The ribbons were dense, featuring <2% porosity (Fig. 3.3b), and had a bulk yttria content of 6.8 mol% $YO_{1.5}$[a] measured by standardized EPMA. Further analysis of the microstructure showed some inhomogeneity in the chemical composition, which were related to a small content of cubic phase with higher $YO_{1.5}$ content than the average. The bulk of the 7YSZ consisted of tetragonal grains with 5–6% $YO_{1.5}$. While the tetragonal phase does not transform upon cooling from thermal excursions as high as 1400°C, it readily undergoes substantial transformation to the monoclinic form when the ribbons are crushed and ground; concomitantly, a minute amount of monoclinic phase was detected by XRD and attributed to surface transformation upon polishing after sintering. This has important implications for the evolution of the interaction zone, which will be discussed further in Chapter 5. Single crystalline YSZ (containing ~20% $YO_{1.5}$, hereafter 20YSZ) was obtained as plates approximately 10 mm x 10 mm x 0.5 mm in size and oriented along the 100 direction (MTI Corp, Richmond, CA). The 20YSZ was single phase cubic and effectively free of any porosity. In addition, some experiments were carried out on single crystalline $Gd_2Zr_2O_7$, which was grown using the floating zone technique by researchers at the University of Warwick, UK [147].

In all other cases, the desired BOs could not be externally sourced as dense plates and dense pellets were produced internally following Fig. 3.2. Powders of the relevant oxides were either purchased or produced by reverse co-precipitation. Powders were typically ball milled in a liquid medium to break agglomerates and to reduce the powder size for enhanced sintering kinetics. A planetary ball mill

[a] Unless otherwise mentioned, compositions are provided in units of single cation mole percent.

(Across International PQ-N04, Livingston, NJ) was used with YSZ jars and spherical YSZ milling media (1 mm diameter). A powder-to-media mass ratio of 1:9 was used together with a 1:2 powder-to-liquid (200 proof ethanol) mass ratio. Milling times were typically 1–4 hours at 350 RPM. After milling, the media was quickly separated from the product using a coarse sieve and added back to the jar for a 30-minute cleaning stage, which substantially increased the yield of the fine powder. The final product dried overnight and was ground with a mortar and pestle prior to uniaxial pressing. This milling procedure produced a submicron powder, which was found to be critical to enable densification of the rare-earth zirconates (e.g., $Gd_2Zr_2O_7$).

Green pellets were produced by uniaxial pressing using dies with an inner diameter of either 6 or 13 mm (MTI Corp, Richmond, CA) with compaction in a hydraulic press (Carver Inc., Wabash, IN) to ~150 MPa. Enough powder was weighed to produce a 1–2 mm thick pellet (at 100% density). Polyvinyl alcohol binder (1–2 drops) was mixed into the powder using a mortar and pestle to increase the green strength of the pressed pellet. Steric acid dissolved in ethanol was used as a lubricant and was applied to the die surfaces prior to powder addition.

Sintering procedures for the green pellets varied for each barrier oxide and will be briefly discussed in subsequent paragraphs. In general, however, green pellets were sintered in box furnaces (Lindberg/MPH, Riverside, MI) with a lab air atmosphere. The pellets were placed upon platinum foil within a covered alumina crucible. After sintering, all pellets had one surface polished to a ≤1 μm finish to ensure the diffusion couple featured a flat geometry, maintaining the 1D assumption.

Dense compacts of ZrO_2, HfO_2, and $Gd_2Zr_2O_7$ (GZO) were produced by uniaxial pressing and sintering of externally procured powders. A nominally pure ZrO_2 compact was directly produced

from a fine (<3 μm) powder (99.7% ZrO_2, <75 ppm HfO_2[b], Alfa-Aesar, Ward Hill, MA). The powder was ground with a mortar and pestle to break soft agglomerates but was not ball milled. The pressed pellet was sintered at 1500 °C for 24 h. Because lower sintering temperatures did not achieve the appropriate density, the compact went through the tetragonal → monoclinic transformation when cooling from 1500 °C, leading to substantial microcracking but with sufficient integrity to be tested for its interaction with CMAS. The pellet was ion polished (Leica EM TIC 3X, 8 kV, 3 mA), which provided a mostly planar surface (Fig. 3.3a) for CMAS testing. The HfO_2 powder (99% excluding ZrO_2, ZrO_2 < 1.5%, Alfa Aesar, Ward Hill, MA) was received with powder particle sizes typically <5 μm. The powder compacts were readily sintered to near theoretical density by 24 h at 1500 °C. However, grain growth during sintering led to microcracking and subsequent grain pullout during surface polishing of the sintered pellets (Fig. 3.3d). A gentle polishing technique, starting with 3 μm colloidal diamond polishing solution, was developed to minimize grain pullout and produce a flat surface for the diffusion couple experiments (Fig. 3.3e). The received GZO powder (Praxair Surface Technologies, Indianapolis, IN) was a spherical thermal spray powder with an initial diameter of ~50 μm. The ball milling procedure, detailed above, proved critical for obtaining high-density pellets—the experience is that powder of diameter >1 μm will not sufficiently sinter by conventional techniques. Pressure-assisted sintering techniques, such as Spark Plasma Sintering (SPS) or more appropriately Current-assisted densification (CAD) [148] yielded nominally dense, but oxygen-deficient pellets, which, cracked significantly upon reoxidation. However, with

[b] Purities for commercially acquired materials are reported by manufacturers in weight percent.

sufficiently milled powder, pressureless sintering in air at 1600 °C for 48 h produced dense pellets of GZO (Fig. 3.3c).

A powder with a nominal bulk composition of $7YO_{1.5}$–HfO_2 (7YSH) was produced using reverse co-precipitation following procedures detailed in the literature [149]. Hafnium tetrachloride (99.9% excluding ZrO_2, ZrO_2 <0.5%, Alfa Aesar, Ward Hill, MA) and yttrium nitrate hexahydrate (99.9%, Alfa Aesar, Ward Hill, MA) precursors were dissolved in ethanol and the solutions were calibrated to determine the relevant yield of oxide per gram of precursor solution. (To reduce the effect of absorbed volatiles on weight measurements, all crucibles were heated to 1000 °C, extracted from the furnace at ~120 °C, and cooled within an evacuated desiccator prior to weighing.) The appropriate amount of precursor solutions was mixed and added dropwise to an ammonium hydroxide bath with pH > 10. The product was centrifuged to separate out the desired mixed-hydroxide precipitates, which were subsequently washed with ethanol multiple times (with repeated centrifuging to separate out the supernatant). After washing, the product was dried and converted to the desired oxide by pyrolysis at 1000 °C and 700 °C for 4 h each (two temperatures are used to ensure proper conversion of iron-based precursors, if present). The resulting powder ball milled, pressed, and was sintered at 1500 °C for 24 h. This resulted in a dense, two-phase microstructure (Fig. 3.3f) consisting of monoclinic hafnia (containing no detectable yttria) and cubic hafnia (containing ~13% $YO_{1.5}$). The resulting pellet did not show evidence of microcracking, Fig. 3.3(f), unlike pure HfO_2, Fig. 3.3(d,e).

3.1.2 Calcium-magnesium-alumino-silicates

The diffusion couples featured one of two model silicate melts: $C_{33}M_9A_{13}S_{45}$ or $C_{24}A_{17}S_{59}$[c]. The former (hereafter abbreviated CMAS) is representative of actual engine deposits from operation in desert environments, but neglects the Fe and Ni observed in the engine deposits [36]. The latter (hereafter abbreviated CAS) is the lowest eutectic of the $CaO–AlO_{1.5}–SiO_2$ ternary system. Some relevant properties are summarized in Table 3.1. (The experimental design, Fig. 3.1, precluded using Fe-containing silicates—FeO_x present in the melt reduces in the presence of graphite, altering the melt properties and generating gas that disturbs the melt and precludes diffusion analysis.) The chosen silicate compositions have several advantages that motivated their selection. First, both compositions are thermodynamically stable as a single-phase liquid at target TBC temperatures (≥1300°C)—the absence of solid phases in the melt simplifies the diffusion analysis and quantification. Second, these compositions have been widely studied both within and outside of the University of California, Santa Barbara—the novel results herein can be compared to a wide body of work on or using these melts [63,93,94,150–152], including fundamental melt properties [59,91] and thermodynamic equilibrium experiments with some relevant BOs [58]. Third, the compositions represent a wide range of relevant melt properties, including the Ca:Si ratio and the melt viscosity. Recent evidence has built support for the importance of the melt Ca:Si ratio as the dominating factor for BO-melt reactions, e.g., Refs. [10,77,79]. The CMAS and CAS compositions herein span a range of Ca:Si of 0.41–0.73, capturing regions where some reactive phases are stable in one melt but not

[c] The concentrations of molten silicate constituents are expressed in mole percent of the oxide formulae based on a single cation, using the first letter of the oxide, i.e., C=CaO, M=MgO, $A=AlO_{1.5}$ and $S=SiO_2$.

the other (e.g., $ZrSiO_4$ is thermodynamically stable in CAS, but not in CMAS [58]). The CMAS and CAS melt also differ significantly in their viscosity, Table 3.1, and capture the majority of the range of possible melt viscosities (within the constraints of being a single phase liquid and free of iron) [10,59]. As the diffusivity of network forming cations (e.g., Zr^{4+}) has been found to be roughly inversely proportional to the melt viscosity [104,111–113], the implication is the two melt compositions were expected to capture a significant range of the possible diffusion rates. In some cases, additional melt compositions were used to probe specific questions, which will be specifically addressed as relevant.

The silicate compositions were produced following previously developed procedures [59]. Briefly, crystalline C(M)AS was produced by solid state reaction from the individual oxides (99.95% CaO, 99.95% MgO, 99.97% Al_2O_3, 99.99% SiO_2; Alfa Aesar, Ward Hill, MA), then melted at 1400°C in a graphite crucible in an inert atmosphere, held for 4 hours, and quenched to form a glass. This approach ensured homogeneity and consistent, rapid "melting" in the dissolution experiments. The glass was crushed down to -200 mesh (<74 μm), which facilitated packing in the crucible assemblage shown in Fig. 3.1. The amorphous nature of the C(M)AS was confirmed via X-ray diffraction (Panalytical Empyrean, Malvern, UK).

In some cases, dense glass rods were used in place of powdered glass. The glass rods were produced by placing the powdered glass in an appropriately sized graphite crucible for the desired rod dimensions. The assemblage was then heated to ~1400°C in a vacuum furnace (which facilitated the removal of entrained air, especially for the viscous CAS melt), held for 1 h, then quenched by shutting off the hot zone. To help obtain higher quench rates, gettered argon was backfilled into the furnace

immediately following the hot zone shutdown. The rods were inspected for any internal crystallization or bubbles via optical microscopy, and they were flattened and polished along one end for the diffusion couple experiments.

3.2 Experimental procedure

Once the amorphous silicate powder was created and the BOs were densified, polished, and cut, the materials could be assembled into the graphite crucible depicted in Fig. 3.1. The graphite crucible was created from cutting a large plate of graphite (McMaster-Carr, Atlanta, GA) with appropriately spaced rows of 4 mm diameter holes milled into the plate. The BO was added followed by the graphite tube (Ohio Carbon Blank, Kirtland, OH). The tube constrained the area of contact between the BO and the C(M)AS to the top of the BO coupon only, which preserved the 1D nature of the diffusion problem. In cases where the tube outer diameter was too small (i.e., the tube was slightly below tolerance) graphite paint was used to seal the small gap between the outer tube wall and the inner crucible wall. Finally, the silicate glass powder was added slowly and was periodically compacted by hand using a small punch. However, short duration experiments (0–2 min) with glass powder resulted in significantly cracked glass on quenching, rendering concentration profiles unrecoverable. This is attributed to a high density of voids near the BO-melt interface—which coalesced and migrated away from the interface in longer duration experiments—and was remedied by using fabricated dense glass rods in place of powder for these short duration experiments. In either case, sufficient C(M)AS was added to ensure the melt remain semi-infinite throughout the duration of the diffusion experiment (typically ~4 mm in length). The location of the BO in the assemblage minimized the driving force for melt density-driven convection resulting from the incorporation of

heavier cations from the dissolving oxide. Neither the BO or the melt reacted with the graphite—no reduction of the BO was observed, and the melt did not wet the graphite.

The crucible-sample assemblages were heated by insertion into a pre-heated tube furnace utilizing a high-purity alumina tube (Coorstek, Golden, CO). One end of the tube was left open to allow for rapid insertion and extraction of the sample while the other was sealed. Gettered Ar (with measured oxygen concentration <1 ppb) was flowed at 1 l/min through the furnace to minimize oxidation of the graphite. Care was exercised to minimize temperature gradients in the hot zone and to ensure the thermal excursions experienced by multiple samples were reproducible. The protocol was designed to maximize the heating and cooling rates of the sample. The time necessary for the samples to reach thermal equilibrium upon insertion into the hot zone was minimized by first preheating the samples for 60 s at 800 °C. The actual temperature reached in this time remained below the C(M)AS glass transition temperature (Table 3.1) and therefore was not expected to induce any dissolution or diffusion. After preheating, the sample was rapidly inserted into the hot zone of the furnace, held for the desired exposure time, and then rapidly extracted and quenched in flowing air.

Multiple experimental temperatures and durations were studied to yield a systematic understanding of BO-melt kinetics. The plurality of experiments was carried out at 1300 °C, but temperatures of 1200, 1300, 1350, and 1400 °C were studied. Experimental duration ranged from 1–240 min. The shorter exposures (1–10 min) were typically used in the quantification of the dissolution and diffusion rates. Longer duration experiments provided insight about the evolving microstructure of the dissolution front and, in some cases, the formation of crystalline products, including reactive crystallization phases.

3.3 Characterization

Sample assemblages, after heat treatment, were mounted in epoxy (Allied High Tech Products Inc., Rancho Dominguez, CA) and cross-sectioned using a low-speed diamond saw. Excess graphite was removed (e.g., from the glass-free region of the tube) and multiple cross-sections were mounted in 1" diameter epoxy discs. The samples were polished following standard metallographic techniques, down to 0.25 μm finish with colloidal diamond (Allied High Tech Products, Inc., Rancho Dominguez, CA). The polished epoxy discs were coated either with gold-palladium (for scanning or transmission electron microscopy) or with carbon (for electron probe microanalysis). Thin lamellas for transmission electron microscopy (TEM) were produced using focused ion beams (FIB, Helios 600, FEI, Hillsboro, OR) from appropriate regions of the polished samples.

The samples' microstructural evolution at the BO-melt interface were primarily characterized by scanning electron microscopy (SEM) using a FEI XL-30, FEI Nova NanoSEM 650, and Thermo Fisher Apreo C (FEI: Hillsboro, OR; Thermo Fisher: Waltham, MA) with secondary electron (SE) and backscattered electron (BSE) imaging. High spatial resolution microstructural and phase analysis was carried out using transmission electron microscopy (TEM) in a FEI Tecnai G2 Sphera (200 kV) or Scanning TEM (STEM) in a Thermo Fisher Talos G2 (200 kV), equipped with ChemiSTEM electron dispersive x-ray spectroscopy (EDS). While phase identification was aided using semi-quantitative chemical analysis via EDS in the both SEM (SEM-EDS) and in the TEM (TEM-EDS), reported phase constitutions were determined using standardized wavelength dispersive spectroscopy (WDS) in an electron microprobe (EPMA, Cameca SX-100) whenever features were large enough (typically >1 μm).

The rate of BO dissolution into the melt and the diffusivity of cations therein was quantified by collecting concentration profiles within the melt. The method is depicted schematically in Fig. 3.4. The composition of the polished cross sections (Fig. 3.4a) were determined by EPMA and WDS. This technique shares the spatial resolution limitations of SEM-EDS but can be automated, has significantly higher energy resolution, and is standardized to several in-house standards for BO-silicate interactions. Multiple (2–4) line scans (each consisting of dozens of spot scans) running perpendicular to the BO-melt interface were collected for each sample (Fig. 3.4b)—cross comparison between these scans ensured that the sample was free of melt convection [95]. Counting times for BO constituents (e.g., Zr^{4+}, Y^{3+}, Gd^{3+}, etc.), Ca, and Si were 50 s on-peak and off-peak. Al and Mg were combined on the same detector with 20 s on-peak and off-peak. The WDS analyzing crystals used were LTAP for Al and Mg, LPET for Zr, Y, and Ca, and TAP for Si [153]. Line scans were typically collected at 15 kV and 10 nA. Typical spot sizes were 2 μm, except for samples with small diffusion distances where a 1 μm beam was used.

3.4 Quantification

The measured concentration profiles (e.g., Fig. 3.4c for 7YSZ dissolution) could be fit to oxide dissolution and diffusion models developed in the geochemical literature [96,97]. Spatially- and temporally evolving concentration profiles within the melt can be described using the following expression:

$$\frac{\partial C_i}{\partial t} = D_i\left(\frac{\partial^2 C_i}{\partial x^2}\right) - u(t)\left(\frac{\partial C_i}{\partial x}\right) \tag{3.1}$$

wherein x is the distance from the crystal-melt interface, t is the exposure time, C_i is the concentration of component i in the melt, D_i is an appropriate diffusion coefficient[d] for component i, and $u(t)$ is the time-dependent rate of melt growth, related to the solid oxide dissolution rate by the relative densities of melt and oxide, i.e. $u_{ox}(t) \equiv u(t)\ (\rho_m/\rho_{ox})$ [97,154]. The temporal dependence of the melt growth rate can be written as

$$u(t) = u_o\left[C_{i,\mathrm{sat}} - C_i(0,t)\right] \tag{3.2}$$

where $u_o = u(t = 0)$ is an initial melt growth rate (proportional to the initial solid oxide dissolution rate) and $C_i(0,t)$ is the concentration of component i at the oxide-melt interface, which evolves over time towards a saturation value, $C_{i,sat}$, the asymptotic value of $C_i(0,t)$ at long times. This assumption is further discussed below. The dependence of $u(t)$ on $C_i(0,t)$ means that the solid oxide dissolution rate depends on both the intrinsic rate that atoms can be detached from the solid oxide and subsumed into the melt (an initial dissolution rate, which scales with u_o) and the diffusive flux away—the balance of u_o and D_i controls how $C_i(0,t)$ evolves with time and therefore the time dependent dissolution rate.

[d] In this case, the diffusivity in Equations (1) and (3) is an *effective binary diffusion coefficient*, (EBDC) [101,102] representing the transport of component i in a constant background of all other melt components combined, i.e., all cross terms in the diffusion matrix are ignored. This approximation makes quantification of the diffusivity possible without the time-intensive process of determining a diffusion matrix for a 5–6 component melt and is commonly applied in multicomponent systems.

Given that none of the BO components are present in the melt at the start of the experiment, $C_i(x,0) = 0$. The boundary conditions are (i) a semi-infinite body along the diffusion direction, i.e. $C(\infty,t) = 0$, and (ii) a mass balance at the oxide-melt interface given by

$$D_i\left[\frac{\partial C_i(0,t)}{\partial x}\right] = u(t)\left[C_i(0,t) - C_{i,ox}\right] \tag{3.3}$$

where $C_{i,ox}$ represents the concentration of component i in the dissolving oxide.

The parameters in Equations (1–3) were fit to experimental concentration profiles using an explicit finite difference method with second-order central difference approximations. The Python package LMFIT was used for the minimization of the error in the fitting [155]. A one-minute time correction was applied to the prescribed exposure period to account for the thermal lag during heating and any transient dissolution and diffusion that occurs during heating. The correction factor was determined using exposed-wire fast-response, type K thermocouples, which were directly embedded into the CMAS during multiple calibration runs at different temperatures. The one-minute correction was found to apply to all experiments because, while the dissolution rates may be higher at the higher temperatures, the heating times are shorter because samples are introduced into a hotter furnace. Confidence on this approach is reflected in the consistency of the determined diffusivities with experimental duration (Chapter 4, e.g., Table 4.1). The approximate dissolution distance, L, of the 7YSZ was calculated at any exposure time by using the dissolution and diffusion parameters obtained from Equations (1–3) to determine $u_{ox}(t)$, then integrating over time.

Two parameters in Equations (1–3) must be known to fit for the diffusivity (D_i) and the initial melt growth rate (u_o): the composition of the dissolving oxide and the saturation concentration of the

dissolving species. The solid oxide composition was determined by averaging multiple spot scan analyses in EPMA and was insensitive to experimental duration. The saturation concentration in the melt was obtained by fitting the interface concentration of the principal BO species[e] (e.g., Zr for 7YSZ) as a function of time to a simple exponential rise function,

$$C_i(0,t) = C_{i,sat}[1 - \exp(-a\,t)] \tag{3.4}$$

where the saturation concentration is given by $C_{i,sat}$ and a is a rate constant. This phenomenological description provides an un-biased estimation of the saturation concentration. In the case of multicomponent BOs, the concentration of the non-principal species (e.g., Y for 7YSZ) at the interface continues to increase after saturation of the principal species, but no longer at the rate shown in Equation 4. In some cases, the minor component continued to increase throughout all experimental durations studied (up to 240 min). Fortunately, the initial dissolution rate for the BO applies to all constituents—the diffusivity of the minor component was found by fitting equations 1–3 with a fixed u_o resolved from fitting the principal component concentration profiles.

[e] The principal species of a multi-component oxide is assumed to be the equilibrium determining species for the dissolution process [97], i.e., its approach towards saturation is expected to be primarily responsible for changing the dissolution rate vis-à-vis Equation 3.2.

3.5 Figures and tables

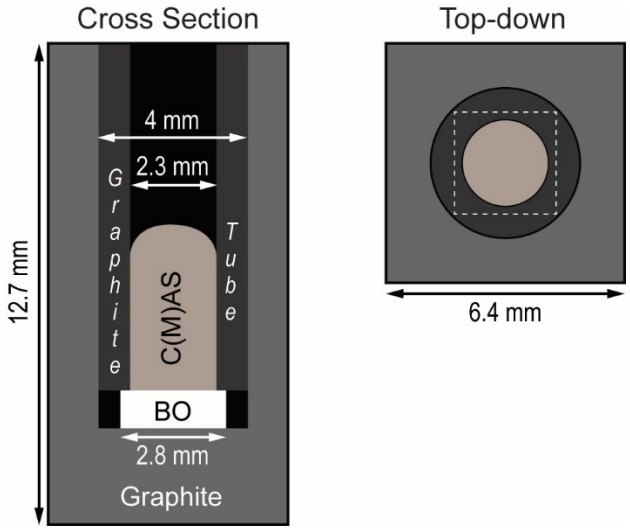

Fig. 3.1: Schematic of the experimental assemblage. The BO-C(M)AS diffusion couple is contained within a graphite crucible. A graphite tube prevents the C(M)AS from running over the side of the square BO and maintains the 1D nature of the diffusion couple. The graphite tube, C(M)AS, and BO inner assemblage is readily removed from the outer crucible for sample preparation.

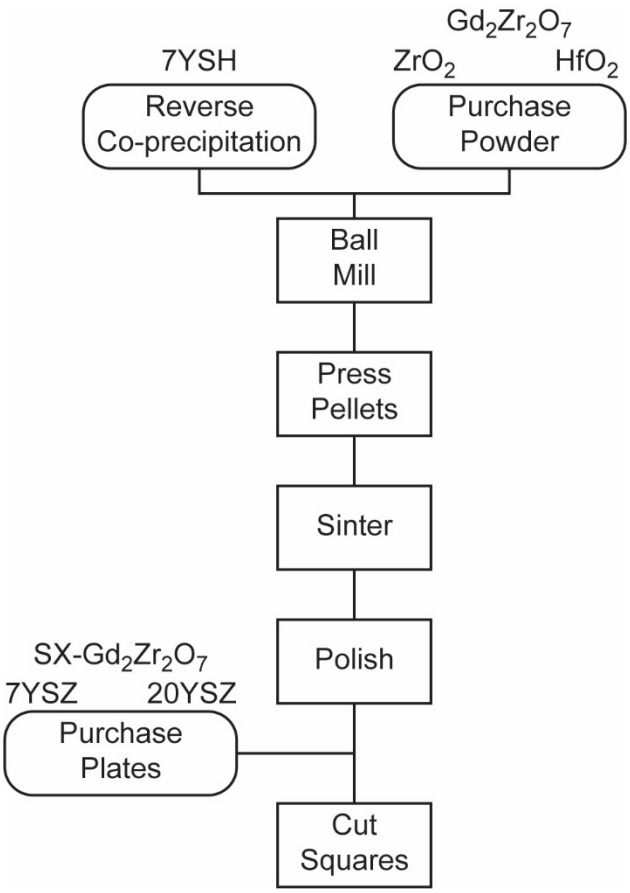

Fig. 3.2: Flow chart of the experiment techniques used to produce dense barrier oxides. Starting points are represented by rounded rectangles.

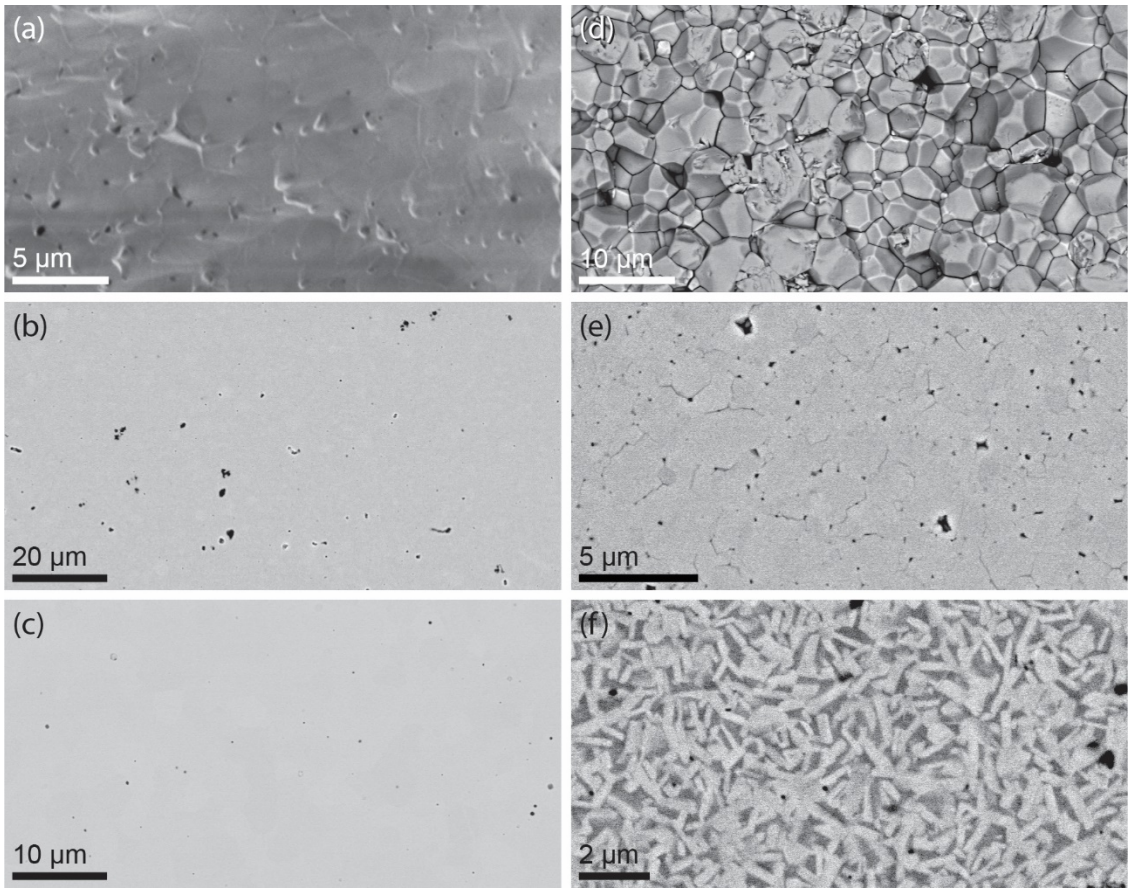

Fig. 3.3: Representative micrographs of the pristine barrier oxides investigated, including (a) ZrO_2, (b) 7YSZ, (c) $Gd_2Zr_2O_7$, (d,e) HfO_2, and (f) HfO_2–$7YO_{1.5}$. The rare earth free oxides (a,d,e) required special polishing treatments to ensure a planar front for the dissolution and diffusion experiments. The ZrO_2 was ion-polished to produce a principally planar front (a). The HfO_2 microcracked, which resulted in grain pullout (d) if polished too aggressively; the latter was minimized (e) by a gentle polishing procedure starting with 3 μm diamond polishing fluid. Adding 7% $YO_{1.5}$ to the HfO_2 (f) resulted in a secondary cubic phase (darker contrast) with ~13% $YO_{1.5}$ and prevented microcracking.

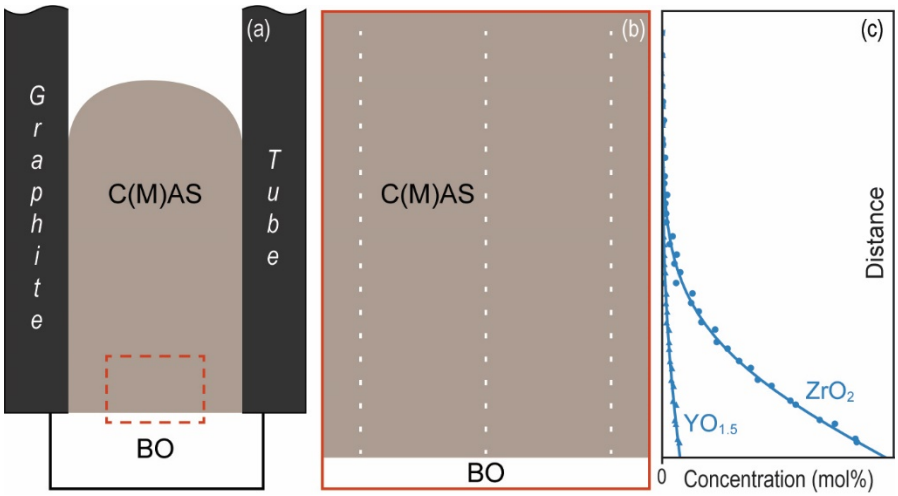

Fig. 3.4: Polished diffusion couple cross-sections (a) were analyzed with electron probe microanalysis to quantify the dissolution and diffusion kinetics. Multiple line scans (b) were collected from the BO-C(M)AS interface and superimposed to ensure the sample was free of convection. An example concentration profile from the dissolution of 7YSZ is shown in (c).

Table 3.1: A summary of some relevant properties for silicate glasses used in this investigation. Melting behavior and viscosities are pertinent to Chapter 4 and Chapter 6.

	CMAS	**CAS**
Composition*	$C_{33}M_9A_{13}S_{45}$	$C_{24}A_{17}S_{59}$
Liquidous Temperature (°C) [59,135]	~1270	~1170
T_g (°C) [59]	764	802
$\eta_{1300, G}$ (Pa·s)†	5.2	1700
$\eta_{1300, FS}$ (Pa·s)‡	3.1	110
$\eta_{1350, G}$ (Pa·s)	2.8	740
$\eta_{1350, FS}$ (Pa·s)	2.1	62
$\eta_{1400, G}$ (Pa·s)	1.5	330
$\eta_{1400, FS}$ (Pa·s)	1.4	36
NBO/T **	1.22	0.41

* Composition reported in single cation mole percent, i.e., C=CaO, M=MgO, A=$AO_{1.5}$, S=SiO_2

† Viscosity calculated using the Giordano model [87].

‡ Viscosity calculated using the FactSage model [51]. Note the variance between the FactSage and Giordano models for the CAS melt.

** Non-bridging oxygens per tetrahedra, a measure of melt network connectivity. The calculation assumes all $AlO_{1.5}$ acts as a network former.

CHAPTER 4. CHARACTERIZING DISSOLUTION AND DIFFUSION KINETICS

As elaborated in the background, the rate of melt saturation directly limits the nucleation and growth rate of reactive crystallization phases and is therefore of critical importance to understand. Two processes affect melt saturation: the dissolution of barrier oxides (BOs) into the melt and the diffusion of those cations throughout the melt. Therefore, quantitative characterization of the dissolution and diffusion kinetics enables a deeper understanding of melt saturation, which then affords an assessment of the conditions needed for crystallization. This chapter quantifies the dissolution and diffusion process for three barrier oxides: 7YSZ, HfO_2, and $Gd_2Zr_2O_7$ (GZO). The results will be discussed regarding the active dissolution mechanism, the fitting methodology and sensitivities therein, the observed trends in the quantified dissolution and diffusion kinetics, and some broader takeaways for TBC/EBC experiments with molten silicates overall.

It is important to note that quantifying the dissolution kinetics required capturing the system before any crystallization (either reactive or recrystallization) occurred. The fitting method used, Equation 3.1 to 3.3, considers the only flux of BO constituents into the interface melt to be from dissolution of the pristine oxide while the only flux within the melt is via diffusion—the balance of these two processes is readily determined by experimental measurables. Crystallization, however, provides another mechanism for BO material leaving the melt, which upsets the balance of Equations 3.1 to 3.3. In theory a system with active crystallization is still tractable, but it is practically much more complex, requiring a spatiotemporal understanding of the crystallized phase(s) composition, size, geometry, redissolution, etc. The rapid crystallization of GZO precludes a rigorous quantification of

this dissolution rate by the current methodology—the pertinent dissolution rate will instead be estimated for comparison to 7YSZ and HfO_2.

4.1. Results

A representative group of micrographs for quantified experiments is shown in Fig. 4.1. Short duration experiments (<10 min) for 7YSZ and HfO_2 showed no evidence of crystallization—these experiments are readily quantified and will therefore be discussed within this chapter. Experiments on GZO, however, showed rapid and extensive crystallization (discussed further in Chapter 5) for all conditions, even those at the limits of the experimental design. In this case, a direct measurement of the dissolution rate was not possible; only the diffusion rate was quantified for GZO.

4.1.1. Concentration profiles from 7YSZ dissolution

Concentration profiles, obtained from the dissolution of 7YSZ, are the main result and are shown in Fig. 4.2 for CMAS and Fig. 4.3 for CAS for each experimental temperature of (a,b) 1300 °C, (d,e) 1350 °C, or (g,h) 1400 °C. (Note that the profiles are plotted from a common origin at the interface, but the interface is receding over time. However, the recession is small compared with the scale of the distribution.) Concentration profiles of ZrO_2 and $YO_{1.5}$ after 10 min of exposure, shortly after melt saturation occurred, for all melt composition and temperature combination are compared in Fig. 4.4. The abscissae in Fig. 4.4 are normalized by the square root of the hold time to facilitate comparison between different exposure times. The results show a monotonic decrease in the yttria and zirconia and by extension an increase in C(M)AS concentration away from the interface, i.e., the results were convection-free. The ZrO_2 concentration in the melt was significantly higher than that of $YO_{1.5}$, as expected from the composition of the dissolving 7YSZ.

The salient finding is that the concentration of both Zr^{4+} and Y^{3+} at the YSZ-melt interface increases with time towards a saturation value, Fig. 4.2(c,f,i) and Fig. 4.3(c,f,i). The Zr^{4+} evolution can be empirically fit to Equation 3.4 to determine the "saturation level", which was in the range 3–4 mole% for both CMAS and CAS and was reached after 5–6 min for CMAS and 4–6 min for CAS. Conversely, the interfacial yttria concentration kept increasing up to 240 min, the maximum exposure time studied. The implication is that the excess ZrO_2 associated with this continued dissolution of $YO_{1.5}$ is removed by reprecipitation of the Y-depleted tetragonal YSZ after ~10 min. This suggests that zirconia is the local equilibrium-determining species [97] for the dissolution of 7YSZ.

No evidence of the "uphill diffusion" behavior, often reported in the geological literature e.g., [101], was observed in the concentration profiles. The melt constituents show concentration profiles varying only due to dilution—the inference is that the diffusion of yttria and zirconia is largely decoupled from that of the C(M)AS components. In some cases, however, a small dip in the Y^{3+} and Zr^{4+} concentrations were observed near the dissolving 7YSZ-melt interface. This is attributed to the re-growth of interfacial grains during cooling as the melt boundary layer becomes supersaturated with the YSZ constituents [95]. This phenomenon was most evident for zirconia at longer times, after saturation of the interfacial melt and reprecipitation of zirconia had started. Data points near the interface showing these effects were not included in the quantification of the concentration profiles or in determining the crystal-melt interface concentration. These were instead estimated by extrapolating the concentration profiles to the crystal-melt interface.

The concentration profiles were well fit to the dissolution and diffusion model described in Chapter 3, which fully captures the dissolution and diffusion processing and the resulting time-dependent concentration at the BO-melt interface. Table 4.1 lists the experimental parameters for each 7YSZ diffusion couple, the values for D and u_o estimated by fitting the data to Equations (3.1 to 3.3), and the calculated dissolution distances after 10 min, L_{10}. The saturation concentrations, diffusivities, initial melt growth rate and solid front recession increased with increasing test temperature. For experiments where it was not possible to accurately determine u_o because saturation was achieved before the end of the test, u_o was adopted from the values for shorter times (<10 min). Diffusion and melt growth rates were slower in the (higher viscosity) CAS melt but the C_{sat} values were similar to, but slightly higher than, those for CMAS.

The crystal dissolution experiments on the polycrystalline 7YSZ were repeated for multiple temperatures to estimate the activation energies and pre-exponential factors for diffusion, the initial melt growth rate (u_o), and the dissolution distance (L_{10}). The calculated diffusivities could be reliably fit to a typical Arrhenius equation,

$$D = D_o \exp(-Q/RT) \tag{4.1}$$

with a pre-exponential factor, D_o, and an activation energy, Q, as shown in Fig. 3.4(a). The temperature dependence of u_o follows a modified Arrhenius equation,

$$u_o = A\,T \exp(-E_a/RT) \tag{4.2}$$

with a pre-exponential factor, A, and an activation energy, E_a. However, the data could not be reliably fit to the modified pre-exponential factor, as seen in Fig. 3.4(b). The values of u_o for CMAS in Table

4.1 exhibit significant dispersion and there is no discernible variability in u_o with temperature for CAS. Nevertheless, the dissolution distance after 10 min, calculated by integration of the dissolution rate (Equation 3.2), was also found to exhibit Arrhenius behavior as shown in Fig. 3.4(c). As the time dependent dissolution rate depends on the interface concentration, which in turn depends on the rate of diffusion, the Arrhenius behavior of L_{10} likely largely reflects the Arrhenius behavior for diffusion. The fitting parameters for the best fit lines shown in Fig. 3.4 are presented in Table 4.2.

4.1.2. Concentration profiles from HfO_2 dissolution

Dense HfO_2 pellets were exposed to CMAS and CAS at 1300 °C to study the dissolution and diffusion kinetics—the resulting concentration profiles are shown in Fig. 4.6 and the ZrO_2 concentration profile from 7YSZ dissolution at 1300 °C for 10 min is shown for comparison. (Concentration profiles could not be obtained for pure ZrO_2 pellets due to the disruptive *t* to *m* transformation on cooling from the sintering conditions—the latter rendered the pellet surface cracked and non-planar.) The Hf^{4+} concentration at the interface was also observed to increase with time (Fig. 4.6b,d), reaching a saturation value between 5–10 min, with a saturation value slightly higher than Zr^{4+} from 7YSZ dissolution under otherwise identical conditions. Conversely, the Hf^{4+} concentration profiles do not reach as far as Zr^{4+} from 7YSZ dissolution, indicating a lower diffusivity of the former. Quantification of the concentration profiles focused on short duration (≤10 min) experiments shown in Fig. 4.6. Again, the dissolution and diffusion model discussed in Chapter 3 is well fit to the experimental data. The experimental conditions, D, u_o, and L_{10} are summarized in Table 4.3.

The HfO_2 reacted extensively with the CAS melt beyond ~10 min of exposure to form hafnon ($HfSiO_4$) and Hf-cyclosilicate ($Ca_2HfSi_4O_{12}$). The formation and growth of these phases will be discussed at length in Chapter 5, but the formation of these phases did have a noteworthy effect on the concentration profiles. The significant crystallization observed in long duration experiments (e.g., 60 and 240 min) consumed Hf^{4+} near the hafnon-melt interface, yielding a significant decrease in the measured interface concentration with time below the saturation value measured near 10 min, Fig. 4.7. Conversely, the same exposures to the CMAS melt, which did not undergo reactive crystallization, maintained approximately the same interface concentration as observed at 10 min. The implication is that the saturation concentration measured (and represented by C_{sat} in Equation 3.2 and 3.4) is representative of the maximum solubility of the dissolving oxide(s) in contact with the melt assuming the relevant reactive crystallization phases are kinetically suppressed[a]. As it is this saturation concentration that ultimately controls the dissolution kinetics (à la Equation 3.2), this finding emphasizes the importance of quantifying the dissolution kinetics before any crystallization occurs, which will bring the system towards the true equilibrium concentrations.

4.1.3. Concentration profiles from $Gd_2Zr_2O_7$ dissolution

Unlike 7YSZ and HfO_2, $Gd_2Zr_2O_7$ (GZO) was observed to undergo rapid crystallization, seen as already well-established at 3 min (e.g., Fig. 4.1d). The crystallization (and subsequent microstructural evolution) of GZO will be discussed further in Chapter 5, but the rapid crystallization of new phases is important to identify here as it precludes quantification of the dissolution kinetics—no

[a] This has been observed in the geochemical literature and has been referred to as a "metastable saturation concentration" therein, e.g., Ref. [96] and Fig. 19 therein.

experiments could capture a case where $C(0,t) < C_{sat}$, which is required to quantify u_o per Equations 3.1 to 3.3. However, in the limit of $C(0,t)$ approaching C_{sat} the value of $u(t)$ approaches 0 and Equation 3.1 recovers Fickian diffusion. Thus, the diffusivities of Zr^{4+} and Gd^{3+} can still be quantified.

Concentration profiles of ZrO_2 and $GdO_{1.5}$ obtained from the dissolution of single crystalline GZO into CMAS at 1300 °C are shown in Fig. 4.8, which again features a time-normalized abscissa to facilitate the comparison of different experimental durations. Unfortunately, experiments with the single crystalline GZO often showed concentration profiles with instabilities, which were attributed to melt density driven convection due to the dissolution of a heavier Gd^{3+} species (compared to $YO_{1.5}$). As a result, only the 10 min exposure was quantified. The presented profile in Fig. 4.8 is, however, free of convection and is compared to the equivalent profile from 7YSZ dissolution.

Even before quantification, the concentration profiles of Fig. 4.8 imply that the dissolution of GZO must be significantly faster than that of 7YSZ. The Zr^{4+} concentration profile (Fig. 4.8a) is markedly similar between 7YSZ and GZO dissolution, despite the latter having significantly less ZrO_2 in the dissolving BO (93% vs. 50%). The presumed enhanced dissolution rate of GZO and significant concentration of RE oxide lead to significantly more Gd^{3+} dissolved into CMAS than Y^{3+} under otherwise identical conditions (Fig. 4.8c). The Gd^{3+} interface concentration remains stable between 10 and 60 min, indicating Gd^{3+} is saturated, whereas that of Y^{3+} continues to increase (Fig. 4.8d). Note that despite the extensive crystallization, the interface concentration of Zr^{4+} and Gd^{3+} (Fig. 4.8b,d) did not decrease between 10 and 60 min—as was observed for HfO_2 (Fig. 4.7)—but remained

at the plateau value. The concentration profiles were well fit to standard semi-infinite diffusion solutions; the estimated diffusivities and dissolution distance (L_{10})[b] are reported in Table 4.4.

4.2. Discussion

4.2.1. The dissolution mechanism

The salient finding from the work presented herein is the identification of the active dissolution mechanism, revealed by comparing the concentration profiles (e.g., Fig. 4.2 and Fig. 4.3 for 7YSZ) to the expected profiles shown in Fig. 2.12 and discussed in Chapter 2. The dissolution of 7YSZ and HfO_2 featured a two-stage dissolution mechanism. In the first, and transient, stage, the dissolution rate is controlled by mixed diffusion and interface kinetics, i.e., neither D nor u_o are small enough to independently limit dissolution rate. The manifestation is that the first stage features an evolving concentration of the dissolving oxides at the BO-melt interface, and the interface melt remains beneath the critical value necessary to reach saturation, therefore delaying the nucleation of phases incorporating melt constituents. After the transient stage, typically around 5–10 min for 7YSZ and HfO_2, the interface melt becomes saturated and further dissolution rate becomes limited by the diffusive transport of material away from the interface. The semi-infinite melt leveraged in the experimental geometry ensures that continued diffusion—and therefore dissolution—will occur. The dissolution mechanism, and namely the balance of D and u_o, will be a central point of discussion throughout the rest of the dissertation. The non-instantaneous buildup of BOs in the melt has

[b] The calculated dissolution distance only accounts for the dissolved Gd^{3+} content, not that captured in crystallized phases, and therefore represents a lower bound estimate. This will be discussed further in Section 4.2.3.

important implications on the formation of reaction zones observed in longer duration experiments (e.g., >10 min), which will be discussed in Chapter 5. The balance of D and u_o on finite length scales, relevant to actual coatings, has important implications for coating design, which will be discussed further in Chapter 6. Note that this finding is atypical in the literature—few studies have investigated cases where u_o is sufficiently small to matter and therefore this represents a significant knowledge gap in the literature. The results indicate that HfO_2 would be a good material for fundamental investigations on the transient stage of dissolution.

Unlike 7YSZ and HfO_2, GZO dissolves rapidly such that the initial transient stage could not be captured with the experimental methods employed herein. In all cases to date, experiments have shown evidence of crystallization (even after only 1 min) therefore precluding quantification of u_o. While GZO must have a transient stage (the interface concentration cannot instantaneously jump to saturation), it appears to be short enough to elude experimental observation. The implication is that the dissolution rate of GZO, i.e., u_o, must be sufficiently large relative to the diffusivity. In all practical sense, then, the dissolution mechanism of GZO is controlled by removing Gd^{3+} and Zr^{4+} from the interface, which occurs by diffusion (i.e., following Fig. 2.12a) and by the crystallization of apatite and fluorite.

4.2.2. The dissolution and diffusion fitting method and sensitivities therein

Having established the broad features of the dissolution mechanism, the relevant PDE needed to fit the concentration profiles is identified (see Section 3.4 and equations therein). Equation 3.1 is a diffusion-advection PDE with a time varying flux at one boundary (Equation 3.3). The equation is not trivial to fit to experimental data—the non-linear PDE must be discretized into an ODE and

numerically solved through time for each guess at the fitting parameters—and, as a result, each fit takes multiple minutes to complete. This section will discuss the sensitivity of the fitting parameters (D and u_o) to two changes: first, whether a simpler model, more quickly and easily fit to experimental data, can afford the same results as the full PDE; second, how the fitting results of the full PDE depend on input parameters, namely the concentration (and its units), the spatial coordinate, and the experimental duration.

Sensitivity of D and u_o to the fitting equation

Example concentration data for Zr^{4+} from the dissolution of 7YSZ into CMAS at 1350 °C for 3 min is shown in Fig. 4.9 together with the best fit lines determined using three different models: the full PDE (Equation 3.1 to 3.3), the PDE of Equation 3.1 but without the advection term, and a simple complimentary error function (erfc) solution to standard Fickian diffusion, namely

$$C(x,t) = C_o \mathrm{erfc}(x/\sqrt{4Dt}) \tag{4.3}$$

where the concentration at the interface is given by C_o and is time-invariant in this simplified equation. The best fit line from each of the three models overlap significantly but the erfc model slightly underpredicts near the interface.

The diffusivity predicted by each model agree within typical uncertainty. Even the simplest model, the complementary error function, accurately predicts the diffusivity compared to the full model (12.3±0.6 vs. 12.6±0.8 $\mu m^2/s$, respectively). The positive implication of this is that the diffusivity can be measured from incomplete data sets where the full dissolution kinetics have not been established. For example, this provides assurance that the diffusion kinetics of GZO measured by this work

should be accurate even though rapid crystallization in this system precludes using the full PDE. This also enables long duration experiments, which are less sensitive to heating and cooling effects, to provide estimates of diffusivity with less experimental uncertainty. (This experimental duration sensitivity will be elaborated later in this section.) The obvious disadvantage is that Equation 4.3 does not capture any information about the dissolution kinetics—the interface concentration is taken to be a fixed value with respect to time, which does not follow experimental observations. The question then is whether the full PDE can be simplified while accurately predicting u_o.

While diffusion profiles typically extend 100's of microns into the melt, the dissolution distances are ~2 orders of magnitude smaller—the third model in Fig. 4.9 investigates whether or not the advection term of Equation 3.1 can be ignored because of this significant difference in scale. (The dissolution process, i.e., the increasing concentration at the interface, is still captured with the boundary condition Equation 3.3.) The fit superimposes over that of the full PDE and the model is ~5 times less computationally demanding. The advection-free model predicts the same diffusivity (within error) of the other models but significantly affects the predicted value of u_o. This highlights that the advection term is important—its exclusion results in a faster buildup of material at the interface requiring a lower value of u_o under otherwise identical conditions. Therefore, the experience to date is that D is relatively insensitive to the model used (even basic diffusion equations accurately quantify D), but accurate determination of u_o requires the full PDE of Equation 3.1.

Sensitivity of D and u_o to model inputs

The fitting parameters were found to be sensitive to the input data, namely each measurement in the concentration profile carries a concentration value, a spatial coordinate, and an experimental duration which are provided to the model for fitting. Standardized concentration data, ideally collected via wavelength dispersive spectroscopy to ensure better energy resolution, was critical for accurately determining the interface concentrations and the diffusivities. The high-quality concentration data from EPMA provided fitting parameters with significantly lower error than equivalent concentration profiles collected by SEM-EDS. In particular, quantification of low concentration species, such as $YO_{1.5}$ from 7YSZ dissolution, e.g., Fig. 4.4(b), demanded EPMA to obtain measurable signal over the noise. Having low noise data also proved critical for accurately quantifying interface concentrations necessary to assess u_o. Furthermore, converting the concentration data units affected the fitting results. The raw output from EPMA was in weight percent units and, because the concentration of each element is determined by direct comparison to a standard, each measurement point did not necessarily sum to 100%. Unit conversion necessitates a normalization of the data, which could systematically affect one element more than others. (Although the data reported in the figures of this dissertation are shown in mole percent on a single cation basis, which is arguably more intuitive, the fitting parameters reported in Table 4.1 to Table 4.4 were determined by fitting concentration profiles in weight percent, the raw output of the EPMA.) Therefore, accurate quantification of both D and u_o requires standardized concentration data from which the raw output form (unit) should be used—this serves as the most fundamental starting point.

Quantifying u_o relies on an accurate determination of the saturation concentration and therefore the interface concentrations for each experimental duration. Two effects hindered measurement of the interface concentration: first, some BO regrowth was observed during the rapid quench, which often affected the first 1–10 μm of the concentration profile, depending on the diffusivity; therefore, near interface points could not be considered and the interface concentration was determined by extrapolation from the rest of the concentration profile. (Similar effects have been widely reported in the crystal dissolution literature, e.g., [95–97], where it is known as "the quench effect".) Second, the EPMA stage indexed by the nearest micron, sometimes introducing drift between the programmed and actual measurement locations on the order of ±1–2 μm. The significant slope of the concentration profile near the interface meant this error led to significant changes of the extrapolated interface concentration. To eliminate the error, the actual measurement locations (and therefore the distances to the interface) were measured using secondary electron imaging in the SEM, which allowed the beam damage from EPMA measurements to be clearly seen on the sample.

The fitting parameters were also sensitive to the experimental duration and, by extension, the time correction factor used to account for the sample heating time. The experimental durations reported in Table 4.1, Table 4.3, and Table 4.4 are the nominal durations, i.e., the length of time the sample spent in the furnace hot zone; despite the small size of the assemblage, it required a finite time to reach thermal equilibrium with the hot zone. Thus, a finite heating time exists, which must be corrected to accurately quantify the kinetics. Fig. 4.10 plots the fitting parameters obtained for D_{Zr} and u_o (in this case from 7YSZ dissolution into CMAS at 1350 °C) vs. the nominal experimental duration; three different time corrections (0, 1, and 2 min) are plotted in the figure. The actual time

correction factor was determined to be approximately 1 min (see Section 3.4), so the other two lines represent an under- and over-correction.

The diffusivity, Fig. 4.10(a), asymptotically approaches a value at longer times regardless of the time correction used. This is a logical result of any time correction becoming less significant as the experimental duration increases—for example, an experimental duration uncertainty of 60 s is very significant when the experimental duration is 180 s but becomes insignificant when the nominal experimental duration is many 100's of seconds. Thus, the most accurate determination of diffusivity results from long duration experiments, provided the experiment is free of convection and ideally substantial crystallization. Because the diffusivity was largely insensitive to the model used, i.e., the dissolution component does not need to be assessed for accurate diffusivity quantification, experiments after crystallization occurs can be used to provide a diffusivity estimate that is largely insensitive to uncertainty in experimental duration. One might expect that seeing a duration-dependent diffusivity (e.g., the 1 min correction curve in Fig. 4.10a) indicates inadequate time correction; this is, unfortunately, not necessarily the case as some dependence of diffusivity on duration could result from the dissolution experiments by way of concentration-dependent diffusivities. For example, ZrO_2 polymerizes silicate melts [110]. Its addition (to an initially ZrO_2-free melt) by the dissolution of 7YSZ would locally increase the melt viscosity and slow down the diffusion kinetics. Increased experimental durations means that more ZrO_2 will be present in the melt and diffusion may occur at a slower rate. Ultimately, concentration-dependent diffusivities were not rigorously investigated by this work.

The effect of experimental duration on u_o is not as easy to circumvent. Short time experiments are critical for the accurate determination of u_o and thus demand an accurate time correction. These points are supported by Fig. 4.10(b); as u_o cannot be determined after melt saturation has occurred, the 10 min experiment is excluded from this plot. The 3 min experiments show significantly smaller error bars than the 5 min experiments. This is attributed to the fact that $C(0, t)$ changes more significantly with time during the beginning of dissolution (i.e., the slope of Fig. 4.2f is highest at low times), which provides sensitivity to the model to determine u_o from a given experimental duration and an extrapolated interface concentration. Given that short times are necessary, the time correction factor used will significantly alter the determined value of u_o, as seen in Fig. 4.10(b). Thus, an experimental determination of the time correction is crucial.

4.2.3. Trends in the diffusion and dissolution kinetics

The model developed by Zhang is well fit to our concentration profiles and enables the full quantification of the diffusion and dissolution rates when the transient stage of dissolution can be captured. This section will describe the importance of melt temperature, melt composition, and BO composition for D, u_o, and L_{10} (i.e., the values of Table 4.1–Table 4.4 and Fig. 3.4). Experiments on 7YSZ, which feature the most complete set of kinetic data, best describe the importance of temperature and melt composition. These experiments will then be compared to HfO_2 and GZO experiments to understand the role of the BO composition on the kinetics, within the same melt and temperature (typically 1300 °C).

Trends in *D*

The diffusivities determined by this work (Table 4.1–Table 4.4 and Fig. 3.4a) are in relatively good agreement with the literature for diffusion in silicate melts [100]. The diffusivities of the rare earth cations (Y^{3+} and Gd^{3+}) were higher than that of Zr^{4+} and Hf^{4+} in both melts, consistent with expectations based on their ionic field strengths (Fs)[c] [156]. The Fs for Y^{3+} and Gd^{3+} is ~0.57 and ~0.55, respectively, closer that of Mg^{2+} (~0.44), a well-known modifier. Conversely, Zr^{4+} and Hf^{4+} have Fs ~0.89 and ~0.90, respectively, closer to that of intermediate cations like Al^{3+} (~0.94) but reported to act like a network former in most silicate melts [110]. The activation energies for both Zr^{4+} and Y^{3+} diffusion in Table 4.2, based on the fits in Fig. 3.4(a), are also within the observed range of values in the literature (*ca.* 200–500 kJ/mole). The values for Zr^{4+} are higher as expected for a putative network former. Moreover, the activation energy for Y^{3+} diffusion is higher than values reported for modifiers in the literature (e.g., Ca^{2+}, Mg^{2+}), corroborating general trends of increasing diffusivities and activation energies with increasing ionic strength of the diffusing cation [100,101]. (This may also suggest that Y^{3+} could act as an intermediate oxide in the CAS and CMAS melts, thereby allowing it to take a network-forming role.) Diffusivities of Zr^{4+} and Y^{3+} are higher in the CAS melt (Si:O~0.36) than the less polymerized CMAS melt (Si:O~0.3), following general trends in the literature [100].

The diffusivities of any one cation (e.g., Zr^{4+}) were intermediately affected by the melt temperature but strongly affected by the melt composition. Increasing the temperature from 1300 °C to 1400 °C

[c] The cation field strength is defined as $F_S = Z/(R_c+R_a)^2$, where Z is the charge, R_c and R_a are the cation and anion radii, respectively, with the appropriate coordination number, CN. For the smaller cations (Al) CN is assumed to be 4, and for the larger cations (Mg, Y, Gd, Zr, Hf) CN is taken as 6.

increased the diffusivity at most by a factor of ~6 (Table 4.1). Conversely, at any temperature, changing the melt from CMAS to CAS (going from the low to high viscosity melt) decreased the diffusivity by at least an order of magnitude. This importance of the melt composition is seen for both 7YSZ (Table 4.1, Zr^{4+} and Y^{3+}) and HfO_2 (Table 4.3, Hf^{4+}). The dependence of diffusivity on melt composition and temperature will be discussed further in Chapter 6, where the former will be correlated to the melt viscosity.

Unlike the melt composition, the BO composition had little effect on the cation diffusivities, i.e., within a single cation, such as Zr^{4+}, the diffusivity of that cation is not strongly affected by what that cation dissolves from. For example, the diffusivity of Zr^{4+} within CMAS at 1300 °C from 7YSZ and GZO are similar within the experimental error (4.0±0.2 and 5.0±0.2, respectively, *cf.* Table 4.1 and Table 4.4). The implication is that the amount of any particular cation in the dissolving BO does not significantly affect the cation's diffusivity. While the dissolution of a new cation into a silicate melt will locally change the melt structure (either breaking or forming bridging oxygens), this finding suggests the change to the melt structure has a negligible impact on the diffusivities—i.e., the diffusivities are not strongly concentration dependent. Furthermore, the diffusivities of the equivalent cations investigated are nearly identical within the same melt at the same temperature. For example, the diffusivity of Zr^{4+} is within a factor of ~2–3 to that of Hf^{4+} (*cf.* Table 4.1 and Table 4.3), and the diffusivity of Y^{3+} is comparable to that of Gd^{3+} (*cf.* Table 4.1 and Table 4.4). The latter is consistent with the limited observations in the geochemical literature for rare-earth oxide diffusivities, which vary by a factor of only ~1.6 across the lanthanide row [100]; less comparative data is available for Zr^{4+} and Hf^{4+}, primarily due to lack of diffusion data on the latter, but their

similar Fs corroborate their similar diffusivities. The broad implication is that the diffusion kinetics will likely be similar across a range of relevant BOs.

Trends in u_o

The dissolution kinetics, conversely, show a more complicated relationship to melt temperature. In theory, the melt growth rate, u_o, should follow a modified Arrhenius equation described by Equation 4.2. Experimentally, however, this equation is poorly fit to the experimental data for 7YSZ (Fig. 3.4b). In the CMAS melt, a temperature dependence on u_o was observed, but the large error of each measurement yielded a poor fit. The CAS melt, conversely, showed no discernable temperature dependence; it is unclear whether this is because the CAS melt is relatively insensitive to temperature or if experimental errors are masking the true temperature dependence. The value of u_o changes significantly with melt composition, especially at higher temperatures (e.g., 1400 °C)—the latter is a direct consequence of the varying temperature dependence in each melt. But, unlike the diffusion kinetics, changing the melt composition does not dominate u_o as relative to increasing the temperature by 100 °C; in this case, increasing the temperature of CMAS by 100 °C increases u_o by roughly the same as changing the melt composition from CAS to CMAS at 1400 °C.

The gathered evidence suggests that u_o can be strongly affected by the BO composition and, specifically, the ratio of RE oxide to base metal (Zr or Hf) oxide. Pure HfO_2 experienced the lowest value of u_o, about 3x lower than that of 7YSZ in CAS. (In CMAS, u_o of HfO_2 and 7YSZ were equivalent within the error of the measurement.) The value of u_o for 7YSZ was low enough to enable quantification, but that for GZO was not. The latter reached saturation in <3 min in the present

experiments, consistent with rapid saturation observed in the literature, e.g., Fig. 2.9a–c. This is despite the GZO having a similar Zr^{4+} saturation concentration compared to 7YSZ (Fig. 4.8b) and nearly equivalent D_{Zr} (*cf.* Table 4.1 and Table 4.4) in CMAS. This necessitates a larger value of u_o for GZO to satisfy mass balance. The working hypothesis is that the differences in u_o between the investigated BOs is primarily a function of their RE oxide content rather than dissolving oxide's crystal structure—further investigation is ultimately needed, but there is some literature evidence for the hypothesis [63,98]. This will be discussed further in Chapter 6 in the context of modeling dissolution.

Although u_o for GZO cannot be directly ascertained from the current experiments, one can estimate it via guess and check using the determined diffusivities and the dissolution distance after 10 min (~7.5 μm, Table 4.4). The detailed steps are: (i) use the experimentally determined diffusivity, C_{sat}, and the estimated value of u_o to simulate concentration profiles for 100's of experimental durations up to the desired time (e.g., nominal 10 min); (ii) extract the interface concentration for every simulated time step, $C(0,t)$, and calculate $u_{ox}(t)$ following Equation 3.2 and multiplying by the ratio of the melt density to the crystal density; (iii) integrate $u_{ox}(t)$ with respect to time to calculate a dissolution distance; (iv) compare the result of step 3 to the dissolution distance found by mass balance by integrating the concentration profiles, update the guess of u_o and repeat from step 1. Following this procedure for Gd^{3+}, the dissolution distance of 7.5 μm requires $u_o \approx 0.8$ μm/s, an order of magnitude larger than that measured for 7YSZ in equivalent conditions (~0.07 μm/s, Table 4.1). This estimate of u_o for GZO provides two important implications: first, if the estimated u_o is accurate,

it highlights just how much faster the dissolution process occurs for GZO over 7YSZ and provides evidence that the concentration of trivalent cations in the BO is critical for its dissolution rate; second, if the estimated u_o is not accurate, it implies that another process must be enhancing the ability for GZO to be incorporated into the melt, e.g., the crystallization of fluorite and apatite provides a non-diffusion-limited process of decreasing the concentration at the interface to enhance the dissolution rate.

Trends in L_{10}

To address some of the issues with u_o, such as experimental uncertainty and inability to be quantitatively measured for fast dissolving species, the dissolution distance (in μm) at a given time (e.g., L_{10}) can be compared between melt conditions and dissolving species. If u_o is known, the dissolution distance can be calculated through an integration with respect to time of $u_{ox}(t)$, the time dependent dissolution rate of the BO (defined in Section 3.4). As $u_{ox}(t)$ is a function of both D and u_o, this measurement looks at the interplay of both kinetic parameters and how they ultimately affect the dissolution distance. In the event that u_o cannot be measured, such as for GZO, the dissolution distance at a given time could still be estimated by other methods, such as: (i) direct measurement in electron microscopy comparing the edge of the BO (where no melt was present) to the center; or (ii) estimation by integrating the concentration profile in the melt and using mass balance to determine the amount of dissolved BO (assuming the dissolution process does not significantly alter the melt density). In practice, the former was inaccurate due to the small dissolution distances (typically <5

μm) experienced within this work and the latter better predicted the dissolution distances.[d] The dissolution distance at 10 minutes was calculated[e] for each quantified experiment and are presented in Fig. 3.4c, Table 4.1, Table 4.3, and Table 4.4.

Comparing results of L_{10} shows that the melt composition is more impactful than the melt temperature. First, consider the data from 7YSZ dissolution (Table 4.1). The values of L_{10} vary from 0.36–5.1 μm, approximately an order of magnitude. Increasing the temperature by 100 °C increased L_{10} by a factor of ~2.8 for both the CAS and the CMAS melts (or by a factor of ~1.5–1.9 for a 50 °C increase). This temperature dependence is arguably due primarily to the increase in diffusivity, especially for CAS where the early u_o does not change significantly. Comparatively, L_{10} changed by a factor of ~5 when the melt composition was changed at any given temperature. Because the dissolution distance involves both the interface dissolution rate and the associated composition gradient driven diffusional dissipation, the consistently lower values of u_o and D for CAS lead to lower dissolution rates at all temperatures, i.e., the highest value of L_{10} for CAS (at 1400 °C) is less than the lowest value of L_{10} for CMAS (at 1300 °C).

Comparing the data of YSZ to that of HfO_2 (Table 4.3) and GZO (Table 4.4) shows comparable trends to those observed for u_o: the dissolution distance is enhanced when the amount of rare-earth oxide is increased in the dissolving BO. The rare-earth-free HfO_2 has the lowest value of L_{10}, but not

[d] This calculation does not account for any barrier oxides present in recrystallized or reaction products. If these phases are present, the predicted dissolution distance represents a minimum estimation of the true value.

[e] L_{10} of 7YSZ and HfO_2 was calculated through integration of $u_{ox}(t)$. L_{10} of GZO was calculated by integration of the concentration profile.

significantly different from 7YSZ, varying by a factor of ~1.5 at most (within the CMAS melt). (Recall that the determined value of u_o for HfO_2 was slightly higher than that of 7YSZ—although equivalent within experimental error—indicating the lower L_{10} for HfO_2 resulted from the lower diffusivities.) The dissolution distance of GZO, determined by integrating the concentration profile and using mass balance to convert to a depth of GZO dissolved, is calculated to be ~3.8 μm or ~7.5 μm from the Zr^{4+} or Gd^{3+} concentration profiles, respectively. The discrepancy in the calculated dissolution distances results from the integration not accounting for the crystallization, which was significant for GZO even by 3 minutes (Fig. 4.1d). As the primary crystallization product was a Gd-depleted zirconia (fluorite), any crystallization preferentially captures ZrO_2 from the melt. (This phase was measured to contain approximately 16–19% $GdO_{1.5}$ by TEM-EDS, see Chapter 5.) The implication is that the dissolution distance estimated by the Gd^{3+} concentration profile (~7.5 μm) is more accurate but still underestimates the true dissolution distance as it fails to account for $GdO_{1.5}$ present in the fluorite or apatite grains formed in the reaction. Regardless, the minimum dissolution distance of 7.5 μm is significantly higher than that observed for YSZ (~1.8 μm, Table 4.1) or HfO_2 (~1.2 μm, Table 4.3) under otherwise equivalent conditions.

4.3. Synopsis

Key trends in the diffusion and dissolution kinetics have been established. The diffusivity of the trivalent rare earth cations is larger than that of tetravalent cations (Zr^{4+} or Hf^{4+}). Of the conditions studied in this dissertation, diffusivities were strongly affected by the melt composition and only weakly affected by the BO composition (i.e., cations of an equivalent valence diffuse at similar rates). Temperature played an intermediate role over 100 °C range. The dissolution kinetics were either

weakly dependent on temperature (CAS melt) or moderately dependent (CMAS melt). The melt composition affected dissolution rates more significantly, with the CMAS melt dissolving the BO faster at all temperatures. The BO composition, however, arguably has the largest effect on the dissolution rates; increasing the concentration of trivalent cations in the BO (e.g., $Gd_2Zr_2O_7$ vs. 7YSZ) increased the dissolution rate significantly, affording rapid melt saturation and significant crystallization. The relative importance of the dissolution and diffusion kinetics on coating-relevant length scales will be addressed in Chapter 6.

4.4. Figures and tables

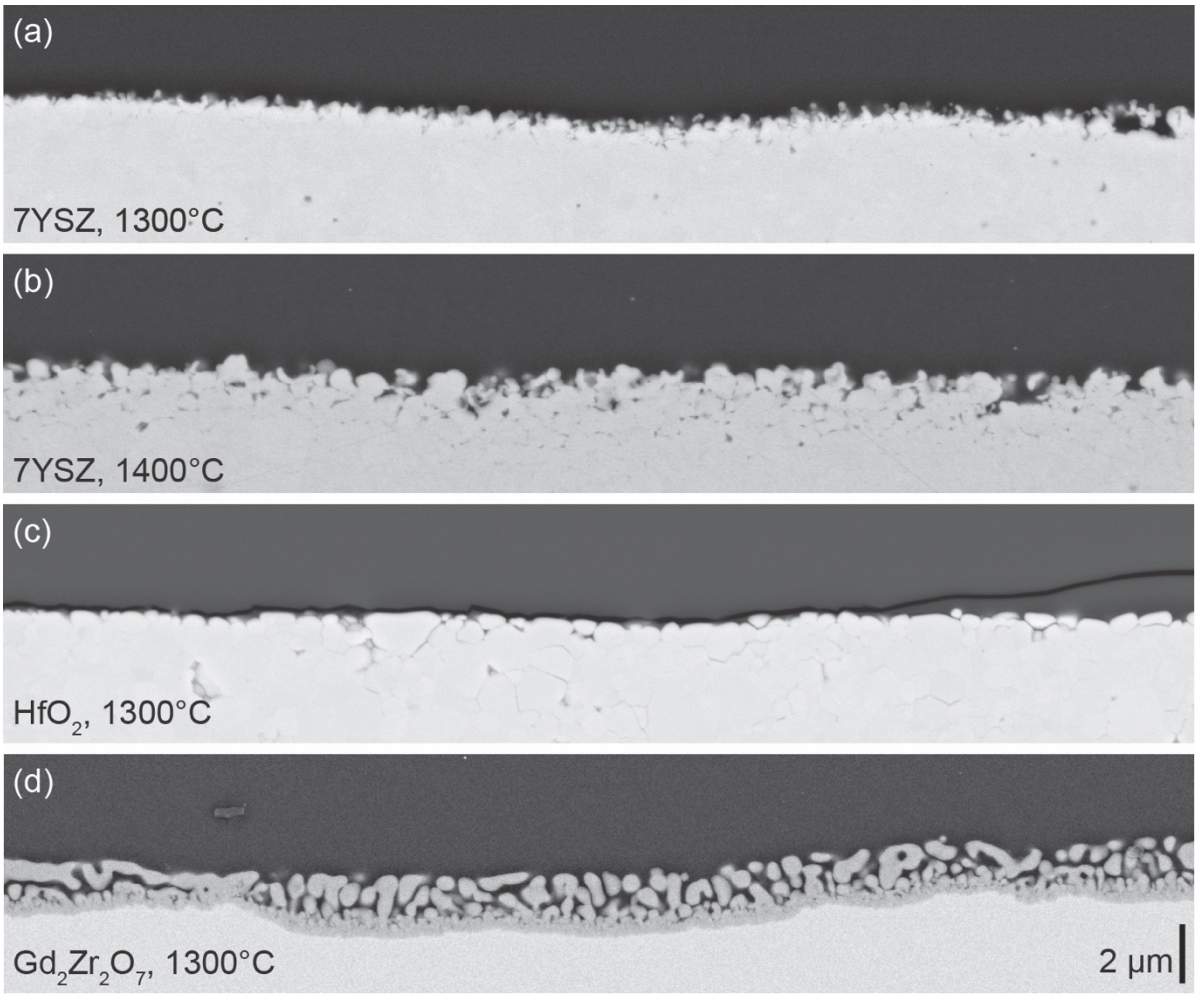

Fig. 4.1: Representative interfaces between quantified BOs and $C_{33}M_9A_{13}S_{45}$ after 3 min of exposure. The microstructures of 7YSZ at (a) 1300 °C or (b) 1400 °C, and that of (c) HfO_2 at 1300 °C were free of crystallization, allowing quantification of both diffusion and dissolution rates. Conversely, only diffusivities were quantified for $Gd_2Zr_2O_7$—rapid and extensive crystallization at 1300 °C (d) precludes quantification of dissolution.

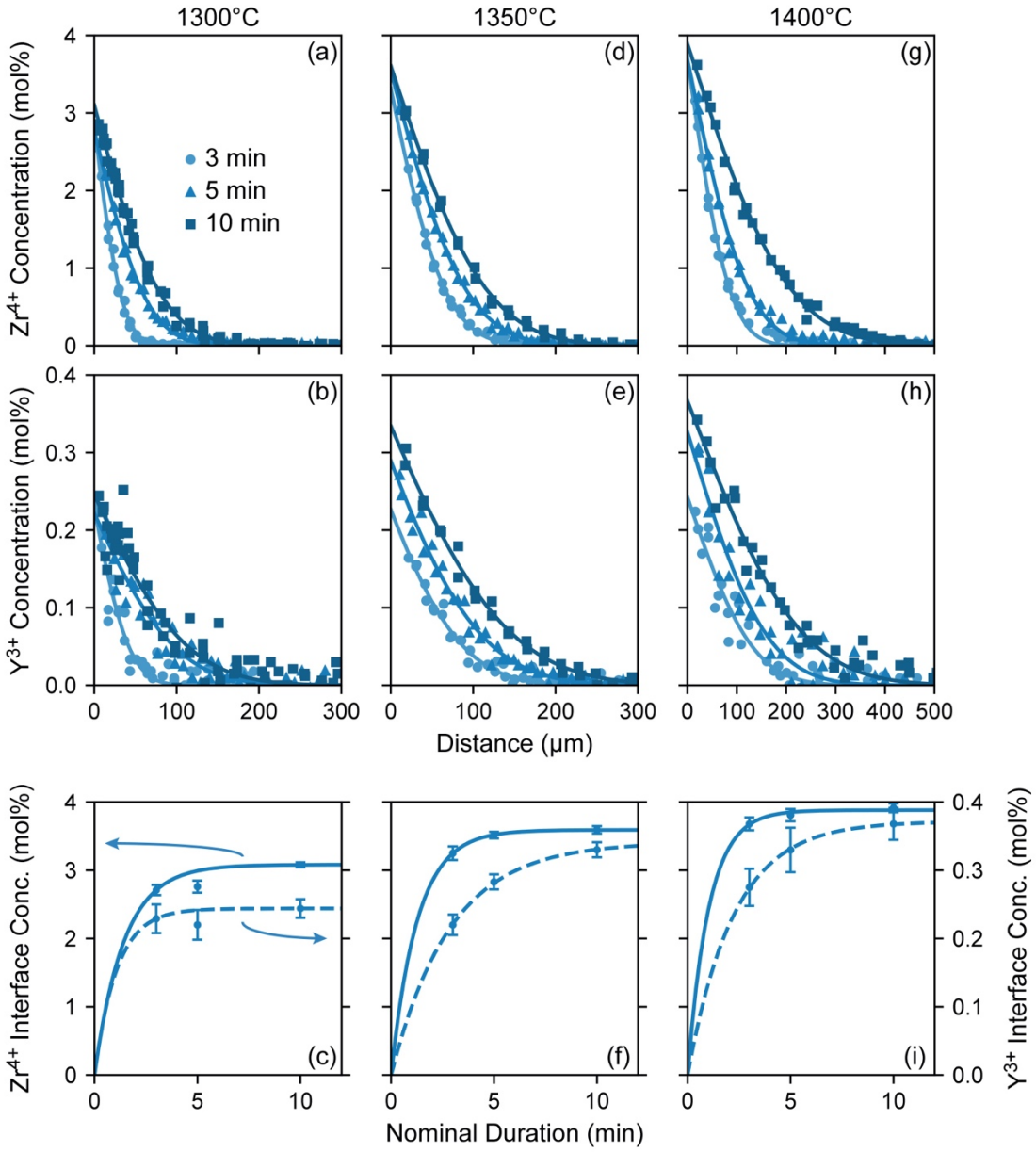

Fig. 4.2: Concentration profiles for (a,d,g) Zr^{4+} and (b,e,h) Y^{3+} determined from the dissolution of 7YSZ into $C_{33}M_9A_{13}S_{45}$ at 1300 °C, 1350 °C, and 1400 °C. The interface concentration, i.e., the concentration at x=0, (c,f,i) of Zr^{4+} (solid line) and Y^{3+} (dashed line) increase with time towards saturation indicating the dissolution mechanism is controlled by both diffusion and detachment of cations from the solid into the melt. Longer duration experiments (e.g., 60 or 240 min, not shown) indicate the Y^{3+} interface concentration continues to increase with time, whereas Zr^{4+} remains stable near the concentration at 10 min or decreases.

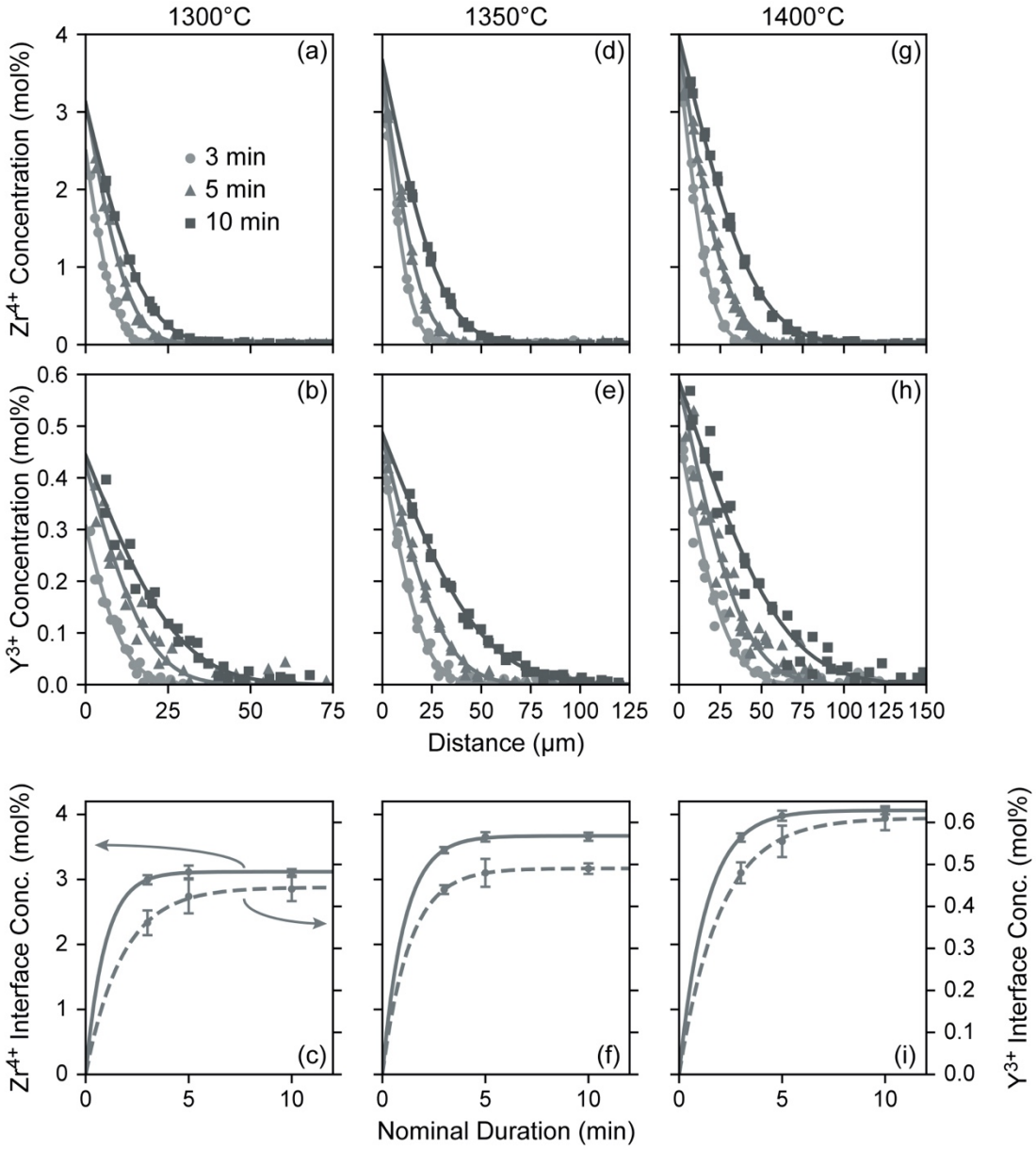

Fig. 4.3: Concentration profiles for (a,d,g) Zr^{4+} and (b,e,h) Y^{3+} determined from the dissolution of 7YSZ into $C_{24}A_{17}S_{59}$ at 1300 °C, 1350 °C, and 1400 °C. The interface concentration, i.e., the concentration at x=0, (c,f,i) of Zr^{4+} (solid line) and Y^{3+} (dashed line) increase with time towards saturation indicating the dissolution mechanism is controlled by both diffusion and detachment of cations from the solid into the melt. Longer duration experiments (e.g., 60 or 240 min, not shown) indicate the Y^{3+} interface concentration continues to increase with time, whereas Zr^{4+} remains stable near the concentration at 10 min or decreases.

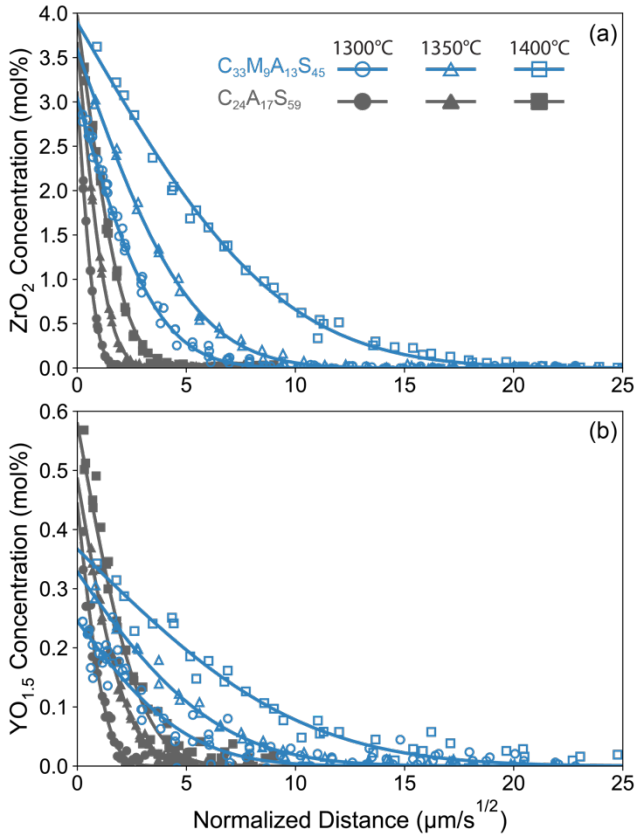

Fig. 4.4: Concentration profiles of (a) ZrO_2 and (b) $YO_{1.5}$ from YSZ dissolution into CMAS and CAS melts at 1300°C, 1350°C, and 1400 °C. The abscissa is a time-normalized distance; the extent of propagation along the abscissa is proportional to the cation diffusivity for each experiment. The diffusive lengths are larger for CMAS than CAS. Concentrations at the dissolution front (x=0) are generally larger for the CAS melt. Temperature increases the diffusive distance.

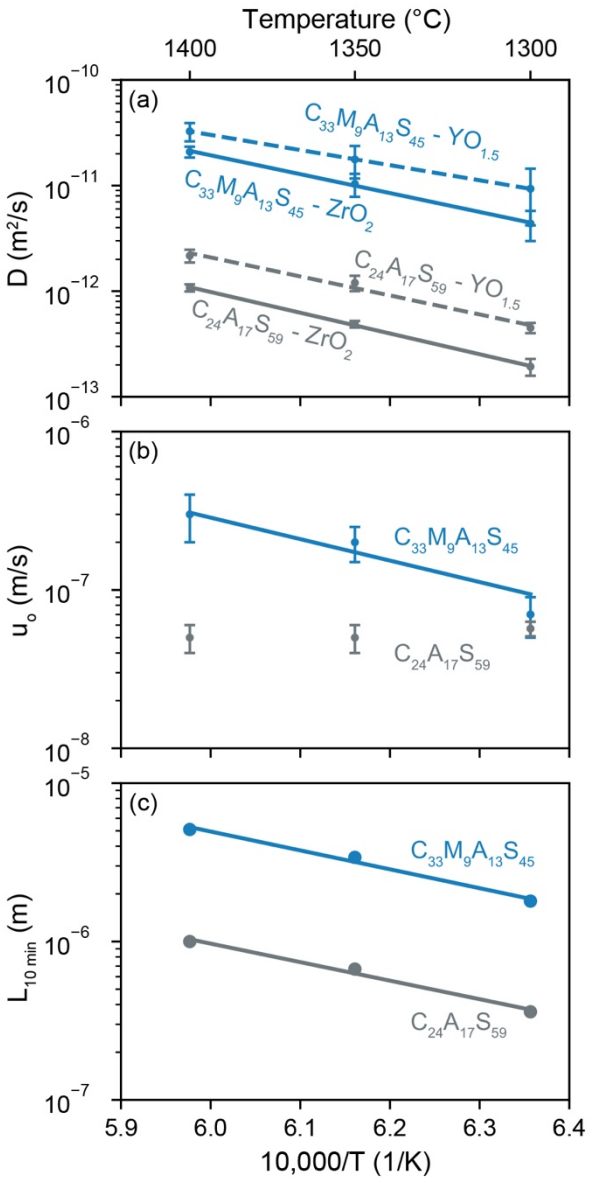

Fig. 4.5: The trends with temperature and melt composition for (a) diffusivities, D, of Y^{3+} and Zr^{4+}, (b) the initial melt growth rate, u_o, and (c) the dissolution distance after 10 min, $L_{10\ min}$. The diffusivities and dissolution distance after 10 min are well fit to an Arrhenius equation, providing activation energies and pre-exponential factors, Table 4.2. The initial melt growth rate, u_o, should also follow an Arrhenius dependence, but experimental uncertainty yields poor fits, especially for the CAS melt where no temperature dependence on u_o was discernable.

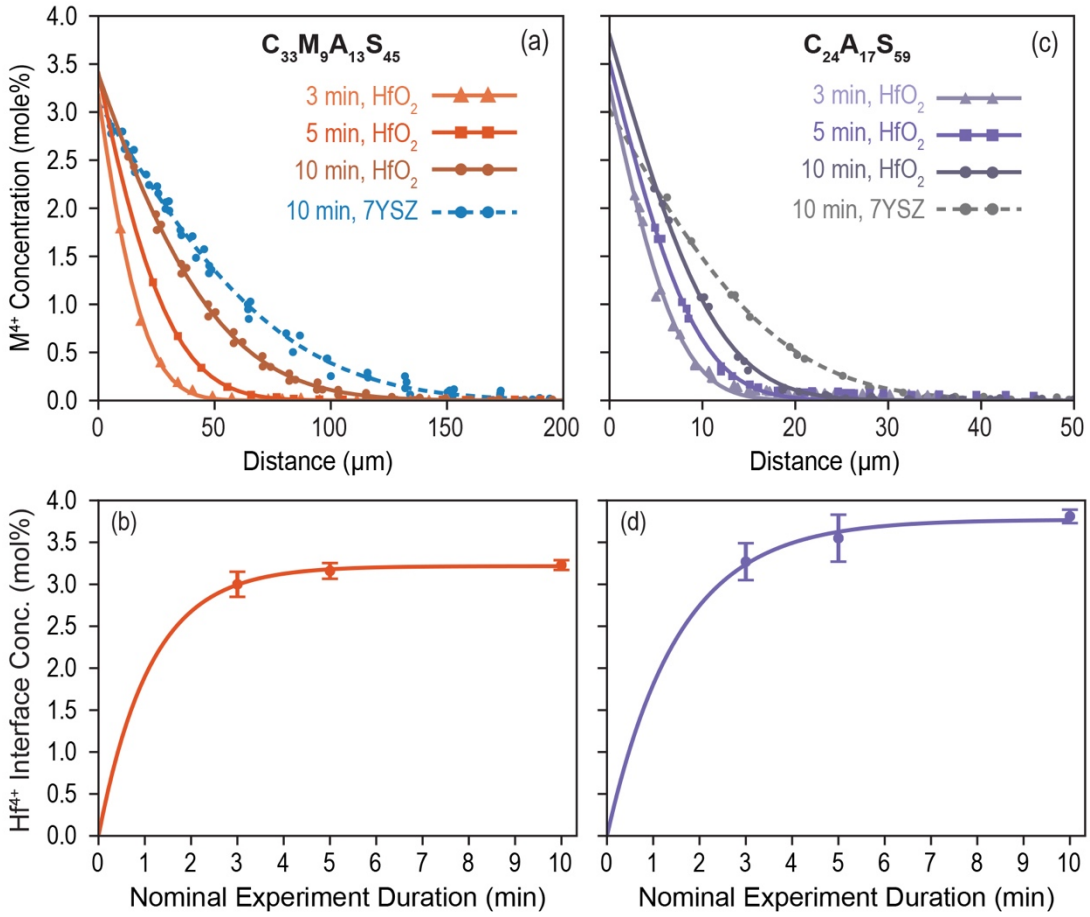

Fig. 4.6: Concentration profiles from the dissolution of HfO_2 into (a) CMAS and (c) CAS at 1300 °C; the 10 minute concentration profile of ZrO_2 from the dissolution of 7YSZ is shown for comparison. The concentration at the interface (b,d) is observed to increase with time towards saturation by 10 min for both melts.

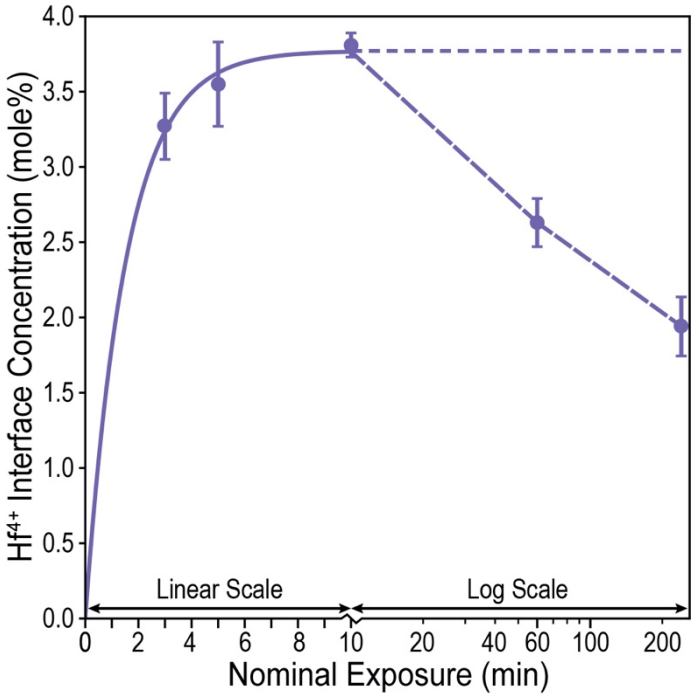

Fig. 4.7: Concentration at the HfO_2-melt interface for CAS. At short times, the concentration is observed to increase with time towards a plateau by approximately 10 min (*cf.* Fig. 4.6d). After 10 min, however, the nucleation of reactive crystallization phases begins, which subsequently grow with time. Growth of these phases leads to a concomitant decrease in the interface concentration as the system approaches a new equilibrium. (Note the change of scale in the plot after 10 minutes to a log scale.)

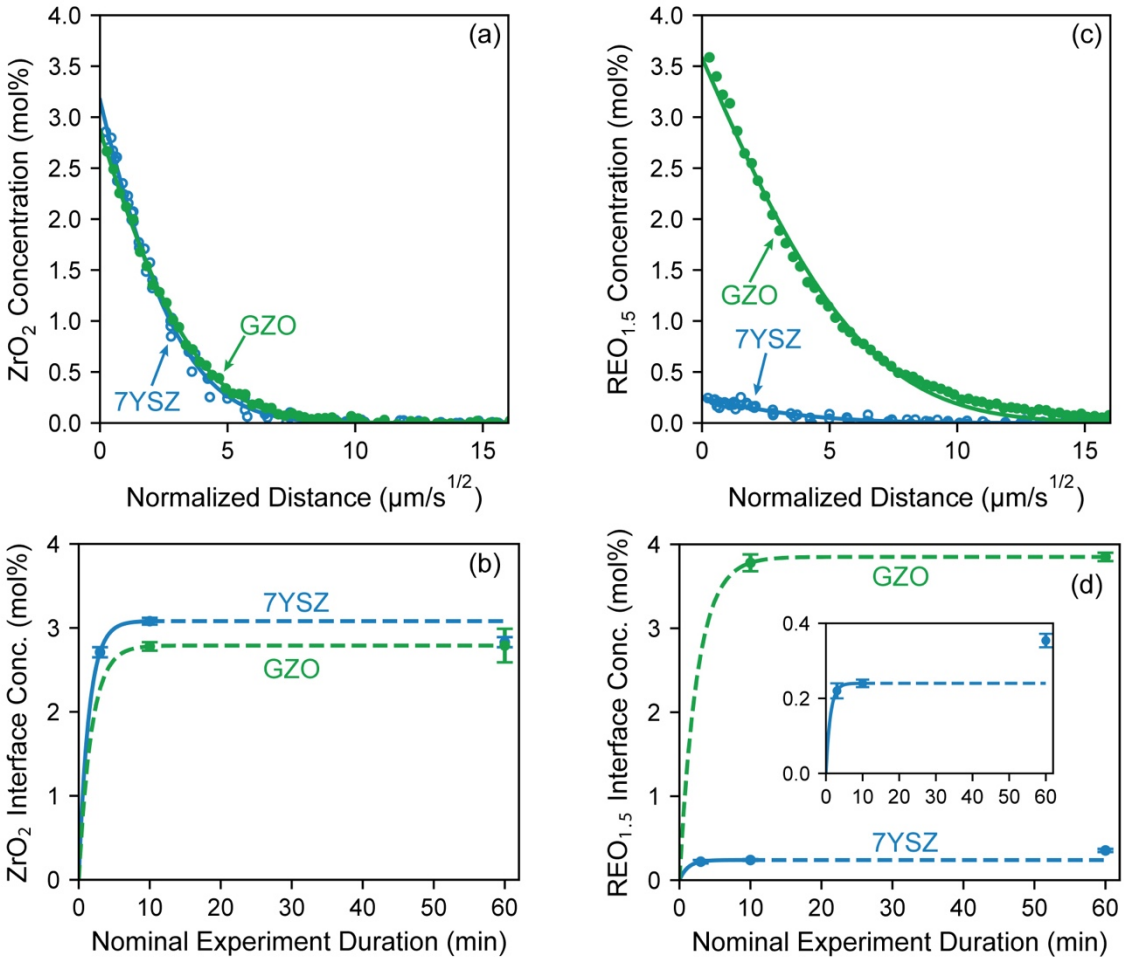

Fig. 4.8: Concentration profiles from the dissolution of $Gd_2Zr_2O_7$ into CMAS at 1300 °C for 10 min, with comparison to data from 7YSZ dissolution. The ZrO_2 concentration profiles (a) are nearly identical between GZO and 7YSZ. Slightly less ZrO_2 is dissolved at saturation (b) for GZO, but the value is consistent with that of 7YSZ at 60 min. (Note that the rate at which saturation occurs for GZO is not known and a rough fit is represented by a dashed line.) Conversely, significantly more $GdO_{1.5}$ is dissolved into the melt from GZO than $YO_{1.5}$ from 7YSZ (c,d). Critically, the rapid dissolution of GZO affords significant crystallization and presumed CMAS resistance.

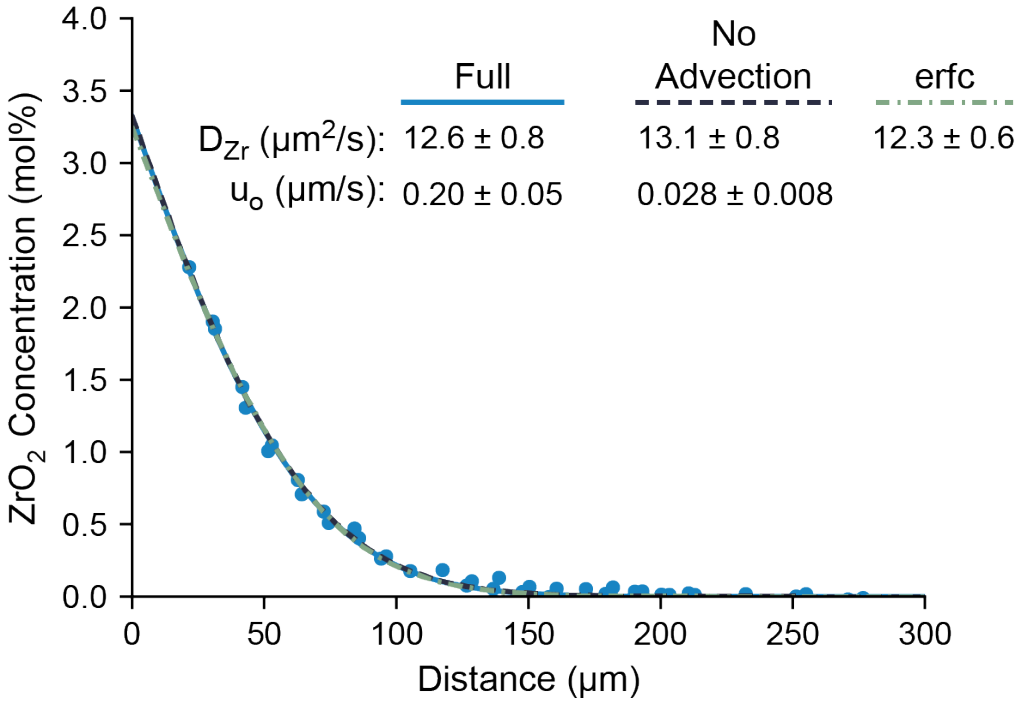

Fig. 4.9: A ZrO_2 concentration profile (from the dissolution of 7YSZ into CMAS at 1350 °C for 3 min) is fit by three different methods and the resulting fitting parameters are compared. The full PDE (Equation 3.1, blue solid line) serves as the baseline. Removing the advection component from Equation 3.1 (No Advection, dashed navy line) had little effect on D_{Zr} but did alter the value of u_o; therefore, the full PDE is necessary to accurately capture the dissolution kinetics. Fitting the data to a simple complementary error function solution without any dissolution component (erfc, dot-dashed green line) predicted an equivalent value of D_{Zr} to the full PDE.

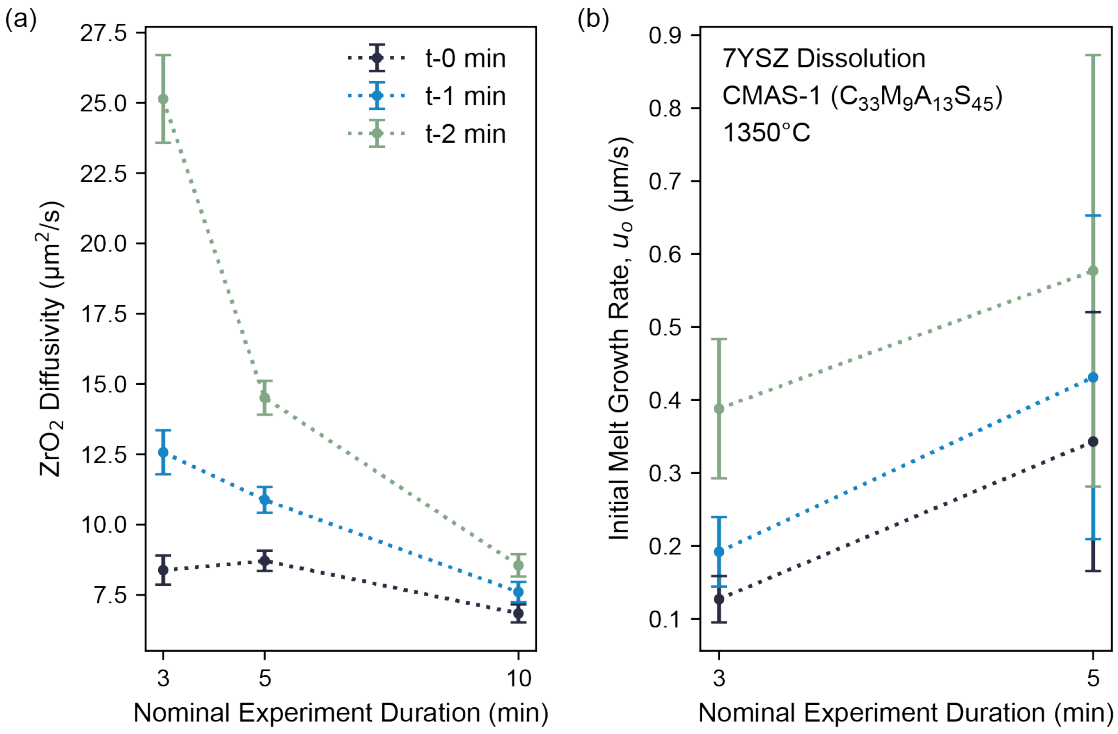

Fig. 4.10: The determined fitting parameters were sensitive to the experimental duration, i.e., the time correction applied to account for the sample heating time affects the fitting results. The fitting parameters from 7YSZ dissolution into CMAS at 1350 °C are shown for three correction times: 0, 1, and 2 minutes off the nominal duration. The time correction used becomes less impactful to the diffusivity (a) at long nominal experimental durations, indicating longer duration experiments provide the best estimate of D. Conversely, short duration experiments are critical for accurate determination of the initial melt growth rate, u_o (b). Long duration experiments feature large errors on the fitting parameters; thus, accurate determination of the time correction to use is critical. Measuring the CMAS temperature *in situ* showed the melt took approximately one minute to reach the nominal experimental temperature. A one-minute time correction was then applied to all kinetic measurements.

Table 4.1: Summary of fitting results for 7YSZ dissolution.

Melt Composition	Temperature (°C)	Time (min)	D_{Zr} ($\mu m^2/s$)	D_Y ($\mu m^2/s$)	u_o ($\mu m/s$)	L_{10}^* (μm)
$C_{33}M_9A_{13}S_{45}$	1300	3	3.2 ± 0.3	5 ± 2	0.07 ± 0.02	1.8
		5	5.9 ± 0.4	15 ± 4	0.06 ± 0.01	
		10	4.0 ± 0.2	8 ± 2	Saturated	
	1350	3	12.6 ± 0.8	24 ± 4	0.20 ± 0.05	3.4
		5	10.9 ± 0.5	17 ± 2	0.4 ± 0.2	
		10	7.6 ± 0.4	12 ± 1	Saturated	
	1400	3	20 ± 2	40 ± 10	0.3 ± 0.1	5.1
		5	19 ± 1	30 ± 9	0.5 ± 0.3	
		10	23.7 ± 0.6	28 ± 5	Saturated	
$C_{24}A_{17}S_{59}$	1300	3	0.16 ± 0.01	0.4 ± 0.1	0.057 ± 0.006	0.36
		5	0.23 ± 0.01	0.5 ± 0.1	0.08 ± 0.02	
		10	0.19 ± 0.01	0.45 ± 0.08	Saturated	
	1350	3	0.49 ± 0.02	1.2 ± 0.1	0.05 ± 0.01	0.67
		5	0.45 ± 0.01	1.0 ± 0.2	0.11 ± 0.01	
		10	0.52 ± 0.01	1.4 ± 0.1	Saturated	
	1400	3	0.98 ± 0.05	2.5 ± 0.4	0.05 ± 0.01	1.0
		5	1.12 ± 0.07	1.9 ± 0.3	0.11 ± 0.06	
		10	1.13 ± 0.05	2.1 ± 0.2	Saturated	

* Calculated dissolved distance of YSZ considering only dissolution and diffusion after 10 minutes of exposure, i.e. dissolution concurrent with significant reprecipitation is not considered.

Table 4.2: Arrhenius parameters determined for the dissolution and diffusion kinetics of 7YSZ.

	Melt Composition	
	$C_{33}M_9A_{13}S_{45}$	$C_{24}A_{17}S_{59}$
$D_{o,Zr}$ (m^2/s)	1.1	0.61
Q_{Zr} (kJ/mol)	340	380
$D_{o,Y}$ (m^2/s)	0.012	0.13
Q_Y (kJ/mol)	270	340
A (m/sK)	0.0089	N/A
E_a (kJ/mol)	250	N/A
$L_{0,10}$ (m)	71.1	10.2
Q_L (kJ/mol)	228	224

Table 4.3: Summary of fitting results for HfO_2 dissolution at 1300 °C.

Melt Composition	Oxide Composition	Time (min)	D_M ($\mu m^2/s$)	u_o ($\mu m/s$)	L_{10}^* (μm)
$C_{33}M_9A_{13}S_{45}$	7YSZ	3	3.2 ± 0.3	0.07 ± 0.02	1.8
		5	5.9 ± 0.4	0.06 ± 0.01	
		10	4.0 ± 0.2	Saturated	
	HfO_2	3	1.3 ± 0.2	0.11 ± 0.04	1.2
		5	1.6 ± 0.1	0.16 ± 0.06	
		10	2.02 ± 0.04	Saturated	
$C_{24}A_{17}S_{59}$	7YSZ	3	0.16 ± 0.01	0.057 ± 0.006	0.36
		5	0.23 ± 0.01	0.08 ± 0.02	
		10	0.19 ± 0.01	Saturated	
	HfO_2	3	0.15 ± 0.02	0.02 ± 0.01	0.31
		5	0.11 ± 0.02	0.03 ± 0.02	
		10	0.072 ± 0.004	Saturated	

* Calculated dissolved distance considering only dissolution and diffusion after 10 minutes of exposure, i.e. dissolution concurrent with significant reprecipitation is not considered.

Table 4.4: Summary of fitting results for $Gd_2Zr_2O_7$ dissolution.

Melt Composition	Time (min)	D_{Zr} ($\mu m^2/s$)	D_{Gd} ($\mu m^2/s$)	L_{10}^* (μm)
$C_{33}M_9A_{13}S_{45}$	10	5.0 ± 0.2	11.1 ± 0.2	>7.5

* The value of 7.5 μm was determined from integrating under the Gd^{3+} concentration profile and converting via mass balance; this does not account for Gd^{3+} that crystallized in apatite or fluorite, both of which were present at 10 min. Therefore, the true dissolution distance is greater than 7.5 μm.

CHAPTER 5. MICROSTRUCTRUAL DEVELOPMENT OF T/EBC OXIDES EXPOSED TO MOLTEN SILICATES

The dissolution mechanism elaborated in the previous chapter has important implications on how the reaction zones develop once crystallization begins. Namely, the dissolution flux into the interface melt is comparable to the diffusive flux away from the interface, which results in a measurable buildup of the coating oxides at the interface melt towards a saturation value. The critical implication is that crystallization of new phases will require some incubation time after saturation. Further complicating matters, the dissolving BO cations will not diffuse at the same rate in the bulk melt—the relative buildup of those cations will not in proportion to the BO. In sum, the dissolution rate of the BO, relative diffusivities of all cations therein, and their relative saturation concentration have a direct impact on the development of the reaction zone. Crystallization may occur via metastable phases and the formation of a phase may block another by systematically depleting a cation from the melt.

This chapter will cover in detail the crystallization (both reprecipitated phases and reaction products) and subsequent microstructural development for multiple BOs, including: ZrO_2, HfO_2, ZrO_2-$7YO_{1.5}$ (7YSZ), ZrO_2-$20YO_{1.5}$ (20YSZ), HfO_2-$7YO_{1.5}$ (7YSH), and $Gd_2Zr_2O_7$ (GZO). The oxides were chosen to both investigate relevant materials for current and next-generation coatings and to provide insight into the fundamental effect of individual cations (e.g., the differences between Zr^{4+} and Hf^{4+}, the impact of small yttria additions on reactive crystallization, and the crystallization under large concentration of rare-earth (RE) oxide). The mechanisms of reactive crystallization for the different BOs will be discussed in the context of the relevant thermodynamics. The results between different BOs will also be discussed to elucidate key trends highlighting the effect of melt

composition, temperature, and BO composition. A summary of the key crystalline phases relevant in the presented BO-C(M)AS interactions is presented in Table 2.2.

5.1. Results

5.1.1. ZrO_2

Nominally pure ZrO_2 was exposed to the acidic CAS melt to investigate zircon ($ZrSiO_4$) formation, a reaction product. Zircon formation was readily achieved in CAS, showing already substantial coverage after 1 h at 1300 °C, as noted in Fig. 1.1. The average coverage is somewhat lower than that displayed in this figure, but still relatively abundant when compared to 7YSZ (as shown later). The zircon crystals are anisotropic in shape and in intimate contact with the ZrO_2. The as-sintered compact showed substantial microcracking as the ZrO_2 pellets had to be sintered above the monoclinic to tetragonal transformation temperature (as elaborated in Section 3.1.1). The CAS melt does penetrate the cracks within the compact near the surface and zircon formation may occur at some larger pores, as marked by the arrow in Fig. 1.1.

5.1.2. HfO_2

Mechanism

By inference from the similarity in phase equilibria between the ZrO_2-SiO_2 [157] and the HfO_2-SiO_2 [133] systems, pure hafnia should form hafnon ($HfSiO_4$) by reaction with a silicate melt of sufficiently acidity like CAS. The essential features of the dissolution-crystallization mechanism are illustrated in Fig. 5.2. After 1 h at 1400 °C the surface is largely covered with $HfSiO_4$, Fig. 5.2(a), with dissolution continuing locally at a few remaining gaps in the product layer where the melt is in direct

contact with HfO_2. The concentration gradient in the melt, visible in Fig. 5.2(b), are notably bowed about these gaps. The Hf^{4+} diffuses into the melt and reprecipitates as $HfSiO_4$ on the growing hafnon layer as illustrated in (b). As the edges of the hafnon layer represent the shortest diffusion distances, the growth promotes lateral propagation of the reaction product until HfO_2 is no longer exposed to the melt and subsequent reaction could only occur through solid state diffusion through the hafnon layer.

Evolution of reaction in acidic melts

Reactive crystallization upon interaction of CAS with pure HfO_2 compacts occurs shortly after Hf^{4+} saturates at the interface melt, with formation of a few crystallites of hafnon as well as a Hf-cyclosilicate phase after only 10 min at 1300 °C, Fig. 5.3(a). After 1 h the coverage is quite extensive, as shown in Fig. 5.3(b,d) and dominated by hafnon, with no cyclosilicate detected in this cross section. The extent of hafnon coverage is seemingly greater than that of zircon on ZrO_2, Fig. 1.1, and the morphology of the crystals is somewhat different, but in both cases they appear to adhere well to the substrate, in spite of the more extensive microcracking in ZrO_2. Some large cyclosilicate grains were observed after 4 h at 1300 °C, as shown in Fig. 5.3(c), but most of the surface is covered with hafnon. The cyclosilicate is no longer present after 1h at 1400 °C, where the hafnon layer is much more uniform and nearly complete as shown in Fig. 5.3(f), except for small gaps as in Fig. 5.2.

Evolution in basic melts

No reactive crystallization was observed for HfO_2 interacting with the basic CMAS melt (Ca:Si=0.73). An example for 1 h at 1300 °C is given in Fig. 5.3(e). There is significant penetration

by preferential dissolution along the grain boundaries, enhanced by a network of microcracks like that in Fig. 3.3(e), down to ~19 μm from the surface.

5.1.3. YSZ

Mechanism

Examination of the interfaces between the silicate melts and 20YSZ or 7YSZ, displayed in Fig. 5.4 and Fig. 5.5, respectively, provides insight into the evolution at the interaction front. Short time experiments on single crystal 20YSZ (Fig. 5.4) clearly reveal the main features of the dissolution-reprecipitation mechanism. A dissolution front forms between the 20YSZ and the CMAS melt and remains planar for times under 10 min (Fig. 5.4a). ZrO_2 saturation at the interface leads to reprecipitation of YSZ with modified composition at approximately 10 min (Fig. 5.4b,c). Closer examination shows the growth is fed by dissolution of the underlying 20YSZ, as shown in the inset of Fig. 5.4(b), with gradual undercutting of the boundary between the single crystal and the precipitate. The reprecipitated grains grow to form an essentially continuous layer separated from the dissolving 20YSZ by a thin layer of melt (Fig. 5.4d) arguably resulting from the merger of the undercut boundaries. The thin melt layer is connected to the bulk melt through small channels interpenetrating the reprecipitated fluorite, which at this stage contained ~8% $YO_{1.5}$ and 6% CaO.

The evolving interaction zones between C(M)AS and polycrystalline 7YSZ are illustrated in Fig. 5.5. In all cases, localized dissolution at the grain boundaries dislodges individual oxide grains and generates a distributed ("mushy") interaction zone. The depth of the mushy zone at a given time step increases as the melt viscosity decreases, either by increasing the melt temperature, (cf. Fig. 5.5c,d) or changing its composition, (cf. Fig. 5.5c,g). For a given melt composition, increasing the melt

temperature had a similar effect to increasing the exposure time, i.e., the reaction zone morphology does not fundamentally change but it does increase in depth. However, the reprecipitated zirconia grains were noticeably larger and blockier for exposures to the CAS melt, (e.g., Fig. 5.5f–h) suggesting comparatively faster coarsening of the reprecipitated grains.

Evolution in acidic melts

The reactive crystallization phase expected for CAS is $ZrSiO_4$ (zircon, ZS), and it appears in discrete, approximately equiaxed, particles above the broader oxide/melt interface, as shown in Fig. 5.6(b,c). The onset of zircon formation is actually at ~1 h, but it is hardly detectable on the interface, most of which appears devoid of zircon as in Fig. 5.6(a). The few crystallites found at 1 h are >500 μm apart and <5 μm in size. The population of zircon crystals increases by 4 h, as illustrated in Fig. 5.6(b) but is still rather sparse with only a dozen ~10 μm sized grains observed across a 4 mm interface—yttria-depleted *t*-zirconia remains the dominant mode of crystallization up to 4 h. Thus, zircon forms slower and sparser than zircon from pure ZrO_2 or hafnon from pure HfO_2, *cf.* Fig. 1.1 and Fig. 5.3. Furthermore, zircon coverage is noticeably smaller after 4 h at 1400 °C, albeit with crystals of similar size, Fig. 5.6(c).

Evolution in basic melts

Conversely, there was no zircon or other reactive phase formation on 7YSZ at 1300 °C when exposed to the more basic CMAS melt, even after 4 h; instead, the 7YSZ develops a mushy zone of reprecipitated zirconia, which grows to be substantially sized, Fig. 5.5(a-c). To better understand its formation, the mushy zone for 7YSZ exposed to CMAS at 1300 °C for 60 min (Fig. 5.5b) was further

characterized using TEM. The lamella in Fig. 5.7(a) encompasses most of the mushy zone thickness; the corresponding EDS elemental mapping is shown in Fig. 5.7(b). The EDS signal integrated at 17 nm intervals (pixel height) was then used to plot the local average Y:Zr ratio along the mushy zone in Fig. 5.7(c). The Y:Zr ratio is lowest closest to the bulk melt, consistent with reprecipitation of Y-depleted zirconia, and essentially the same as the pristine composition at the bottom of the melt penetrated region. However, note the spots with higher Y:Zr ratios also evident in the EDS map of Fig. 5.7(b), suggestive of heterogeneities associated with a small fraction of cubic YSZ in the as-received material that results from partitioning during fabrication, as noted in Chapter 3.

Three distinct types of grains are evident in Fig. 5.7(a). Those at the upper part of the mushy zone, shown in more detail in Fig. 5.7(d) exhibit twinned structures indicative of the tetragonal to monoclinic transformation upon cooling [56]. The EDS line scan in Fig. 5.7(c), taken vertically along Fig. 5.7(b), indicates that this region is Y-depleted compared with the starting material. The corresponding elemental map in Fig. 5.7(e) reveals grains with a core-shell morphology where the outer layer has distinctly lower $YO_{1.5}$ content and no detectable CaO, compromising the phase stability of the tetragonal YSZ [56]. The fraction of twinned grains decreases with increasing distance from the macroscopic boundary with the bulk melt. Near the middle of the mushy zone the Y concentration of the YSZ grains is 5–6%; core-shell structures are not noticeable, and the grains are not transformed. Closest to the pristine material, where the contact between melt and YSZ was shortest, the YSZ grains appear to retain their original composition and there is no evidence of transformation twins. In this region some areas show Y contents above the average, reflected by the brighter blue areas in Fig. 5.7(b), arising from the retained cubic phase described earlier. A

quantitative comparison of the yttria concentrations in the elemental maps in Fig. 5.7(b) shows that the composition of the grain cores across the entire mushy zone are essentially the same. The evidence indicates that the fraction of the Y-depleted outer shells of the grains in Fig. 5.7(a) increases from the bottom to the top of the mushy zone.

5.1.4. 7YSH

Mechanism

The mechanism of mushy zone development of 7YSH is similar to those previously discussed but with a new feature introduced by the two-phase microstructure. The yttria-stabilized cubic phase dissolves preferentially relative to m-HfO_2 in both acidic and basic melts, albeit at a higher rate in the latter, as shown in Fig. 5.8. There is no significant microcracking or interconnected porosity in these samples, and therefore no open path for melt penetration. However, because the volume fraction of the cubic phase is of order 30%, there is a percolating network that develops as it dissolves, allowing ready access of the melt to the remaining material and outward transport of the dissolved species.

Evolution in acidic melts

Similarly to pure HfO_2, reactive crystallization starts at ~10 min, forming a few small (~1 μm) hafnon particles, as shown in Fig. 5.8(a), which grow in size but with very sparse coverage even after 60 min, e.g., Fig. 5.8(b) Concomitantly, there is a recession of ~2.4 μm of the cubic phase from the surface after 10 min, leaving a porous network of monoclinic HfO_2 particles which grows to ~7 μm after 60 min. Nevertheless, there are no visible signs of microcracking at the HfO_2 boundaries in either case, presumably because the grains remain below the critical 2–3 μm size [158]. A cyclosilicate grain was

observed in the 60 min sample away from the HS particle (not shown), but its presence on the surface was even more sparse than that of hafnon. The predominant mode of crystallization is then the reprecipitation of m-HfO_2 on the existing network.

Evolution in basic melts

No reactive crystallization was observed in the 7YSH specimens but the dissolution is somewhat faster than in the acidic melt, as noted by comparing the images after 10 min, where the depleted zone is doubled for the basic melt relative to the acidic one, ~4.8 μm vs. 2.4 μm, cf. Fig. 5.8(a,c). After 60 min the depleted zone has grown to ~19 μm, shown in Fig. 5.8(d), about 2.7 times the recession in the acidic melt. Some of the HfO_2 crystals closer to the surface appear to have coarsened in both samples but they remain immune to microcracking.

5.1.5. GZO

$Gd_2Zr_2O_7$ underwent rapid crystallization in both CAS and CMAS melts. The temporal microstructural evolution of single crystalline GZO exposed to CMAS at 1300 °C is shown in Fig. 5.9 for 3, 10, and 60 min. The samples clearly consist of two zones: a network of globular, Gd-depleted fluorite grains, which are surrounded by melt, and a dense layer of reaction products immediately adjacent the pristine BO. The latter consists of apatite and nascent fluorite grains at 10 min, identified by TEM-EDS (Fig. 5.10). Both zones grow substantially between 3, 10, and 60 min—the fluorite zone increases in thickness from ~1.5 to ~2.8 to ~7.8 μm (with grain coarsening clearly observed), and the dense layer increases in thickness from ~0.5 to ~0.7 to ~2.1 μm. The interface of the reaction layer and the pristine GZO is clearly delineated by Z-contrast and remains markedly

planar up to 60 min. However, a large extent of cracking was observed in the single crystalline GZO, which is attributed to thermal stresses developed on quenching.

The concentration of Zr^{4+} and Gd^{3+} within the reaction zone of the 10 min exposure, Fig. 5.9(b), was further investigated by TEM-EDS spot analysis and is shown in Fig. 5.10(b,c). The reprecipitated fluorite grains were found to have a largely consistent Gd^{3+} concentration throughout the mushy zone, containing ~18% Gd^{3+}. The apatite grains contained ~20% Ca^{2+} and ~4% Zr^{4+}, indicating a significant evolution from the nominal, defect-free composition. The Zr^{4+} concentration in the melt was spatially invariant, around 1.1–1.4%. (Note that this is significantly lower than the concentration of Zr^{4+} measured at the interface with the bulk melt in Chapter 4, ~2.8 %, Fig. 4.8.) The Gd^{3+} concentration in the melt was ~4.1% near the top of Fig. 5.10(b), consistent with that measured in the concentration profiles (Fig. 4.8), but this decreased further into the reaction zone—a minimum concentration of ~2.3% was measured adjacent to the apatite grains.

Due to the limited availability of the single crystalline GZO, additional experiments with CAS were carried out on dense polycrystalline GZO compacts. The exposure temperature was lowered to 1200 °C in an attempt to slow down the reaction kinetics, but the compacts readily crystallized even after only 1 min (Fig. 5.11).[a] After 1 min of exposure—representing the time needed for the sample assemblage to reach 1200 °C—a ~0.1 μm layer of globular grains (presumably reprecipitated zirconia) were observed immediately above the pristine GZO. The dissolution front remains planar, with just the onset of preferential grain boundary dissolution being observed (e.g., inset of Fig. 5.11a); grain

[a] The experimental temperature was decreased to 1200 °C for these experiments to slow down nucleation such that the onset could be captured.

boundary recession worsened initially with increased duration (e.g., 2 or 3 min, Fig. 5.11b,c) but a mostly planar interface was recovered by 10 min (Fig. 5.11e). Acicular grains, characteristic of apatite, appeared at 2 min of exposure (Fig. 5.11b) but were absent from longer duration experiments. Likewise, grains of a different morphology appeared at 3 min (Fig. 5.11c) but subsequently disappeared. The small scale of the reaction zone precluded composition measurements by SEM-EDS or EPMA.

5.2. Discussion

5.2.1. Crystallization in RE-free or lean systems

This section will compare the crystallization and microstructural development for systems with no or little RE content (i.e., ZrO_2, HfO_2, 7YSZ, and 7YSH). The effect of melt composition and BO composition on reactive crystallization will be elaborated first. The development of the mushy zone observed in 7YSZ exposures will then be discussed in great detail.

Thermodynamic foundation

To provide context for understanding the phase evolution in the systems investigated it is insightful to examine the equilibrium scenarios toward which the relevant combinations of oxides and silicate melts are driven. Unfortunately, thermodynamic databases [50,51] describing CMAS/oxide equilibria do not include a description of HfO_2-based phases, precluding the calculation of the equilibria for multicomponent systems involving hafnia. Those databases, however, have extensive information on ZrO_2-based phases and a validated description for a wide range of silicate melts. Given the similarity in crystallography, chemical behavior and binary phase equilibria with many

oxides one may build on the multicomponent phase equilibria for ZrO_2 in understanding of the behavior for similar HfO_2 systems in the present study.

ZrO_2 (and HfO_2 by extension) containing little or no rare earth content are thermodynamically predicted to form compounds with acidic melts but not with basic melts. The equilibrium phase fields for a partial isopleth between the acidic $C_{24}A_{17}S_{59}$ (CAS) with increasing concentration of ZrO_2, 7YSZ, and 20YSZ are shown in Fig. 5.12(a–c), respectively, for the temperature range relevant to that studied experimentally. All molar concentrations are based on a single cation formula unit, as noted earlier, e.g., 7YSZ is $Zr_{0.93}Y_{0.07}O_{1.965}$. The evolution of phase fractions at 1300°C with the addition of ZrO_2, 7YSZ, and 20YSZ are shown in Fig. 5.12(d–f), starting with one mole of melt in each case. The isopleths reveal that saturation occurs upon addition of only a small amount of the oxide, ~0.0025 moles, and should lead in all cases to the precipitation of zircon. The volume of liquid increases slightly (~0.2%) during this period and is not detectable at the scale of the graphs but starts decreasing immediately upon the start of ZS crystallization. The predicted crystallization path with increasing ZrO_2 addition follows the fields L+ZS → L+ZS+An → L+ZS+An+Z[b] in Fig. 5.12(a). Absent anorthite the onset of Z formation is shifted to higher ZrO_2 addition and the "kink" in the phase fraction of melt disappears. The presence of yttria in the dissolving BO shifts the fields where anorthite is stable to lower temperatures, cf. Fig. 5.12(b,c), increasing the likelihood of its suppression in experiments with 7YSZ and removing it altogether for 20YSZ. Note that the phase fractions of L, ZS and An in Fig. 5.12(d) do not change upon addition of ZrO_2 above 0.11 moles (~10% ZrO_2), when the system enters the four phase field, i.e., moles added to the system remain solid. However,

[b] Phase abbreviations used in the crystallization paths are fully described in Table 2.2.

the presence of yttria in 7YSZ and 20YSZ enables the reprecipitated phase to evolve in composition. For example, when 7YSZ is added it dissolves in the melt reprecipitates as a tetragonal phase (Z) that is predicted to evolve in composition from ~0.4% to ~1.4% $YO_{1.5}$ over the range displayed in Fig. 5.12(b). In consequence, the relative amount of L increases slightly and that of ZS decreases slightly with YSZ addition in Fig. 5.12(e).

The intrinsic phase(s) and reaction products become unstable upon increasing the melt temperature or melt basicity. Increasing the temperature to 1350 °C eliminates the feasibility of anorthite as a thermodynamically viable phase and reduces the range of compositions over which zircon forms as the only reaction product. Zircon becomes unstable by 1400 °C, Fig. 5.12(a–c), whereupon saturation of the melt should lead only to reprecipitation of the tetragonal zirconia upon additions of ZrO_2 and 7YSZ, and cubic zirconia upon additions of 20YSZ. If zircon were kinetically suppressed the L/L+Z boundary would extrapolate to lower temperatures leading to the reprecipitation of zirconia upon saturation. (Note that an additional phase, namely the cyclosilicate $Ca_2ZrSi_4O_{12}$, CZS, is predicted to form at temperatures below ~1250 °C.) No reactive crystallization phases are predicted in the more basic CMAS upon additions of ZrO_2, 7YSZ, or 20YSZ, Fig. 5.12(g–i). In all cases the dominant field in the temperature range of interest is L+Z—or L+Z+F if enough yttria is present—with zircon only emerging at very large additions of oxide well beyond the limits of Fig. 5.12. Apatite is notably absent from the calculations for both melts, indicating even the 20YSZ does not contain sufficient yttria to enable reactive crystallization[c].

[c] Apatite appears as a stable phase for both CAS and CMAS after ~50 mol% of 20YSZ addition. This represents substantial BO dissolution and is not expected to be observed in practice.

While the databases do not include hafnia, the higher melting temperatures of HfO_2 vs. ZrO_2 (ΔT_M=43 °C) and $HfSiO_4$ vs. $ZrSiO_4$ (ΔT_M=74 °C) and expected similarity in phase equilibria suggests that the temperatures identified for the phase fields in ZrO_2 would be moderately elevated for HfO_2. This would imply $HfSiO_4$ and $Ca_2HfSi_4O_{12}$ should be more stable in the HfO_2 based systems, and probably absent in the CMAS-HfO_2 systems.

Melt effects on reactivity

The effect of melt composition on the interaction with RE-free or lean oxides involves both thermodynamic and kinetic factors. Isothermal pseudo-ternary sections between ZrO_2 (Fig. 5.13) or 7YSZ (Fig. 5.14) with varying Ca:Si ratios along pseudo-binary axes with compositions $C_{(100-x)}S_x$ ($0 \le x \le 100$), $C_{(83-x)}A_{17}S_x$ ($0 \le x \le 83$) or $C_{(78-x)}M_9A_{13}S_x$ ($0 \le x \le 78$) delineate the melts for which zircon is stable as the primary crystallization phase. Notably, the thermodynamic prediction [50] of the stability limit for both ZrO_2 and 7YSZ corresponds to Ca:Si <0.51 ($x \approx 55$) for the ternary silicates and Ca:Si<0.44 ($x \approx 54$) for the quaternary silicates. By comparison, zircon is stable for Ca:Si < 0.5 in the ternary CaO-SiO_2-ZrO_2 system [130], but with the cyclosilicate phase $Ca_2ZrSi_4O_{12}$ [128]. This suggests that the zircon stability is dominated by the Ca:Si ratio and only moderately sensitive to minor additions of MgO and $AlO_{1.5}$. Therefore, the silicate compositions selected in this study behave as expected with regard to the crystallization of zircon and, by extension, hafnon, as primary phases, but only with the pure MO_2 oxides. The $MSiO_4$ phases do form in the compositions containing Y but not as primary crystallization products, as elaborated below.

Oxide reactivity and products

The results suggest that the reactive crystallization of Hf-based phases in acidic melts is more favorable than their Zr-based counterparts. The $MSiO_4$ phases (zircon/hafnon) form readily, albeit significantly more slowly than those typically associated with CMAS mitigation in TBCs, e.g., apatites in rare-earth zirconates [60]. (For example, hafnon appears in about 10 min upon exposure to CAS at 1300 °C, Fig. 5.3(a), whereas apatite had a well-established layer by 10 min in Fig. 5.9(b). On coating-relevant length scales, apatite forms in <20 s during the reaction of $Gd_2Zr_2O_7$ EB-PVD coatings with CMAS at 1300 °C, Fig. 2.9 [11].) Zircon coverage on ZrO_2 appears slightly less extensive than hafnon on HfO_2 after 60 min at 1300 °C, cf. Fig. 1.1 and Fig. 5.3(b,d). Furthermore, hafnon exhibits more extensive coverage of the HfO_2 surface at 1400 °C than at 1300 °C (cf. Fig. 5.3d,f)—this is in contrast with zircon, which exhibits much less coverage at 1400 °C (cf. Fig. 5.6b,c) and is not predicted to be thermodynamically stable at that temperature (Fig. 5.12a–c). Note that the relative stability of hafnon vs. zircon with temperature in the CAS melt is arguably larger than that expected from the differences in their incongruent melting temperatures in the binary systems, ~74 °C. Importantly, the addition of Y, even in small amounts, significantly reduces the tendency to form the $MSiO_4$ in their respective systems as shown in the experimental results. This will be discussed in the next section.

A second difference between systems arises from the formation of the $Ca_2HfSi_4O_{12}$ cyclosilicate in the HfO_2 systems at 1300 °C, but not in ZrO_2 systems with CAS. It is reported that CZS is stable in the CaO-SiO_2-ZrO_2 system [130] at temperatures as high as 1479 °C, where it forms a eutectic with $ZrSiO_4$ and SiO_2 (cristobalite). The stability is evidently reduced by the addition of $AlO_{1.5}$, as shown

by the isopleth between CAS and ZrO_2, where the cyclosilicate is only stable below ~1250 °C in combination of zircon and anorthite (Fig. 5.12a). A similar field exists in the calculated phase equilibria between CAS and 7YSZ below ~1250 °C. Indeed, the Zr-cyclosilicate has been experimentally observed in the dissolution of YSZ into the CAS melt used in this dissertation at 1200 °C [63]. Conversely, the cyclosilicate is stable in the reaction with HfO_2 at 1300 °C, with hafnon, but not at 1400 °C, confirming the expectation with the trends in phase equilibria hypothesized earlier.

Effect of $YO_{1.5}$ additions on reaction product formation

The most consequential effect of moderate Y additions to ZrO_2 or HfO_2 is the significant suppression of the zircon, hafnon, or Hf-cyclosilicate formation in the CAS melt. Earlier experiments to establish the equilibrium between intimately mixed CAS and 25mol% ZrO_2 or 7YSZ [58] at 1300 °C for 50 h were fully consistent with the predictions of the isopleths in Fig. 5.12(a,b)—the predicted equilibrium phases for ZrO_2 are L+Z+ZS+An with addition of 7% $YO_{1.5}$ only suppressing anorthite. However, the present observations clearly reveal that when 7YSZ is gradually dissolved into CAS it does not form ZS first as expected from Fig. 5.12(b), but Z with a modified composition and ZS only at longer times and as a minor phase, Fig. 5.5(e-f) and Fig. 5.6. The effect is clearly kinetic suggesting that nucleation of Z is favored over that of ZS. A likely rationale is that nucleation and growth of the reprecipitated Y-depleted Z can take place epitaxially over the parent tetragonal particles facilitated by a similar crystal structure and a minimal difference in lattice parameters [159]—this point will be further elaborated below. In contrast, zircon has a complex crystal structure with no evident crystallographic orientation to favor nucleation on the parent 7YSZ phase and

requires more complex atomic rearrangements owing to the need for reorientation of the $(SiO_4)^{4-}$ tetrahedra across the interface. Moreover, while minor Y^{3+} incorporation is feasible in zircon [58], it would tend to de-stabilize the structure as it would arguably substitute for the aliovalent Zr^{4+}.

Effect of $YO_{1.5}$ additions on the mushy zone size

The overarching effect of a similar 7% $YO_{1.5}$ additions to HfO_2 is broadly the same regarding the hindrance to hafnon formation, but the underlying scenario is quite different. While 7YSZ is predominantly single phase tetragonal solid solution except for a minor fraction of fluorite (Fig. 5.7), 7YSH was designed as a two-phase microstructure wherein the fluorite phase is intended to control the grain size of the monoclinic HfO_2 during sintering to prevent microcracking on cooling. That goal was accomplished, but at the expense of the C(M)AS resistance as illustrated in Fig. 5.8. In essence, the fluorite phase dissolves much faster than the monoclinic phase in both acidic and basic melts, but there is no Y-depleted fluorite or tetragonal phases that could form given the phase diagram [160,161]. Therefore, the competition is between reprecipitating m-HfO_2 with minimal Y content on the existing m-HfO_2 network, which can take place epitaxially, or forming hafnium silicate or cyclosilicate which requires a separate heterogeneous nucleation event. The latter is only feasible for the acidic melt as inferred from the behavior of the ZrO_2 systems, but the lack of hafnon coverage suggests this is less favored kinetically. Instead, the apparent "growth" of the HfO_2 grains near the surface of the compacts in Fig. 5.8 suggests that m-HfO_2 is reprecipitating on the existing hafnia network.

Even in exposures to the basic CMAS melt, which does not form any reaction products, adding 7% $YO_{1.5}$ exacerbated the extent of the mushy zone. While it is difficult to compare the experimental

results of ZrO_2 to 7YSZ—the former is badly cracked due to transformation induced stresses—a hypothetical comparison of a dense, crack-free ZrO_2 is possible. When pure ZrO_2 is dissolved, any excessive dissolution after interface saturation (relative to what is necessary to negate diffusional losses) must result in the reprecipitation of nominally pure ZrO_2. (This is reprecipitation is unlikely to occur unless the reprecipitated zirconia incorporates small amounts of melt constituents like CaO; in this case, the reprecipitation would help slightly to seal infiltration pathways.) Conversely, the small yttria content in 7YSZ ensures, upon ZrO_2 saturation of the interfacial melt, an appropriately small $YO_{1.5}$ concentration in the melt (~0.25% for CMAS at 1300 °C, Fig. 4.2a,b)—this is well beneath the equilibrium $YO_{1.5}$ concentration determined from mixed powder experiments (~1.6%) [58]. The melt $YO_{1.5}$ concentration increases after ZrO_2 saturation by further dissolving the 7YSZ and reprecipitating a yttria-depleted zirconia, which captures the excess ZrO_2 from the melt. Unfortunately, the buildup of $YO_{1.5}$ in this way is slow—the dissolving 7YSZ contains ~7% $YO_{1.5}$[d] and the reprecipitated phase captures ~3% $YO_{1.5}$. The reprecipitated phase also nucleates on the partially dissolved 7YSZ grains, forming a shell (Fig. 5.7e) that impedes the dissolution of those grains and drives dissolution further into the compact. The net effect is that a significant amount dissolution continues after ZrO_2 saturation, which drives the formation of the large mushy zones observed experimentally for 7YSZ. The mechanisms relevant to 7YSZ and its mushy zone will be further discussed in the next section.

[d] The initially dissolving 7YSZ is fluoritic with a larger $YO_{1.5}$ content. Its exact composition could not be ascertained but is expected to be ~10–16% $YO_{1.5}$ depending on the processing history, Fig 2.5.

For two-phase materials like 7YSH, the mushy zone can be made even worse due to the preferential dissolution of one phase. As elaborated above, the fluorite preferentially dissolves (as observed in 7YSZ dissolution) adding both HfO_2 and $YO_{1.5}$ to the melt. Upon HfO_2 saturation, however, only the fluorite would dissolve (the monoclinic phase contains effectively no $YO_{1.5}$ to contribute). Excess HfO_2 will reprecipitate on the monoclinic hafnia network resulting in a large mushy zone of only monoclinic hafnia. Worse still, substantial grain boundary penetration was observed in the 7YSH beneath the monoclinic mushy zone, Fig. 5.8(d). This indicates the later stage of fluorite dissolution occurs primarily by the grain boundaries.

Crystallization in YSZ

Given the technological relevance of YSZ and the dominance of reprecipitation in these experiments, a deeper discussion on the mushy zone and its formation is warranted. Before discussing that, however, it is worthwhile to gain insight from the simpler mechanistic scenario presented by the dissolution of single crystal, cubic 20YSZ, shown in Fig. 5.4. The process starts with a planar front, e.g., Fig. 5.4(a), and no solute in the melt. The dissolution rate through the transient depends on the initial melt growth rate, u_o, and the evolving interfacial concentration, $C_i(0,t)$, which in turn depends on the diffusional transport rate, as described by Equations 3.2 and 3.3.

Saturation of the melt at the interface leads to nucleation of a reprecipitated zirconia phase by ~10 min (Fig. 5.4b,c). These two experiments, performed under the same conditions, generated either very sparse or rather abundant nucleation after the same time, suggesting that nucleation starts and accelerates rapidly at ~10 min. The first phase to form upon saturation of the CMAS melt should be

tetragonal ZrO_2 with ~1% $YO_{1.5}$ and ~2% CaO (Fig. 5.12i), and thus nucleation is heterogeneous. This has two important implications: one is the creation of a crystallographic boundary between the tetragonal and fluorite phases, and the second is that the growth involves an evolution of the reprecipitated composition toward the values observed at longer times, i.e., ~8% $YO_{1.5}$ and ~6% CaO. The reprecipitated phase does not dissolve substantially and its growth is fed by dissolution of the neighboring 20YSZ material, as illustrated in the inset of Fig. 5.4(b). This process leads to undercutting of the precipitate and melt penetration along the original boundary. Away from the early grains, dissolution continues with a concentration gradient normal to the interface, which is increasingly disrupted by continued nucleation and growth. As the growth centers evolve into fluorite with higher Y and Ca contents, they merge into a nearly continuous layer (Fig. 5.4d) and become separated from the substrate by a thin layer of glass resulting from the linking of the undercut boundaries. It is hypothesized that thereafter the main dissolution-reprecipitation process takes place across the glass layer between the original crystal and the reprecipitated fluorite, with the excess Y^{3+} migrating toward the top of the fluorite layer through narrow glass channels within the reprecipitated layer, and then into the melt. (These would correspond to potential boundaries between grains of the reprecipitated layer with different orientation, which would not close because they are wetted by the melt). The dissolution front, while wavy, remains fairly planar as it moves into the crystal as there are no boundaries to be penetrated in the single crystalline 20YSZ. Moreover, some of the reprecipitated fluorite at the boundary with the bulk melt must arguably re-dissolve in response to the long-range diffusion into the unsaturated melt. (The overlaying "plumes" of fluorite above the continuous layer in Fig. 5.4(d) are assumed to form during cooling, but their morphology could be influenced by variations in melt composition associated with the redissolution process.)

Dissolution of the polycrystalline 7YSZ occurs fundamentally in the same way but it is further complicated by the presence of grain boundaries and the associated minor fraction of cubic YSZ. In the earliest stages of the dissolution, before significant penetration along the grain boundaries occurs, the 7YSZ behaves similarly to the single crystal 20YSZ at the mesoscopic scale. The dissolution rate is controlled by Equation 3.2 but over an arguably extended and somewhat rougher and undulating reaction front. Upon saturation, however, the reprecipitation of Y-depleted zirconia begins, eventually developing a large mushy zone as the melt continues to penetrate the grain boundaries.

The dissolution and reprecipitation mechanism for polycrystalline 7YSZ inferred from Fig. 5.7 is schematically depicted in Fig. 5.15. The pristine oxide exhibits a microstructure similar to that observed in the bottom of the lamella of Fig. 5.7(a). The primary phase is tetragonal with lower Y^{3+} content than the bulk average plus a minor fraction of a Y-enriched cubic phase (Fig. 5.15a). The cubic zirconia regions are expected to dissolve faster than the bulk tetragonal phase owing to their higher concentration of Y^{3+} [98], explaining the absence of cubic phase in the upper part of the mushy zone. As the dissolution front advances along the grain boundaries the melt becomes saturated with ZrO_2, leading to the reprecipitation of a tetragonal phase with an even lower Y^{3+} content (<3 mol%) than that in the pristine material and no detectable Ca^{2+}. The onset of reprecipitation occurs when the mushy zone is only a few grain diameters thick, (<5 μm in Fig. 5.5a). Given the similarity in lattice parameters (<0.02% for the 2-3% difference in composition [159]), the reprecipitated oxide nucleates epitaxially on the surface of the remaining grain cores and grows around them forming a shell, as shown in Fig. 5.7(e) and schematically in Fig. 5.15(b). The thickness of the shell is largest

near the macroscopic boundary with the melt and decreases with distance into the mushy zone, consistent with the relative contact time with the melt and the average Y content in Fig. 5.7(c).

The growth of the shells is fed primarily by the dissolution of the cubic phase at the bottom of the mushy zone, which concomitantly promotes melt penetration between the initial tetragonal grains. Thus, the undercutting phenomena between the reprecipitated and parent phase observed in the 20YSZ dissolution is not applicable to 7YSZ. There may still be a driving force for dissolution of the grain core away from the cubic phase, and that may contribute partially to the growth of the shells. However, the epitaxial growth of the shell on the remaining tetragonal core and the absence of a true crystallographic boundary precludes melt penetration and the evolution of the thin glass layer observed in 20YSZ, Fig. 5.4(d), between the pristine and reprecipitated material. Once the shell surrounds the remaining core dissolution is kinetically constrained by the need for outward diffusion. It is further noted that growth of reprecipitated, Y-depleted tetragonal ZrO_2 on single crystal 7YSZ columns produced by EB-PVD also occurs without any boundary separation between the parent and product phases [56]. The latter, however, eventually separate from the former due to dissolution at re-entrant points in the highly convoluted feathery morphology.

It is intriguing that although only the shells are depleted of yttria, the entire core-shell grain transforms to the monoclinic phase upon cooling, cf. Fig. 5.15(b,c). This is at variance with the reprecipitated layer on the inner surfaces of partially dissolved EB-PVD columns, where the remaining column retains the non-transformable 7YSZ composition [56]. Arguably, the shell has a sufficiently low Y content to be transformable to the monoclinic phase upon cooling, assuming its thickness is above a critical value [162]. Conversely, the core of the underlying grain has been

rendered metastable because it has lost some Y from the nominal value owing to the partitioning of the cubic phase. This tetragonal phase (~5–6 mole% $YO_{1.5}$) is actually transformable under mechanical stress as noted in the experimental section. The inference is that when the shell transforms it induces a sufficiently high stress on the core to trigger the monoclinic transformation. This is consistent with the structure of the particles in Fig. 5.7(d), where the martensitic transformation twins traverse the shell and the core reflecting a common shear process. The initial volume expansion of the shell into the much more compliant glass leads to an outward radial expansion and arguably development of a tensile dilatation stress in the core, which may also contribute to the transformation. Moreover, particles closer to the bottom of the mushy zone with a thinner or no distinguishable shell do not transform on cooling. Because the monoclinic transformation is disruptive, these observations provide context for the effects of the incipient partitioning of the t' phase into tetragonal and cubic phases in plasma sprayed coatings prior to the exposure to the molten silicate.

5.2.2. Crystallization in RE-rich systems (GZO)

Thermodynamic foundations

The crystallization of rare-earth based phases, notably apatite, is observed in barrier oxides with sufficient RE content (e.g., $Gd_2Zr_2O_7$, GZO). Isopleths and the corresponding crystallization pathways are shown for GZO dissolution into CAS at 1200 °C and CMAS at 1300 °C in Fig. 5.16,

matching the experimental exposure conditions (Fig. 5.9 and Fig. 5.11). When exposed to the acidic CAS melt, the predicted crystallization path[e] with increasing GZO addition follows the fields

$$\text{L+CZS} \rightarrow \text{L+CZS+ZS} \rightarrow \text{L+ZS} \rightarrow \text{L+ZS+CGS}$$

$$\rightarrow \text{L+ZS+CGS+Ap} \rightarrow \text{L+ZS+Ap} \rightarrow \text{L+ZS+Ap+Z}.$$

The apatite phase fraction increases monotonically through the calculation range, whereas zircon begins to decrease upon the formation of *t*-zirconia. Both cyclosilicate phases (CGS and CZS) quickly become unstable. The extensive formation of reactive phases more than doubles the consumption of the liquid relative to RE-lean BOs (*cf.* Fig. 5.12d-f). Suppressing both zircon and the Zr-cyclosilicate from the calculation, on the basis that the phases may be kinetically delayed, simplifies the crystallization pathway, Fig. 5.16(e). In this case, reprecipitated zirconia is predicted to crystallize first followed shortly after by the Gd-cyclosilicate then by apatite. The quantity of reprecipitated zirconia and apatite monotonically increases as more GZO is dissolved into the system, whereas the Gd-cyclosilicate is consumed in favor of apatite. The fraction of apatite formed is similar to that in the non-suppressed calculation, but less melt volume is converted as no zircon is formed. A notable observation is that the reprecipitated zirconia phase remains tetragonal throughout the calculated range, even if zircon is suppressed. This limits the solubility of Gd^{3+} in the reprecipitated phase, thereby affording more Gd^{3+} available to form apatite and ancilliary reaction products [58].

The CMAS melt reacting with GZO at 1300°C follows a crystallization path of

[e] The calculation with CAS suppressed anorthite. The latter was incorrectly predicted to be stable above the known liquidus of CAS [58]. Suppressing the anorthite phase correctly recovered the eutectic melting temperature without having to suppress the other eutectic phases.

$$L+Z \rightarrow L+Ap+Z \rightarrow L+Ap+Z+F \rightarrow L+Ap+F \rightarrow L+Ap+F+Mel$$

which is at variance from CAS in two important ways. First, Zr-based reaction phases are made unstable by the decreased silica concentration in the CMAS melt (as predicted for the RE-lean BOs). Second, the reprecipitated material, although initially nucleating as tetragonal zirconia, becomes dominated by fluorite. The result is that the reprecipitated phase captures more Gd^{3+}. The key implication of both differences is a reduction in the melt consumption (conversion) at equilibrium. Crystallization of melilite is presumably due to the evolution of the melt composition as apatite crystalizes—its formation is typically observed in exposures of CMAS to pure rare-earths (e.g., Ref. [58]).

An important observation from the thermodynamic calculations is that, for both melts, a Zr-based phase is predicted to form shortly before the Gd-based apatite phase. This remains true even if some Zr-based phases are kinetically suppressed. For example, Zr-cyclosilicate is the first Zr-based phase predicted for the CAS melt, with reprecipitated Z not appearing until ~0.28 moles of dissolution; when Zr-cyclosilicate and zircon are suppressed, Z nucleation begins much earlier, after ~0.004 moles of GZO addition.

Crystallization in GZO

The experimental results highlight the speed at which GZO dissolves into both melts studied, affording crystalline (reprecipitated or reactive) products. Crystallization occurs quickly enough that capturing the stage before nucleation (i.e., similar to Fig. 5.4a) has been elusive, which also precludes a rigorous quantification of its dissolution rate as done for HfO_2 and 7YSZ. The dissolution-

crystallization mechanism will therefore be inferred using the available results and experience in other systems.

Single crystalline GZO, when exposed to CMAS at 1300 °C, rapidly establishes a layer of reprecipitation and, most importantly, apatite, Fig. 5.9. The latter's presence at 3 min is difficult to confirm from the SEM images (e.g., Fig. 5.9a) of the dense crystallization layer but is clearly established by 10 min in significant quantities, Fig. 5.9(b) and Fig. 5.10. This can be readily compared to the 20YSZ, which only shows the onset of reprecipitation for the same experimental conditions. As established in Chapter 4, these observations clearly illustrate the enhanced dissolution rate of GZO enabling rapid crystallization, even of Zr-based phases despite GZO's comparatively small ZrO_2 concentration relative to YSZ, *cf.* Fig. 5.4 and Fig. 5.9. Furthermore, no reactive crystallization was observed for 20YSZ into CMAS, even after 240 min.

The morphology of the reaction zones depicted in Fig. 5.9 suggests that the reprecipitated zirconia forms before apatite in the reaction between GZO and CMAS. This interpretation is supported by multiple pieces of evidence: first, the calculated crystallization path, Fig. 5.16(d), predicts *t*-zirconia crystallization before apatite. (Furthermore, the larger diffusivity of Gd^{3+} relative to Zr^{4+} would exacerbate the delay of apatite in a 1D dissolution-diffusion experiment, i.e., the effective rate of BO dissolution is Zr-rich relative to the 1:1 ratio of GZO.) Second, the larger grains are exclusively reprecipitated zirconia and persist near the interface with the bulk melt (Fig. 5.9); apatite is only found near the bottom of the reaction zone adjacent to much smaller, and presumably newer, reprecipitated grains. Third, apatite has been previously observed to form shortly after reprecipitated zirconia in the exposure of EB-PVD GZO to CMAS [11]. The important implication on the

mechanism is the early saturation of Zr^{4+} in the melt will slow down the dissolution rate of the BO (per the dissolution mechanism, Equations 3.1 and 3.2) and enable the crystallization of reprecipitated zirconia (containing a reduced amount of Gd^{3+})—both factors decelerate the rate of Gd^{3+} addition to the melt needed for apatite formation. How this mechanism observed in 1D, semi-infinite diffusion couples translates to TBC relevant length scales will be investigated in the next chapter.

The globular reprecipitated grains coarsen with time (cf. Fig. 5.9a-c) but remain notably different in morphology than the reprecipitated grains formed from 20YSZ—those in GZO do not merge but remain discontinuous, surrounded by melt like the polycrystalline 7YSZ. At any given time, however, the reprecipitated material appears relatively homogenous in composition throughout the crystallization zone—all grains contain ~18% $GdO_{1.5}$ in Fig. 5.10(b), similar to 4 h exposures, with identical melt composition and temperature, previously reported in the literature [66]). The mixed crystallization layer grows in thickness between 10 and 60 min, but the apatite grains therein do not grow substantially in length into the reprecipitated zirconia layer.

Given apatite is observed at 10 min and it is expected to be a key Gd^{3+}-containing crystallization product, apatite's lack of apparent growth indicates a balance between its formation rate and its redissolution as the semi-infinite melt removes Gd^{3+} and Zr^{4+} from the interface.

Both Zr^{4+} and Gd^{3+} show concentrations within the crystallization zone that are at or below those measured at the interface with the bulk melt. For instance, the concentration of Zr^{4+} in the crystallization zone is consistent throughout the thickness, at about 1.2±0.2 %; this is, however, only half the concentration at the interface with the bulk melt, which was closer to 3.2 % at 10 minutes.

The Gd^{3+} concentration at the top of the reaction zone is consistent with the value measured by the concentration profiles (~3.6 %, Fig. 4.8c), but it becomes significantly lower, ~2.3 %, near the bottom where apatite is present (Fig. 5.10b). The latter is consistent with the concentration of Gd^{3+} in the melt at equilibrium determined in GZO-CMAS mixed powder experiments [58]. It is unclear, however, whether the concentration of Zr^{4+} and Gd^{3+} measured within the reaction zone melt (Fig. 5.10b,c) are indicative of local thermodynamic equilibrium or of quench effects during cooling (as previously described). The latter would have important implications on the validity of composition measurements taken after cooling from mixed powder experiments (e.g., Ref. [94]), which often have short diffusion distances.

The microstructural evolution when exposed to CAS is fundamentally similar to CMAS but is complicated by the expanded menu of thermodynamically viable phases for CAS. The GZO rapidly reacted with the more viscous CAS melt, Fig. 5.11, despite the lower temperature (1200 °C) intended to retard the crystallization kinetics. The layer of small, globular grains observed after 1 min are consistent with reprecipitated zirconia. The latter suggests the reprecipitated phase forms before a Zr-based reactive phase (zircon or cyclosilicate), at variance with the thermodynamic predictions, Fig. 5.16(a,b), but consistent with similar observations in 7YSZ and 7YSH elaborated above. This also provides evidence that the CAS saturates in Zr^{4+} before Gd^{3+}, which is consistent with the inferred mechanism of the CMAS melt and with the thermodynamic and kinetic considerations elaborated above. Additional phases appear at 2 and 3 min (Fig. 5.11b,c) but are not observed in the 5 or 10 min experiments, suggesting they are metastable. The needle-like grains in Fig. 5.11(b) are strongly indicative of apatite, but the protruding grain in Fig. 5.11(c) (and throughout the sample)

are difficult to identify. The latter's morphology is consistent with some hafnon or Hf-cyclosilicate grains observed in Fig. 5.3 but could be the Gd-cyclosilicate predicted thermodynamically in this system. Some further investigation leveraging TEM-EDS and electron diffraction will be necessary to fully characterize the microstructural evolution in CAS at 1200 °C.

The crystallization and apparent redissolution of phases (e.g., the needle-like grain in Fig. 5.11b and the protruding grain in Fig. 5.11c) observed in CAS is in contrast with the microstructural evolution observed in CMAS. The current hypothesis involves the formation of metastable, kinetically favored, phases that redissolve upon the crystallization of the thermodynamically favored phase. Such a mechanism was observed in literature experiments dissolving ~10 wt% Gd_2O_3 powder into the same CAS melt at 1200 °C [93]. Therein, apatite rapidly crystallized as the only product upon the initial dissolution of Gd_2O_3; longer duration experiments, however, showed the initial apatite redissolved, eventually completely, in favor of the Gd-cyclosilicate phase. The expected dissolution distance of the GZO within the present experiments, though not directly quantifiable[f], is expected to be small for the conditions of Fig. 5.11—integrating an estimated concentration profile using Table 4.2 yields a dissolution distance of 0.1–0.4 μm for 1–10 min, respectively. The implication is that if apatite forms after 2 min, as expected from Fig. 5.11(b), it may not yet be thermodynamically stable based on the total amount of GZO dissolved and the thermodynamic assessment, Fig. 5.16(b), and therefore susceptible to further dissolution.

[f] Concentration profiles cannot be directly measured using the standard procedure as their estimated length are <10 μm, equivalent to 1–3 spots in the EPMA.

5.3. Synopsis

Multiple barrier oxides were exposed to an acidic and a basic silicate melt and the resulting crystallization and microstructural evolution were elucidated. Rare-earth free or lean oxides were unreactive with basic melts but can form Zr or Hf-based silicates. The latter, namely $HfSiO_4$ and $Ca_2HfSi_4O_{12}$, were found to be more stable than their Zr-based counterparts. As a result, pure HfO_2 readily reacted with the acidic melt to form a well-adhered reaction layer which shielded the underlying HfO_2 from further dissolution. Unfortunately, the HfO_2 microcracks as a result of its anisotropic CTE, affording melt infiltration pathways which are particularly deleterious for non-reactive melts. The addition of 7% $YO_{1.5}$ to the hafnia created a second phase, which constrained grain growth and prevented microcracking; but, the yttria addition effectively eliminated the Hf-silicate phases by a kinetic preference for hafnia reprecipitation. The effect worsened the size of the mushy zone and was found to equally apply to the common TBC material 7YSZ, which showed less reactive crystallization than thermodynamically anticipated. Instead, 7YSZ reprecipitated zirconia as shells on partially dissolved tetragonal grains that were slightly Y-lean in the pristine condition due to partitioning of the 7YSZ into a cubic+tetragonal microstructure. The cubic phase preferentially dissolved, leaving behind a mushy zone of *t*-zirconia that was non-transformable on cooling but transformable on the application of stress. The yttria-depleted zirconia shells transformed on cooling thereby applying stress to, and triggering the disruptive transformation of, the *t*-zirconia cores.

The rare-earth rich oxide, $Gd_2Zr_2O_7$, rapidly induced crystallization in either melt. The dissolution was sufficiently fast as to preclude capturing the onset of crystallization, as was possible for all barrier oxides in the previous paragraph. The mechanism is inferred to have reprecipitated zirconia, forming

before Gd-based reaction products (e.g., apatite) or Zr-based (e.g., zircon). While reprecipitated zirconia should decelerate apatite's crystallization, the relative impact appears to be minor for this material, at least for the CMAS melt. However, some benefit may exist for minimizing the time where Zr^{4+} is saturated in the melt but Gd^{3+} is not—this would be most easily achieved by enriching slightly the rare-earth concentration of the barrier oxide. Finally, some dissolution of reactive phases was observed, particularly for the CAS melt; this mechanism must be understood further but would have important implications on the stability of infiltration-inhibiting crystallization in thermal barrier coatings.

5.4. Figures

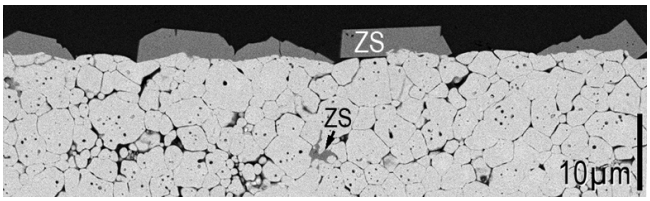

Fig. 5.1: Zircon (ZS) formation on nominally pure (not stabilized) ZrO_2 after interaction with the CAS melt at 1300 °C for 60 min. The extensive microcracking of the substrate is a result of sintering in the tetragonal phase field and the subsequent disruptive transformation to the monoclinic phase upon cooling.

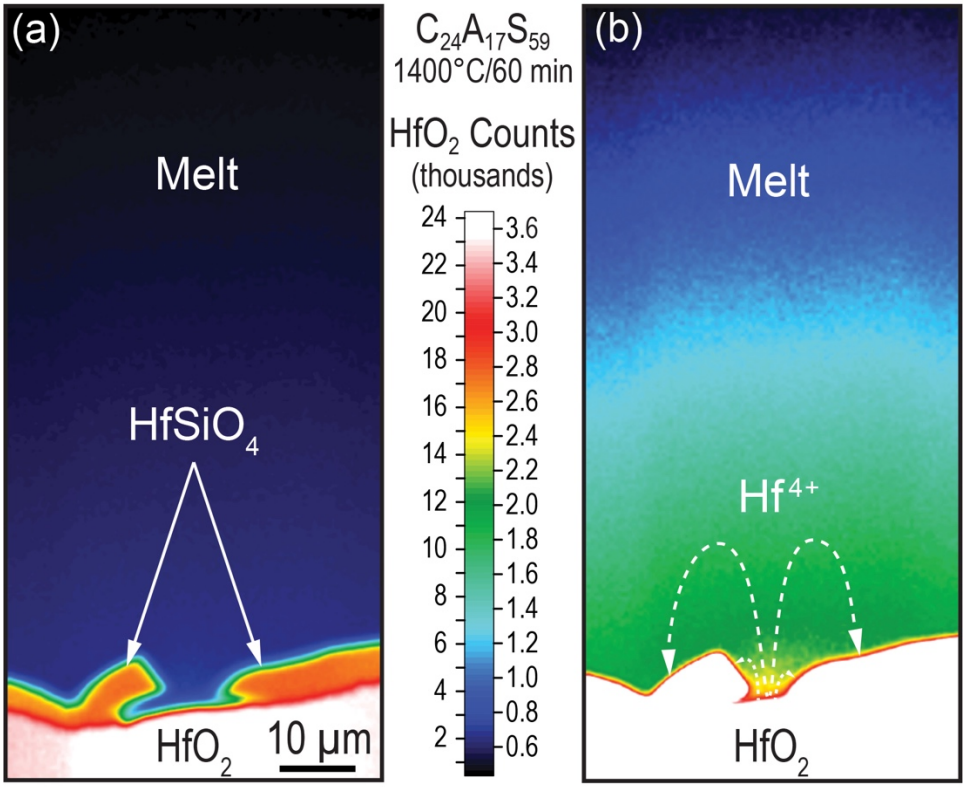

Fig. 5.2: Elemental mapping of HfO_2 concentration after exposure of a dense HfO_2 compact to $C_{24}A_{17}S_{59}$ melt at 1400 °C for 60 min. (a) Shows the formation of a layer of hafnon on the surface of the HfO_2 compact, with a gap wherein dissolution is still taking place. (b) shows the same region but with a different concentration scale, which illustrates the dissolution of HfO_2 from the gap and its transport to the surfaces of the product layer, where it reprecipitates. The concentration scales are shown in the middle.

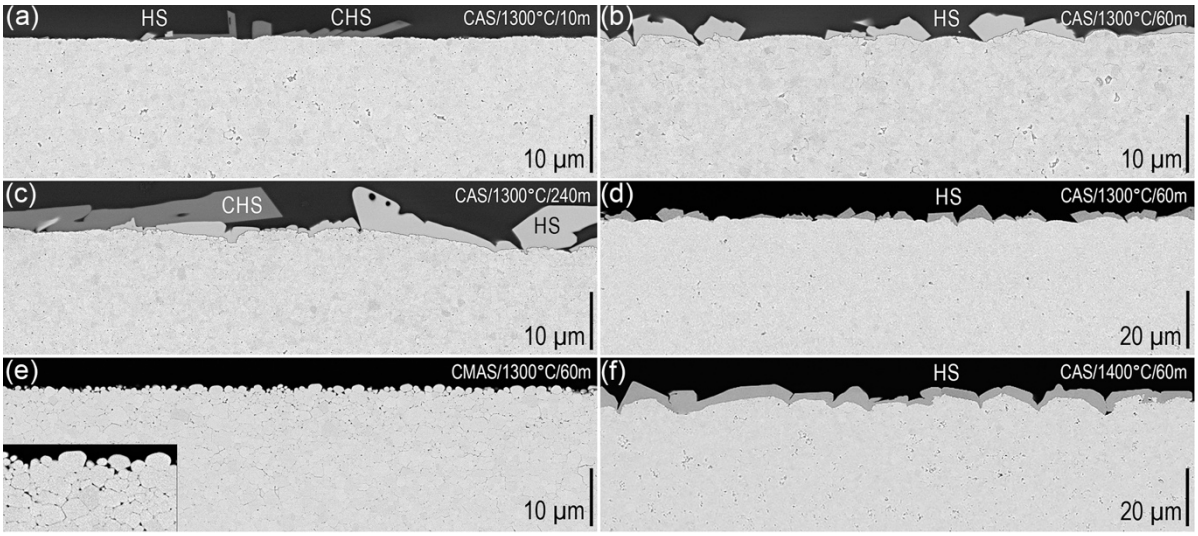

Fig. 5.3: Reacted interfaces of pure HfO_2 compacts exposed to CAS melts at 1300 °C for (a) 10 min, (b,d) 60 min, (c) 240 min, (e) CMAS melt at 1300 °C for 60 min, and (f) CAS melt at 1400 °C for 60 min. Reactive crystallization products include primarily hafnon (HS=$HfSiO_4$) and a Ca-Hf cyclosilicate (CHS=$Ca_2HfSi_4O_{12}$). Note the absence of reactive crystallization products in (e), where CMAS penetrates extensively along the grain boundaries down to ~19 µm.

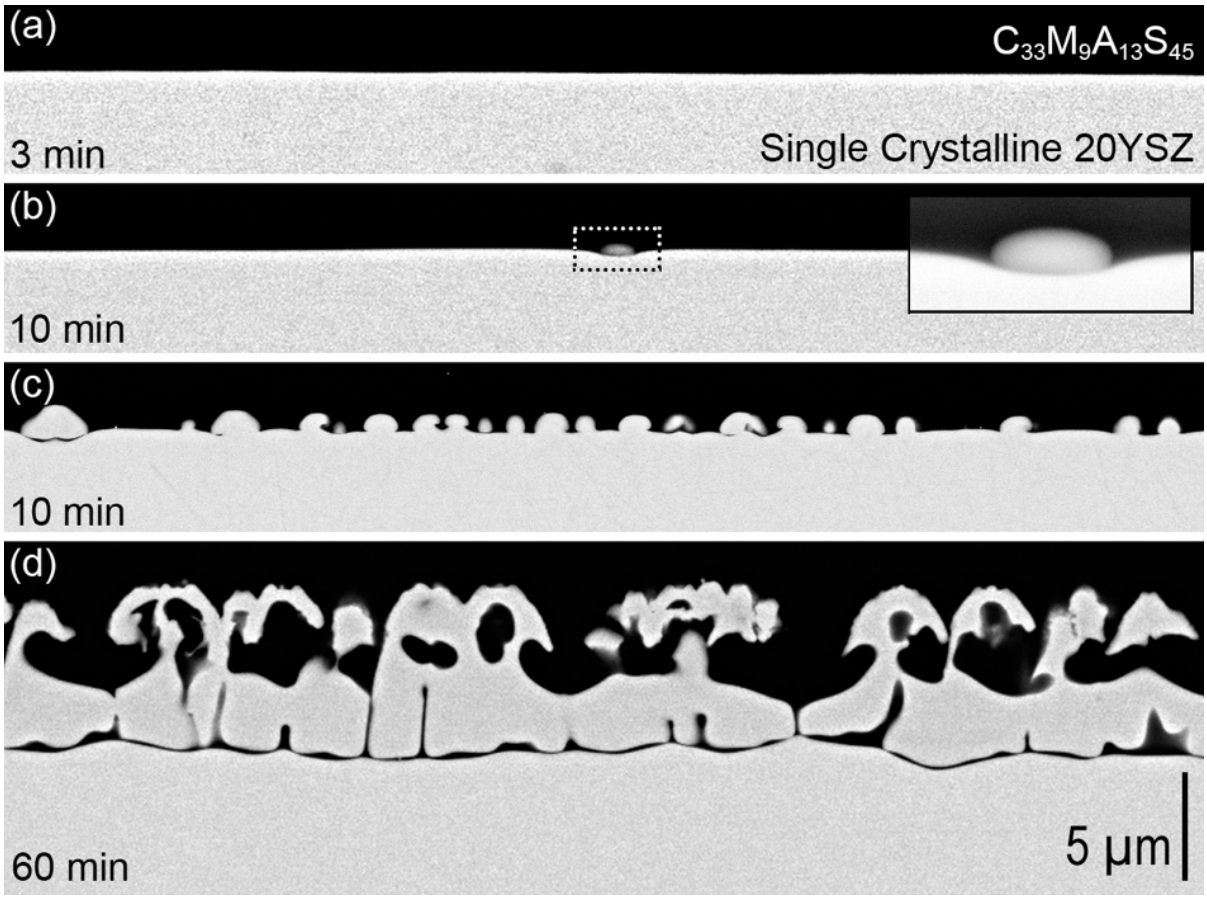

Fig. 5.4: BSE micrographs illustrating the dissolution reprecipitation mechanism in single crystalline 20YSZ with CMAS at 1300°C. The early dissolution front in (a) is planar after 3 min. (b) Shows the first evidence of reprecipitation of fluorite after 10 min, which evolves rapidly as shown by a duplicate experiment (c) for the same nominal time. Note in the inset in (b) the preferential dissolution feeding the growth of the new fluorite grain from the immediate vicinity of the nucleation site. (d) The reprecipitated fluorite forms an essentially continuous layer after 60 min, separated from the single crystal by a continuous thin glass film.

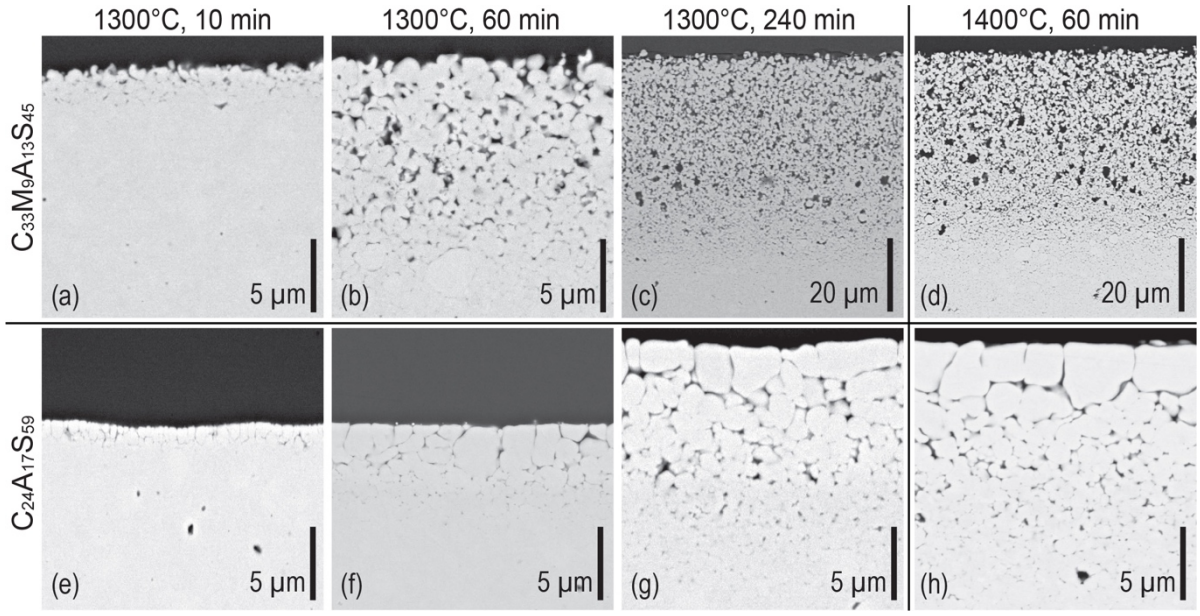

Fig. 5.5: Sequence of evolution of the reaction layer in polycrystalline 7YSZ with (a–c) CMAS and (e–g) CAS at 1300°C, and comparison with exposures at 1400°C for 60 min (d,h). The dissolution occurs preferentially at the grain boundaries with the evolution of a diffuse dissolution-reprecipitation "mushy zone" where the average $YO_{1.5}$ concentration increases as illustrated in Fig. 5.7.

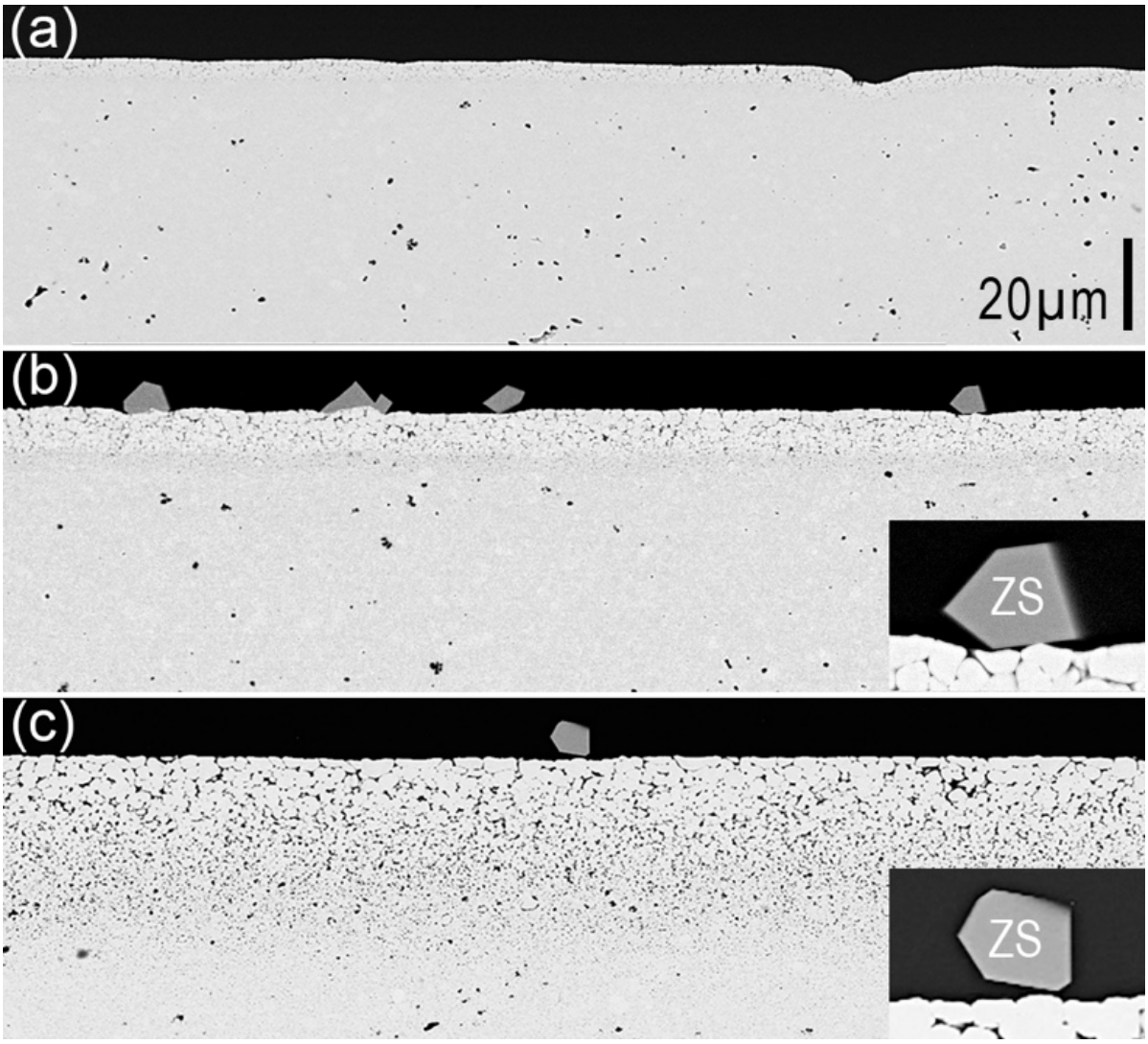

Fig. 5.6: Interfaces between 7YSZ polycrystalline compacts and (a-c) CAS melts for (a) 60 min at 1300 °C, (b) 240 min at 1300 °C, and (c) 240 min at 1400 °C. The faceted particles above the surface in (b) and (c) are $ZrSiO_4$ (ZS). The insets show details of zircon particles in (b) and (c).

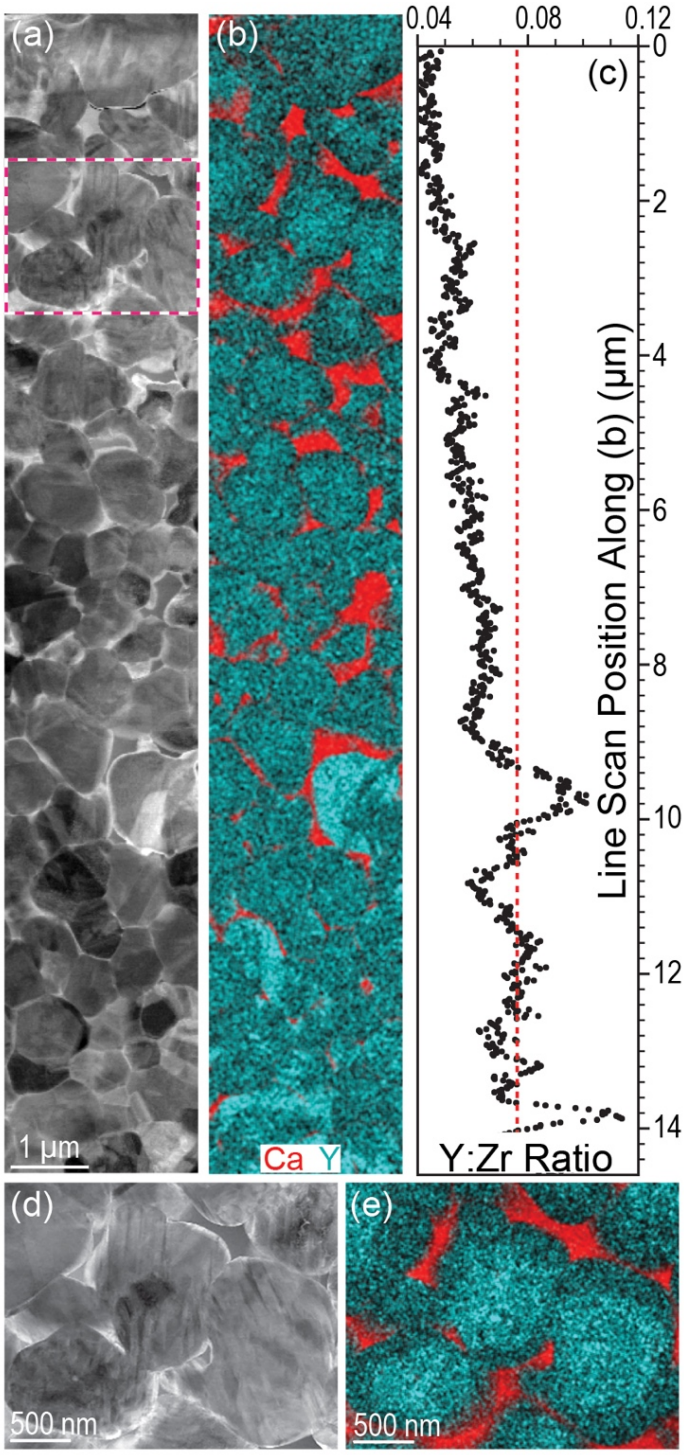

Fig. 5.7: TEM analysis of the mushy zone (a,b) from the specimen in Fig. 5.5(b). The annular dark field image in (d), taken from the area marked in (a), showed evidence of transformation on cooling reflected in twinning of the reprecipitated grains. These transformed grains are more evident toward the top of the mushy zone. EDS maps from (b) the overall lamella and (e) the reprecipitated grains corresponding to the image in (d), show the distributions of Y (blue) and Ca (red). (c) depicts the average Y:Zr ratio as a function of depth in the mushy zone, taken by integration across the EDS map in (b) at 17 nm intervals.

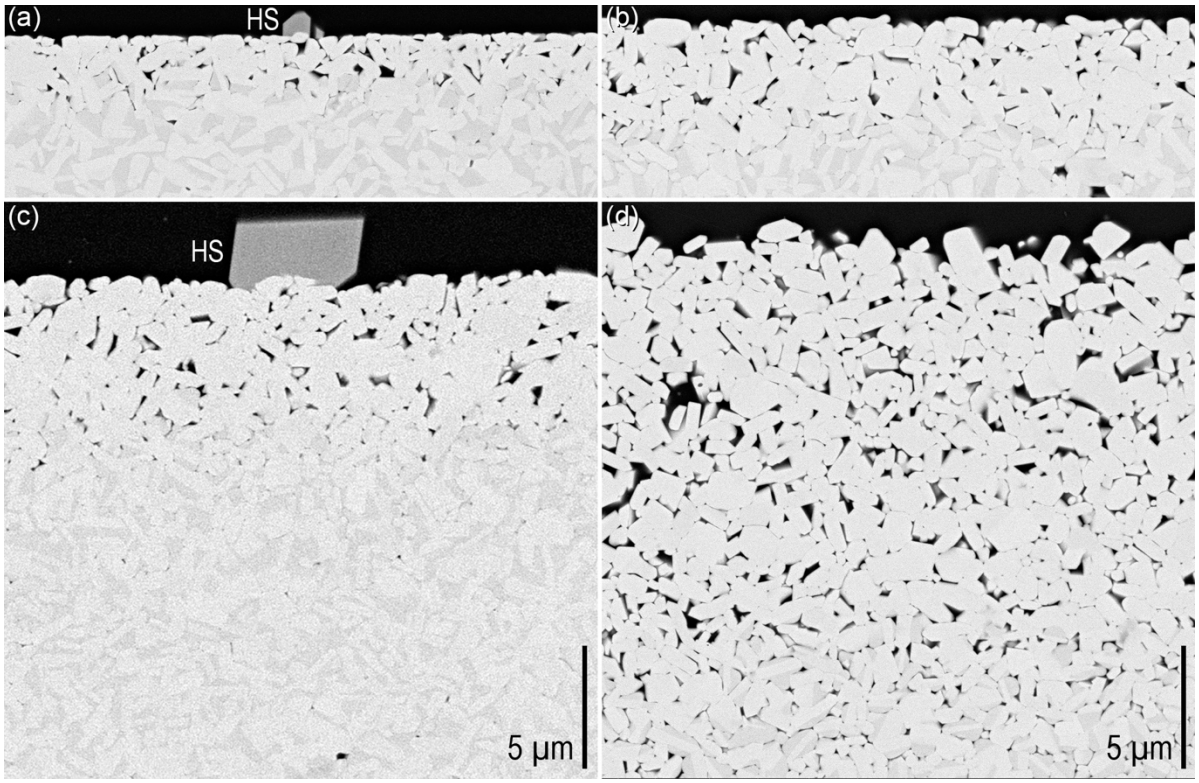

Fig. 5.8: Reacted interfaces of the 7YSH two-phase pellet after 1300 °C exposures to (a,b) CAS for 10 and 60 min, respectively, and (c,d) CMAS for 10 and 60 min, respectively. Note the preferential dissolution of the Y-rich cubic phase (darker gray) leaving behind a network of porous monoclinic HfO_2. Hafnon is only formed in the CAS melt and appears as times as short as 10 min, but the coverage is less extensive than in pure HfO_2 at comparable times.

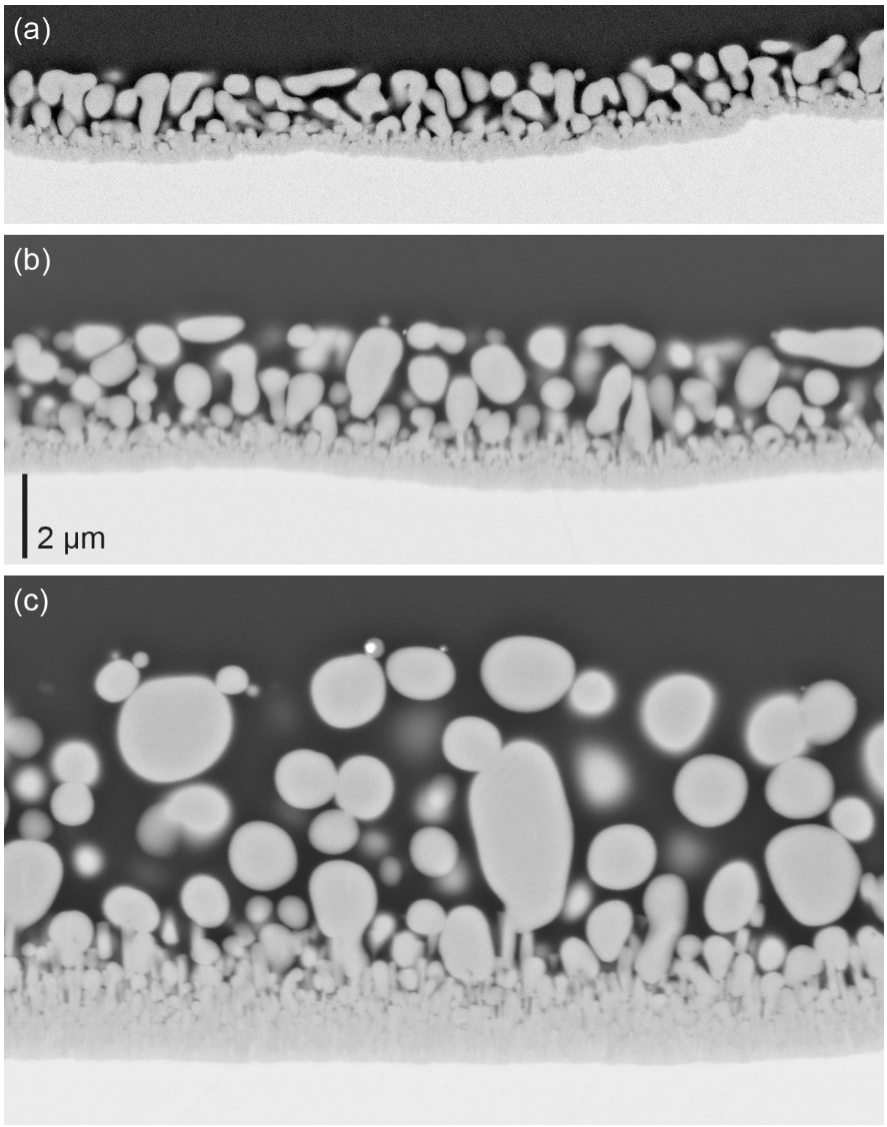

Fig. 5.9: Exposures of single crystalline $Gd_2Zr_2O_7$ to CMAS for (a) 3 min, (b) 10 min, and (c) 60 min. The reaction zone consists of globular reprecipitated zirconia grains, which coarsen over time, and needle-like apatite grains.

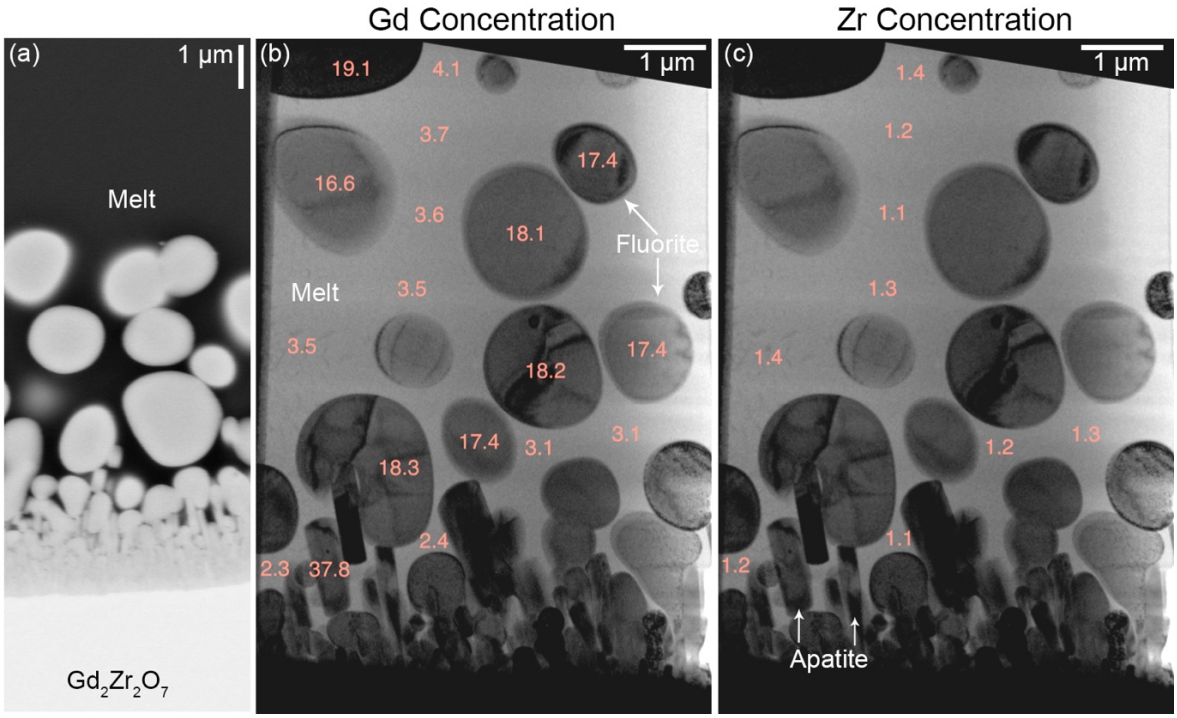

Fig. 5.10: (a) Reaction zone between the CMAS melt and the $Gd_2Zr_2O_7$ at 1300 °C for 10 min, consisting of spherical precipitates and needle-like grains. TEM analysis (b,c) confirms the presence of globular fluorite and apatite as the reaction products. The fluorite precipitates in (b) show $GdO_{1.5}$ concentrations around 18%. A slight concentration gradient of Gd^{3+} was observed in the melt (b), with the concentration being lowest near the apatite grains and highest near the top of the reaction zone. Conversely, the concentration of Zr^{4+} in the melt was relatively constant throughout the lamella (c).

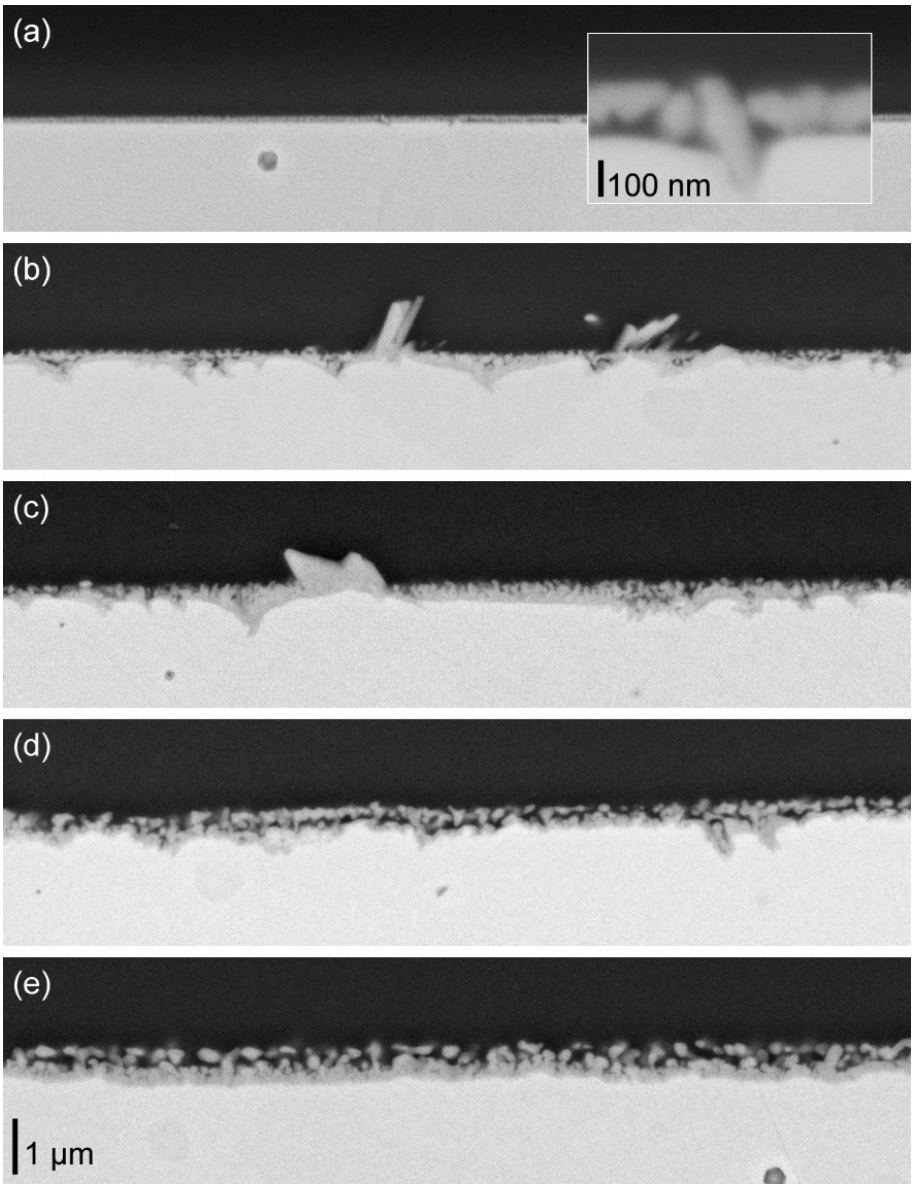

Fig. 5.11: Exposures of polycrystalline $Gd_2Zr_2O_7$ to $C_{24}A_{17}S_{59}$ at 1200 °C for (a) 1 min, (b) 2 min, (c) 3 min, (d) 5 min, and (e) 10 min. Crystallization was observed after only 1 min (a) in the form of fine globular grains along the interface. The needle-like phase in (b) is reminiscent of apatite, but the phase is not observed in subsequent experiments indicating it may redissolve.

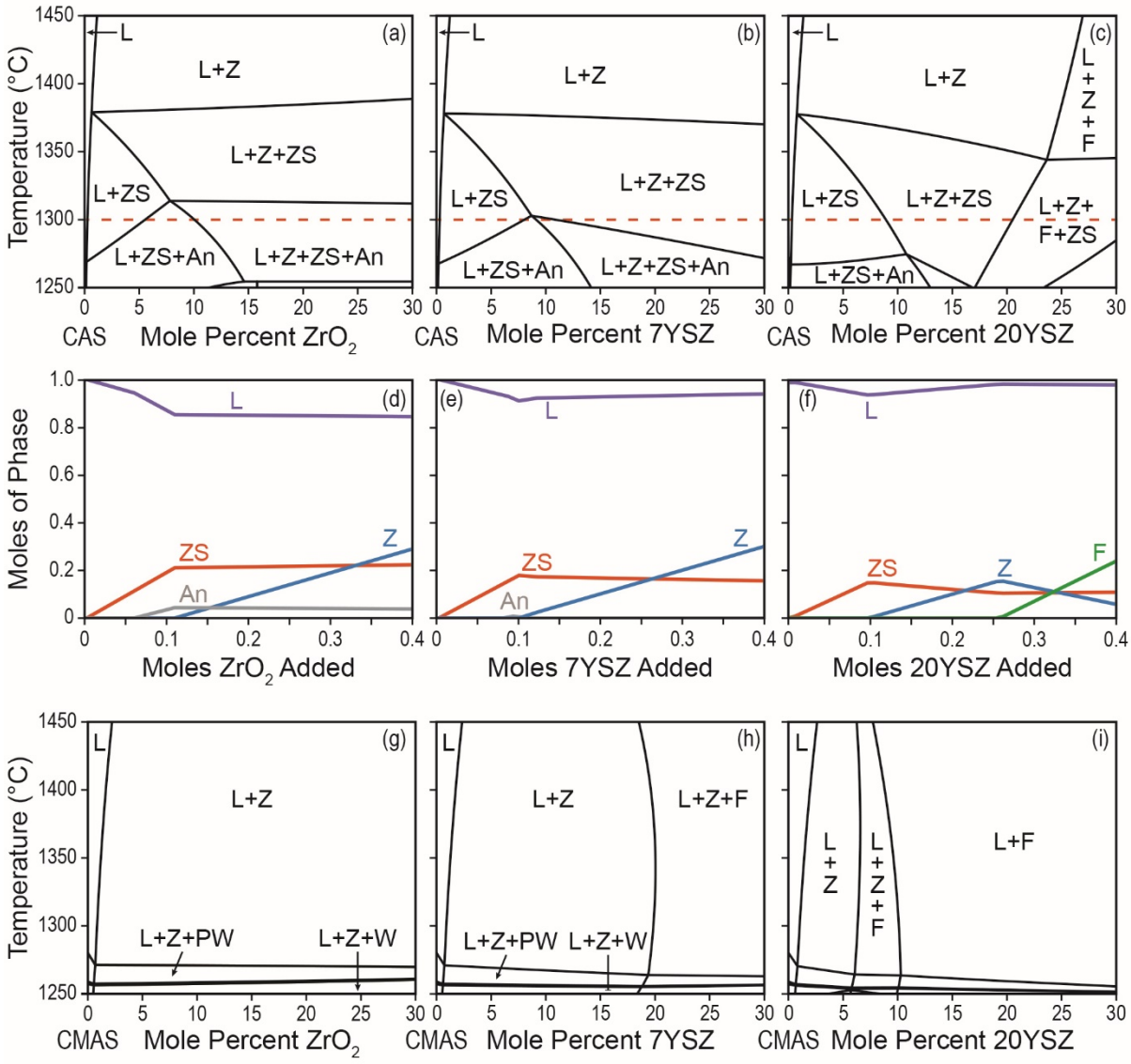

Fig. 5.12: Calculated isopleths for the dissolution of (a) ZrO_2, (b) 7YSZ, and (c) 20YSZ into the $C_{24}A_{17}S_{59}$ (CAS) melt. The corresponding evolution of the phase fractions at 1300 °C is shown in (d-f). All systems are expected to form zircon (ZS) after the melt (L) becomes saturated, with reprecipitated tetragonal zirconia (Z) forming after approximately 10 mole percent of the solid oxide is dissolved. The Zr-cyclosilicate (CZS) appears only below 1250 °C (not shown), consistent with its absence from this work and observations elsewhere [63]. The anorthite phase (An) does not form in these experiments. Calculated isopleths for the dissolution of (g) ZrO_2, (h) 7YSZ, and (i) 20YSZ into the $C_{33}M_9A_{13}S_{45}$ (CMAS) melt are also shown. Reprecipitated zirconia is the only phase expected to form above ~1275 °C.

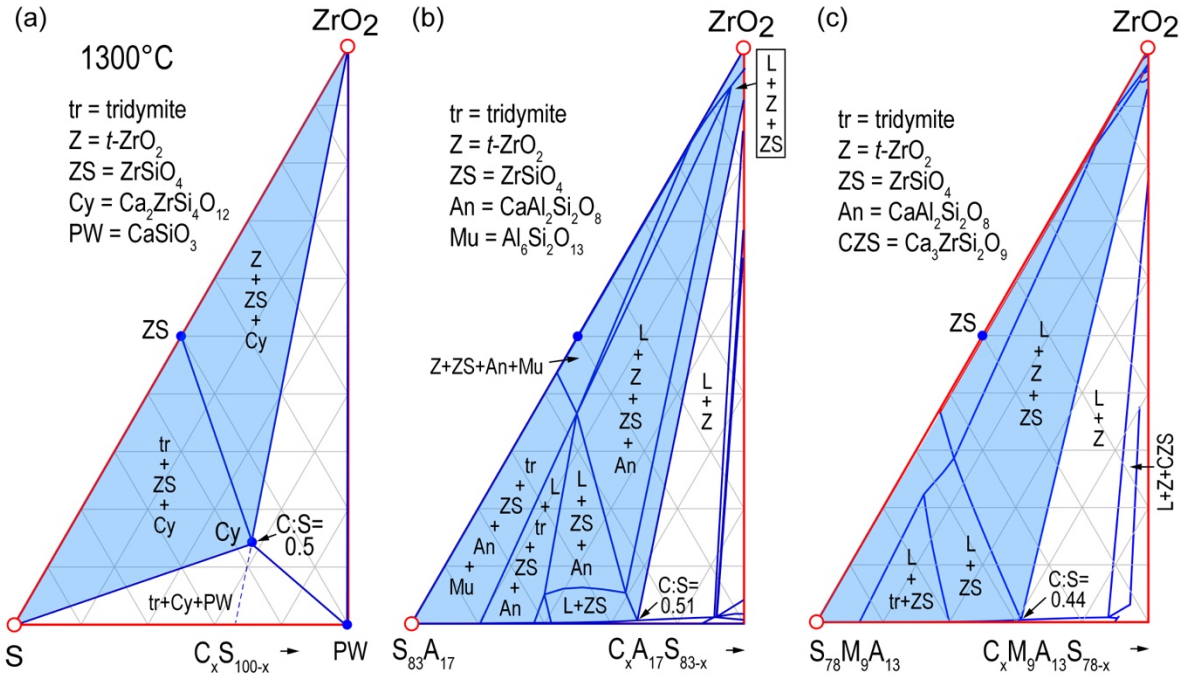

Fig. 5.13: Calculated isothermal pseudo-ternary sections between ZrO_2 with varying Ca:Si ratios along pseudo-binary axes with compositions (a) $C_{(100-x)}S_x$ ($0 \le x \le 100$), (b) $C_{(83-x)}A_{17}S_x$ ($0 \le x \le 83$), or (c) $C_{(78-x)}M_9A_{13}S_x$ ($0 \le x \le 78$) [50]. Regions forming zircon (ZS) are shaded in blue and the critical C:S ratio for zircon formation is noted on the diagrams. The latter appears to be insensitive to $AlO_{1.5}$ additions but does decrease modestly from the addition of MgO.

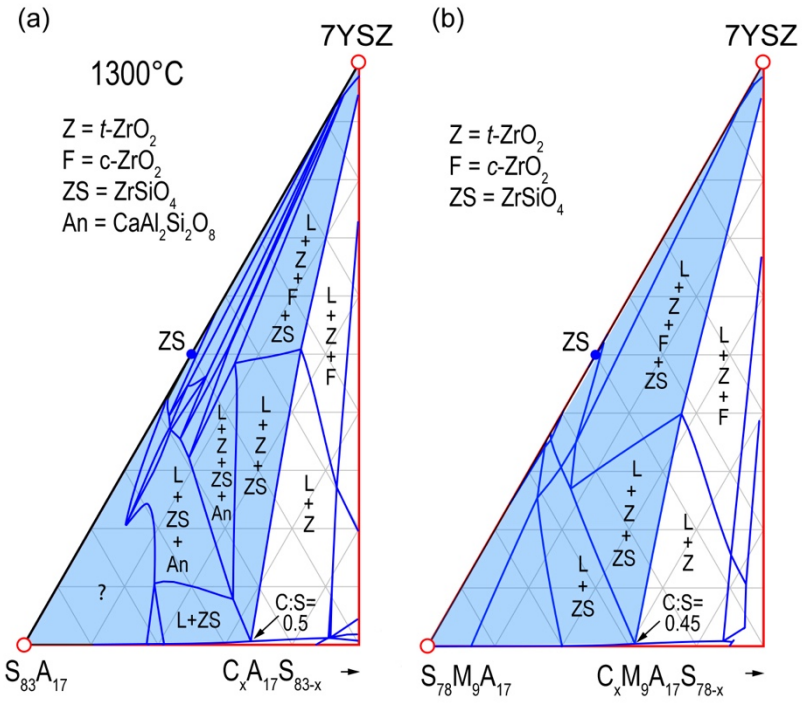

Fig. 5.14: Calculated isothermal pseudo-ternary sections between ZrO_2 with varying Ca:Si ratios along pseudo-binary axes with compositions (a) $C_{(83-x)}A_{17}S_x$ ($0 \le x \le 83$) or (b) $C_{(78-x)}M_9A_{13}S_x$ ($0 \le x \le 78$) [50]. Regions forming zircon (ZS) are shaded in blue and the critical C:S ratio for zircon formation is noted on the diagrams. The latter decreases modestly from the addition of MgO but remains comparable to the critical ratios for ZrO_2 (Fig. 5.13) indicating minimal impact from the addition of $YO_{1.5}$.

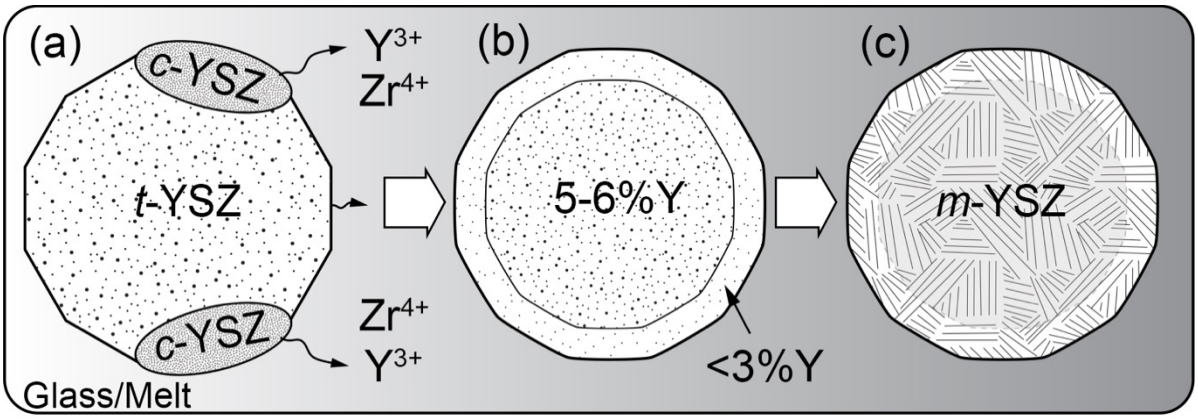

Fig. 5.15: Schematic of the dissolution-precipitation mechanism leading to the de-stabilization of 7YSZ. The as-received material in (a) is 6.8% $YO_{1.5}$ but partially decomposed into a minor amount of cubic phase and a majority tetragonal phase that is slightly lean in stabilizer than the average (~5–6% $YO_{1.5}$). Upon exposure to the CMAS melt the cubic phase dissolves faster, and a smaller amount of the tetragonal phase dissolves concurrently. (b) Y-depleted tetragonal phase precipitates epitaxially forming a shell on the remaining undissolved tetragonal core. (c) The shell transforms to the monoclinic phase upon cooling, and the ensuing stresses trigger transformation of the marginally stabilized core.

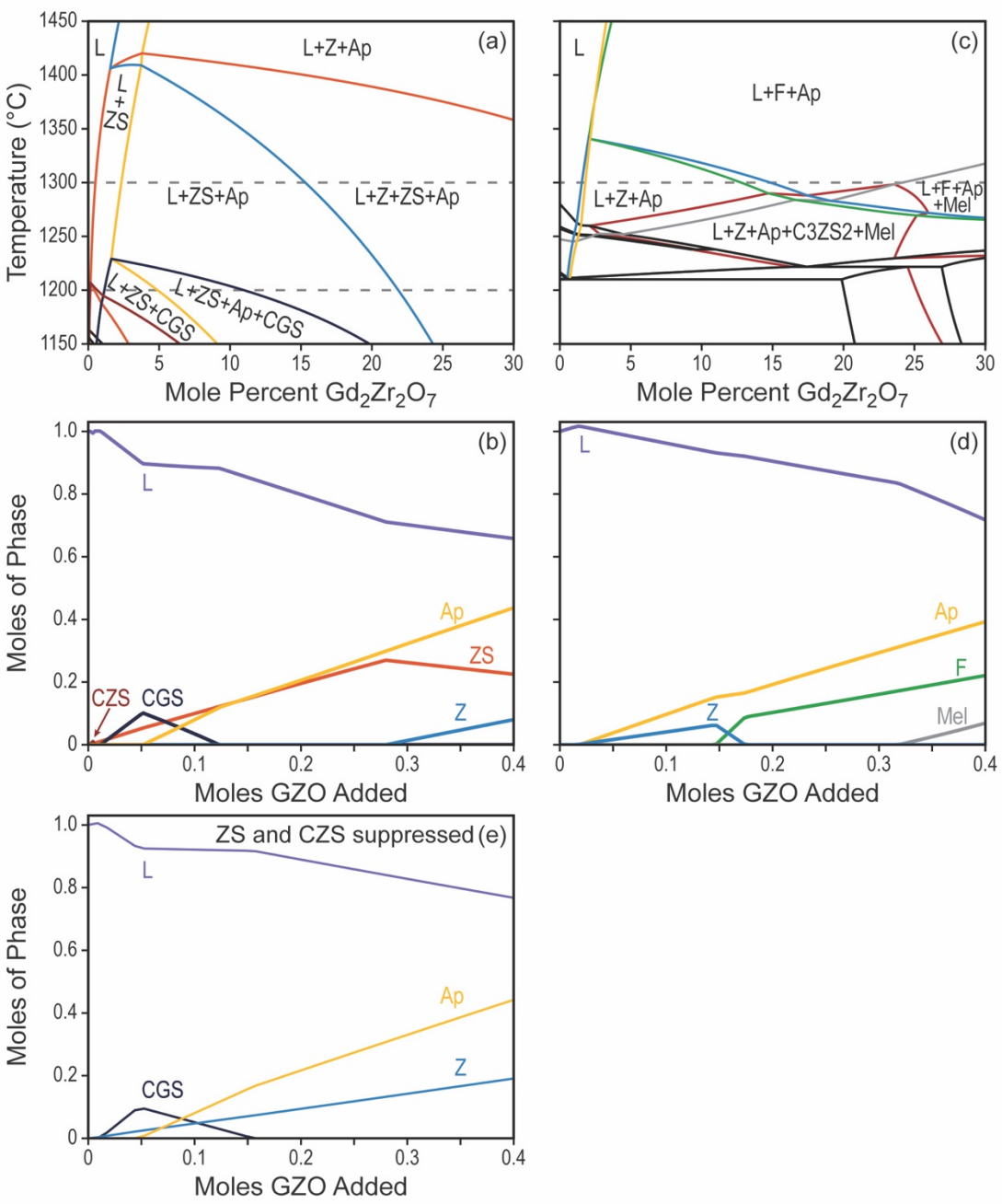

Fig. 5.16: Calculated isopleths for the dissolution of $Gd_2Zr_2O_7$ (GZO) into (a) $C_{24}A_{17}S_{59}$ and (c) $C_{33}M_9A_{13}S_{45}$. The corresponding evolution of the phase fractions is shown in (b) for CAS at 1200 °C (not fully characterized experimentally) and (d) for CMAS at 1300 °C. (The abscissa of b,d is in a single cation basis of GZO added, i.e., $Gd_{0.5}Zr_{0.5}O_{1.75}$.) Both systems are expected to form apatite (Ap) but its nucleation is preceded by a short-lived Gd-cyclosilicate (CGS) in the CAS melt. Crystallization of reprecipitated t-zirconia (Z) is preceded by both Zr-cyclosilicate (CZS) and zircon (ZS) in the CAS melt. No Zr-based reactive phases are predicted for the CMAS melt, but the initially t-zirconia (Z) is predicted to evolve into the Gd-enhanced cubic phase (F). The crystallization pathway of (b) is recalculated in (e) assuming kinetic suppression of ZS and CZS.

CHAPTER 6. MODELING AND IMPLICATIONS FOR COATINGS

As elaborated in the background (Chapter 2), reactive crystallization is initially rate limited by saturation of the melt, which depends in turn on the rates of coating dissolution and diffusion. These rates were quantified fully for 7YSZ in two melts and at three temperatures in Chapter 4 (and quantified for a subset of conditions for HfO_2 and $Gd_2Zr_2O_7$), but the methodology necessitated significant concentration gradients in the melt over distances of 10–1000 μm. In contrast, the relevant length scale of TBC porosity is generally less than 2 μm. However, the kinetic parameters determined from the semi-infinite experiments can be used with a suitable models to estimate the dissolution and diffusion behavior—and subsequently the melt saturation times—on the scale of the typical intercolumnar gaps in EB-PVD or dense, vertical cracked microstructures in APS TBCs [163,164].

This chapter presents three finite element (FE) models, roughly in order of increasing complexity and assumptions, that quantify the time necessary to saturate an intercolumnar gap with TBC constituents. The models explore: (i) isothermal diffusion within a representative 2D rectangular gap; (ii) the effect of a finite interface detachment rate (i.e., non-immediate saturation of the interface) and finite diffusivities in 1D isothermal conditions; and (iii) simultaneous dissolution, diffusion, and infiltration of a simplified 2D intercolumnar gap under an imposed thermal gradient. Each model simplifies the engineered geometric complexity of a real TBC; perfect wetting is assumed, feathery or porosity features, such as those of Fig. 2.1(a), are simplified as straight boundaries, and any coating tortuosity is ignored. This assumption greatly reduces the geometric complexity of the model and allows the fundamental impact of each kinetic process to be more clearly ascertained. The

results provide valuable and previously unavailable insight into TBC-CMAS interactions of length scales very difficult to probe experimentally. The collective results will then be discussed in the context of guiding the design of next-generation coatings and methods to reduce the number of experiments needed to be undertaken.

6.1. 2D isothermal diffusion model

To ascertain the rate of diffusional transport, the diffusion of TBO cations into an intercolumnar gap was modeled using the finite element method (FEM) package NDSolve in Wolfram Mathematica [165]. As a first approximation a static melt (no flow) was modeled in a 2D rectangular gap (2 x 2.8 μm), which was based on an actual microstructure depicted in Fig. 2.1(a,b). To understand the effects of varying the diffusivity alone, the dissolution behavior was first assumed to be rate limited by diffusion, i.e., the interface saturates immediately following Fig. 2.12(a). The relevant two-dimensional diffusion equation is given by:

$$\frac{\partial C_i}{\partial t} = D_i \left(\frac{\partial^2 C_i}{\partial x^2} + \frac{\partial^2 C_i}{\partial y^2} \right) \tag{6.1}$$

with an initial condition of $C_i(t=0, x,y)=0$ and a boundary condition of $C_i(t,x,y)=1-\exp(-3000t)$. (The boundary condition reaches unity effectively immediately but is consistent with the initial condition at $t=0$.)

Notwithstanding the simplicity of the model, the results clearly indicate that melt saturation occurs rapidly under diffusion-controlled regimes. For example, concentration profiles across the gap calculated using $D \approx 11$ μm^2/s (similar to Y^{3+} or Gd^{3+} diffusion in $C_{33}M_9A_{13}S_{45}$ at 1300 °C) are shown in Fig. 2.1(c). A substantive concentration profile across approximately half the gap width is

established already after 1 ms, and the time to reach the near-saturation condition is ~70 ms. (The estimated infiltration distance in this time following Jackson et al. [24] is ~17 μm, only ~5% of the total TBC thickness.) Repeating the calculation over a range of diffusivities (10^{-13}–10^{-10} m^2/s) representative of those experimentally measured in Chapter 4 reveals that saturation would occur in approximately 0.01–10 s. Given that a slow diffusivity arises from a high viscosity melt, these timescales for diffusion are likely faster than that of the time necessary for significant infiltration [24,56]. Moreover, note in Fig. 2.1(b) that many of the gaps are much smaller than that modeled, which would further decrease the times necessary to saturate the melt. Ultimately, it is unlikely that slow diffusivities would significantly hinder the saturation levels needed to trigger reactive crystallization and lead to large melt infiltration distances. It is then valuable to better understand the role of finite interface detachment rates (i.e., finite u_o) on the saturation time.

6.2. 1D isothermal dissolution and diffusion model

To capture the simultaneous effects of finite dissolution (interface detachment) and diffusion, the full non-linear PDE and boundary conditions of Equations 3.1–3.3 must be incorporated into a model. This demand exceeds the current capabilities of Mathematica but was accomplished using COMSOL Multiphysics® [166]. The model used the experimentally determined kinetic constants for 7YSZ (determined in Chapter 4, Table 4.1) and saturation concentrations (e.g., Fig. 4.2) to afford insight into melt saturation for the common TBC material. To further reduce the geometric complexity, a simple 1D finite element model featuring two 7YSZ dissolution point sources separated by a 1 μm wide, melt-filled gap was created. This model, shown schematically in Fig. 2.2(a), is representative of the leading front of the infiltrating melt, but does not consider the rate of viscous

flow or the thermal gradient present in actual TBCs. The time scale thus only represents the contact time between the walls of the coating channel and the melt volume element (i.e., the duration of active dissolution and diffusion).

An exemplary scenario of the evolution of the calculated Zr^{4+} concentration profile across the 1 μm gap for 7YSZ dissolving into CMAS at 1300 °C is illustrated in Fig. 2.2(b). The concentration scale is normalized by the saturation value determined in the semi-infinite melt experiments, 3.08 mol% at 1300°C. The calculations show that the Zr^{4+} concentration reaches saturation at approximately 3.0 s from the start of exposure, considerably faster than the estimated time for saturation from the experiment at the same temperature, ~5.4 min. More significantly, the concentration profiles simulated by the model are essentially flat, implying that diffusion is rapid in this scale (consistent with the conclusion of the 2D diffusion-only model, Fig. 2.1). Thus, the melt saturation is controlled by the initial detachment rate (i.e., by u_o) with minimal diffusional constraints. The concentration profiles of Fig. 2.2(b) are re-cast for comparison to other melt and temperature combinations in Fig. 2.2(c). The latter shows the Zr^{4+} concentrations at the boundaries (C_{max}) and center (C_{min}), as a function of time, for 7YSZ dissolving into both CMAS and CAS melts at 1300°C and 1400°C. For all but the CAS melt at 1300°C, where diffusion is the slowest, the concentration minimum lags only slightly behind the maximum, consistent with the presence of only small concentration gradients within the melt. However, the CAS melt at 1300 °C did exhibit flat concentration profiles in the later stages of dissolution and was calculated to obtain saturation at a similar time to 1400 °C; thus, the impact of low diffusivities, if present, are only pronounced in the early stages of 7YSZ dissolution.

The results also provide some insight into the effect of melt composition and temperature. Melt saturation occurs first for the more de-polymerized CMAS melt relative to CAS at equivalent temperatures. (Note that saturation also occurs faster for CMAS at 1300 °C than CAS at 1400 °C; the implication is that the changing melt composition has a larger effect on saturation times than changing the temperature under the conditions tested.) Importantly, the saturation times are similar or decrease at higher temperatures as the enhanced dissolution and diffusion kinetics counteract the increased concentration necessary to reach melt saturation. While this model provides useful insights into melt saturation on smaller length scales, it lacks any context for the concomitant infiltration that would occur in a real TBC.

6.3. Model of dissolution, diffusion, and infiltration under a thermal gradient

The final model develops a coupled approach to understand the competition between infiltration and melt saturation via the dissolution and diffusion kinetics. The key benefit to this approach is that changes to the model parameters—namely the kinetics and gap geometry—can be immediately put into context by how the infiltration distance at melt saturation changes. To more accurately capture this infiltration, the model considers a thermal gradient through thickness, which incorporates a spatial dependence to the kinetics not previously explored. This complexity requires multiple assumptions (to be enumerated) that likely affect the accuracy of the results; therefore, the model is not predictive but can serve to illuminate the general trends and dependences on critical variables.

6.3.1. Methods

The 2D finite element model was created and evaluated in COMSOL Multiphysics [166]. A rectangular sample geometry was built with a height of 350 μm and a width of either 0.5, 1, or 2 μm,

shown schematically in Fig. 2.3(a). (Note that only the intercolumnar gap was explicitly modeled—the regions labeled "TBC" in Fig. 2.3(a) were not included.) The height was chosen to be consistent with previous work that modeled infiltration alone [24]; the widths represent a range in possible intercolumnar gap sizes that may be exposed to molten silicates, broadly consistent with the microstructure depicted in Fig. 2.1(b). The top of the geometry was set to 1300 °C and the bottom to 1100 °C to mimic the temperature goals of future engines; a linear thermal gradient (~0.57 °C/μm) was imposed between, assuming the TBC temperature had reached steady state prior to its encounter with the siliceous debris. The melt $C_{33}M_9A_{13}S_{45}$ was chosen for this model because it is representative of actual engine deposits observed in service hardware [36,56] and has a low viscosity meaning the infiltration rate will be more severe. The melt was given an initial penetration distance of 10 μm at t=0; this provided stability to the infiltration calculations and is roughly consistent with the wider intercolumnar gaps found near column tips, e.g., Fig. 2.1(a). To reduce the mesh size necessary, the geometry was split into two separate domains: an upper domain where silicate melt was present (where the dissolution and diffusion physics would be enabled), and a lower domain were silicate melt was not yet present and no dissolution or diffusion would take place. This is represented by the boundary in the magnified view of Fig. 2.3(a). Two mapped (i.e., rectangular pattern) meshes were used to represent the entire geometry, e.g., Fig. 2.3(b), one for each domain. In the upper domain, a symmetric distributed mesh with 50 elements along the x-direction was used with an element ratio of 4, and a distribution of 250 elements ran along the y-direction. This mesh geometry ensured that there was sufficient mesh resolution near the vertical walls to capture the early stages of diffusion in the melt when large concentration gradients could exist. In the lower domain, the same

mesh setup was used, but with much lower resolution as no physics other than the steady-state temperature gradient were calculated within that region.

Infiltration

The infiltration kinetics were captured by moving the boundary between the two domains—the mesh, being anchored to this boundary, was then deformed downwards as the melt infiltrated in the model[a] (The large quantity of elements along the y-direction ensured that the mesh displacement distances between time steps was much smaller than the diffusion distances.) The infiltration velocity was calculated using the model reported by Krämer et al. [56], based on capillary flow through porous media, and later extended by Jackson et al. [24] to account for infiltration under a thermal gradient. The pertinent infiltration velocity, *dh/dt*, is given by:

$$\frac{dh}{dt} = \frac{8r}{k_t}\left(\frac{\omega}{1-\omega}\right)^2\left(\frac{\sigma_{LV}\cos\theta}{\eta(h)h}\right) \tag{6.2}$$

which depends on multiple parameters relating to the TBC microstructure and the melt properties. Related to the TBC, r is the radius of the intercolumnar gap (taken to be half the width for this model), k_t is the tortuosity, and ω represents the pore fraction open to flow, i.e., the area fraction of intercolumnar gaps. The tortuosity was taken as unity to be consistent with the simplified model geometry, Fig. 2.3(a) used to simplify the dissolution front; the feathery pore surfaces of real TBCs

[a] This method does not accurately capture the true nature of a silicate melt infiltrating into a TBC, wherein "new" melt is flowing into the intercolumnar gap from the top. By contrast, the model's infiltration method effectively means the melt at the top of the intercolumnar gap is stationary and exposed to dissolution from t=0. However, the key region of interest was the infiltration front alone (i.e., the moving melt-air boundary) where this assumption has negligible impact.

will increase tortuosity (to ~2) [24] and would approximately half the infiltration rate. The coating porosity (ω) was taken as 0.1 (10%) to be consistent with previous works [24,56]. Relating to melt properties, ϑ is the contact angle of the melt with the TBC (perfect wetting was assumed so $\cos\vartheta = 1$ [b]), σ_{LV} is the liquid surface tension, and η is the melt viscosity. The surface tension of $C_{33}M_9A_{13}S_{45}$ can be estimated using an existing model in the literature [167] to be ~0.4 J/m^2 at 1400 °C; the model fails to capture temperatures other than 1400 °C, but the temperature variability of surface tension is expected to be much smaller than that of viscosity and can be considered negligible in this context.

The key parameter controlling the infiltration rate in Equation 6.2 is the melt viscosity. The latter depends on temperature and, therefore, the depth of infiltration (h) at any point through the TBC's thickness. The viscosity of $C_{33}M_9A_{13}S_{45}$ can be readily calculated using the Giordano model [87] by

$$\log_{10}\eta = -4.55 + \frac{4700.1}{T - 681.8} \tag{6.3}$$

where -4.55 is a constant, the values 4700.1 and 681.8 are determined based on the composition of the melt, and T is the absolute temperature. Note that the available viscosity models do not account for the presence of typical TBC cations in the melt (e.g., Zr^{4+} or Y^{3+}); thus, it was assumed that the moderate dissolution of TBC cations into the melt did not significantly alter its viscosity.

Dissolution and diffusion

The dissolution and diffusion kinetics were again captured using the full non-linear PDE (Equations 3.1 and 3.2), which was incorporated into COMSOL using the built-in diffusion-convection

[b] Even if the wetting is not perfect, the cosine of the wetting angle will be close to unity.

module. The boundary condition of Equation 3.3 was applied to the vertical boundaries—representing the TBC columns either side of the intercolumnar gap—and the local concentration of the diffusing species was evaluated along the boundary. This added to the computational time but enables an accurate calculation of the flux along the entire boundary, which is important for this strongly spatially dependent model. No flux boundary conditions were applied to the top and bottom boundaries of the melt region (preventing diffusion outside of the penetrated region). The initial condition was null concentration within the intercolumnar gap.

Two key assumptions were made to render the model tractable. First, it was assumed that dissolution did not move the vertical boundaries. One can estimate the amount of TBC dissolution needed to fully saturate the gap is on the order of 1% of the gap width—this width change is negligible for the diffusion and infiltration calculations and negates the need for moving the mesh at all horizontally. Second, if multiple diffusing species were present (e.g., Zr^{4+} and Y^{3+} from 7YSZ dissolution), the model did consider the proportion of each species in the dissolving oxide, but the species were treated independently from each other regarding the dissolution rate via Equation 3.2. For example, calculations for the dissolution rate of Y^{3+} did not consider whether Zr^{4+} had already saturated. In reality, the saturation of a major species clearly controls the overall dissolution rate of oxide and therefore the flux of minor species into the melt (e.g., Fig. 4.2 and 4.3), but this effect adds significant complexity to the model. Furthermore, the model does not yet account for any formation of $REO_{1.5}$-depleted ZrO_2 phases, which would additionally hurt the ability to saturate the melt in Y^{3+}. Therefore, the model provides an estimate for the "best-case scenario" for the dissolution rates and

melt saturation times—the impact should be minor for major species but would underestimate saturation times for minor species significantly.

The key difference with this model was that the diffusivity, D, and initial interface detachment rate, u_o, were evaluated as a function of temperature using their Arrhenius descriptions (Equations 4.1 and 4.2), and therefore varied spatially along the vertical direction in the model. This largely was enabled by the wealth of experimental data collected for 7YSZ as described in Chapter 4 (Tables 4.1 and 4.2).[c] Therefore, 7YSZ serves as the basis for the TBC in Fig. 2.3(a). However, some exploration into varying u_o will be presented in the results; in this case, the temperature dependence of u_o (i.e., the activation energy) was maintained but the pre-exponential factor was adjusted to shift the value of u_o at all temperatures up or down—the reported value for u_o will be that at 1300 °C (the coating surface).

Crystallization

A final key assumption was that no reprecipitation or crystallization—reactive or intrinsic as a result of undercooling—would occur within the melt. This assumption has two key implications. First, no reactive or intrinsic crystallization means the melt would continue to infiltrate up to the point where the melt viscosity reaches the glass transition. (The temperature range of the model presented herein remains well above the glass transition temperature, ~764 °C, but captures ~150 °C of undercooling

[c] Note that this model was run with preliminary data than that reported in Table 4.1 and that used in Section 6.2. The diffusivities of Zr^{4+} and Y^{3+} are essentially identical, but the estimate of u_o at the time was 0.09 μm/s (rather than 0.07 μm/s in Table 4.1). This difference should not impact the key conclusions.

[59].) Second, minor elements captured by reprecipitated phases (e.g., $YO_{1.5}$ for Y-depleted zirconia) will saturate faster in the model than expected.

6.3.2. Results and discussion

Dissolution of 7YSZ

To establish a baseline, the first set of results explores the dissolution of 7YSZ, where the results of Chapter 4 are immediately applicable. The distribution of Zr^{4+} and Y^{3+} reveal that the concentration profiles are nearly uniform through the width of the channel but evolve over time to reach a saturation value, as shown in Fig. 2.4(a,b). Plots of the edge and center concentrations as a function of time (Fig. 2.4c,d) reveal no significant differences across the profile for Zr^{4+} or Y^{3+}. Again, the dissolution of 7YSZ into an intercolumnar gap is primarily limited by the rate of interface dissolution rather than by diffusion within the gap, consistent with the isothermal and stationary results of Fig. 2.2. The melt becomes saturated with Zr^{4+} after ~2 s. However, the low $YO_{1.5}$ content in the 7YSZ increases the time for Y^{3+} saturation substantially to ~60 s. Conversely, the "saturation" levels are referred to those at which dissolution would nominally stop, while the concentrations needed to form reaction products are likely to be lower in relevant cases.

With calculated saturation times, the corresponding infiltration distance can be determined simultaneously from the model. The infiltration distance over time, given by integrating Equation 6.2, can be seen in Fig. 2.5. The maximum infiltration rate occurs at t=0; this is of little surprise as the infiltration rate scales by the inverse of the penetrated distance and melt viscosity, which are a minimum at the coating surface. The rate of infiltration under these conditions is very rapid, reaching ~90 μm of infiltration after only ~2 s (the point the melt becomes saturated in Zr^{4+}, Fig. 2.5). The

infiltration rate does decrease as the melt viscosity increases at larger penetration distances. Even still, substantial infiltration, ~270 μm, has occurred by the point of Y^{3+} saturation; this is particularly bad considering this value represents the best-case scenario as previously elaborated.

Dissolution of $Y_2Zr_2O_7$

To better understand the effect of effect of increasing the interface reaction rate on the saturation times and flow behavior, a hypothetical infiltration of $Y_2Zr_2O_7$[d] was considered by making a few key assumptions. First, the diffusivities of $YO_{1.5}$ and ZrO_2 are taken to be independent of the crystal composition, as generally supported by comparing values in Tables 4.1, 4.3 and 4.4 for a given temperature and melt composition. Second, it is assumed that the rate of interface detachment (u_o) for $Y_2Zr_2O_7$ is like that estimated for GZO at 1300°C, ~0.8 μm/s (Chapter 4); this represents a significant increase from 0.07 μm/s for 7YSZ. Repeating the calculation with the new crystal composition and interface reaction rate shows substantial decrease in the time needed to reach saturation, approximately 0.5 s for both species, Fig. 2.7(a,b). The change in Y^{3+} saturation time is most consequential, arising from a combination of both increased $YO_{1.5}$ content in the crystal and the increased interface reaction rate. However, note that because the increased u_o equally affects Zr^{4+}, the Zr^{4+} saturation time decreased by about a factor of 4, despite a significant reduction in ZrO_2 crystal content. (Melt saturation notably remains limited by the interface detachment rates, as evident by the similarity between the concentration minimum and maximum within the gap, despite

[d] $Y_2Zr_2O_7$ was chosen over the more typical $Gd_2Zr_2O_7$ (GZO) for this analysis due to the lack of available temperature-dependent diffusion data for Gd^{3+}. In principle, however, Gd^{3+} should diffuse at a comparable rate to Y^{3+}.

the order-of-magnitude increase to u_o.) The concomitant infiltration distance at saturation is substantially reduced to 50-60 μm, Fig. 2.7(c). It is anticipated that the formation of apatite would occur at shorter infiltration distances, arresting the flow closer to the surface as shown by experimental work.

Parametric study

The previously discussed results for 7YSZ and $Y_2Zr_2O_7$ afford valuable insight for relevant TBC compositions. However, a more fundamental understanding of the importance of the kinetic parameters is complicated by the fact that changing the composition affects both the proportions of each element dissolving and the overall dissolution rate. To better isolate and understand the effect of D and u_o on saturation times, a parametric study was undertaken assuming the dissolving oxide was compositionally pure. Multiple intercolumnar gap widths (500 nm, 1 μm, and 2 μm) were also investigated to better understand the dissolution mechanism across multiple length scales.

The Arrhenius coefficients for Zr^{4+} and Y^{3+} diffusion were used, which represented an element with "slow" and "fast" diffusion, respectively. Three values of u_o were investigated: 10 nm/s, 100 nm/s (similar to 7YSZ), and 1 μm/s (similar to the estimate for $Y_2Zr_2O_7$). A summary of all collected saturation times and infiltration depths is presented in Fig. 2.6. Both the saturation time and the infiltrated depth at saturation decrease with increasing u_o or decreasing intercolumnar gap size. The maximum time for saturation was calculated to be 32.2 s, which occurred for Zr^{4+} diffusion in the largest intercolumnar gap size and at the slowest rate of dissolution. Conversely, the minimum time,

which occurred for Y^{3+} diffusion in the 0.5 μm gap with u_o=1 μm/s, was only 0.09 s. The concomitant infiltration distances spanned between 263 and 18 μm, respectively.

Again, the results of Fig. 2.6 suggest that u_o primary limits melt saturation. In the low limit of u_o=10 nm/s, the melt penetrates the TBC severely even for the relatively small 0.5 μm wide gap. Increasing the initial dissolution rate from u_o from 10 to 100 nm/s has the most significant effect on the time until saturation, leading to a factor of 7 decrease to the saturation time and approximately halving the infiltration depth under otherwise identical conditions. While further increasing u_o to 1 μm/s shows a seemingly less significant impact to the saturation time, the rapid initial infiltration rates mean the overall penetrated distance does decrease substantially (again by a factor of ~2) as a result. In most of the simulations, diffusion has little effect on saturation times throughout the gap—the concentration minimum closely follows the maximum (e.g., Fig. 6.8a) even for the slower diffusing Zr^{4+} cations—and the concomitant infiltration depths only slightly change if diffusion rates increase.

However, diffusion does appear to be important in the limit of large gap sizes and u_o. For example, the minimum concentration of Zr^{4+} lags the maximum significantly for the 2 μm gap with u_o=1 μm/s, Fig. 6.8(b); in this case the center of the gap saturates ~1 s after the dissolution front, being clearly limited by diffusion in the second half of dissolution. Increasing the diffusivity to that representative of Y^{3+} decreases the saturation time by ~1.5 s and prevents an additional 44 μm of infiltration, the largest difference observed from diffusivity effects. This observation has important implications for RE zirconates (e.g., $Gd_2Zr_2O_7$). The fast dissolution kinetics of these materials may introduce diffusional constraints to melt saturation within large intercolumnar gaps present in the TBC. Fortunately, apatite formation relies on saturation of the faster diffusing RE species and these can

continue to increase in concentration after Zr^{4+} saturation. Still, care should be taken in TBC processing to avoid the formation of large gaps.

6.4. Implications for TBCs

The models presented above represent the first attempts at implementing portions of the envisioned ICME framework in the context of TBC infiltration (Fig. 2.11). Additional efforts are needed to increase their accuracy, extensibility to material systems not yet studied, completeness to real-world geometries, and integration into the broader framework. Yet they still illustrate some key lessons for TBC design. The models overwhelmingly demonstrate that melt saturation on TBC relevant length scales is dominated by interface detachment (u_o) and not by the diffusion kinetics. (That is, the active dissolution mechanism follows Fig. 2.12(b) rather than Fig. 2.12(c) as observed in the semi-infinite experiments presented in Chapter 4.) The experimental results presented in Chapters 4 and 5 have shown, both qualitatively and quantitatively, that u_o increases as the quantity of RE in the dissolving material increases. Therefore, the key conclusion is that the selection of novel oxide compositions for CMAS mitigation should focus on those stable and refractory phases rich in RE^{3+} to ensure effective reactive crystallization. This both maximizes the thermodynamic driving force for apatite crystallization—a point already established in the literature as discussed in Chapter 2—and ensures the coating dissolves rapidly to minimize the time needed to saturate the melt and minimize the infiltration.

In some senses, the strong role that u_o and intercolumnar gap width play on melt saturation—and the weak role D plays—is a favorable situation for designing CMAS-resistant coatings. The kinetic data gathered in Chapter 4—and the larger quantity of diffusion data in the geochemical literature

[100]—suggest that the diffusivity is unlikely to be altered significantly by materials selection. The rare earth cations diffuse at similar rates (cf. Table 4.1 and 4.4 and data available in Ref. [100]). Likewise, the diffusivity of Zr^{4+} is comparable to Hf^{4+} (Table 4.3). Instead, the diffusivity is strongly affected by the melt composition—something wholly outside of engineering control of in-service parts—and by the temperature of the melt. While the latter can in principle be controlled, in practice the desire for higher temperature gas turbine engines largely removes the range over which control can be exercised. Conversely, while u_o also depends on the melt composition and temperature, it can clearly be controlled by the composition of the coating by tailoring the RE content. (The bulk dissolution rate can also be improved by engineering the coating microstructure with high surface area, e.g., by ensuring a feathery microstructure is produced.) This means the bulk dissolution rate of the coating can be maximized—though composition and engineered microstructural features—potentially to the point where diffusion becomes limiting to melt saturation, which tends to be fast on these length scales (e.g., Fig. 2.1). Finally, the impact of intercolumnar gap size (Fig. 2.6) can be minimized by careful coating deposition processing to minimize the quantity of large gaps sizes (e.g., those > 2 μm), but this would be a challenging processing problem.

6.5. Relating kinetics to melt properties

The experiments presented in Chapter 4 are too tedious to collect for all possible melt compositions that could be ingested into an engine, particularly as higher temperatures increase the size of the liquid-forming composition space. Therefore, implementing a full ICME-based approach to predict coating degradation becomes largely intractable unless the kinetic processes (D and u_o) can be

predicted for arbitrary melt compositions. This section will address and discuss these links, as well as highlight where additional work is necessary.

As discussed in Chapter 2, the diffusivity of high valence or large cations typically decrease as the melt viscosity increases. If a cation acts as a network former in the silicate melt, the diffusivity will be inversely proportional to the melt viscosity via the Eyring relationship [104,107,108] (Equation 2.1). The applicability of the Eyring relationship to the diffusion data for Zr^{4+} and Y^{3+} (Table 4.1) is investigated in Fig. 2.8. The data represent six different melt-temperature combinations—$C_{33}M_9A_{13}S_{45}$ (lower viscosity) or $C_{24}A_{17}S_{59}$ (higher viscosity) each at either 1300°C, 1350°C, or 1400°C—providing a total of six different melt viscosities for comparison. The ordinate of each data point represents the average of three experimentally determined diffusivities for a given melt-temperature combination (Table 4.1, but divided by the melt temperature of the experiment), whereas the viscosity values on the abscissa are derived from literature viscosity models [51,87].

Overall, the diffusivities of both Zr^{4+} and Y^{3+} are well fit to the Eyring relationship provided an appropriate viscosity model for each melt composition is used, Fig. 2.8(a). However, applying a single viscosity model to both melts provides generally poorer fits, Fig. 2.8(b,c). In this case, the CMAS viscosity was estimated using the Giordano model [87], which was recently shown to match closely to experimental viscosities [91]. However, that model poorly predicts the viscosity of the CAS melt [91], which was instead calculated with the viscosity model developed by FactSage (version 8.1). The best-fit lines yield a diffusive jump distance, l, of $l_{Zr} \approx 7.2$ Å, roughly consistent with previous estimates [111], and $l_Y \approx 4.6$ Å. The magnitude of these estimates, much larger than the relevant ionic

radii, suggest the diffusing species for Zr and Y are polyhedral (i.e., some oxygen diffuses with the cation).

There are two key implications. First, Fig. 2.8(a) suggests that the diffusivity of, at least some, cations relevant to barrier oxides could be reasonably estimated if the melt viscosity is known or can be accurately predicted. This immediately reduces the number of diffusion couples necessary to enable the envisioned ICME approach. Second, the results suggest that both Zr^{4+} and Y^{3+} are incorporated into the melt as network formers, within the relevant concentrations from 7YSZ dissolution. This was not surprising for Zr^{4+}, which has a large ionic field strength (~0.89, Table 2.1) and has repeatedly been shown to act as a network former [110].[c] But, it was surprising for Y^{3+}, which has historically been identified as a network modifier [105,168]. However, more recent work has identified amphoteric behavior for REs when added to synthetic C(M)AS melts [91].Additional work is needed to confirm that Y^{3+} (and other relevant RE species) remain in a network forming role *(i)* when present in higher concentration (e.g., a few mole percent, near saturation) and *(ii)* in a variety of melt compositions relevant to CMAS attack.

Unfortunately, less is known about how the initial interface detachment rate, u_o, correlates to melt and coating composition. First, the bulk of the geological literature has investigated crystal dissolution rate-limited only by diffusion (i.e., u_o is so large it cannot be experimentally measured); as

[c] No studies, to the author's knowledge, have investigated whether the diffusivity of Hf^{4+} could be correlated to melt viscosity. However, the relationship is expected to hold given the similarity in the ionic field strength to Zr^{4+}, Table 2.1.

a result, there is no literature assessment of how u_o is expected to change. Second, the experiments of this dissertation were insufficiently broad to answer this question.

6.6. Synopsis

Finite element models on length scales relevant to TBCs suggest diffusion is unlikely to limit melt saturation in actual applications. When finite dissolution rates are considered, e.g., for 7YSZ, simulated concentration profiles within the model intercolumnar gaps are largely flat but increase in concentration with time, indicating u_o primarily limits dissolution, the subsequent melt saturation, and would delay reactive crystallization. The concomitant infiltration distances at melt saturation, before any reactive phases can nucleate or grow, can be substantial at up to 250 μm (~70% of the modeled TBC thickness). But infiltration distances are reduced to <60 μm (~20% of the overall thickness) if u_o is increased to ≥0.8 μm/s, the estimate for $Gd_2Zr_2O_7$ dissolution from Chapter 4. Therefore, the search for novel TBC compositions should focus on those that show rapid dissolution ($u_o \geq 0.8$ μm/s) into CMAS and exhibit favorable reactive phases for sealing channels. While the models are useful for comparing the importance of each kinetic parameter, the general dearth of kinetic data available today limits their capability in the envisioned ICME approach to coating design. However, diffusion kinetics appear to be well correlated to the melt viscosity provided an appropriate viscosity model is used. Additional work to correlate D and u_o to melt composition and/or coating composition would significantly help further development of the ICME approach.

6.7. Figures

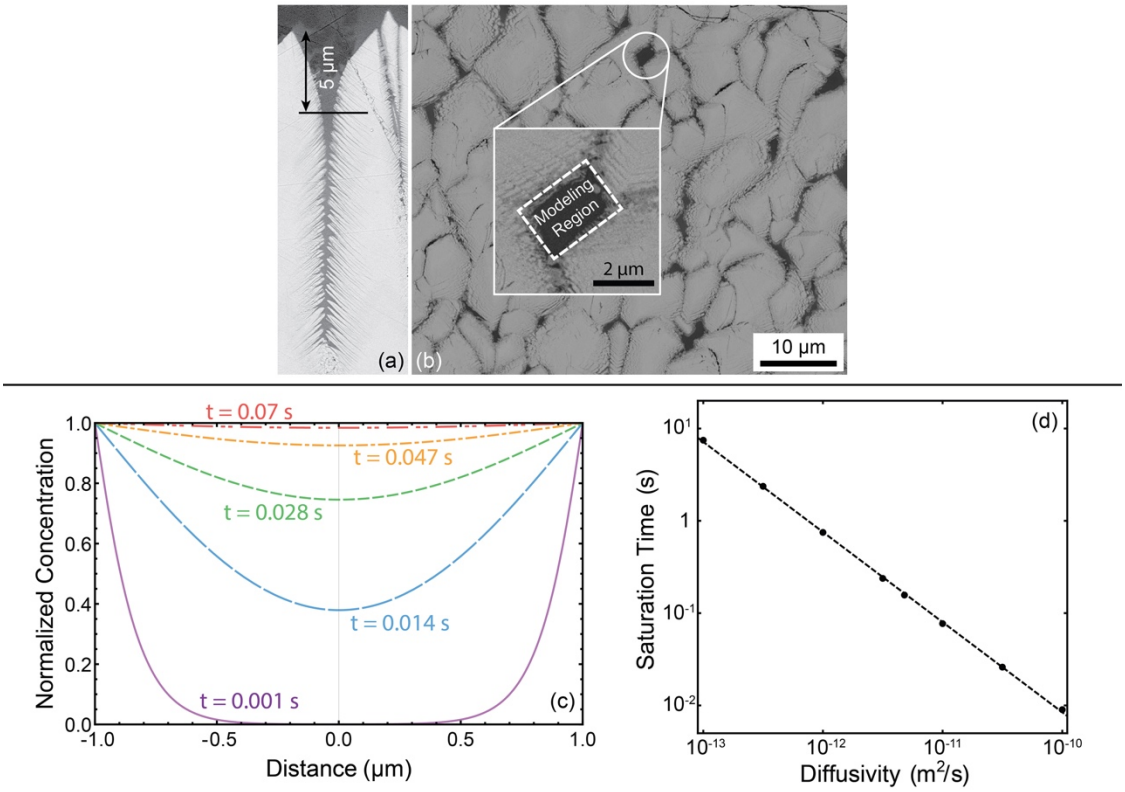

Fig. 6.1: (a) BSE-SEM cross-section image of two TBC columns and (b) a top-down image of a TBC specimen polished to approximately 5 µm beneath the column tips, marked in (a). The highlighted intercolumnar gap of (b) was modeled using the finite element method approximating a size of 2.8 µm x 2.0 µm, representing a relatively large intercolumnar gap. (c) Calculated concentration profiles along the short dimension of the simulated volume for $D \approx 18 \times 10^{-11}$ m^2/s assuming diffusion-limited dissolution (i.e., the interfaces immediately saturate). (d) Effect of diffusivity on the time for the minimum concentration in the simulated volume to reach 95% of saturation.

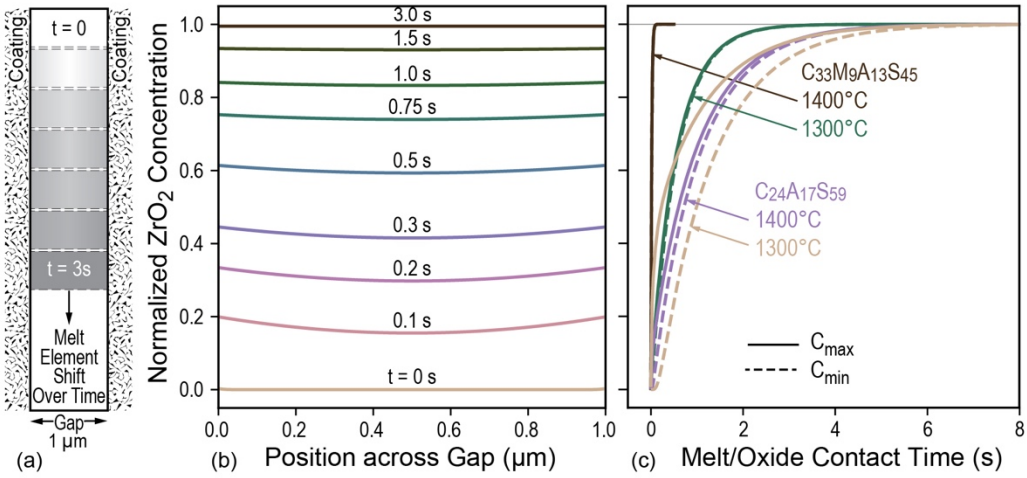

Fig. 6.2: A simple 1D finite element model, shown schematically in (a), to investigate dissolution and diffusion on length scales typical of EB-PVD intercolumnar gaps. Simulated (b) normalized ZrO_2 concentration profiles of 7YSZ dissolution into CMAS at 1300°C (each line represents a different time step in the simulation) show flat concentration profiles; this indicates that the dissolution is primarily limited by the detachment of atoms from the YSZ, not the diffusion of these atoms. The (c) concentration maxima (solid lines) and minima (dashed lines) in the gap plotted as a function of contact time compare the dissolution and diffusion kinetics for CMAS and CAS melts at 1300°C and 1400°C. Notable here is that increasing temperature leads to faster saturation of the melt, despite an increased saturation concentration.

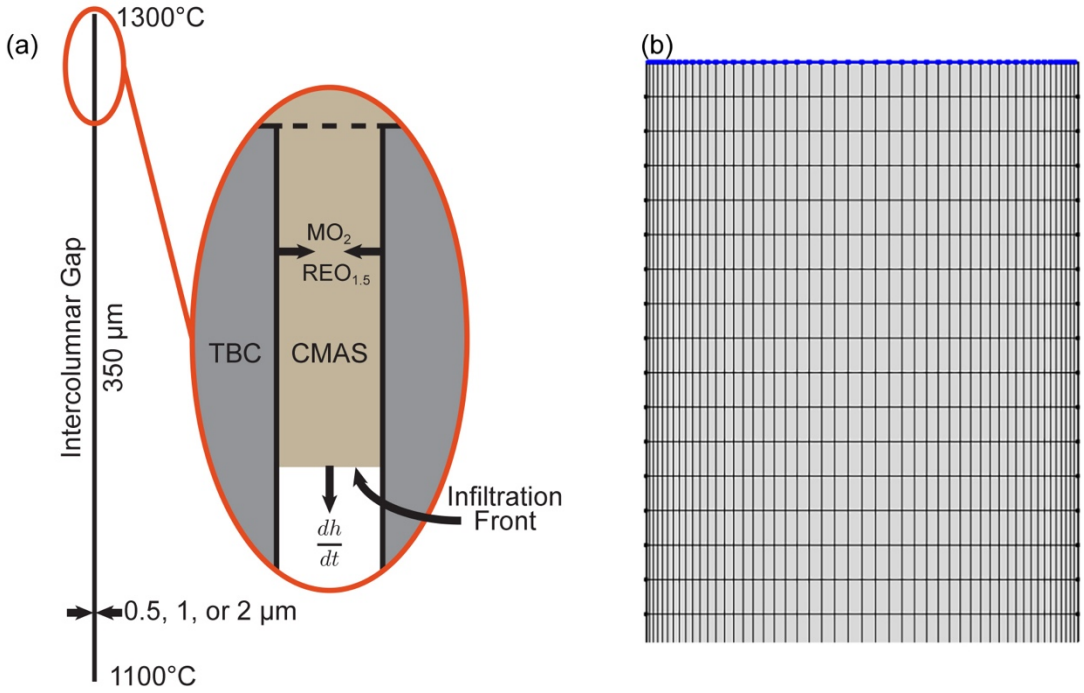

Fig. 6.3: A dissolution, diffusion, and infiltration model was designed to provide context to the calculated saturation times. The geometry (a) was a simplified rectangular intercolumnar gap 0.5, 1, or 2 µm wide and 350 µm tall (representing a 350 µm thick TBC). A 200 °C thermal differential was imposed between the coating surface and bottom. A melt domain was established initially at the top of the model intercolumnar gap in which dissolution and diffusion were modeled. This region used a mapped mesh (b) for higher accuracy near the dissolution front. Infiltration was captured by prescribing a moving boundary velocity *(dh/dt)* to the melt domain boundary.

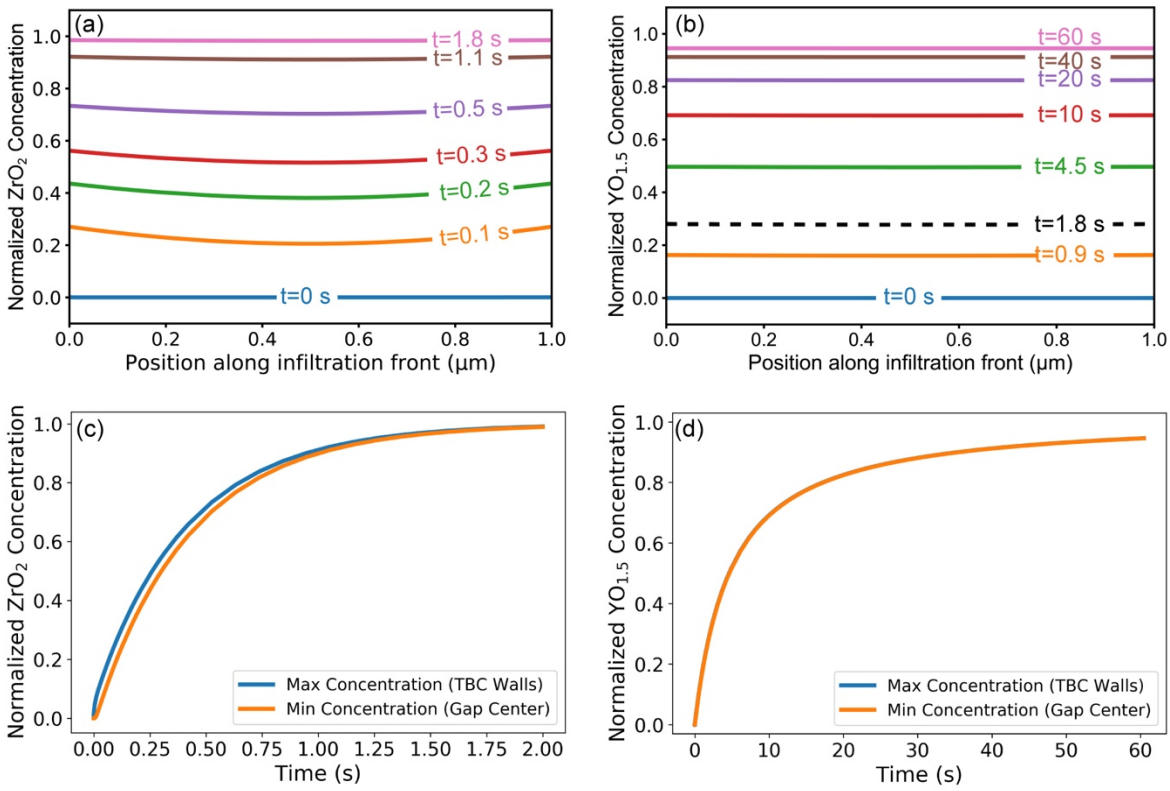

Fig. 6.4: Simulated normalized concentration profiles at the infiltration front for (a) ZrO_2 and (b) $YO_{1.5}$ from the dissolution of 7YSZ for a 1 μm gap width. The flat concentration profiles for each indicate dissolution is primarily limited by the detachment of atoms, not by diffusion. Note the time necessary to saturate the melt in $YO_{1.5}$ is significantly longer than ZrO_2, primarily due to the low $YO_{1.5}$ concentration in the dissolving 7YSZ. (c,d) The time dependence of the concentration maxima (at the dissolution front) and minima (at the gap center) along the infiltration front.

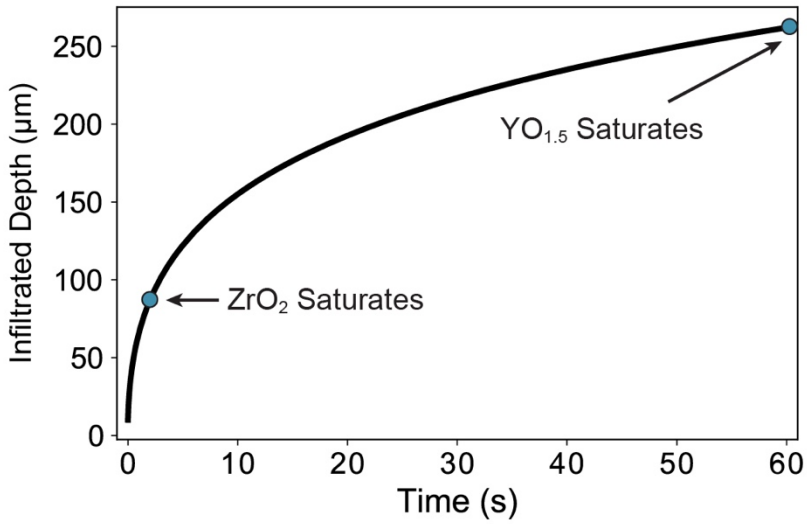

Fig. 6.5: The depth of $C_{33}M_9A_{13}S_{45}$ infiltration into the model TBC geometry (gap width of 1 μm) as a function of time, calculated via integrating Equation 6.2 considering the temperature-dependent (and therefore spatially dependent) viscosity. The infiltrated distance upon ZrO_2 saturation and $YO_{1.5}$ saturation, from Fig. 2.4, are plotted for reference.

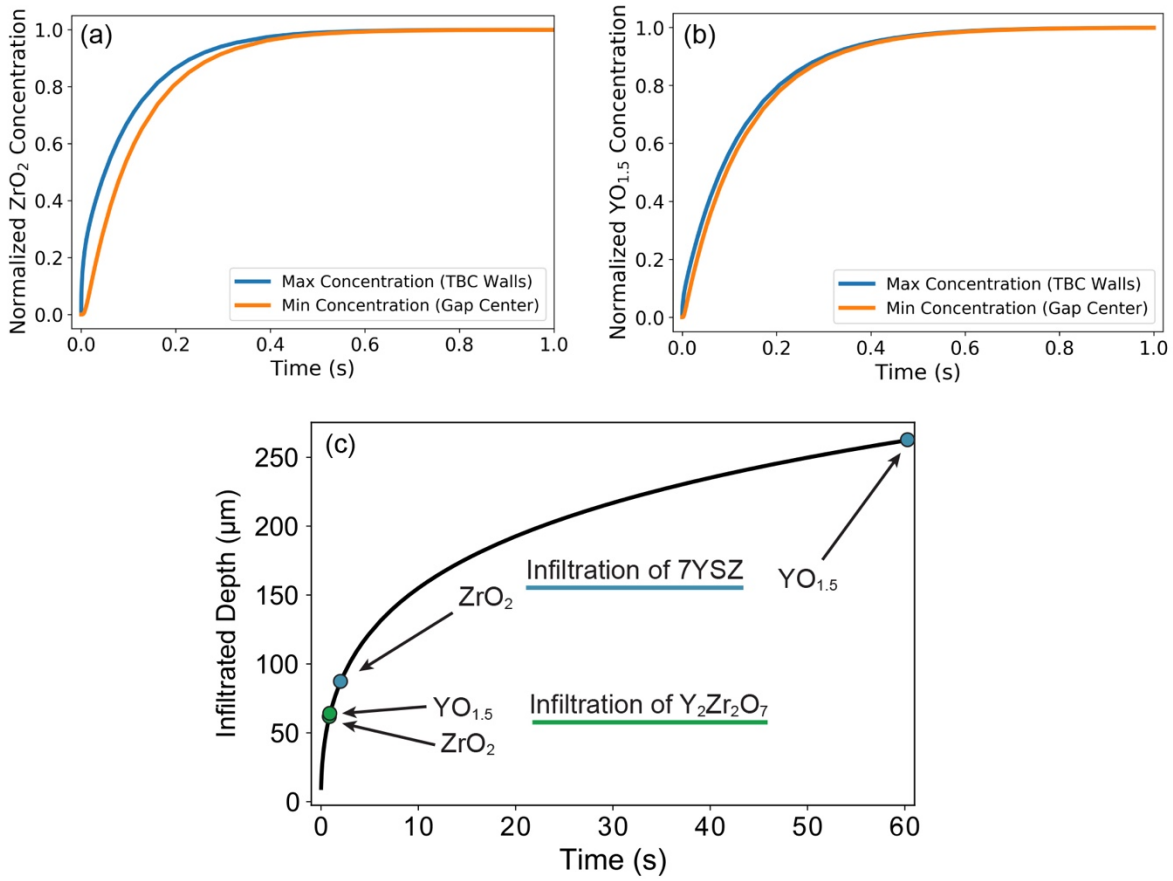

Fig. 6.6: Simulated concentration maxima and minima for (a) ZrO_2 and (b) $YO_{1.5}$ from the dissolution of $Y_2Zr_2O_7$ for a 1 μm gap width. These calculations used diffusivities determined for 7YSZ (e.g., those used in Fig. 2.4) but used the estimated value of u_o from GZO dissolution at 1300 °C (0.8 μm/s, as discussed in Chapter 4). (c) The calculated infiltration depth at saturation for $Y_2Zr_2O_7$ is compared to 7YSZ from Fig. 2.5. The $Y_2Zr_2O_7$ saturates the melt with $YO_{1.5}$ much faster than 7YSZ; also note that ZrO_2 saturates faster despite the lower overall concentration in $Y_2Zr_2O_7$.

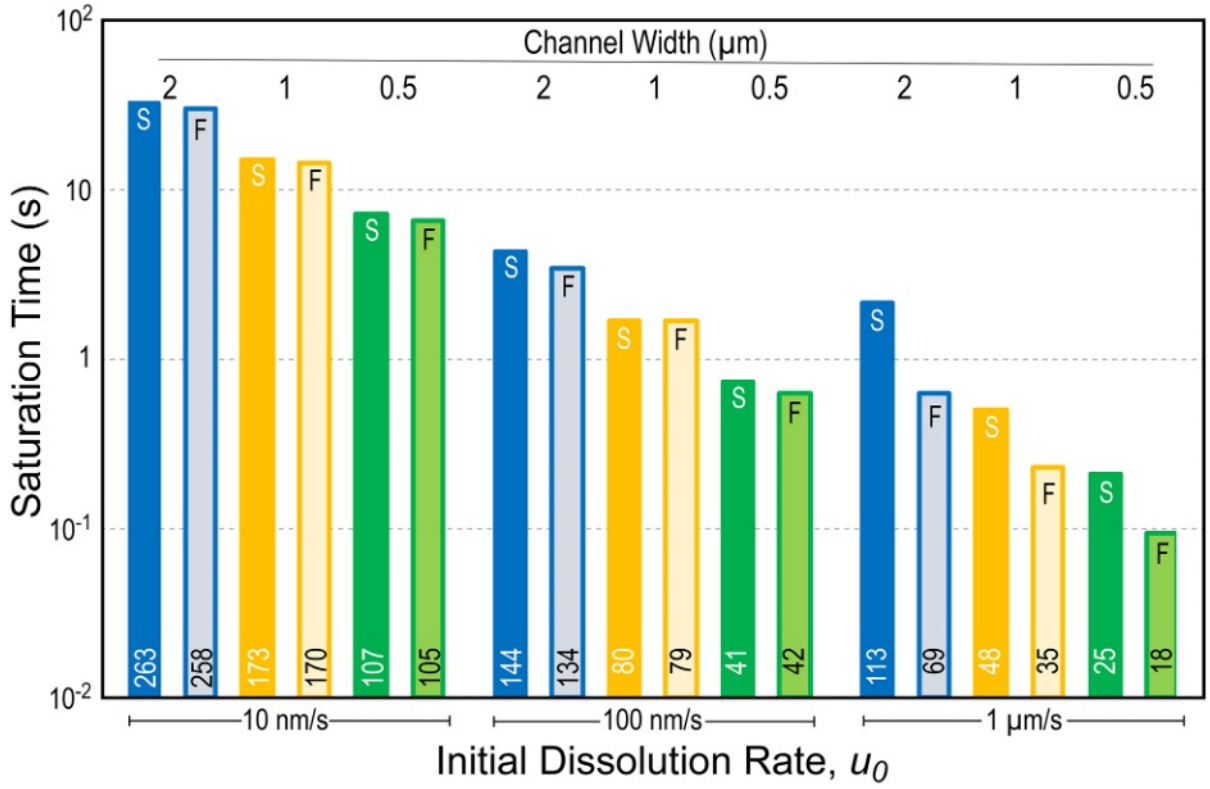

Fig. 6.7: A comparison of saturation times for different combinations of parameters in the simulation of Fig. 2.3, for 3 different channel widths and 3 different initial dissolution rates. S and F represent two extremes of diffusion coefficients derived from the experimental results for 7YSZ, where S is the slower diffusivity representing Zr^{4+} and F is the faster diffusivity representing Y^{3+}. The differences are minimal at the lower dissolution rates, but more significant at the faster interface detachment rates (u_o). The numbers at the bottom of the bars are the calculated infiltration depths for each saturation time.

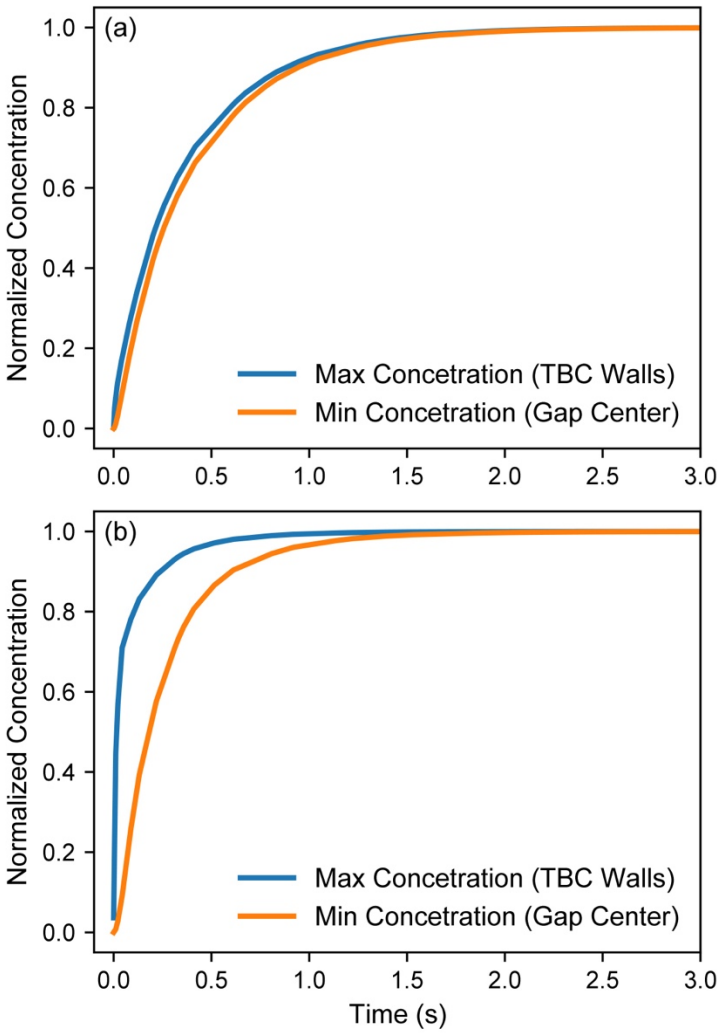

Fig. 6.8: Example concentration maximum and minimum for Zr^{4+} diffusion within (a) the 1 μm gap with u_o=0.1 μm/s and (b) the 2 μm gap with u_o=1 μm/s. The latter shows diffusion limiting melt saturation during the second half of the dissolution period.

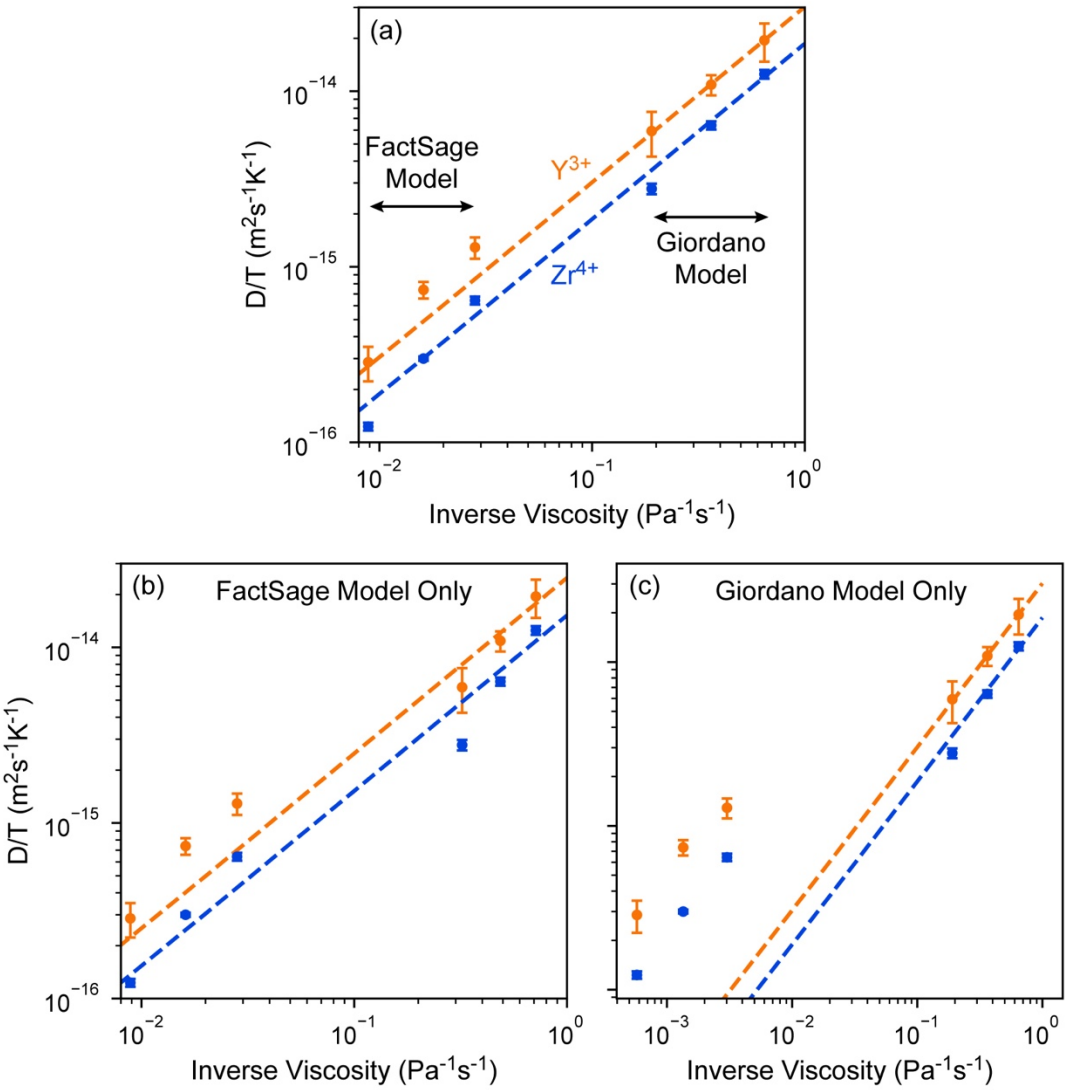

Fig. 6.9: Temperature-normalized Zr^{4+} and Y^{3+} diffusivity (determined from 7YSZ dissolution, Table 4.1) plotted against the inverse melt viscosity (determined using available viscosity models [51,87]). The dashed lines represent the best fit using the Eyring equation (Equation 2.1, using l as a fitting parameter). (a) The best results are obtained when the Giordano model is applied to $C_{33}M_9A_{13}S_{45}$ and the FactSage model is applied to $C_{24}A_{17}S_{59}$. Worse fits are obtained if only (b) the FactSage model or (c) the Giordano model are used. Note the different scale on the abscissa of (c).

CHAPTER 7. EFFECTS OF IRON OXIDE ADDITIONS ON YTTRIUM-GARNET PHASE STABILITY

Much of the work on this dissertation has been limited to Fe-free melts, partly because of the issues arising from the possibility of changing the oxidation state of Fe in the melt. Some issues are related to the experimental set up involving melt containment in a graphite crucible, which can lead to reduction of the Fe. More importantly, however, is the lack of a proper description of important crystalline phases including Fe in the thermodynamic database, notably solid solutions based on yttrium-iron garnets.

Rare-earth garnets are important reaction products between T/EBCs and silicate melts. They feature substantial solubility for cations found in CMFAS (Ca^{2+}, Mg^{2+}, $Fe^{2+/3+}$, Al^{3+}, Si^{4+}) melts as well as T/EBC cations like Y^{3+} [58] and Yb^{3+} [65], and therefore can capture significant melt volume per mole of barrier oxide dissolved. Garnet competes with apatite for many of the same cations but has been shown to crystallize slower than apatite in relevant systems [66]. This would imply decreased CMFAS resistance for the barrier oxide if garnet is preferred over apatite, particularly for segmented thermal barrier coatings (TBCs) where rapid crystallization is essential for arresting melt penetration. The existing thermodynamic databases [169] have not been properly calibrated to predict when garnet might form (relative to experiments) and its composition. While the databases are useful in predicting the phase evolution for most silicate melts, the inadequate thermodynamic description of the garnet phase is particularly relevant for melts rich in aluminum [127] and iron [170], which can promote garnet formation. This chapter systematically probes the thermodynamics of garnet formation in the Y-Ca-Mg-Fe-Al-Si-O system at 1400 °C using sufficiently long reaction times

(≥100 h) to promote equilibration of mixed-powder systems. The results provide insight on how the Fe:Al ratio affects: (i) the solubility limits of Ca^{2+}, Mg^{2+}, and Si^{4+} in yttrium iron/aluminum garnets, (ii) the cation preference for each crystallographic site in the garnets, and (iii) the competition between garnet and other relevant crystalline phases such as apatite, spinel, and olivine.

7.1. Background on the garnet crystal structure

The primary challenge in deriving a thermodynamic description of garnet lies in its complex crystal structure and chemistry, which involves three different cation sites and affords, in principle, a broad range of cation substitutions. The garnet structure is cubic with a characteristic stoichiometry $A_3B_2T_3O_{12}$, Fig. 7.1. Neither the cation nor the anion sublattices readily accommodate vacancies; the latter contains 12 oxygen ions per unit formula and therefore constrains the stoichiometry of the cation sublattice such that charge neutrality is maintained. The cation sites A, B, and T correspond to different oxygen polyhedra, where A is a dodecahedral site (coordination number CN=8), B is an octahedral site (CN=6), and T is a tetrahedral site (CN=4). The sites vary in size significantly and therefore can accept a variety of cations across the periodic table largely dependent on their ionic radii. This study focuses on those elements relevant to model silicate melts within the aforementioned Y-Ca-Mg-Fe-Al-Si-O (Y-CMFAS) space. These elements exist in both natural (geologic) and synthetic (technical) garnets.

Natural garnets are often alkaline-earth silicates that form at elevated (geological) pressures—examples endmembers[a] relevant to CMFAS are pyrope ($Mg_3Al_2Si_3O_{12}$), grossular ($Ca_3Al_2Si_3O_{12}$),

[a] Referred as the basis for a series, e.g., pyrope and grossular are the endmembers of a series formed by substitution of Ca^{2+} for Mg^{2+} or vice-versa.

and andradite ($Ca_3Fe_2Si_3O_{12}$). The dual oxidation state of iron enables further, non-alkaline-earth, variations of garnet, e.g., almandine ($Fe_3Al_2Si_3O_{12}$) where all iron is present as Fe^{2+}. The endmembers may show large, if not complete, solid solubilities with each other via particular substitutions; for example, an almandine-pyrope series exists by substituting Fe^{2+} with Mg^{2+}. Importantly, there is no evidence of these endmembers or their solid solutions at ambient pressure—reflected in the absence of CMFAS garnets in typical phase diagrams at ambient pressure [136,138,171–173]. Even at geological pressures, some endmembers elude observation. A notable example is $Mg_3Fe_2Si_3O_{12}$ (iron as Fe^{3+}), which was hypothesized in 1938 (and named khoharite) but has not appeared in natural garnets and has yet to be created synthetically [174]. In this case, one would expect a series between andradite and khoharite to show only limited solubility even at extreme pressures (>10,000 atm).

The more common synthetic garnets, namely $Y_3Al_5O_{12}$ (YAG) and $Y_3Fe_5O_{12}$ (YIG), are readily synthesized at ambient pressures and appear in the respective phase diagrams [122,123]. Here, Y^{3+} occupies the dodecahedral site, whereas Al^{3+}/Fe^{3+} occupy both the octahedral and tetrahedral sites. Research into these materials is extensive but focuses on applications other than gas turbine engines. Rare-earth doped YAG produces active laser media or phosphors [175,176], perhaps most notably as Nd:YAG [177,178]. YIG is a ferrimagnetic material with applications as a microwave filter and an attenuator [179]. Like many of the natural garnets, YIG and YAG are fully miscible, i.e., one can create a YAG-YIG series wherein Al^{3+} is fully interchangeable for Fe^{3+} [180].

The literature suggests that the natural garnets are partially soluble in YIG/YAG. For example, the garnet endmember menzerite, $(Y_2Ca)(Mg_2)(Si_3)O_{12}$, provides evidence for a stable Y-CMS garnet [181]. Moreover, chemically complex garnets have been observed as a reaction product between

barrier oxides and molten silicates, indicating that there is indeed a range of solid solubility between YIG/YAG and the natural garnets. For example, Poerschke et al. noted garnet as an equilibrium product in the reaction between $YO_{1.5}$ and $C_{33}M_9A_{13}S_{45}$ [58]. Naraparaju et al. observed its formation in exposures of ZrO_2-65 wt% Y_2O_3 to Icelandic volcanic ash, which contained both iron and aluminum [125]. However, no prior studies have systematically investigated the mutual solubility limits of YIG/YAG with the natural garnets such as pyrope, grossular, andradite, and the hypothetical khoharite. (The mutual solubility of YAG with pyrope and grossular was investigated by Godbole et al. [127] as a part of a sister study undertaken simultaneously to this study, which focuses on YIG and mixed YIG/YAG. However, YIG/YAG should show limited solubility of the natural garnets presumably because the latter are not thermodynamically stable at ambient pressures.[b] That is, Ca^{2+}, Mg^{2+}, Fe^{2+}, and Si^{4+} should show only partial solubility into YIG or YAG at ambient pressures.

For a systematic analysis of the solubilities of Ca^{2+}, Mg^{2+}, and Si^{4+} into YIG and YAG, it is necessary to understand which sites each cation may occupy in the garnet structure. The summary of this is presented in Table 7.1, which was derived based on consideration of cation size; comparison to the site occupancy of natural garnets, YIG, and YAG; and on Pauling's rules. The conclusion was that Y^{3+} and Ca^{2+} can only occupy the dodecahedral site; likewise, Si^{4+} ions occupy only the tetrahedral sites. Natural garnets indicate Mg^{2+} ions can occupy both the dodecahedral and octahedral sites. Fe^{3+} and Al^{3+} can be located in both the octahedral and tetrahedral sites, but not the dodecahedral site.

[b] While gas turbine engines operate at high pressures, typically ~1–50 atm, the lab synthesis of natural garnets requires orders of magnitude higher pressures, typically >10,000 atm [182]. Therefore, gas turbine engines will be assumed as having pressures equivalent to ambient for the purpose of this chapter.

Ferrous iron (Fe^{2+}) shows the most complex behavior—it has been observed in all three cation sites [183]. In practice Fe^{2+} is most often found in the dodecahedral site (e.g., almandine [184]) and very rarely observed in the tetrahedral site. However, some dual occupation in the dodecahedral and octahedral sites can be expected [185,186]. Therefore, iron can occupy all three garnet cation sites depending on its oxidation state. As there is no strong evidence for vacancies on the oxygen sublattice, it is assumed that cation substitutions must be either isovalent or involve a coupled substitution to maintain charge neutrality; for example, the substitution of Ca^{2+} for Y^{3+} in the YIG dodecahedral site would be coupled with a substitution of Si^{4+} for Fe^{3+} in the tetrahedral site.

These site occupation rules allow a constrained composition space to be constructed. Substitution in the YAG-pyrope-grossular series and the YIG-khoharite-andradite series are shown in Fig. 7.2(a), respectively. The constraint of no oxygen vacancies limits the valid composition space to the plane highlighted between each corner, which is shown in Fig. 7.2(b). These Gibbs triangles capture all possible substitutions of Ca^{2+} and Mg^{2+} in the dodecahedral sites and coupled substitution of Si^{4+} into the tetrahedral sites. The compositional variables x and y can be assigned to the number of Ca^{2+} and Mg^{2+} ions in the dodecahedral site, respectively, per formula unit. Thus, YAG and YIG can be represented by the coordinates (x,y)=(0,0), pyrope and khoharite by (3,0), and grossular and andradite by (0,3), Fig. 7.2(b). For simplicity, dodecahedral Fe^{2+} is not represented in Fig. 7.2 but will be similarly assigned the compositional variable v.[c] Additional compositional variables, z and w, can represent the substitution of Mg^{2+} or Fe^{2+} ions, respectively, for Fe^{3+} or Al^{3+} in the octahedral site; note $0 \leq z,w \leq 2$ as there are two octahedral sites per formula unit. The total extent of Ca^{2+}, Mg^{2+}, and

[c] The data will later show that the concentration of Fe^{2+} in the synthesized garnets is generally low.

Fe^{2+} (if applicable) substitution is constrained by the three available tetrahedral sites for Si^{4+} charge compensation, i.e., $x+y+z+v+w \leq 3$. Therefore, Mg^{2+} or Fe^{2+} substitution in the octahedral site (e.g., $z,w \neq 0$) limits the allowed values of x and y, as depicted in Fig. 7.2(c). The latter represents the full theoretical range of garnet solid solution in the Y-CMAS system and the Y-CMFS system excluding Fe^{2+}, which would require additional dimensions.

These composition variables allow the definition of a general formula for yttrium iron/aluminum garnets. The simplest case is for the iron-free ($v=w=0$) Y-CMAS garnet, which can be written as:

$$[Y_{(3-x-y)}Ca_xMg_y][Al_{(2-z)}Mg_z][Al_{(3-x-y-z)}Si_{(x+y+z)}]O_{12} \quad (7.1)$$

The addition of iron complicates the formula, but it follows the same general pattern, namely:

$$[Y_{(3-x-y-v)}Ca_xMg_yFe^{2+}{}_v][Fe^{3+}{}_{(2-z-w)}Mg_zFe^{2+}{}_w][Fe^{3+}{}_{(3-x-y-z-v-w)}Si_{(x+y+z+v+w)})O_{12} \quad (7.2)$$

where composition variables v and w represent Fe^{2+}. A general equation for garnets in the Y-CMFAS system can also be written but is complicated by the uncertainty of Al^{3+} and Fe^{3+} partitioning between the octahedral and tetrahedral sites. For a mixed YIG-YAG composition, the general formula for the garnet is:

$$[Y_{(3-x-y-v)}Ca_xMg_yFe^{2+}{}_v][(Fe,Al)_{(2-z-w)}Mg_zFe^{2+}{}_w][(Al,Fe)_{(3-x-y-z-v-w)}Si_{(x+y+z+v+w)}]O_{12} \quad (7.3)$$

where Al^{3+} is assumed to preferably fill the tetrahedral site but can overflow to the octahedral site if the sum of Al^{3+} and Si^{4+} exceeds 3 atoms per formula unit (apfu). Conversely, if the concentration of Al^{3+} and Si^{4+} does not reach 3 apfu, the remainder of the site can be filled by Fe^{3+}.

The garnet framework of Fig. 7.2(c) and of Equations 7.1–7.3 enable this study to address the following questions regarding the solubility of CMFAS cations into YIG/YAG:

(i) What are the maximum solubilities of Ca^{2+}, Mg^{2+}, Si^{4+}, and Fe^{2+} (if applicable) in yttrium garnets?

(ii) What is the feasible extent of Ca^{2+}, Mg^{2+}, and Fe^{2+} (if applicable) substitution in the dodecahedral site?

(iii) Given that Mg^{2+} and Fe^{2+} can occupy both the dodecahedral and octahedral sites, how do they each partition between the sites?

(iv) How does the relative stability and fraction of the garnet phase change with respect to other crystalline phases and the liquid at 1400 °C?

The above questions were addressed in a collaborative study between UC Santa Barbara (UCSB) and the University of Minnesota (UMN) to understand garnet formation in the YIG/YAG-CMFAS systems. The approach was divided into three different based systems, namely (i) YAG (Y-CMAS), (ii) YIG (Y-CMFS), and (iii) mixed Y(3A:I)G (Y-CMFAS) wherein the Al:Fe ratio was 3, set to mimic typical ratios of iron oxide and aluminum oxide found in representative silicate melts [187]. Results for the YAG system, wherein all cations have a single oxidation state, [d] were recently published by Godbole et al. [127] and served to guide experiments for the more complicated iron-containing systems—YIG and Y(3A:I)G—investigated here.

The core theme of this chapter is how the Fe:Al ratio of the nominal system affects the questions posed above in the context of the published YAG results cited.

[d] In addition to garnet, other relevant silicate phases are complicated by the multiple oxidation states of iron. For example, the spinel phase has a nominal composition of $MgAl_2O_4$, wherein Fe^{2+} can substitute for Mg^{2+} and Fe^{3+} can substitute for Al^{3+}.

7.2. Experimental Methods

7.2.1. Synthesis and heat treatment

Compositions representing theoretically possible garnets were synthesized following Equations 7.1–7.3. Namely, each nominal composition can be represented by a combination of x, y, and z which were systematically varied to capture the relevant compositional space shown in Fig. 7.2(c).[e] The compositions synthesized within the Y-CMFS and Y-CMFAS systems are shown in Table 7.2. Nominal compositions were limited to $x+y+z \leq 2$ as previous work on the YAG system had shown garnet was often unstable beyond those bounds [127].

Each nominal composition was synthesized using reverse co-precipitation (described in detail in Chapter 3). Specifically, for this work, precursor solutions of tetra-ethyl ortho-silicate (TEOS 98% purity, Acros Organics), high purity nitrates of calcium, magnesium, aluminum, yttrium, and iron (all with ≥99.9% purity, Alfa Aesar) were prepared in 200 proof ethanol. The precursor solutions were then calibrated to determine the precise concentrations and oxide yields. These precursor solutions were added dropwise to solutions containing excess ammonium hydroxide, maintaining the pH ≥ 10, to precipitate mixed metal hydroxides. For the compositions containing calcium, ammonium carbonate (Acros Organics) was also added to precipitate hydroxide-carbonate mixtures. The precipitates were then separated, dried and calcined between 600 °C and 1000 °C (depending on the specific composition) to produce oxides.

[e] Compositions were synthesized assuming all Fe as Fe^{3+}, i.e., $v=w=0$. Iron reduction occurred on heat treatment often resulting in $v \neq w \neq 0$.

Powders were pressed into 6 mm diameter pellets and equilibrated at 1400 °C. Most compositions partially melt at this temperature and samples had to be placed in platinum foil boats contained within covered alumina crucibles for the heat treatment. In some cases, the melt climbed out of the Pt-foil boat containing them, leading to segregation which hindered proper analysis. These problematic samples were placed within a Pt-wire coil, depicted in Fig. 7.3, which provided proper containment. Comparative studies varying the heat treatment time revealed 100 h was sufficient to reach equilibrium. All samples were quenched under flowing air to ensure the ex-situ observed microstructure was representative of the heat treatment temperature.

7.2.2. Characterization

Each equilibrated sample was bisected for phase analysis using X-ray diffraction (XRD) and electron microscopy. The XRD portion was crushed in a mortar and pestle for powder diffraction using a Panalytical Empyrean diffractometer with a Cu-Kα source. Scans were performed over the range $10° \leq 2\theta \leq 75°$. Samples for electron microscopy were mounted in epoxy and polished to 0.25 μm for backscattered electron imaging in a scanning electron microscope (SEM, ThermoFisher Scientific, Apreo-C). Chemical analysis was collected semi-quantitatively using electron dispersive spectroscopy (EDS) and fully quantitatively using electron probe microanalysis (EPMA, Cameca SX-100) equipped with wavelength dispersive spectroscopy (WDS). The EPMA-WDS analysis was generally of higher quality and leveraged geologic standards to calibrate the signal from the unknown samples. Multiple (~5–10) spots scans were averaged for each phase in each sample. Beam conditions were 15 kV at 10 nA.

In limited cases a definitive phase identification could not be made owing to a combination of (*i*) small phase fractions yielding low XRD peak intensities, (*ii*) multiple overlapping XRD peaks, particularly common in the silicate phases, affording no high-intensity reflections that could definitively be used for identification, or (*iii*) grain sizes smaller than ~1 μm, which is below typical interaction volumes in SEM-EDS and EPMA-WDS. While these issues could be overcome by increasingly sophisticated techniques (e.g., transmission electron microscopy, TEM, diffraction and EDS), it was generally preferred to gather data for a larger number of samples rather than focusing on a more extensive analysis for fewer samples. In a few critical cases, however, TEM diffraction and EDS data were collected (ThermoFisher Scientific Talos G2 200X TEM/STEM equipped with ChemiSTEM). Suitable lamellae were extracted using a focused ion beam (FEI Helios Dualbeam Nanolab 650).

7.2.3. Garnet site assignment

The site occupancies of each equilibrium garnet were estimated using the chemical analysis data, Table 7.3, to shed light on the partitioning preference of the cations. This assignment affords an understanding of, for example, whether Mg^{2+} ions have a preference between the dodecahedral and octahedral sites. The allowed sites for each cation are summarized in Table 7.1 and the relevant garnet formulae were given in Equations 7.1–7.3.

(i) The chemical analysis data was converted from single cation mole percent units into the number of atoms per formula unit (apfu) for garnet to fit 8 cation sites.

(ii) The necessary Fe^{2+} concentration to maintain charge balance—assuming no vacancies or interstitials, as supported by Godbole et al. [127]—was determined by:

$$[Fe^{2+}] = [Si^{4+}] - [Ca^{2+}] - [Mg^{2+}] \quad (7.4)$$

(iii) Cations that can only occupy one site were assigned to that site, viz. all Si^{4+} was assigned to the tetrahedral site and all Y^{3+} and Ca^{2+} to the dodecahedral site.

(iv) The remaining space in the tetrahedral site was filled with Al^{3+} and/or Fe^{3+}; if the sample contained both Fe^{3+} and Al^{3+}, the latter was assumed to fill the tetrahedral site first.[f] Any excess Fe^{3+} and/or Al^{3+} (if applicable) was accommodated into the octahedral site.

(v) Mg^{2+} fills the remainder of the octahedral site, then overflows to the dodecahedral site (if applicable); if there were insufficient Mg^{2+} to fill the octahedral site, the remainder is filled by Fe^{2+}.

(vi) The remaining Fe^{2+} fills the dodecahedral site. The core assumption is that Mg^{2+} fills the octahedral site before Fe^{2+}, which is consistent with the consensus from the geologic literature [183].

This procedure allows for two cross-checks. First, charge balance provides a check that the composition is correct; the Fe^{2+} calculated by Equation 7.4 above should not be negative. Second, the dodecahedral site is not "forced" to be full by the above procedure. Therefore, the sum of Y^{3+}, Ca^{2+}, Mg^{2+}, and Fe^{2+} in the dodecahedral site can be checked to ensure the site contains ~3 apfu. The site assignment procedure worked well, with errors in the assigned formula typically <1% (e.g., the sum of cations in the dodecahedral site may add up to 2.99 rather than 3).

[f] This assumption is supported by some literature that suggests Al prefers the tetrahedral site [183], but the key questions sought by this work can be addressed regardless of Al and Fe preference between the octahedral and tetrahedral site.

7.3. Results

The cumulative evidence from XRD, electron microscopy, and quantitative microchemical analysis informed phase identification in each sample investigated. The phases identified are summarized in Table 7.2, the composition of the equilibrium garnets are listed in Table 7.3, and the cations were assigned to sites in Table 7.4 following the procedure of section 7.2.3 above. The nominal compositions that formed garnet in the YAG system [127], namely those with $x+y+z \leq 2$, also formed garnet in the Y(3A:I)G and YIG systems—the only exception was for YIG(020), which did not form an equilibrium garnet. However, the solubility patterns of Ca^{2+}, Mg^{2+}, and Fe^{2+} in garnet were relatively different from what had been previously observed in the YAG system. Secondary phases were also affected by increasing iron in response to the overall thermodynamics of the system, which might, for example, result in changes to the spinel composition (the $MgAl_2O_4$ spinel phase accepts both Fe^{2+} and Fe^{3+}). Liquid was present in most samples at temperature (amorphous in solidified samples), but spinel, apatite, and yttrium monosilicate were also frequently observed. The results will first focus on the observed trends in garnet composition as the Fe:Al ratio of the as-synthesized compositions increases, then results on the secondary phases will be briefly elaborated.

7.3.1. Ferric iron and aluminum in garnet

The concentration of ferric iron (Fe^{3+}) or aluminum in the equilibrium garnet provides insight on any preference for one cation over the other within the octahedral or tetrahedral sites. Fig. 7.4 plots the concentration of Al^{3+} vs. Fe^{3+} in the equilibrium garnets for all three systems (for the data given in Table 7.3 and Table 7.4). The concentration of Fe^{3+} in YIG and Al^{3+} in YAG has a maximum of 5 apfu (representing full occupancy of the octahedral and tetrahedral sites). As substitutional cations

are added, the amount of Fe^{3+} in YIG decreases to an observed minimum of 1.59 apfu (31.8% of available sites or 19.9% of all cations); the amount of Al^{3+} in YAG decreases to an observed minimum of 1.14 apfu (22.8% of available sites or 14.2% of all cations). In the Y(3A:I)G system, Fe^{3+} and Al^{3+} will both occupy up to 5 apfu between the octahedral site and tetrahedral site, with Al^{3+} preferring the latter. The minimum observed concentration of Fe^{3+}+Al^{3+} in this system was 1.03 apfu (20.6% of available sites or 12.9% of all cations). A key observation is that the equilibrium garnets in the Y(3A:I)G system retain a Al:Fe ratio of ~2.93 (the slope of the best fit line in Fig. 7.4), which is close to the nominal 3:1 ratio. This suggests neither Fe^{3+} or Al^{3+} are preferentially rejected from the garnet structure at 1400 °C.

7.3.2. Concentration of Fe^{2+} in the equilibrium garnets

Ferrous iron (Fe^{2+}) was observed throughout garnets of the YIG and Y(3A:I)G systems, Table 7.4. The concentration of Fe^{2+} followed two key dependencies, depicted in Fig. 7.5. First, the concentration of Fe^{2+} typically increased with the Fe^{3+} concentration in the equilibrium garnet—there was more Fe^{2+} in the YIG system than the Y(3A:I)G system and, within each system, the Fe^{2+} concentration increased with decreasing concentrations of Ca^{2+} *and* Mg^{2+}. Second, the Fe^{2+} concentration was sensitive to the type of alkali earth in the garnet. Ca-free (i.e., Mg-only, x=0) garnets contain the highest concentration of Fe^{2+}, typically 1–5%. Conversely, Ca-only garnets contain very little (often no) Fe^{2+} and the latter was therefore independent of the Fe^{3+} concentration in the garnet. The important implication is that the Fe^{2+} may be present in significant quantities in another phase. Garnets containing both Ca and Mg contain an intermediate amount of Fe^{2+}, 0.4–1.2%, but the concentration was again dependent on the Fe^{3+} concentration. The Fe^{2+} largely

occupied the dodecahedral site and rarely occupied the octahedral site at all, Table 7.4. A small amount of octahedral occupancy is necessary in some samples, e.g., YIG(010), to maintain charge balance and to respect the three apfu occupancy limit of the dodecahedral site.

7.3.3. Garnet stability in Ca-free samples

The Ca-free (x=0) samples provide insight into how Mg^{2+} and Fe^{2+} partition between the dodecahedral and octahedral site and the stability of both cations in iron-containing garnets. The Ca-free plane of Fig. 7.2(c) is shown in Fig. 7.6; the vertical axis represents the occupancy of Mg^{2+} and Fe^{2+} in the octahedral site (i.e., z and *w in Equations 7.1–7.3*) and the horizontal axis represents the occupancy of Mg^{2+} and Fe^{2+} in the dodecahedral site (i.e., y and *v in Equations 7.1–7.3*). The bulk (nominal) concentration of Mg^{2+} in each site is plotted as black dots for each sample. However, the equilibrium garnet—which forms alongside other phases that compete for Mg^{2+}—most often contains different amounts of Mg^{2+} in the dodecahedral or octahedral site. Therefore, the grey, green, and purple points represent the actual measured composition of the equilibrium garnets formed in the YAG, Y(3A:I)G, and YIG systems, respectively. The shift between the nominal composition and the equilibrium composition of the garnet is illustrated with arrows connecting the points. To facilitate comparison to the iron-free YAG system (with w=v=0), the data is plotted in two ways: circles represent the concentration of only Mg^{2+} in each site and squares represent the concentration of Mg^{2+}+Fe^{2+} in each site.

In the pure YAG system (grey circles in Fig. 7.6), Godbole et al. observed that Mg^{2+} generally preferred to be in the octahedral site over the dodecahedral site [127], which is captured by the leftwards and upwards shift in Fig. 7.6. This was especially true for nominal compositions with a high

occupancy in the dodecahedral site. For example, the sample YAG(020) has a nominal composition of $(YMg_2)(Al_2)(AlSi_2)O_{12}$, i.e., it would be intended to have 2 Mg^{2+} apfu in the dodecahedral site. Upon equilibration, the measured garnet composition was $(Y_{2.26}Mg_{0.74})(Al_{1.26}Mg_{0.74})(Al_{1.54}Si_{1.46})O_{12}$ indicating that, of the 2 apfu intended for the dodecahedral site, 0.74 apfu stays, 0.74 goes to the octahedral site, and 0.52 apfu goes to secondary crystalline phases and/or the melt. Conversely, samples where Mg^{2+} was intended in the octahedral site by substituting for Al^{3+} (e.g., 002) showed minimal redistribution between the nominal and equilibrium compositions and effectively no Mg^{2+} entered the dodecahedral site. The implication was the substitution of Mg^{2+} for Y^{3+} in the dodecahedral site is unfavorable in comparison to substitution for Al^{3+} in the octahedral site. Creating a bounding polygon around the grey circles (and additional data not shown in Fig. 7.6 for clarity) highlights the extent of the garnet phase for Mg^{2+} substitution in the YAG system, represented by the grey field within Fig. 7.6.

The trends described above for Mg^{2+} are exaggerated as the Fe:Al ratio increases from YAG to Y(3A:I)G to YIG. Nominal compositions with z=0 showed a more significant redistribution of Mg^{2+} from the dodecahedral site to the octahedral site. For example, the (010) samples had 1 apfu intended for the dodecahedral site (of the 3 dodecahedral apfu); however, the equilibrium garnets showed dodecahedral Mg^{2+} occupation of ~0.54 apfu, ~0.40 apfu, and ~0 apfu for the YAG, Y(3A:I)G, and YIG systems, respectively. Notably, garnet was found to be absent altogether for YIG(020), which formed only spinel and melt. Considering Mg^{2+} alone (circles in Fig. 7.6), the bounding polygon defined by the purple (YIG) and green (Y(3A:I)G) points falls within that defined by the grey (YAG) system, indicating a narrower extent of Mg^{2+} solubility within the Fe-containing garnets. Considering

the concentration of both Mg^{2+} and Fe^{2+} (squares in Fig. 7.6) recovers a significant portion of the stability field observed for the YAG system. Using YIG(010) as an example again, although the sample contains 0 apfu of Mg^{2+} in the dodecahedral site, the site contains ~0.33 apfu of Fe^{2+}. Furthermore, ferrous iron occupied the dodecahedral site even in cases with minimal Mg^{2+} redistribution. YIG(001), for example, showed minimal difference in Mg^{2+} between the nominal and equilibrium garnet compositions, but the latter contained ~0.34 apfu of Fe^{2+}.

Because the decreased Mg^{2+} solubility in the dodecahedral site is met with a concomitant increase in octahedral solubility, the overall Mg^{2+} solubility is only weakly dependent on the Fe:Al ratio. The maximum solubility of Mg^{2+} observed in the new iron-containing garnets was ~1.94 apfu (of a possible 3 apfu), found in the sample Y(3A:I)G(002).[g] This is comparable to the value observed in the YAG(002) sample, ~1.95 apfu, and a few percent smaller than the maximum observed in the Al system, ~2.16 apfu, which occurred for the YAG(0,0.5,2) sample (not investigated in the iron-containing systems). Note, however, that the solubility of Si^{4+} in the iron-containing systems was elevated relative to the iron-free system due to the additional solubility of Fe^{2+} in the former.

7.3.4. Garnet stability in Ca-containing samples

Observations in Mg-free samples

The Ca-containing (x>0) samples showed increased Ca and Si solubility in garnet as the Fe:Al ratio increased, i.e., the equilibrium garnet compositions in the YIG and Y(3A:I)G were closer to the

[g] Unfortunately, the measured YIG(002) composition did not charge balance, which is attributed to some error with the electron microscope. The total Mg^{2+} concentration was measured to be ~24 mol%, roughly comparable to the other systems.

nominal composition than those in the YAG system. The Ca-only (y=z=0) garnet composition shift upon equilibrating is shown in Fig. 7.7, which requires only one dimension as Ca^{2+} can only occupy the dodecahedral site. In the YAG system, effectively equivalent amounts of Ca^{2+} were measured—~0.88 apfu of the 3 dodecahedral apfu—in the (1.5,0,0) and (200) equilibrium garnets indicating the maximum solubility of Ca^{2+} was reached. This solubility limit was readily surpassed in Y(3A:I)G and YIG systems. The maximum observed Ca^{2+} concentration occurred for the YIG(200) sample, which contained ~1.42 apfu. The YAG solubility limit was even exceeded by (100) compositions in the YIG and Y(3A:I)G systems, despite having only half the nominal Ca^{2+}. As the samples are free of Mg^{2+} and contain negligible or no Fe^{2+} (Fig. 7.5) the concentration of Si^{4+} was approximately equivalent to Ca^{2+}.

The key implication is that Ca-based garnets are more stable in the iron-systems, which subsequently decreases the number of secondary phases and their quantity, Fig. 7.7. Garnet is the primary phase in (100) for all three systems, but the YAG system contains substantial amounts of apatite and anorthite. (Notably, no glass was observed in the quenched sample, suggesting that any melt formed during the heat treatment was transient.) The Y(3A:I)G system showed an increased quantity of garnet, suggesting its increased stability, and apatite quantity was substantially reduced; furthermore, anorthite was absent but glass was observed instead. The YIG system shows garnet as the primary phase, with a porous, fibrous, secondary phase that remains unidentified, but is inconsistent with apatite.[h] At (200), the YAG system showed only garnet and glass. The YIG system, comparatively,

[h] The phase was not present in sufficient quantities to appear in XRD, and the phase's porosity precludes a quantitative chemical analysis. SEM-EDS suggests, *qualitatively*, that the phase is depleted in Y and Si, and enriched in Ca and Fe relative to the nominal composition.

consisted of more garnet and the unknown secondary phase. Given the minimal incorporation of Fe^{2+} into the Ca-only garnets (Fig. 7.5), the secondary phase is presumed to be rich in Fe^{2+}.

Observations in samples containing both Ca^{2+} and Mg^{2+}

In the presence of both Ca^{2+} and Mg^{2+}, the same trends with increasing Fe:Al ratio elaborated above hold; namely, increased solubility of Ca^{2+} and Si^{4+}, and stronger preference of Mg^{2+} for the octahedral site. The composition of (101) and (110) garnets are plotted as a bar chart in Fig. 7.8 for each system studied. The intended (i.e., nominal or baseline) composition, representing the garnet formula above the bar chart, is shown in the black bars. The grey, green, and purple bars represent the measured composition of the equilibrium garnet for the YAG, Y(3A:I)G, and YIG systems, respectively.

The concentration of Y^{3+}, Fe^{3+} and Al^{3+}, Ca^{2+}, and Si^{4+} in the equilibrium garnets approached the nominal concentration as the Fe:Al ratio of the system increased. However, Mg^{2+} was more strongly favored in the octahedral site relative to the dodecahedral site as the Fe:Al ratio increased; the implication is that increasing Fe:Al ratio could lead to a shift of Mg^{2+} away from the nominal composition if Mg^{2+} was intended for the dodecahedral site. The latter point is best illustrated with the (110) samples. Whereas the YAG system retained 0.28 Mg^{2+} apfu in the dodecahedral site, the YIG system retained only 0.04 Mg^{2+} apfu. (This preference for Mg^{2+} in the octahedral site caused an enrichment of Y^{3+} in the dodecahedral site relative to the nominal composition, but this enrichment was also smallest for the YIG system—the latter retained much of its Ca^{2+} and had a small amount of Fe^{2+}.) The (101) samples, conversely, experienced minimal Mg^{2+} redistribution, especially for iron-containing samples, as the Mg^{2+} was intended for the more favorable octahedral site. Whereas the YAG system saw 0.21 Mg^{2+} apfu redistribute to the dodecahedral site, the Y(3A:I)G system saw 0.07

apfu and the YIG system had *no* Mg^{2+} redistribute to the dodecahedral site; this was observed concurrently with increasing Ca^{2+} solubilities, from 0.62 (YAG) to 0.7 to 0.98 (YIG) apfu. The result was the YIG(101) equilibrium garnet was nearly identical to the nominal composition. Thus, yttrium iron/aluminum garnets prefer Ca^{2+} over Mg^{2+} in the dodecahedral site; this preference strengthens with increasing Fe:Al of the system.

The microstructural evolution of (101) samples showed similar trends to the Ca-only samples, namely a clear trend towards increased garnet quantity presumably due to the iron-containing samples having equilibrium garnets close to the nominal composition, Fig. 7.8. The YAG system contained garnet, apatite, spinel, and glass. Conversely, the YIG system was primarily garnet with some coarsened apatite grains and very little residual glass. The Y(3A:I)G system shows intermediate behavior, but the spinel phase is notably absent indicating it became thermodynamically unstable. However, the (110) samples, where a significant Mg^{2+} redistribution was observed for all systems, does not show an overwhelming garnet presence for the YIG system. Instead, both the YAG and YIG systems contained garnet, spinel, and glass, with the YIG system showing less glass and larger garnet and spinel grains.

7.3.5. Secondary phase formation

While the primary focus of this work was on garnet formation, some important trends with secondary phases emerged. The key phases observed alongside garnet formation were apatite, spinel, olivine, YMS, and liquid, as noted in Table 7.2.

Apatite, either containing Ca^{2+} or Mg^{2+}, formed alongside garnet in multiple samples, including YIG(002), Y(3A:I)G(100), and the (101) samples for both the YIG and Y(3A:I)G systems. The

composition of the apatite formed was generally consistent between systems and nominal compositions; instead, changing the bulk composition appeared to primarily change the quantity of apatite formed at equilibrium. This point is best illustrated by the (101) samples, shown in Fig. 7.9, which also formed apatite in the YAG system [127]. Increasing the Fe:Al ratio of the system had little effect on the composition of apatite,[i] but the quantity of the phase clearly decreased. Likewise, the quantity of apatite decreases in the (100) samples from the YAG system to the Y(3A:I)G system, and no apatite is observed in the YIG system, Fig. 7.7. The latter consists of large garnet grains, close to the nominal composition, with the unidentified porous phase between them. Only the YIG(002) sample formed a Mg-apatite, comprised of ~12% Mg^{2+}, 52% Y^{3+}, and 36% Si^{4+}.

Spinel was observed to form in samples with $y \geq 1$, i.e., the (010), (020), (011), and (110) samples. The spinel compositions observed in this work contained a significant quantity of Fe^{2+} in the YIG system, 9.9–21.9%, which occasionally made up the majority of the divalent cation site. Less Fe^{2+} was observed as the total Fe content decreased, either through increasing the amount of substitution cations ($x+y+z$) or by switching to the Y(3A:I)G system. Overall, however, the spinels contained comparable or higher amounts of Fe^{2+} than the equilibrium garnets that formed alongside. The Y(3A:I)G system provided additional insight on the trivalent cation site. The spinels preferred Al^{3+} to Fe^{3+}—the Al:Fe^{3+} ratio of the (010), (020), and (011) spinels were 6.4, 5.7, and 9.6, respectively. This is in direct contrast to the garnet phase, which maintained an Al:Fe^{3+} ratio of ~3, Fig. 7.4. Interestingly, despite the variance in spinel composition across the YIG, Y(3A:I)G, and YAG

[i] The apatite composition contained only minor amounts (<1%) of Mg^{2+} indicating a strong preference for Ca^{2+}.

systems, the phase forms in roughly equivalent amounts for a given nominal composition. That is, increasing the Fe:Al ratio does not appear to systematically change the quantity of spinel present.[j]

Olivine was observed in two samples, both in the YIG system, (011) and (021). Notably the Y(3A:I)G system did not form olivine for the (011) composition, indicating that olivine may be stabilized by increasing the Fe:Al ratio of the system. Although olivine can contain mixtures of Fe^{2+} and Mg^{2+}, olivine formed in the YIG system contained far more Mg^{2+} (~64%) than Fe^{2+} (~2.6%) indicating a preference for the forsterite olivine endmember.

Finally, YMS was observed in the (001) and (002) samples across all systems with minimal solid solubility. Interestingly, YMS and liquid were not observed in the same samples—indeed, the only samples where liquid was not observed or expected to be present at temperature were the (001) and (002) samples.

7.4. Discussion

The incorporation of Fe^{3+} and Fe^{2+} into the garnet phase has important implications on the resulting thermodynamics of garnet and secondary phases such as apatite, spinel, and olivine. The results will be discussed with respect to the cation site preference in garnet, the impact of increasing Fe:Al ratio on secondary phase formation, and the implications for barrier coating-CMFAS interactions.

[j] The (020) samples are an exception to this. The YIG system contained more spinel than the YAG and Y(3A:I)G systems, which is attributed to the YIG system not forming garnet.

7.4.1. Cation site preference in garnet

Many of the key questions regarding the thermodynamic stability of aluminum and iron garnets are centered on how the relevant cations partition between the three cation sites and the relative preference for each cation in a given site. Within the YAG system, Godbole et al. noted a slight preference for Ca^{2+} over Mg^{2+} in the dodecahedral site, with observed maximum occupancies of ~0.88 apfu and ~0.72 apfu, respectively, out of the 3 dodecahedral sites [127]. The Mg^{2+} more strongly favored the octahedral site, where its solubility was significantly higher at ~1.91 apfu (of 2 available sites). Analysis of cation site preferences in the YIG and Y(3A:I)G systems is complicated by the addition of Fe^{2+}. As the latter competes with Mg^{2+} and Ca^{2+}, it played an important role in the garnet compositions and site preferences. However, the results suggest that the substitutional cation preference in the dodecahedral site is $Ca^{2+}>Fe^{2+}>Mg^{2+}$, whereas the octahedral site prefers $Mg^{2+}>Fe^{2+}$. These points are discussed further in turn.

First, Mg^{2+} relocated preferentially from the intended dodecahedral site to the octahedral site, regardless of the Ca^{2+} concentration, more strongly as the Fe:Al ratio increased (e.g., Fig. 7.6). This indicates Mg^{2+} becomes progressively unstable in the dodecahedral site. (This hypothesis is consistent with the absence of khoharite, the hypothetical garnet endmember $Mg_3Fe_2Si_3O_{12}$, from the geologic literature [174]. As the present experiments are conducted at ambient pressure, this would further destabilize khoharite.) Indeed, whereas garnet is observed for the YAG and Y(3A:I)G (020) compositions, the YIG (020), $(YMg_2)Fe_2(FeSi_2)O_{12}$, does not form garnet at equilibrium, indicating a significantly decreased stability of Mg^{2+} in the dodecahedral site. This may be because Mg^{2+} is the smallest cation (~0.89 Å) capable of fitting into the dodecahedral site (Table 7.1). Given that Fe^{3+} is

larger than Al^{3+} in both the octahedral and tetrahedral sites by a factor of 1.19–1.25, this may induce an energetic preference for larger cations in the dodecahedral site, consistent with large Y^{3+} and Ca^{2+} occupation of the dodecahedral sites. In practice, the maximum solubility of Mg^{2+} observed in the dodecahedral site decreases to ~0.5 apfu of the 3 available dodecahedral sites in YIG.[k] Like the YAG system, the solubility of Mg^{2+} in iron-based garnets in higher in the octahedral site, ~1.54 apfu of 2 available sites. Furthermore, for any given nominal composition, the octahedral solubility of Mg^{2+} typically increases with increasing Fe:Al ratio. The net effect is that the Mg^{2+} solubility is weakly dependent on the Fe:Al ratio (Table 7.3) but more Mg^{2+} is found octahedrally coordinated (Table 7.4).

The lower dodecahedral Mg^{2+} solubility in the YIG and Y(3A:I)G systems may be due, in part, to the availability of Fe^{2+} as a competing cation. (While some Fe^{2+} was observed in octahedral coordination, Fig. 7.6 and Table 7.4, it overwhelmingly occupied the dodecahedral sites. This suggests Fe^{2+} is more likely to displace Mg^{2+} to the octahedral site than occupy the octahedral site itself; therefore, the rest of the discussion will focus on Fe^{2+} in the dodecahedral site.) The size of Fe^{2+} (0.92 Å) is slightly larger than that of Mg^{2+} (0.89 Å), potentially reducing strain in the lattice, especially along the edge sharing polyhedral [188]. Indeed, a preference for Fe^{2+} over Mg^{2+} in the dodecahedral site is readily observed, Fig. 7.6 and Fig. 7.8. For example, the YIG(010) sample rejected *all* Mg^{2+} from the dodecahedral site and simultaneously replaced approximately one-third of the rejected Mg^{2+} with Fe^{2+}. Furthermore,

[k] The maximum Mg^{2+} dodecahedral site solubility is observed for the YAG (020) composition, which does not form garnet in the YIG system. Instead, the maximum observed solubility of 6.3% comes from the YIG (011) sample. For comparison, the YAG (011) sample contains 8.2% Mg^{2+}, larger than the YIG system.

some samples like YIG(001) suggest some Fe^{2+} is favored in the dodecahedral site regardless of Mg^{2+} occupancy. This sample showed almost no redistribution of its octahedrally coordinated Mg^{2+} to the dodecahedral site, but the latter contained ~0.34 apfu Fe^{2+} at equilibrium—the nominal composition contained 3 apfu Y^{3+} but 0.34 apfu of it was rejected in favor of Fe^{2+}! The ratio of Fe^{2+}:Mg^{2+} in the dodecahedral site appears to decrease when the Mg^{2+} concentration in the octahedral site exceeds 1 apfu, Fig. 7.6. This is likely because octahedral Mg^{2+} (z) most significantly decreases the total iron concentration (given by $Fe_{5-x-y-2z}$), thereby reducing the available Fe^{2+} in the system as suggested by Fig. 7.5. Second, this may suggest that Mg^{2+} in the dodecahedral site is stabilized by Mg^{2+} in the octahedral site, thereby modifying the preference of Mg^{2+} and Fe^{2+} in the dodecahedral site. However, this is in contrast with the lattice strain previously discussed—Mg^{2+} in the octahedral site is even larger than Fe^{3+} and Al^{3+}, Table 7.1. Overall, the evidence suggests that the dodecahedral site favors Fe^{2+} over Mg^{2+} as (i) the Fe:Al ratio in the system increases and (ii) as the Mg^{2+} concentration in the octahedral site decreases.

The modest preference for Ca^{2+} over Mg^{2+} in the dodecahedral site observed for the YAG system becomes much stronger as the Fe:Al ratio increases—data in the YIG system overwhelmingly suggests Ca^{2+} is favored. First, the solubility of Ca^{2+} in the equilibrium garnet, reaching a maximum ~1.42 apfu (of 3 available sites), is considerably higher than the maximum dodecahedral Mg^{2+} concentration, ~0.5 apfu. Second, samples containing both Ca^{2+} and Mg^{2+} retain more Ca^{2+} (and therefore lose less to other phases such as apatite or melt). For example, the (110) samples nominally contain 1 apfu of Ca^{2+} and Mg^{2+} in the dodecahedral site; after equilibration, however, the dodecahedral site contains 0.91 apfu Ca^{2+}, 0.10 apfu Fe^{2+}, and only 0.04 apfu Mg^{2+}. In sum, increasing

Fe:Al ratio exaggerates the preference for Ca^{2+} over Mg^{2+} in the dodecahedral site (due to the increased site solubility of Ca^{2+} and decreased solubility of Mg^{2+}). When coupled with the increasing preference of Fe^{2+} over Mg^{2+}, the dodecahedral site's preference of $Y^{3+}>Ca^{2+}>Fe^{2+}>Mg^{2+}$ is established.

To summarize, the key site preference points are: (*i*) Ca^{2+} is the favored substitutional cation for Y^{3+} in the dodecahedral site and this preference strengthens as the Fe:Al ratio of the system increases; (*ii*) Fe^{2+} is generally found in dodecahedral sites rather than octahedral sites (substituting for Y^{3+} instead of Al/Fe^{3+}), but it is not observed in significant quantities when Ca^{2+} is present; and (*iii*) the overall Mg^{2+} solubility is largely insensitive to the Fe:Al ratio of the system; however, Mg^{2+} more strongly favors the octahedral site as the Fe:Al ratio increases such that, in some cases, effectively all Mg^{2+} redistributes out of dodecahedral coordination.

7.4.2. Iron's impact on secondary phase formation

Understanding the thermodynamic competition between apatite and garnet formation is critical to improve thermodynamic databases that aid coating design. The results have clarified the role of iron with this regard. Apatite, with a defect-free formula of $Ca_2RE_8Si_6O_{26}$, does not contain iron or aluminum in significant (>1%) quantities; therefore, changing the Al:Fe ratio of the system is not expected to directly impact apatite formation or its composition. Still, as the composition of the garnet phase is affected by the Al:Fe ratio, this has a knock-on effect on the formation of apatite. (While the presence of other phases will also influence apatite formation, garnet most directly competes for the relevant cations.)

Increasing the Fe:Al ratio hindered Ca-apatite formation but slightly favored Mg-apatite. In Ca-containing systems, increasing the iron concentration in the system increased the Ca^{2+} and Si^{4+} solubility of the garnet—the net effect was an overall decrease in apatite formation. Conversely, for Ca-free (i.e., Mg-only) samples, Mg-apatite formation occurs earlier for the YIG system than the YAG or Y(3A:I)G systems. Mg-apatite crystallized in the YIG(002) sample whereas the YAG system first formed Mg-apatite for the(0,0.5,2) sample indicating that >2 apfu of Mg^{2+} is necessary to form apatite in that system. This difference between the YAG and YIG systems is attributed to YIG-based garnets lower Mg^{2+} solubility, thereby rejecting more Mg^{2+} to form apatite. However, note that the apatites formed from mixed Ca^{2+} and Mg^{2+} samples (e.g., 101) contain <1% Mg^{2+}, indicating that this benefit to Mg-apatite formation is unlikely to manifest in barrier coating-CMFAS interactions.

Iron (as Fe^{3+} and Fe^{2+}) has further implications on some intrinsic crystallization phases, notably spinel and olivine. Spinel, $(Mg,Fe^{2+})(Al,Fe^{3+})_2O_4$, formation typically occurred in samples where $y \geq 1$, e.g., (010), (020), (110), and (011), indicating the phase needs both a substantial concentration of Mg^{2+} and Al^{3+} or Fe^{3+} to form. For example, (001), while containing the same total Mg^{2+} concentration as (010), has 1 apfu less of Al/Fe due to the nominal placement of Mg^{2+} in the octahedral site. Furthermore, Mg^{2+} is more likely to occupy the garnet's octahedral site; therefore, the garnet phase formed from (001) rejects less Mg^{2+} which could otherwise form secondary phases like spinel. The one exception to the $y \geq 1$ trend was (101), which formed a spinel but only for the YAG system. This is likely because Fe-containing (101) garnets were closer to the nominal composition, containing more Ca^{2+}, Mg^{2+}, and Si^{4+}, Fig. 7.8, meaning less Mg^{2+} was rejected to form a spinel phase. Olivine, $(Mg,Fe^{2+})_2SiO_4$, was typically observed for samples with high Mg^{2+} contents, e.g., $y+z>2$. As

this investigation primarily studies samples with $x+y+z \leq 2$, olivine was rarely observed However, olivine was observed in the YIG(011) sample but not in the YAG(011) or Y(3A:I)G(011) samples. The implication is that olivine may be stabilized in the presence of iron, though further investigation would be needed to confirm this.

7.4.3. Implications for coating-melt interactions

To better interpret the results and their implications on coating-melt interactions, two important considerations are necessary. First, siliceous debris ingested into an engine will often contain all cations in CMFAS (and possibly more). The results from the compositionally simplified samples used in this work must then be couched in terms of the realistic composition of CMFAS ingested into the engine. Second, in some senses, the reactive crystallization of garnet follows the inverse the framework used in Fig. 7.2—rather than adding Ca^{2+}, Mg^{2+}, and Si^{4+} to YIG/YAG, Y^{3+} is added to CMFAS via dissolution of the coating. As coating dissolution often represents the rate limiting step of reactive crystallization (Chapters 4–6), garnets where a minimum of Y^{3+} is needed (i.e., where the solubilities of Ca^{2+}, Mg^{2+}, Fe^{2+}, and Si^{4+} are maximized) are the most likely to form in practice. However, as the solubility of these substitutional cations in garnet is ultimately limited, garnet formation requires a coating with sufficient Y^{3+} content (or other small rare earth element) and a CMFAS with sufficient Fe+Al content.

The key implication of this work is that garnet formation is more likely for CMFAS with a high Fe:Al ratio. Such a melt would be best equipped to crystallize garnet when one considers the relevant composition range of CMFAS melts [187]. First, though garnet requires a high Fe+Al concentration to form, these constituents are not typically abundant in sufficient concentrations. However, an

increasing Fe:Al ratio maximizes the solubility of Ca^{2+}, Mg^{2+}, Si^{4+} in garnet and affords Fe^{2+} solubility. These constituents will both decrease the amount of Fe+Al needed—making garnet formation more likely for realistic melts—and decrease the Y^{3+} required from the coating (Fig. 7.8). Of garnet's substitutional cations, Si^{4+} will be present in the highest amounts in CMFAS melts. Therefore, the extent of substitution is likely to be limited by the available Ca^{2+} and Mg^{2+}. A high Ca^{2+} concentration (e.g., a high Ca:Si ratio) will help to minimize the amount of Y^{3+} needed to form garnet. Mg^{2+} will primarily occupy the octahedral site, and therefore help decrease the amount of Fe+Al needed; however, the quantity of Mg^{2+} is also often limited (e.g., <10%) in CMFAS melts.

A key consideration is the competition between garnet and apatite formation. Thermodynamically, garnet more effectively crystallizes CMFAS (per mole of Y^{3+} dissolved) than apatite, as supported by this work and observations in the literature [124,127]. But garnet nucleates slower, often enveloping apatite grains. For thermal barrier coatings, where rapid reactive crystallization is critical for coating survival, garnet may hinder apatite formation and worsen penetration.[1] In the YAG system, Godbole et al. [127] noted the Al:Si ratio was a key predictor of garnet vs. apatite formation—high Al:Si favored garnet and low Al:Si favored apatite. However, this metric becomes less useful as the Fe:Al ratio increases. Garnets formed in the Y(3A:I)G and YIG systems had higher concentrations of Si^{4+} and concomitantly lower $Al+Fe^{3+}$ concentrations. (Indeed, the YIG(101) equilibrium garnet had Si≈(Fe+Al), Fig. 7.8.) Therefore, the implication is apatite formation will be further hindered in CMFAS with high Fe:Al ratios due to greater competition with garnet. This was readily observed in

[1] In the short-term garnet is expected to be detrimental. However, longer term garnet could serve as a valuable high-temperature phase to crystallize remaining pools of CMFAS atop the coating.

the Ca-containing samples, which showed a clear decrease in Ca-apatite quantities as the Fe:Al ratio increased.[m]

7.5. Synopsis

Garnet formation was studied in the Y-CMFAS (with 3Al:1Fe) and Y-CMFS systems at 1400°C, and the results were compared to equivalent experiments carried out in the Y-CMAS system [127]. Yttria is critical to garnet stability in all three systems. The equilibrium garnets studied had no strong preference for Fe^{3+} or Al^{3+} in the octahedral or tetrahedral sites. However, the Fe:Al ratio directly affected the solubility of other cations—most importantly in the dodecahedral site. The key trends with increasing Fe:Al ratio were:

1. Ca^{2+} solubility in the dodecahedral site increases. Ca-containing garnets were closer to the nominal composition.
2. Mg^{2+} loses solubility in the dodecahedral site with a concomitant increase in octahedral solubility. The overall solubility (i.e., considering both sites) is largely insensitive to the Fe:Al ratio.
3. Fe^{2+} is present in increasing quantities primarily occupying the dodecahedral site. Less Fe^{2+} is observed in Ca-containing garnets, indicating a dodecahedral site cation preference of $Ca^{2+}>Fe^{2+}>Mg^{2+}$.

[m] In contrast to this is the fact that Mg-apatites were observed earlier in the YIG system. Ultimately, however, this is not expected to be impactful for barrier coating applications. Molten CMFAS typically contain more Ca^{2+} than Mg^{2+} [187], favoring Ca-apatite formation. Furthermore, the results suggest apatite strongly prefers Ca^{2+} to Mg^{2+} (e.g., Fig. 7.9). Therefore, in practice, increasing the Fe:Al ratio is ultimately expected to decrease apatite formation due to competition with garnet formation.

4. Si^{4+} solubility in the tetrahedral site increases.

The key trends highlighted above suggest that garnet will be more likely to form in CMFAS as the Fe:Al ratio increases, which minimizes the amount of Y^{3+}, Fe^{3+}, and Al^{3+} required to form the phase. These garnets are expected to form at the detriment of other reactive phases (e.g., apatite). Therefore, CMFAS with high Fe:Al may be particularly detrimental to TBC infiltration.

7.6. Figures and tables

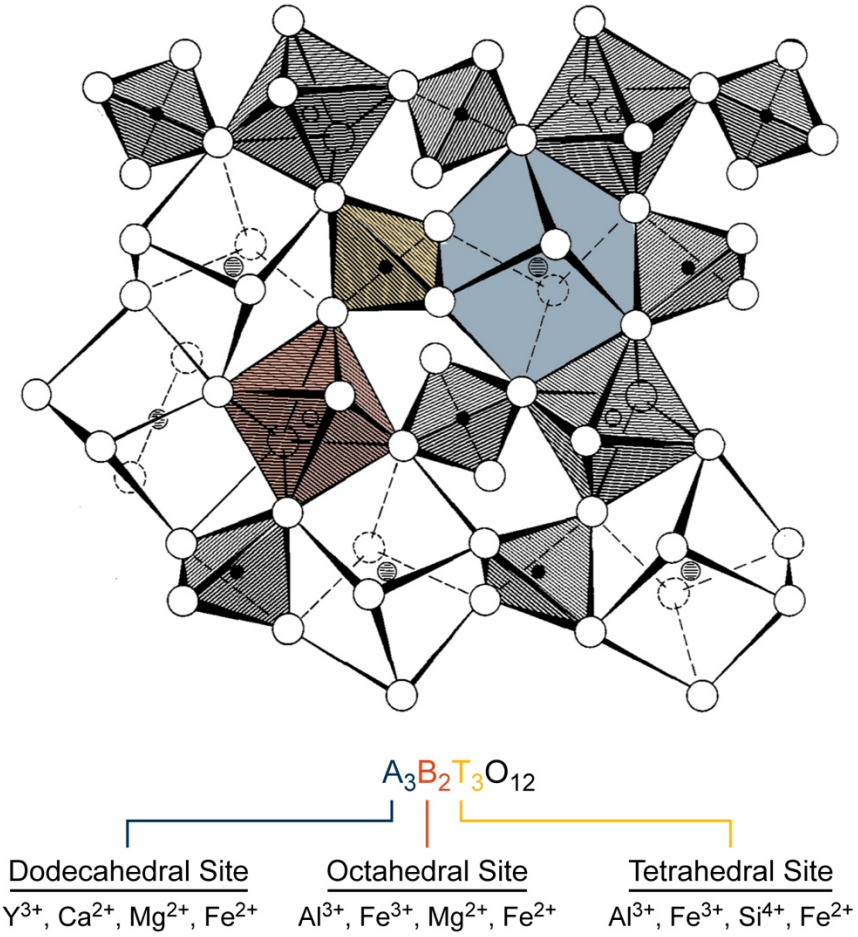

Fig. 7.1: Portion of the garnet crystal structure, including dodecahedral sites (blue, distorted cubes), octahedral sites (red), and tetrahedral sites (yellow). Oxygen anions are shown as large white circles. Note the significant amount of shared polyhedron edges. Figure adapted from Ref. [188].

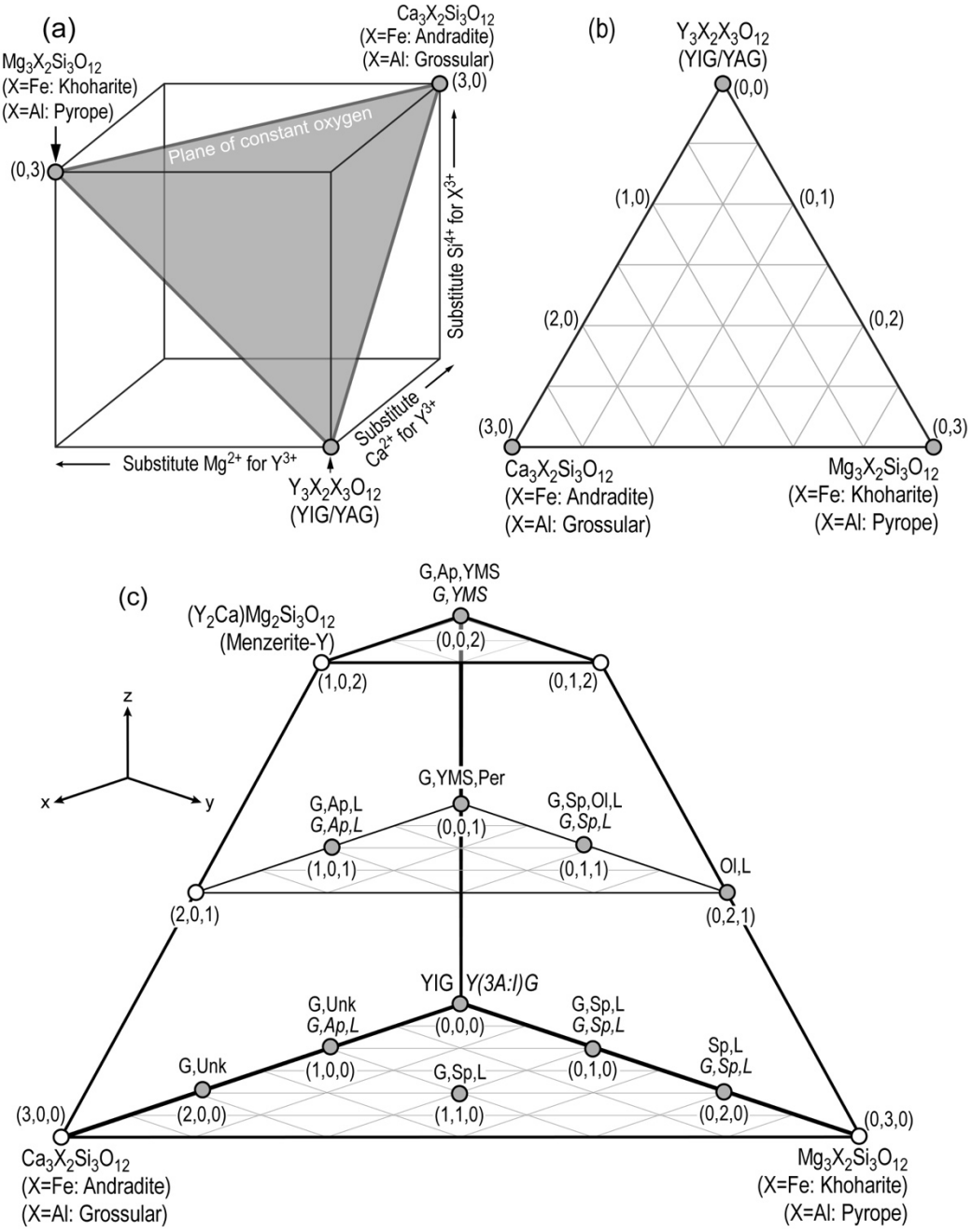

Fig. 7.2: Starting with $Y_3Al_2Al_3O_{12}$ or $Y_3Fe_2Fe_3O_{12}$, Ca^{2+} or Mg^{2+} can substitute for Y^{3+} in the dodecahedral site. However, equimolar substitution of Si^{4+} for tetrahedral Al^{3+} or Fe^{3+} is necessary to maintain charge neutrality. This constrains the relevant composition space to the plane of constant oxygen (a) to a Gibbs triangle shown in (b). Further substitution of Mg^{2+} for octahedral Al^{3+} or Fe^{3+} (with coupled tetrahedral Si^{4+}:Al/Fe^{3+} substitution) can be represented in a third dimension (c), which represents the relevant composition volume for all nominal compositions (Table 7.2). Note that octahedral substitution (z) limits the maximum dodecahedral substitution (x,y) allowed. (This framework considers all iron to be Fe^{3+}, i.e., nominal compositions were synthesized without considering Fe^{2+}. Upon equilibration, iron reduction occurs and Fe^{2+} can further substitute into the dodecahedral and octahedral sites. This is neglected in this figure as two additional dimensions would be required.)

Fig. 7.3: Illustration of the coiled wire design to support samples that melted substantially without climb or dripping out of the container. The porous structure of the sectioned sample suggests gas evolution during the partial reduction of Fe^{3+} to Fe^{2+}.

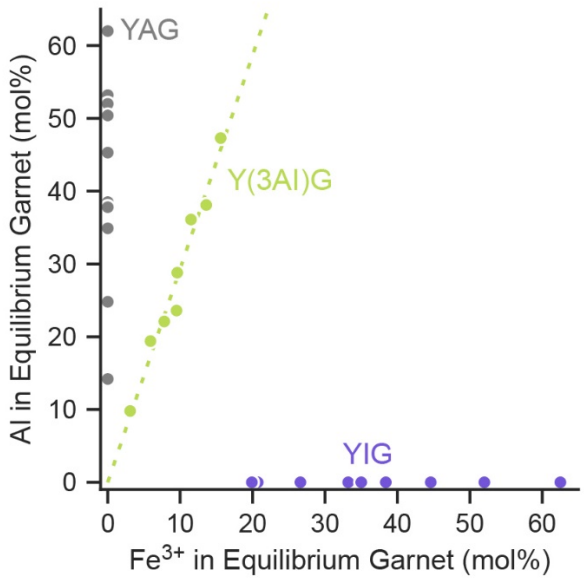

Fig. 7.4: Concentration of Al^{3+} and Fe^{3+} in equilibrium garnets formed across all three systems in the presence of different amounts of Ca^{2+}, Mg^{2+}, and Si^{4+}. The equilibrium garnets in the Y(3A:I)G system maintain an Al:Fe ratio of ~2.93. This indicates there is no strong preference for Al or Fe in the octahedral and tetrahedral sites.

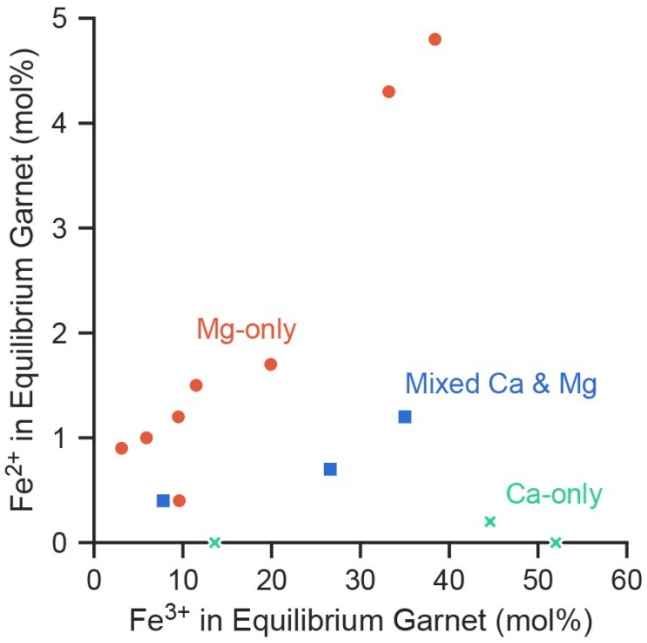

Fig. 7.5: Concentration of Fe^{2+} in equilibrium garnets formed in the YIG and Y(3A:I)G systems. Two key trends emerge. First, the Fe^{2+} concentration depends on the alkali earths present: Ca-only garnets contain little or no Fe^{2+} whereas those containing no Ca (i.e., Mg-only) contain the most. Mixed alkali garnets show intermediate Fe^{2+} concentrations. Second, the Mg-containing garnets show increasing Fe^{2+} with increasing Fe^{3+}.

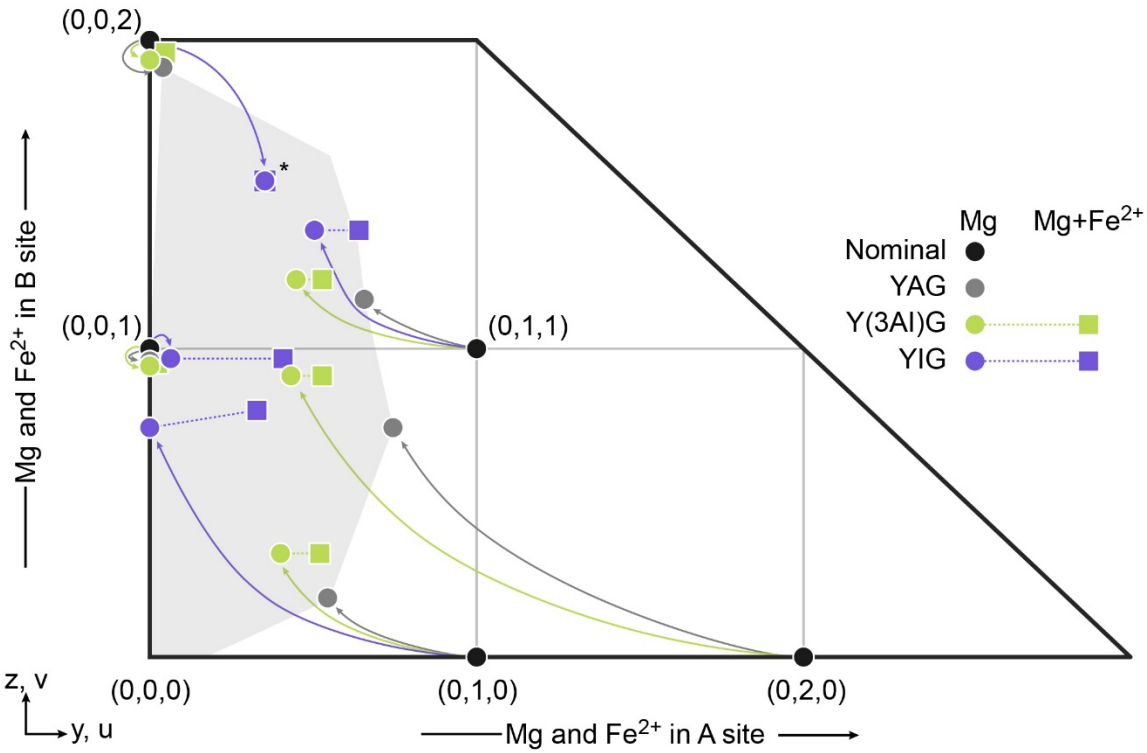

Fig. 7.6: The site preference for Mg^{2+} and Fe^{2+} ions is clearly observed in Ca-free samples (the x=0 plane of Fig. 7.2). Mg^{2+} largely prefers the octahedral (B) site, as indicated by the upwards and leftwards shift of the arrows. This preference became stronger as the Fe:Al ratio increased (i.e., from YAG to YIG). The data for the Y(3A:I)G and YIG systems fall within the garnet stability field (grey shaded region) determined in the YAG system [127]. However, the former systems incorporate some Fe^{2+}, which unlike Mg^{2+} largely prefers to occupy the dodecahedral (A) site. One notable observation is that garnet was not observed for the YIG(020) composition, further emphasizing the octahedral site preference for Mg^{2+} in garnets with high Fe:Al ratios.

* Sample does not charge balance (contains more Mg^{2+} than Si^{4+}).

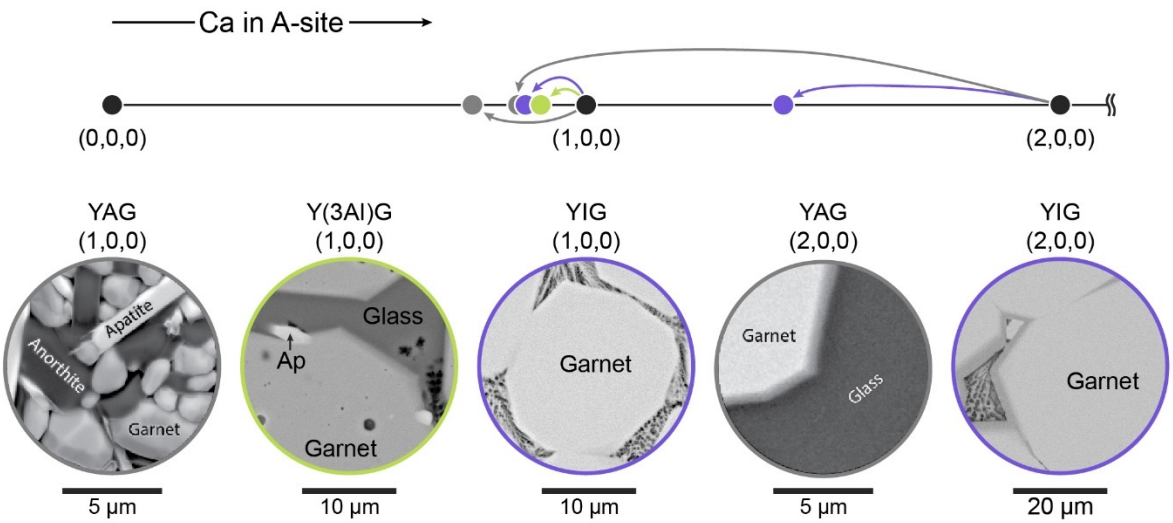

Fig. 7.7: Composition shifts between nominal and equilibrium garnets for the Ca-only (y=z=0) samples, and corresponding representative micrographs. (Because Ca^{2+} can only occupy the dodecahedral site, the composition shifts is represented by a number line.) The solubility of Ca^{2+} was enhanced in the Y(3A:I)G and YIG samples relative to the YAG samples—the maximum solubility observed was 10.7% in the YAG system and 17.7% in the YIG system. (Unfortunately, synthesis of the Y(3A:I)G(200) composition failed.) The increased Ca^{2+} solubility concomitantly increased the phase fraction of garnet, importantly reducing the amount of apatite for the (100) samples and the amount of melt for the (200) samples.

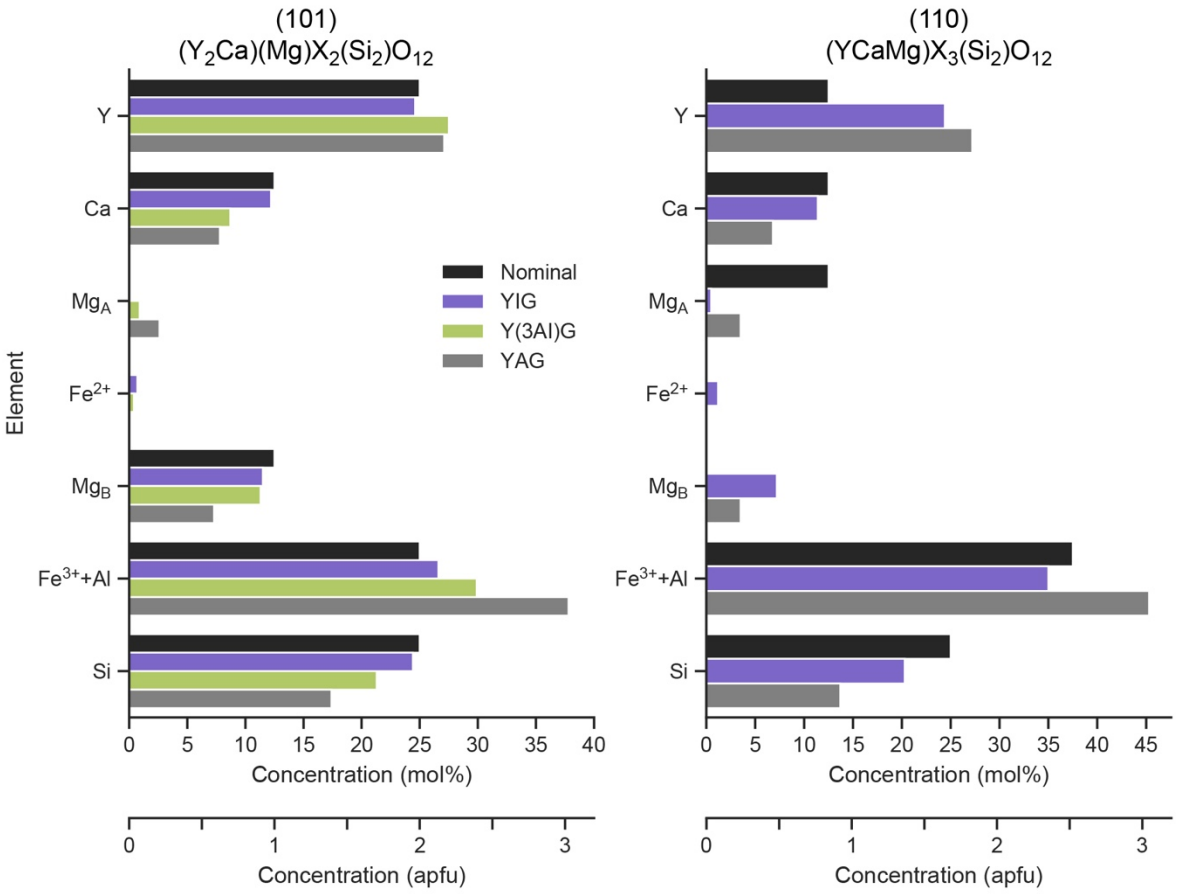

Fig. 7.8: The composition of the mixed alkali garnets (101) and (110) formed for all systems. In general, increasing the Fe:Al ratio increased the Ca^{2+} and Si^{4+} concentrations, with concomitant decreased Y^{3+}, Fe^{3+}, and Al^{3+}. The result are garnets closer to the nominal composition (shown in black). Increasing the Fe:Al ratio had minimal impact on the total Mg^{2+} content but did result in a greater shift of Mg^{2+} from the dodecahedral site to the octahedral site, consistent with the Ca-free samples (Fig. 7.6).

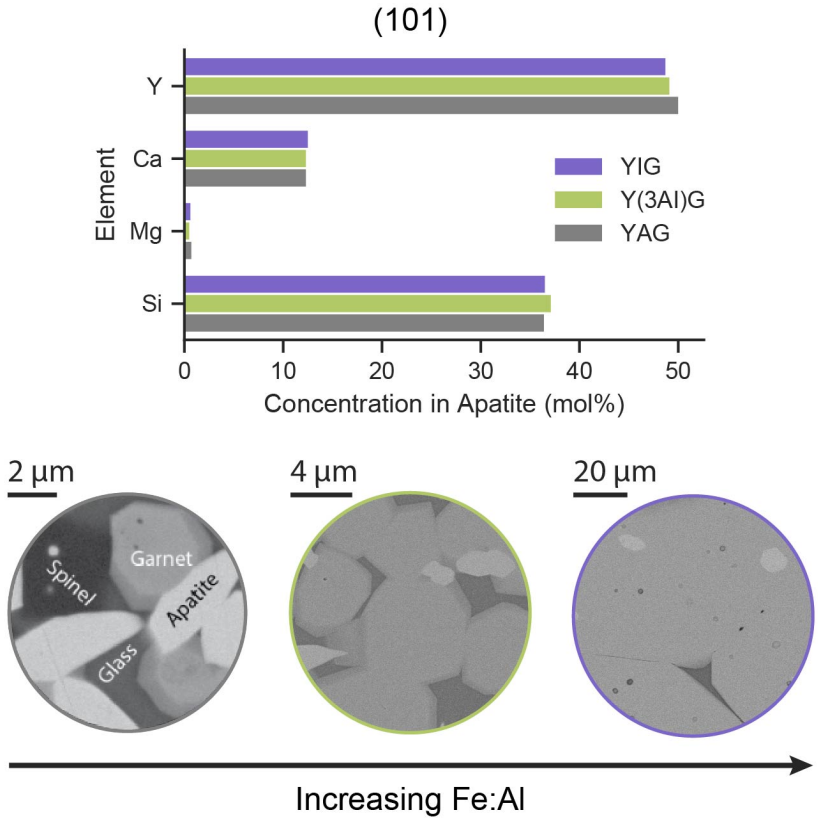

Fig. 7.9: Apatite compositions formed for the (101) samples and representative micrographs. The composition of apatite is largely unaffected by the nominal Fe:Al ratio. However, the quantity of apatite decreased with increasing Fe:Al, indicating a decrease in stability.

Table 7.1: Cation radii of the different species present in the Y-CMFAS system in coordination of 4, 6, or 8. The columns indicate whether the species can occupy specific sites in the garnet crystal structure.

Dodecahedral (A) Site (CN=8)			Octahedral (B) Site (CN=6)			Tetrahedral (T) Site (CN=4)		
Cation	Radius	Fit	Cation	Radius	Fit	Cation	Radius	Fit
Ca^{2+}	1.12 Å	Y	Ca^{2+}	1.0 Å	N	Mg^{2+}	0.57 Å	N
Y^{3+}	1.02 Å	Y	Y^{3+}	0.90 Å	N	Fe^{3+}	0.49 Å	Y
Fe^{2+}	0.92 Å	Y	Fe^{2+} *	0.78 Å	Y	Al^{3+}	0.39 Å	Y
Mg^{2+}	0.89 Å	Y	Mg^{2+}	0.72 Å	Y	Si^{4+}	0.26 Å	Y
Fe^{3+}	0.78 Å	N	Fe^{3+} *	0.64 Å	Y			
			Al^{3+}	0.54 Å	Y			
			Si^{4+}	0.40 Å	N			

* Iron can occupy two spin states, high and low, in 6-fold coordination. The radii listed in the table are for high spin. Those for low spin are 0.61 Å for Fe^{2+} and 0.55 Å for Fe^{3+}.

Table 7.2: Summary of nominal compositions investigated in the YIG and Y(3A:I)G systems. The phases observed at equilibrium are also provided.

		Nominal Garnet Composition						
System	**Coordinate**	**CaO**	**MgO**	**$YO_{1.5}$**	**$AlO_{1.5}$**	**FeO_x**	**SiO_2**	**Observed Phase List**
YIG	(000)	0	0	37.5	0	62.5	0	**G**
Y(3A:I)G	(000)	0	0	37.5	46.87	15.63	0	**G**
YIG	(010)	0	12.5	25	0	50	12.5	**G**, Sp, L
Y(3A:I)G	(010)	0	12.5	25	37.5	12.5	12.5	**G**, Sp, L
YIG	(020)	0	25	12.5	0	37.5	25	Sp, L
Y(3A:I)G	(020)	0	25	12.5	28.12	9.38	25	**G**, Sp, L
YIG	(001)	0	12.5	37.5	0	37.5	12.5	**G**, YMS, Per
Y(3A:I)G	(001)	0	12.5	37.5	28.12	9.38	12.5	**G**, YMS
YIG	(002)	0	25	37.5	0	12.5	25	**G**, Ap, YMS
Y(3A:I)G	(002)	0	25	37.5	9.37	3.13	25	**G**, YMS
YIG	(011)	0	25	25	0	25	25	**G**, Ol, Sp, L
Y(3A:I)G	(011)	0	25	25	18.75	6.25	25	**G**, Sp, L
YIG	(021)	0	37.5	12.5	0	12.5	37.5	Ol, L
YIG	(100)	12.5	0	25	0	50	12.5	**G**, Ukn*
Y(3A:I)G	(100)	12.5	0	25	37.5	12.5	12.5	**G**, Ap, L
YIG	(200)	25	0	12.5	0	37.5	25	**G**, Ukn*
YIG	(110)	12.5	12.5	12.5	0	37.5	25	**G**, Sp, L
YIG	(101)	12.5	12.5	25	0	25	25	**G**, Ap, L
Y(3A:I)G	(101)	12.5	12.5	25	18.75	6.25	25	**G**, Ap, L

* This phase remains unknown. It does not appear in XRD and contains significant porosity precluding compositional analysis. We presume it crystallized from the melt during the quench.

Table 7.3:Measured composition of equilibrium garnets.

		Equilibrium Garnet Composition						
System	**Coordinate**	**CaO**	**MgO**	**$YO_{1.5}$**	**$AlO_{1.5}$**	**FeO_x**	**SiO_2**	**Measurement Method**
YIG	(000)	—	—	37.5	—	62.5	—	EDS
Y(3A:I)G	(000)	—	—	37.1	47.3	15.6	—	EPMA
YIG	(010)	—	9.3	33.4	—	43.2	14.1	EPMA
Y(3A:I)G	(010)	—	9.2	31	36.1	13	10.7	EPMA
Y(3A:I)G	(020)	—	16.8	30.9	23.6	10.7	18	EPMA
YIG	(001)	—	12.9	32.4	—	37.5	17.2	TEM-EDS
Y(3A:I)G	(001)	—	11.8	37.2	28.8	10	12.2	EPMA
YIG	(002)	—	23.7	33.1	—	20.7	22.5	EDS
Y(3A:I)G	(002)	—	24.2	36.9	9.8	4	25.1	EPMA
YIG	(011)	—	23.6	29.5	—	21.6	25.3	EPMA
Y(3A:I)G	(011)	—	20.9	30.7	19.4	6.9	21.9	EPMA
YIG	(100)	10.9	—	26.5	—	52	10.6	EPMA
Y(3A:I)G	(100)	11.3	—	25.8	38.1	13.6	11.2	EPMA
YIG	(200)	17.7	—	19.6	—	44.8	17.9	EPMA
YIG	(110)	11.4	7.7	24.4	—	36.2	20.3	EPMA
YIG	(101)	12.2	11.5	24.6	—	27.3	24.4	EPMA
Y(3A:I)G	(101)	8.7	12.2	27.5	22.1	8.2	21.3	EPMA

Table 7.4: Cation site occupancies of equilibrium garnets following Equations 7.2 and 7.3.

System	Coordinate	Equilibrium Garnet Stoichiometry			
		Dodecahedral	Octahedral	Tetrahedral	
YIG	(000)	(Y_3)	(Fe_2^{3+})	(Fe_3^{3+})	
Y(3A:I)G	(000)	$(Y_{2.97}Fe_{0.03}^{2+})$	$(Fe_{1.23}^{3+}Al_{0.77})$	(Al_3)	
YIG	(010)	$(Y_{2.67}Fe_{0.33}^{2+})$	$(Fe_{0.06}^{2+}Mg_{0.74}Fe_{1.2}^{3+})$	$(Fe_{1.87}^{3+}Si_{1.13})$	
Y(3A:I)G	(010)	$(Y_{2.48}Mg_{0.4}Fe_{0.12}^{2+})$	$(Mg_{0.34}Fe_{0.95}^{3+}Al_{0.71})$	$(Al_{2.14}Si_{0.86})$	
Y(3A:I)G	(020)	$(Y_{2.47}Mg_{0.43}Fe_{0.1}^{2+})$	$(Mg_{0.91}Fe_{0.66}^{3+}Al_{0.43})$	$(Al_{1.56}Si_{1.44})$	
YIG	(001)	$(Y_{2.59}Mg_{0.06}Fe_{0.34}^{2+})$	$(Mg_{0.97}Fe_{1.03}^{3+})$	$(Fe_{1.62}^{3+}Si_{1.38})$	
Y(3A:I)G	(001)	$(Y_{2.98}Fe_{0.02}^{2+})$	$(Mg_{0.94}Fe_{0.01}^{2+}Fe_{0.77}^{3+}Al_{0.28})$	$(Al_{2.02}Si_{0.98})$	
YIG	(002)	$(Y_{2.65}Mg_{0.35})$	$(Fe_{0.46}^{3+}Mg_{1.54})$	$(Fe_{1.2}^{3+}Si_{1.8})$	*
Y(3A:I)G	(002)	$(Y_{2.95}Fe_{0.05}^{2+})$	$(Mg_{1.94}Fe_{0.02}^{2+}Fe_{0.04}^{3+})$	$(Fe_{0.21}^{3+}Al_{0.78}Si_{2.01})$	
YIG	(011)	$(Y_{2.36}Mg_{0.5}Fe_{0.14}^{2+})$	$(Fe_{0.62}^{3+}Mg_{1.38})$	$(Fe_{0.98}^{3+}Si_{2.02})$	
Y(3A:I)G	(011)	$(Y_{2.46}Mg_{0.45}Fe_{0.08}^{2+})$	$(Mg_{1.22}Fe_{0.47}^{3+}Al_{0.30})$	$(Al_{1.25}Si_{1.75})$	
YIG	(100)	$(Y_{2.12}Ca_{0.87}Fe_{0.01}^{2+})$	$(Fe_{2.0}^{3+})$	$(Fe_{2.15}^{3+}Si_{0.85})$	†
Y(3A:I)G	(100)	$(Y_{2.06}Ca_{0.9}Fe_{0.03}^{2+})$	$(Fe_{1.06}^{3+}Al_{0.94})$	$(Al_{2.1}Si_{0.9})$	†
YIG	(200)	$(Y_{1.57}Ca_{1.42}Fe_{0.01}^{2+})$	$(Fe_{2.0}^{3+})$	$(Fe_{1.57}^{3+}Si_{1.43})$	
YIG	(110)	$(Y_{1.95}Ca_{0.91}Mg_{0.04}Fe$	$(Fe_{1.42}^{3+}Mg_{0.58})$	$(Fe_{1.38}^{3+}Si_{1.62})$	
YIG	(101)	$(Y_{1.97}Ca_{0.97}Fe_{0.06}^{2+})$	$(Fe_{1.08}^{3+}Mg_{0.92})$	$(Fe_{1.05}^{3+}Si_{1.95})$	
Y(3A:I)G	(101)	$(Y_{2.2}Ca_{0.7}Mg_{0.07}Fe_{0.0}^{2+}$	$(Mg_{0.9}Fe_{0.62}^{3+}Al_{0.47})$	$(Al_{1.3}Si_{1.7})$	

* Sample has $Mg^{2+}>Si^{4+}$, (1.89 apfu vs. 1.8 apfu, respectively). This precludes a calculation of Fe^{2+} concentration by the described site assignment procedure. However, all Fe is accounted for as Fe^{3+}.

† Sample has $Ca^{2+}\geq Si^{4+}$, precluding calculation of Fe^{2+} by the described site assignment procedure. However, the measured total Fe concentration was greater than the amount of Fe^{3+} that could fit in the octahedral and tetrahedral sites. The excess Fe was set as Fe^{2+} and assigned to the dodecahedral site. (Further supporting this assignment, the measured concentrations of Y^{3+} and Ca^{2+} were insufficient to fill the dodecahedral site. Adding Fe^{2+} got the site to within 0.01 apfu or less of the expected occupancy.)

CHAPTER 8. CONCLUSIONS

The primary goal of this investigation was to enhance the fundamental understanding of the kinetics and thermodynamics of thermal and environmental barrier oxide interactions with molten silicates. The resulting insight would inform the design of novel coating chemistries and architectures to improve the temperature capabilities of next-generation gas turbine engines. Experiments were designed such that quantitative data could be gathered to enable or improve models predicting the thermochemical degradation of coatings—a part of a larger Integrated Computational Materials Engineering (ICME) framework.

One dimensional diffusion couples were used to investigate the dissolution and diffusion rates of barrier coating oxides (BOs) into molten silicates, representing the first rigorous quantification of these kinetic processes BOs. The dissolution mechanism of BOs was rate-limited by both the rate at which atoms are detached from the BO into the melt (u_o) and their diffusivity (D) therein. This resulted in an initial transient period in the concentration profiles, during which the concentration at the BO-melt interface increased with time towards a saturation value. (The critical implication is that reactive crystallization—the thermochemical interaction that dictates coating survivability—will depend on the time required to achieve saturation at the oxide-melt interface.) The duration of this transient period was longest for BOs with little or no rare-earth (RE) oxides, including pure HfO_2 (a candidate EBC material) and 7YSZ (the current industry standard TBC). Conversely, the transient period for $Gd_2Zr_2O_7$ was substantially shorter—both Zr^{4+} and Gd^{3+} rapidly saturated the interface melt and a substantial amount of crystallization resulted even in the shortest duration experiments.

The measured concentration profiles were fit to crystal dissolution and diffusion models to quantify u_o and D for the BOs HfO_2, 7YSZ, and $Gd_2Zr_2O_7$ into the silicate melts $C_{33}M_9A_{13}S_{45}$ and/or $C_{24}A_{17}S_{59}$ primarily at 1300 °C. (7YSZ was also investigated at 1350 and 1400 °C, which enabled the Arrhenius parameters for D and u_o[a] to be determined.) The observed diffusivities were in the range of ~0.1–20 $\mu m^2/s$ for Zr^{4+}/Hf^{4+} and ~0.4–40 $\mu m^2/s$ for Y^{3+}/Gd^{3+}. The resulting diffusivities were more sensitive to the melt composition than to the temperature within the conditions tested. Isovalent cations diffused at roughly comparable rates, with the rare earths diffusing ~3x faster than Zr^{4+} or Hf^{4+}. (The implication is that the diffusivity is relatively insensitive to the dissolving BO.) Conversely, the BO composition had a strong effect on u_o; for example, u_o for $Gd_2Zr_2O_7$ was estimated to be ~0.8 μm/s, approximately an order of magnitude larger than that of 7YSZ (0.07 μm/s), which immediately explains the decreased transient time and earlier onset of crystallization observed in the former. Melt composition and temperature had a comparable, and intermediate, impact on u_o.

Crystallization was observed once the interface melt had saturated in at least one constituent. The early stages of crystallization were investigated using SEM and the results were compared to the expected thermodynamic response to understand deviations from equilibrium. RE-lean BOs (i.e., ZrO_2, HfO_2, 7YSZ, and HfO_2-$7YO_{1.5}$) were unreactive with the Ca-rich $C_{33}M_9A_{13}S_{45}$ melt but formed $(Zr,Hf)SiO_4$ and $Ca_2HfSi_4O_{12}$ with the Si-rich $C_{24}A_{17}S_{59}$ melt. But the quantity of the zircon/hafnon was substantially reduced when 7% $YO_{1.5}$ was present in the dissolving BO, in contrast

[a] The Arrhenius behavior for u_o was only determined for the $C_{33}M_9A_{13}S_{45}$ melt.

with the negligible change predicted by equilibrium CALPHAD calculations performed using ThermoCalc. The implication is that small amounts of RE oxide (i.e., those amounts insufficient to saturate the melt relative to the amount necessary to form apatite) kinetically impedes reactive phases based on Zr^{4+} or Hf^{4+} in favor of the arguably easier to crystallize reprecipitated phases. The reprecipitated phases, whether forming as a shell around pristine grains or crystallizing independently, exhibit a much lower driving force for dissolution and consequently lead to the development of a "mushy zone", which would have poor erosion resistance. In addition, a Y-enriched cubic phase was observed in both 7YSZ and HfO_2-$7YO_{1.5}$ which preferentially dissolved into both melts and worsened the "mushy zone" development. Low $YO_{1.5}$ additions would, therefore, be deleterious to the thermochemical response of the coating. However, crystallization occurred rapidly when the RE-rich $Gd_2Zr_2O_7$ was dissolved into either melt, with Zr-based reprecipitated phases forming before RE-based reactive ones (albeit only slightly). Results with the CAS melt suggest metastable phases crystallized and subsequently redissolved in the very early stages.

The Hf-based silicate phases appear to show enhanced stability over their Zr-based equivalents. A Hf-cyclosilicate, $Ca_2HfSi_4O_{12}$, was observed at 1300 °C (losing stability by 1400 °C) but the Zr-cyclosilicate was absent from all experiments, i.e., below 1300°C. Similarly, whereas the quantity of $ZrSiO_4$ decreased at 1400 °C relative to 1300 °C, that of $HfSiO_4$ increased, showing nearly complete coverage after 60 min. Both $HfSiO_4$ and $Ca_2HfSi_4O_{12}$ were well-adhered to the underlying HfO_2 and shielded the latter from further dissolution into the semi-infinite melt. However, using monoclinic HfO_2 as an EBC oxide will likely be precluded by issues with microcracking arising from its thermal

expansion anisotropy. This is particularly deleterious for non-reactive Ca-rich melts, as these could infiltrate the EBC without a mechanism to arrest the flow.

The quantified rates of D and u_o from semi-infinite experiments were applied to finite element models to better understand what limits melt saturation within TBC intercolumnar gaps. The models indicate that the time until melt saturation (at the gap center) is essentially insensitive to the diffusivity or gap width (within the range 0.5–2 μm). The simulated concentration profiles are essentially flat indicating that dissolution is limited instead by the interfacial detachment rate, u_o. Indeed, increasing u_o (e.g., by modeling the dissolution of $Y_2Zr_2O_7$ instead of 7YSZ) substantially decreased the infiltrated distance at melt saturation. The effect was strongest for Y^{3+} as this benefitted from a simultaneous increased concentration in the dissolving BO; but the benefit was also significant for Zr^{4+} even though the latter had a substantially lower concentration in $Y_2Zr_2O_7$. It is clear, therefore, that future TBC development must consider u_o as a primary design parameter for molten silicate resistance. Considering the experimental evidence—both qualitative and quantitative—the implication is that TBC chemistries with a substantial RE^{3+} concentration (or other divalent or trivalent cations) will be the most promising.

The thermodynamics of garnet—a reactive phase with a nominal formula $Y_3(Fe,Al)_5O_{12}$—formation in the Y+CMF(A)S system was investigated at 1400 °C using precursor-derived powder mixtures and standard chemical analysis techniques. The phase exhibits extensive solid solubility and was poorly represented in thermodynamic databases, causing significant disagreement between models and experiments when garnet was observed experimentally. The work, done in partnership with the database developer, will directly improve the accuracy of these predictions, but several important

findings were also made. The key conclusion is that garnet formation becomes more likely as the Fe:Al ratio of the deposit increases. The latter afforded an increased solubility of Ca^{2+}, Fe^{2+}, and Si^{4+} in the equilibrium garnet. As the divalent cations substitute for Y^{3+} in the garnet dodecahedral site, the implication is that less coating dissolution (the source of Y^{3+}) would be needed to stabilize the garnet phase, favoring its crystallization. Simultaneously, the concomitant equimolar substitution of Si^{4+} for Al^{3+} or Fe^{3+} (necessary to maintain charge balance) reduces the quantity of $FeO_{1.5}$ and $AlO_{1.5}$ needed to stabilize garnet. As the concentration of $FeO_{1.5}$ and $AlO_{1.5}$ in siliceous debris is generally low, and SiO_2 is generally the majority constituent, the enhanced Si^{4+} solubility also increases the likelihood of garnet formation. Indeed, increasing the Fe:Al ratio of the as-synthesized powder significantly increased the quantity of garnet present, often with a concomitant decrease to the quantity of apatite. As the garnet phase has slow crystallization kinetics relative to apatite, this may reduce the potential to block the penetration channels and worsen the subsequent thermomechanical stresses on the coating.

The increased solubility of Ca^{2+} with Fe:Al ratio comes with a concomitant decrease to the stability of Mg^{2+} in the dodecahedral site—which in turn increases its occupancy of the octahedral site with little change to the overall Mg^{2+} solubility. Equilibrium garnets containing Ca^{2+} were also found to contain less Fe^{2+} compared to Ca-free compositions for equivalent amounts of FeO_x in the bulk composition. Therefore, the substitutional cation preference in the dodecahedral site for Y-based garnets is $Y^{3+}>Ca^{2+}>Fe^{2+}>Mg^{2+}$; this site preference became stronger as the Fe:Al ratio of the bulk composition increased. Finally, no strong preference for Al^{3+} or Fe^{3+} was observed in the equilibrium garnets—these largely retained the Fe:Al ratio of the bulk system composition. The implication is

that garnets formed in reactive crystallization will likely retain both Al^{3+} and Fe^{3+}, in contrast with the predictions from current thermodynamic databases. Instead, the Fe:Al ratio of the CMFAS deposit will primarily affect the substitution of the other CMFAS constituents (i.e., Ca^{2+}, Mg^{2+}, and Si^{4+}) as previously elaborated.

Outlook

The work presented in this dissertation has generated considerable insight into the kinetics and thermodynamics of barrier coating oxide interactions with molten silicates, but many outstanding questions remain. With respect to TBC kinetics, the overarching conclusion is that slow rates of BO detachment into the melt represent the major barrier to rapid reactive crystallization. Therefore, additional research focused on the kinetics of rapidly dissolving thermal barrier oxides would be valuable. Oxides containing a high-proportion of trivalent cations—such as RE-aluminum, RE-iron, or pure RE oxides—are of primary interest, which could be deposited as a CMFAS-resistant topcoat to an underlying TBC. With respect to EBCs, HfO_2 showed promising reactive crystallization in acidic melts, but it was unreactive in basic melts and experienced significant microcracking when the grain size exceeded ~3 μm. In principle, both issues could be addressed by incorporating a secondary phase. Additional efforts identifying an appropriate secondary phase is recommended—the studies would need to fully investigate the resistance of the compact to sintering and its resistance to both acidic and basic melts. With respect to the kinetic models of the envisioned ICME framework, a better understanding of how u_o depends on the barrier oxide composition and melt composition is critical. Likewise, the demonstrated relationship between diffusivity and melt viscosity would benefit from additional confirmation. Both goals would be readily accomplished by dissolution and diffusion

studies (following the methodology developed in this dissertation) wherein the RE:(Zr,Hf) ratio of the BO and melt composition is systematically varied across a diverse and representative space. (Dissolving pure HfO_2 into a variety of melt compositions would be best suited to understand melt composition effects on u_o.) The predictive capability of the models themselves could be significantly improved by including realistic coating microstructural features (e.g., feathery columns and coating tortuosity) and their geometric evolution with time. These features would require more sophisticated moving boundaries to treat. The ICME framework would also benefit from further expansion of the thermodynamic databases. Interest in HfO_2 is increasing, yet the element is wholly absent from the current state-of-the-art databases. Instead, ZrO_2 is often substituted for HfO_2 in the calculations, but the concomitant results are often misleading as the two oxides distinctly react when exposed to molten silicates. Likewise, the databases would benefit from including $YbO_{1.5}$, an important RE for EBCs that is likely to exhibit different reactive crystallization behavior to $YO_{1.5}$ (e.g., by more strongly favoring garnet formation over apatite).

REFERENCES

[1] IATA, (n.d.). https://www.iata.org/en/ (accessed February 11, 2021).

[2] IATA Forecast Predicts 8.2 billion Air Travelers in 2037, (n.d.). https://www.iata.org/en/pressroom/pr/2018-10-24-02/ (accessed February 11, 2021).

[3] T.M. Pollock, S. Tin, Nickel-Based Superalloys for Advanced Turbine Engines: Chemistry, Microstructure and Properties, Journal of Propulsion and Power. 22 (2006) 361–374. https://doi.org/10.2514/1.18239.

[4] R.A. Miller, Current status of thermal barrier coatings — An overview, Surface and Coatings Technology. 30 (1987) 1–11. https://doi.org/10.1016/0257-8972(87)90003-X.

[5] N.P. Padture, M. Gell, E.H. Jordan, Thermal Barrier Coatings for Gas-Turbine Engine Applications, Science. 296 (2002) 280–284. https://doi.org/10.1126/science.1068609.

[6] R.S. Lima, Perspectives on Thermal Gradients in Porous ZrO2-7–8 wt.% Y2O3 (YSZ) Thermal Barrier Coatings (TBCs) Manufactured by Air Plasma Spray (APS), Coatings. 10 (2020) 812. https://doi.org/10.3390/coatings10090812.

[7] N.P. Padture, Advanced structural ceramics in aerospace propulsion, Nature Mater. 15 (2016) 804–809. https://doi.org/10.1038/nmat4687.

[8] F.W. Zok, Ceramic-matrix composites enable revolutionary gains in turbine engine efficiency, Am Ceram Soc Bull. 95 (2016) 22–8.

[9] N.P. Padture, Environmental degradation of high-temperature protective coatings for ceramic-matrix composites in gas-turbine engines, Npj Mater Degrad. 3 (2019) 1–6. https://doi.org/10.1038/s41529-019-0075-4.

[10] D.L. Poerschke, R.W. Jackson, C.G. Levi, Silicate Deposit Degradation of Engineered Coatings in Gas Turbines: Progress Toward Models and Materials Solutions, Annu. Rev. Mater. Res. 47 (2017) 297–330. https://doi.org/10.1146/annurev-matsci-010917.

[11] C.G. Levi, J.W. Hutchinson, M.-H. Vidal-Sétif, C. a. Johnson, Environmental degradation of thermal-barrier coatings by molten deposits, MRS Bulletin. 37 (2012) 932–941. https://doi.org/10.1557/mrs.2012.230.

[12] M.P. Boyce, Gas Turbine Engineering Handbook, Gulf Professional Pub., 2002. https://books.google.com/books?id=nEc2OxxT_uMC.

[13] R.C. Reed, The Superalloys: Fundamentals and Applications, Cambridge University Press, 2008. https://books.google.com/books?id=SIUGcd4a-EkC.

[14] C.G. Levi, Emerging materials and processes for thermal barrier systems, Current Opinion in Solid State and Materials Science. 8 (2004) 77–91. https://doi.org/10.1016/j.cossms.2004.03.009.

[15] R.L. Jones, Thermal barrier coatings, in: K.H. Stern (Ed.), Metallurgical and Ceramic Protective Coatings, Springer Netherlands, Dordrecht, 1996: pp. 194–235. https://doi.org/10.1007/978-94-009-1501-5_8.

[16] J.A. Krogstad, S. Krämer, D.M. Lipkin, C.A. Johnson, D.R.G. Mitchell, J.M. Cairney, C.G. Levi, Phase Stability of t′-Zirconia-Based Thermal Barrier Coatings: Mechanistic Insights,

Journal of the American Ceramic Society. 94 (2011) s168–s177. https://doi.org/10.1111/j.1551-2916.2011.04531.x.
[17] T.A. Taylor, D.L. Appleby, A.E. Weatherill, J. Griffiths, Plasma-sprayed yttria-stabilized zirconia coatings: Structure-property relationships, Surface and Coatings Technology. 43–44 (1990) 470–480. https://doi.org/10.1016/0257-8972(90)90098-W.
[18] H.B. Guo, R. Vaßen, D. Stöver, Thermophysical properties and thermal cycling behavior of plasma sprayed thick thermal barrier coatings, Surface and Coatings Technology. 192 (2005) 48–56. https://doi.org/10.1016/j.surfcoat.2004.02.004.
[19] D.M. Gray, Y.-C. Lau, C.A. Johnson, M.P. Borom, W.A. Nelson, Thermal barrier coatings having an improved columnar microstructure, US5830586A, 1998. https://patents.google.com/patent/US5830586A/en (accessed July 3, 2021).
[20] M.J. Maloney, Thermal barrier coating systems and materials, US6117560A, 2000. https://patents.google.com/patent/US6117560A/en (accessed July 1, 2021).
[21] R. Darolia, Thermal barrier coatings technology: critical review, progress update, remaining challenges and prospects, International Materials Reviews. 58 (2013) 315–348. https://doi.org/10.1179/1743280413Y.0000000019.
[22] J.A. Haynes, B.A. Pint, W.D. Porter, I.G. Wright, Comparison of thermal expansion and oxidation behavior of various high-temperature coating materials and superalloys, Materials at High Temperatures. 21 (2004) 87–94. https://doi.org/10.1179/mht.2004.012.
[23] U. Schulz, B. Saruhan, K. Fritscher, C. Leyens, Review on Advanced EB-PVD Ceramic Topcoats for TBC Applications, International Journal of Applied Ceramic Technology. 1 (2004) 302–315. https://doi.org/10.1111/j.1744-7402.2004.tb00182.x.
[24] R.W. Jackson, E.M. Zaleski, D.L. Poerschke, B.T. Hazel, M.R. Begley, C.G. Levi, Interaction of molten silicates with thermal barrier coatings under temperature gradients, Acta Materialia. 89 (2015) 396–407. https://doi.org/10.1016/j.actamat.2015.01.038.
[25] C. Mercer, S. Faulhaber, A.G. Evans, R. Darolia, A delamination mechanism for thermal barrier coatings subject to calcium-magnesium-alumino-silicate (CMAS) infiltration, Acta Materialia. 53 (2005) 1029–1039. https://doi.org/10.1016/j.actamat.2004.11.028.
[26] S. Krämer, S. Faulhaber, M. Chambers, D.R. Clarke, C.G. Levi, J.W. Hutchinson, A.G. Evans, Mechanisms of cracking and delamination within thick thermal barrier systems in aero-engines subject to calcium-magnesium-alumino-silicate (CMAS) penetration, Materials Science and Engineering A. 490 (2008) 26–35. https://doi.org/10.1016/j.msea.2008.01.006.
[27] J.A. Krogstad, M. Lepple, C.G. Levi, Opportunities for improved TBC durability in the CeO2–TiO2–ZrO2 system, Surface and Coatings Technology. 221 (2013) 44–52. https://doi.org/10.1016/j.surfcoat.2013.01.026.
[28] T.A. Schaedler, R.M. Leckie, S. Krämer, A.G. Evans, C.G. Levi, Toughening of Nontransformable t′-YSZ by Addition of Titania, Journal of the American Ceramic Society. 90 (2007) 3896–3901. https://doi.org/10.1111/j.1551-2916.2007.01990.x.
[29] E.M. Donohue, N.R. Philips, M.R. Begley, C.G. Levi, Thermal barrier coating toughness: Measurement and identification of a bridging mechanism enabled by segmented microstructure, Materials Science and Engineering: A. 564 (2013) 324–330. https://doi.org/10.1016/j.msea.2012.11.126.

[30] A.G. Evans, D.R. Clarke, C.G. Levi, The influence of oxides on the performance of advanced gas turbines, Journal of the European Ceramic Society. 28 (2008) 1405–1419. https://doi.org/10.1016/j.jeurceramsoc.2007.12.023.
[31] C.G. Levi, J.W. Hutchinson, M.-H. Vidal-Sétif, C.A. Johnson, Environmental degradation of thermal-barrier coatings by molten deposits, MRS Bulletin. 37 (2012) 932–941. https://doi.org/10.1557/mrs.2012.230.
[32] R.A. Miller, R.G. Garlick, J. Smialek, Phase distributions in plasma-sprayed zirconia-yttria, Ceram. Bull. 62 (1983) 1355–1358.
[33] J.R. VanValzah, H.E. Eaton, Cooling rate effects on the tetragonal to monoclinic phase transformation in aged plasma-sprayed yttria partially stabilized zirconia, Surface and Coatings Technology. 46 (1991) 289–300. https://doi.org/10.1016/0257-8972(91)90171-R.
[34] J.R. Brandon, R. Taylor, Phase stability of zirconia-based thermal barrier coatings part I. Zirconia-yttria alloys, Surface and Coatings Technology. 46 (1991) 75–90. https://doi.org/10.1016/0257-8972(91)90151-L.
[35] D.R. Clarke, C.G. Levi, Materials Design for the Next Generation Thermal Barrier Coatings, Annual Review of Materials Research. 33 (2003) 383–417. https://doi.org/10.1146/annurev.matsci.33.011403.113718.
[36] M.P. Borom, C.A. Johnson, L.A. Peluso, Role of environment deposits and operating surface temperature in spallation of air plasma sprayed thermal barrier coatings, Surface and Coatings Technology. 86–87 (1996) 116–126. https://doi.org/10.1016/S0257-8972(96)02994-5.
[37] F.H. Stott, D.J.D. Wet, R. Taylor, Degradation of thermal-barrier coatings at very high temperatures, MRS Bulletin. 19 (1994) 46–49.
[38] A.G. Evans, F.W. Zok, The physics and mechanics of fibre-reinforced brittle matrix composites, JOURNAL OF MATERIALS SCIENCE. 29 (1994) 3857–3896. https://doi.org/10.1007/BF00355946.
[39] S.L. dos S. e Lucato, O.H. Sudre, D.B. Marshall, A Method for Assessing Reactions of Water Vapor with Materials in High-Speed, High-Temperature Flow, Journal of the American Ceramic Society. 94 (2011) s186–s195. https://doi.org/10.1111/j.1551-2916.2011.04556.x.
[40] R. Anton, V. Leisner, P. Watermeyer, M. Engstler, U. Schulz, Hafnia-doped silicon bond coats manufactured by PVD for SiC/SiC CMCs, Acta Materialia. 183 (2020) 471–483. https://doi.org/10.1016/j.actamat.2019.10.050.
[41] N.S. Jacobson, Silica Activity Measurements in the Y2O3–SiO2 System and Applications to Modeling of Coating Volatility, Journal of the American Ceramic Society. 97 (2014) 1959–1965. https://doi.org/10.1111/jace.12974.
[42] G.C.C. Costa, N.S. Jacobson, Mass spectrometric measurements of the silica activity in the Yb2O3–SiO2 system and implications to assess the degradation of silicate-based coatings in combustion environments, Journal of the European Ceramic Society. 35 (2015) 4259–4267. https://doi.org/10.1016/j.jeurceramsoc.2015.07.019.

[43] L.R. Turcer, N.P. Padture, Towards multifunctional thermal environmental barrier coatings (TEBCs) based on rare-earth pyrosilicate solid-solution ceramics, Scripta Materialia. 154 (2018) 111–117. https://doi.org/10.1016/j.scriptamat.2018.05.032.
[44] A.J. Fernández-Carrión, M. Allix, A.I. Becerro, Thermal expansion of rare-earth pyrosilicates, Journal of the American Ceramic Society. 96 (2013) 2298–2305. https://doi.org/10.1111/jace.12388.
[45] N.A. Nasiri, N. Patra, D. Horlait, D.D. Jayaseelan, W.E. Lee, Thermal Properties of Rare-Earth Monosilicates for EBC on Si-Based Ceramic Composites, Journal of the American Ceramic Society. 99 (2016) 589–596. https://doi.org/10.1111/jace.13982.
[46] E. Bakan, D. Marcano, D. Zhou, Y.J. Sohn, G. Mauer, R. Vaßen, Yb2Si2O7 Environmental Barrier Coatings Deposited by Various Thermal Spray Techniques: A Preliminary Comparative Study, J Therm Spray Tech. 26 (2017) 1011–1024. https://doi.org/10.1007/s11666-017-0574-1.
[47] J.L. Smialek, F.A. Archer, R.G. Garlick, The chemistry of Saudi Arabian sand-A deposition problem on helicopter turbine airfoils, in: 24th International SAMPE Technical Conference, 1992: pp. M63–M77.
[48] M.G. Dunn, A.J. Baran, J. Miatech, Operation of Gas Turbine Engines in Volcanic Ash Clouds, Journal of Engineering for Gas Turbines and Power. 118 (1996) 724–731. https://doi.org/10.1115/1.2816987.
[49] D. Presnall, S.A. Dixon, J.R. Dixon, T. O'donnell, N. Brenner, R. Schrock, D. Dycus, Liquidus phase relations on the join diopside-forsterite-anorthite from 1 atm to 20 kbar: their bearing on the generation and crystallization of basaltic magma, Contributions to Mineralogy and Petrology. 66 (1978) 203–220.
[50] TCOX-10: TCS Metal Oxide Solutions Database, Thermo-Calc Software, Solna, Sweden, n.d. https://www.thermocalc.com.
[51] C.W. Bale, E. Bélisle, P. Chartrand, S.A. Decterov, G. Eriksson, A.E. Gheribi, K. Hack, I.-H. Jung, Y.-B. Kang, J. Melançon, A.D. Pelton, S. Petersen, C. Robelin, J. Sangster, P. Spencer, M.-A. Van Ende, FactSage thermochemical software and databases, 2010–2016, Calphad. 54 (2016) 35–53. https://doi.org/10.1016/j.calphad.2016.05.002.
[52] FToxid: FACT oxide database, GTT-Technologies, Montreal, Canada, n.d. http://www.crct.polymtl.ca/fact/.
[53] A.G. Evans, J.W. Hutchinson, The mechanics of coating delamination in thermal gradients, Surface and Coatings Technology. 201 (2007) 7905–7916. https://doi.org/10.1016/j.surfcoat.2007.03.029.
[54] R.W. Jackson, M.R. Begley, Critical cooling rates to avoid transient-driven cracking in thermal barrier coating (TBC) systems, International Journal of Solids and Structures. 51 (2014) 1364–1374. https://doi.org/10.1016/j.ijsolstr.2013.12.029.
[55] A.G. Evans, D.R. Mumm, J.W. Hutchinson, G.H. Meier, F.S. Pettit, Mechanisms controlling the durability of thermal barrier coatings, Progress in Materials Science. 46 (2001) 505–553. https://doi.org/10.1016/S0079-6425(00)00020-7.
[56] S. Krämer, J. Yang, C.G. Levi, C.A. Johnson, Thermochemical interaction of thermal barrier coatings with molten CaO-MgO-Al 2O 3-SiO 2 (CMAS) deposits, Journal of the American

Ceramic Society. 89 (2006) 3167–3175. https://doi.org/10.1111/j.1551-2916.2006.01209.x.
[57] O. Fabrichnaya, Ch. Wang, M. Zinkevich, F. Aldinger, C.G. Levi, Phase equilibria and thermodynamic properties of the ZrO2-GdO1.5-YO1.5 system, J Phs Eqil and Diff. 26 (2005) 591–604. https://doi.org/10.1007/s11669-005-0004-9.
[58] D.L. Poerschke, T.L. Barth, C.G. Levi, Equilibrium relationships between thermal barrier oxides and silicate melts, Acta Materialia. 120 (2016) 302–314. https://doi.org/10.1016/j.actamat.2016.08.077.
[59] E.M. Zaleski, C. Ensslen, C.G. Levi, Melting and Crystallization of Silicate Systems Relevant to Thermal Barrier Coating Damage, Journal of the American Ceramic Society. 98 (2015) 1642–1649. https://doi.org/10.1111/jace.13478.
[60] S. Krämer, J. Yang, C.G. Levi, Infiltration-inhibiting reaction of gadolinium zirconate thermal barrier coatings with CMAS melts, Journal of the American Ceramic Society. 91 (2008) 576–583. https://doi.org/10.1111/j.1551-2916.2007.02175.x.
[61] J.M. Drexler, C.-H. Chen, A.D. Gledhill, K. Shinoda, S. Sampath, N.P. Padture, Plasma sprayed gadolinium zirconate thermal barrier coatings that are resistant to damage by molten Ca–Mg–Al–silicate glass, Surface and Coatings Technology. 206 (2012) 3911–3916. https://doi.org/10.1016/j.surfcoat.2012.03.051.
[62] U. Schulz, W. Braue, Degradation of La2Zr2O7 and other novel EB-PVD thermal barrier coatings by CMAS (CaO–MgO–Al2O3–SiO2) and volcanic ash deposits, Surface and Coatings Technology. 235 (2013) 165–173. https://doi.org/10.1016/j.surfcoat.2013.07.029.
[63] N. Chellah, M.-H. Vidal-Sétif, C. Petitjean, P.-J. Panteix, C. Rapin, M. Vilasi, Calcium-magnesium-alumino-silicate (CMAS) degradation of thermal barrier coatings: solubility of different oxides from ZrO2-Nd2O3 system in a model CMAS., in: Les Embiez, Fr, 2012.
[64] H. Zhao, C.G. Levi, H.N.G. Wadley, Molten silicate interactions with thermal barrier coatings, Surface and Coatings Technology. 251 (2014) 74–86. https://doi.org/10.1016/j.surfcoat.2014.04.007.
[65] D.L. Poerschke, D.D. Hass, S. Eustis, G.G.E. Seward, J.S. Van Sluytman, C.G. Levi, Stability and CMAS Resistance of Ytterbium-Silicate/Hafnate EBCs/TBC for SiC Composites, Journal of the American Ceramic Society. 98 (2015) 278–286. https://doi.org/10.1111/jace.13262.
[66] D.L. Poerschke, C.G. Levi, Effects of cation substitution and temperature on the interaction between thermal barrier oxides and molten CMAS, Journal of the European Ceramic Society. 35 (2015) 681–691. https://doi.org/10.1016/j.jeurceramsoc.2014.09.006.
[67] R.W. Jackson, E.M. Zaleski, B.T. Hazel, M.R. Begley, C.G. Levi, Response of molten silicate infiltrated Gd2Zr2O7 thermal barrier coatings to temperature gradients, Acta Materialia. 132 (2017) 538–549. https://doi.org/10.1016/j.actamat.2017.03.081.
[68] R.M. Leckie, S. Krämer, M. Rühle, C.G. Levi, Thermochemical compatibility between alumina and ZrO2–GdO3/2 thermal barrier coatings, Acta Materialia. 53 (2005) 3281–3292. https://doi.org/10.1016/j.actamat.2005.03.035.

[69] B. Saruhan, P. Francois, K. Fritscher, U. Schulz, EB-PVD processing of pyrochlore-structured La2Zr2O7-based TBCs, Surface and Coatings Technology. 182 (2004) 175–183. https://doi.org/10.1016/j.surfcoat.2003.08.068.
[70] M.P. Schmitt, A.K. Rai, R. Bhattacharya, D. Zhu, D.E. Wolfe, "Multilayer thermal barrier coating (TBC) architectures utilizing rare earth doped YSZ and rare earth pyrochlores," Surface and Coatings Technology. 251 (2014) 56–63. https://doi.org/10.1016/j.surfcoat.2014.03.049.
[71] K.M. Grant, S. Krämer, G.G.E. Seward, C.G. Levi, Calcium-magnesium alumino-silicate interaction with yttrium monosilicate environmental barrier coatings, Journal of the American Ceramic Society. 93 (2010) 3504–3511. https://doi.org/10.1111/j.1551-2916.2010.03916.x.
[72] K.M. Grant, S. Krämer, J.P.A. Löfvander, C.G. Levi, CMAS degradation of environmental barrier coatings, Surface and Coatings Technology. 202 (2007) 653–657. https://doi.org/10.1016/j.surfcoat.2007.06.045.
[73] H. Zhao, B.T. Richards, C.G. Levi, H.N.G. Wadley, Molten silicate reactions with plasma sprayed ytterbium silicate coatings, Surface and Coatings Technology. 288 (2016) 151–162. https://doi.org/10.1016/j.surfcoat.2015.12.053.
[74] T.S. Key, K.F. Presley, R.S. Hay, E.E. Boakye, Total Thermal Expansion Coefficients of the Yttrium Silicate Apatite Phase Y4.69(SiO4)3O, Journal of the American Ceramic Society. 97 (2014) 28–31. https://doi.org/10.1111/jace.12619.
[75] R.H. Hopkins, J. de Klerk, P. Piotrowski, M.S. Walker, M.P. Mathur, Thermal and elastic properties of silicate oxyapatite crystals, Journal of Applied Physics. 44 (1973) 2456–2458. https://doi.org/10.1063/1.1662596.
[76] V.L. Wiesner, N.P. Bansal, Mechanical and thermal properties of calcium–magnesium aluminosilicate (CMAS) glass, Journal of the European Ceramic Society. 35 (2015) 2907–2914. https://doi.org/10.1016/j.jeurceramsoc.2015.03.032.
[77] W.D. Summers, D.L. Poerschke, M.R. Begley, C.G. Levi, F.W. Zok, A computational modeling framework for reaction and failure of environmental barrier coatings under silicate deposits, Journal of the American Ceramic Society. 103 (2020) 5196–5213. https://doi.org/10.1111/jace.17187.
[78] D.L. Poerschke, J.H. Shaw, N. Verma, F.W. Zok, C.G. Levi, Interaction of yttrium disilicate environmental barrier coatings with calcium-magnesium-iron alumino-silicate melts, Acta Materialia. 145 (2018) 451–461. https://doi.org/10.1016/j.actamat.2017.12.004.
[79] W.D. Summers, D.L. Poerschke, D. Park, J.H. Shaw, F.W. Zok, C.G. Levi, Roles of composition and temperature in silicate deposit-induced recession of yttrium disilicate, Acta Materialia. 160 (2018) 34–46. https://doi.org/10.1016/j.actamat.2018.08.043.
[80] W.D. Summers, D.L. Poerschke, A.A. Taylor, A.R. Ericks, C.G. Levi, F.W. Zok, Reactions of molten silicate deposits with yttrium monosilicate, Journal of the American Ceramic Society. 103 (2020) 2919–2932. https://doi.org/10.1111/jace.16972.
[81] TCOX-6: TCS Metal Oxide Solutions Database, Thermo-Calc Software, Solna, Sweden, n.d. https://www.thermocalc.com.

[82] A. Fluegel, D.A. Earl, A.K. Varshneya, T.P. Seward, Density and thermal expansion calculation of silicate glass melts from 1000°C to 1400°C, Physics and Chemistry of Glasses - European Journal of Glass Science AndTechnology Part B. 49 (2008) 245–257.
[83] M.R. Begley, J.W. Hutchinson, The Mechanics and Reliability of Films, Multilayers and Coatings, Cambridge University Press, 2017. https://books.google.com/books?id=KFtEDgAAQBAJ.
[84] M.R. Begley, LayerSlayer, Santa Barbara, CA, USA, n.d. https://sites.engineering.ucsb.edu/~begley/LayerSlayer.html.
[85] W.D. Summers, M.R. Begley, F.W. Zok, Transition from penetration cracking to spallation in environmental barrier coatings on ceramic composites, Surface and Coatings Technology. 378 (2019) 125083. https://doi.org/10.1016/j.surfcoat.2019.125083.
[86] R. Naraparaju, J.J. Gomez Chavez, P. Niemeyer, K.-U. Hess, W. Song, D.B. Dingwell, S. Lokachari, C.V. Ramana, U. Schulz, Estimation of CMAS infiltration depth in EB-PVD TBCs: A new constraint model supported with experimental approach, Journal of the European Ceramic Society. 39 (2019) 2936–2945. https://doi.org/10.1016/j.jeurceramsoc.2019.02.040.
[87] D. Giordano, J.K. Russell, D.B. Dingwell, Viscosity of magmatic liquids: A model, Earth and Planetary Science Letters. 271 (2008) 123–134. https://doi.org/10.1016/j.epsl.2008.03.038.
[88] A. Fluegel, Glass viscosity calculation based on a global statistical modelling approach, Glass Technology - European Journal of Glass Science and Technology Part A. 48 (2007) 13–30.
[89] V.L. Wiesner, U.K. Vempati, N.P. Bansal, High temperature viscosity of calcium-magnesium-aluminosilicate glass from synthetic sand, Scripta Materialia. 124 (2016) 189–192. https://doi.org/10.1016/j.scriptamat.2016.12.007.
[90] R. Webster, E.J. Opila, Experimental viscosity of CMAS melts as a function of composition and temperature, (2020).
[91] D. Müller, D.B. Dingwell, The influence of thermal barrier coating dissolution on CMAS melt viscosities, Journal of the European Ceramic Society. 41 (2021) 2746–2752. https://doi.org/10.1016/j.jeurceramsoc.2020.11.037.
[92] N. Chellah, Contribution à la compréhension de la dégradation chimique de barrières thermiques en zircone yttriée par les CMAS en vue de proposer une nouvelle composition céramique résistante dans le système ZrO2-Nd2O3, l'Université de Lorraine, 2013.
[93] F. Perrudin, C. Rio, M.H. Vidal-Sétif, C. Petitjean, P.J. Panteix, M. Vilasi, Gadolinium oxide solubility in molten silicate: dissolution mechanism and stability of Ca2Gd8(SiO4)6O2 and Ca3Gd2(Si3O9)2 silicate phases, Journal of the European Ceramic Society. 37 (2017) 2657–2665. https://doi.org/10.1016/j.jeurceramsoc.2017.02.022.
[94] F. Perrudin, M.H. Vidal-Sétif, C. Rio, C. Petitjean, P.J. Panteix, M. Vilasi, Influence of rare earth oxides on kinetics and reaction mechanisms in CMAS silicate melts, Journal of the European Ceramic Society. 39 (2019) 4223–4232. https://doi.org/10.1016/j.jeurceramsoc.2019.06.036.
[95] Y. Yu, Y. Zhang, Y. Chen, Z. Xu, Kinetics of anorthite dissolution in basaltic melt, Geochimica et Cosmochimica Acta. 179 (2016) 257–274. https://doi.org/10.1016/j.gca.2016.02.002.

[96] Y. Zhang, D. Walker, C.E. Lesher, Diffusive crystal dissolution, Contributions to Mineralogy and Petrology. 102 (1989) 492–513. https://doi.org/10.1007/BF00371090.
[97] Y. Chen, Y. Zhang, Olivine dissolution in basaltic melt, Geochimica et Cosmochimica Acta. 72 (2008) 4756–4777. https://doi.org/10.1016/j.gca.2008.07.014.
[98] Y. Zhang, Geochemical kinetics, Princeton University Press, Princeton, N.J., 2008.
[99] C.S.J. Shaw, Effects of melt viscosity and silica activity on the rate and mechanism of quartz dissolution in melts of the CMAS and CAS systems, Contributions to Mineralogy and Petrology. 151 (2006) 665–680. https://doi.org/10.1007/s00410-006-0086-3.
[100] Y. Zhang, H. Ni, Y. Chen, Diffusion Data in Silicate Melts, Reviews in Mineralogy and Geochemistry. 72 (2010) 311–408. https://doi.org/10.2138/rmg.2010.72.8.
[101] Y. Zhang, Diffusion in Minerals and Melts: Theoretical Background, Reviews in Mineralogy and Geochemistry. 72 (2010).
[102] J.B. Wachtman, A.D. Franklin, eds., Mass Transport in Oxides, National Bureau of Standards Publication, 1968.
[103] Y. Liang, Multicomponent Diffusion in Molten Silicates: Theory, Experiments, and Geological Applications, Reviews in Mineralogy and Geochemistry. 72 (2010) 409–446. https://doi.org/10.2138/rmg.2010.72.9.
[104] H. Ni, H. Hui, G. Steinle-Neumann, Transport properties of silicate melts, Reviews of Geophysics. 53 (2015) 715–744. https://doi.org/10.1002/2015RG000485.
[105] W.D. Kingery, Introduction to Ceramics, John Wiley & Sons, Inc., New York, 1960.
[106] J.E. Mungall, Empirical models relating viscosity and tracer diffusion in magmatic silicate melts, Geochimica et Cosmochimica Acta. 66 (2002) 125–143. https://doi.org/10.1016/S0016-7037(01)00736-0.
[107] H. Eyring, Viscosity, Plasticity, and Diffusion as Examples of Absolute Reaction Rates, J. Chem. Phys. 4 (1936) 283–291. https://doi.org/10.1063/1.1749836.
[108] S. Glasstone, H. Eyring, K.J. Laidler, The theory of rate processes, McGraw-Hill, 1941. https://scholar.google.com/scholar?hl=en&q=The+theory+of+rate+processes&btnG=&as_sdt=1%2C5&as_sdtp=.
[109] H. Ni, Y. Zhang, H2O diffusion models in rhyolitic melt with new high pressure data, Chemical Geology. 250 (2008) 68–78. https://doi.org/10.1016/j.chemgeo.2008.02.011.
[110] A. Quintas, D. Caurant, O. Majérus, P. Loiseau, T. Charpentier, J.-L. Dussossoy, ZrO2 addition in soda-lime aluminoborosilicate glasses containing rare earths: Impact on the network structure, Journal of Alloys and Compounds. 714 (2017) 47–62. https://doi.org/10.1016/j.jallcom.2017.04.182.
[111] H. Behrens, M. Hahn, Trace element diffusion and viscous flow in potassium-rich trachytic and phonolitic melts, Chemical Geology. 259 (2009) 63–77. https://doi.org/10.1016/j.chemgeo.2008.10.014.
[112] J. Koepke, H. Behrens, Trace element diffusion in andesitic melts: an application of synchrotron X-ray fluorescence analysis, Geochimica et Cosmochimica Acta. 65 (2001) 1481–1498. https://doi.org/10.1016/S0016-7037(01)00550-6.
[113] J.E. Mungall, D.B. Dingwell, M. Chaussidon, Chemical diffusivities of 18 trace elements in granitoid melts, Geochimica et Cosmochimica Acta. 63 (1999) 2599–2610. https://doi.org/10.1016/S0016-7037(99)00209-4.

[114] T. Schaller, J.F. Stebbins, The Structural Role of Lanthanum and Yttrium in Aluminosilicate Glasses: A 27Al and 17O MAS NMR Study, J. Phys. Chem. B. 102 (1998) 10690–10697. https://doi.org/10.1021/jp982387m.
[115] A.K. Varshneya, Fundamentals of Inorganic Glasses, Elsevier Science, 2013. https://books.google.com/books?id=MSgXBQAAQBAJ.
[116] J. Felsche, The crystal chemistry of the rare-earth silicates, in: Rare Earths, Springer, 1973: pp. 99–197.
[117] S.T. Misture, S.P. Harvey, R.T. Francy, Y.G.S. DeCarr, S.C. Bancheri, Synthesis, crystal structure, and anisotropic thermal expansion of Dy4.67(SiO4)3O, Journal of Materials Research. 19 (2004) 2330–2335. https://doi.org/10.1557/JMR.2004.0294.
[118] J. R. Tolchard, M. Saiful Islam, P. R. Slater, Defect chemistry and oxygen ion migration in the apatite -type materials La 9.33 Si 6 O 26 and La 8 Sr 2 Si 6 O 26, Journal of Materials Chemistry. 13 (2003) 1956–1961. https://doi.org/10.1039/B302748C.
[119] D.L. Poerschke, C.G. Levi, Phase equilibria in the calcia-gadolinia-silica system, Journal of Alloys and Compounds. 695 (2017) 1397–1404. https://doi.org/10.1016/j.jallcom.2016.10.263.
[120] D.L. Poerschke, T.L. Barth, O. Fabrichnaya, C.G. Levi, Phase equilibria and crystal chemistry in the calcia–silica–yttria system, Journal of the European Ceramic Society. 36 (2016) 1743–1754. https://doi.org/10.1016/j.jeurceramsoc.2016.01.046.
[121] P. Mechnich, W. Braue, Volcanic Ash-Induced Decomposition of EB-PVD Gd2Zr2O7 Thermal Barrier Coatings to Gd-Oxyapatite, Zircon, and Gd, Fe-Zirconolite, Journal of the American Ceramic Society. 96 (2013) 1958–1965. https://doi.org/10.1111/jace.12251.
[122] H. Mao, M. Selleby, O. Fabrichnaya, Thermodynamic reassessment of the Y 2O3–Al2O3–SiO2 system and its subsystems, Calphad. 32 (2008) 399–412. https://doi.org/10.1016/j.calphad.2008.03.003.
[123] J.W. Nielsen, E.F. Dearborn, The growth of single crystals of magnetic garnets, Journal of Physics and Chemistry of Solids. 5 (1958) 202–207. https://doi.org/10.1016/0022-3697(58)90068-4.
[124] J.J. Gomez Chavez, R. Naraparaju, P. Mechnich, K. Kelm, U. Schulz, C.V. Ramana, Effects of yttria content on the CMAS infiltration resistance of yttria stabilized thermal barrier coatings system, Journal of Materials Science & Technology. 43 (2020) 74–83. https://doi.org/10.1016/j.jmst.2019.09.039.
[125] R. Naraparaju, J.J. Gomez Chavez, U. Schulz, C.V. Ramana, Interaction and infiltration behavior of Eyjafjallajökull, Sakurajima volcanic ashes and a synthetic CMAS containing FeO with/in EB-PVD ZrO2-65 wt% Y2 O3 coating at high temperature, Acta Materialia. 136 (2017) 164–180. https://doi.org/10.1016/j.actamat.2017.06.055.
[126] N.K. Eils, P. Mechnich, W. Braue, Effect of CMAS Deposits on MOCVD Coatings in the System Y2O3–ZrO2: Phase Relationships, Journal of the American Ceramic Society. 96 (2013) 3333–3340. https://doi.org/10.1111/jace.12502.
[127] E. Godbole, N. Karthikeyan, D. Poerschke, Garnet stability in the Al–Ca–Mg–Si–Y–O system with implications for reactions between TBCs, EBCs, and silicate deposits, Journal of the American Ceramic Society. n/a (n.d.). https://doi.org/10.1111/jace.17176.

[128] S. Colin, B. Dupre, G. Venturini, B. Malaman, C. Gleitzer, Crystal Structure and Infrared Spectrum of the Cyclosilicate Ca2ZrSi4O12, Journal of Solid State Chemistry. 102 (1993) 242–249. https://doi.org/10.1006/jssc.1993.1028.
[129] H. Yamane, T. Nagasawa, M. Shimada, T. Endo, Ca3Y2(Si3O9)2, Acta Cryst C. 53 (1997) 1533–1536. https://doi.org/10.1107/S010827019700721X.
[130] S.Y. Kwon, W.-Y. Kim, P. Hudon, I.-H. Jung, Thermodynamic modeling of the CaO-SiO2-ZrO2 system coupled with key phase diagram experiments, Journal of the European Ceramic Society. 37 (2017) 1095–1104. https://doi.org/10.1016/j.jeurceramsoc.2016.10.011.
[131] K. Robinson, G.V. Gibbs, P.H. Ribbe, The Structure of Zircon: A Comparison With Garnet, American Mineralogist. 56 (1971) 782–790.
[132] J.M. Hanchar, R.J. Finch, P.W.O. Hoskin, E.B. Watson, D.J. Cherniak, A.N. Mariano, Rare earth elements in synthetic zircon: Part 1. Synthesis, and rare earth element and phosphorus doping, American Mineralogist. 86 (2001) 667–680. https://doi.org/10.2138/am-2001-5-607.
[133] D. Shin, R. Arróyave, Z.-K. Liu, Thermodynamic modeling of the Hf–Si–O system, Calphad. 30 (2006) 375–386. https://doi.org/10.1016/j.calphad.2006.08.006.
[134] H. Ibégazène, S. Alpérine, C. Diot, Yttria-stabilized hafnia-zirconia thermal barrier coatings: The influence of hafnia addition on TBC structure and high-temperature behaviour, J Mater Sci. 30 (1995) 938–951. https://doi.org/10.1007/BF01178428.
[135] H. Mao, M. Hillert, M. Selleby, B. Sundman, Thermodynamic Assessment of the CaO–Al2O3–SiO2 System, Journal of the American Ceramic Society. 89 (2006) 298–308. https://doi.org/10.1111/j.1551-2916.2005.00698.x.
[136] R.M. Smart, F.P. Glasser, The subsolidus phase equilibria and melting temperatures of MgO□Al2O3□SiO2 compositions, Ceramics International. 7 (1981) 90–97. https://doi.org/10.1016/0272-8842(81)90003-1.
[137] A. Muan, Phase Equilibria at Liquidus Temperatures in the System Iron Oxide–Al2O3–SiO3 in Air Atmosphere, Journal of the American Ceramic Society. 40 (1957) 121–133. https://doi.org/10.1111/j.1151-2916.1957.tb12588.x.
[138] A. Muan, E.F. Osborn, Phase Equilibria at Liquidus Temperatures in the System MgO-FeO-Fe2O3-SiO2, Journal of the American Ceramic Society. 39 (1956) 121–140. https://doi.org/10.1111/j.1151-2916.1956.tb14178.x.
[139] F. Tsukihashi, H. Kimura, The effect of MgO and Al2O3 additions on the liquidus of the CaO-SiO2-FeOx system at various partial pressure of oxygen., in: Yazawa International Symposium on Metallurgical and Materials Processing: Principles and Technologies, 2003: pp. 851–860.
[140] S. Lakiza, O. Fabrichnaya, M. Zinkevich, F. Aldinger, On the phase relations in the ZrO2–YO1.5–AlO1.5 system, Journal of Alloys and Compounds. 420 (2006) 237–245. https://doi.org/10.1016/j.jallcom.2005.09.079.
[141] O. Fabrichnaya, F. Aldinger, Assessment of thermodynamic parameters in the system ZrO2–Y2O3–Al2O3, Zeitschrift Für Metallkunde. 95 (2004) 27–39.

[142] N.M. Abdul-Jabbar, D.L. Poerschke, C. Gabbett, C.G. Levi, Phase equilibria in the zirconia–yttria/gadolinia–silica systems, Journal of the European Ceramic Society. 38 (2018) 3286–3296. https://doi.org/10.1016/j.jeurceramsoc.2018.03.020.
[143] A.S. Risbud, K.B. Helean, M.C. Wilding, P. Lu, A. Navrotsky, Enthalpies of formation of lanthanide oxyapatite phases, Journal of Materials Research. 16 (2001) 2780–2783. https://doi.org/10.1557/JMR.2001.0381.
[144] J. Wang, H.P. Li, R. Stevens, Hafnia and hafnia-toughened ceramics, J Mater Sci. 27 (1992) 5397–5430. https://doi.org/10.1007/BF00541601.
[145] Creative Commons Legal Code, (n.d.). https://creativecommons.org/licenses/by/2.5/legalcode (accessed July 6, 2021).
[146] R.D. Shannon, Revised effective ionic radii and systematic studies of interatomic distances in halides and chalcogenides, Acta Cryst A. 32 (1976) 751–767. https://doi.org/10.1107/S0567739476001551.
[147] M. Ciomaga Hatnean, M.R. Lees, G. Balakrishnan, Growth of single-crystals of rare-earth zirconate pyrochlores, Ln 2Zr 2O 7 (with Ln=La, Nd, Sm, and Gd) by the floating zone technique, Journal of Crystal Growth. 418 (2015) 1–6. https://doi.org/10.1016/j.jcrysgro.2015.01.037.
[148] O. Guillon, J. Gonzalez-Julian, B. Dargatz, T. Kessel, G. Schierning, J. Räthel, M. Herrmann, Field-Assisted Sintering Technology/Spark Plasma Sintering: Mechanisms, Materials, and Technology Developments, Advanced Engineering Materials. 16 (2014) 830–849. https://doi.org/10.1002/adem.201300409.
[149] D.L. Poerschke, J.S. Van Sluytman, K.B. Wong, C.G. Levi, Thermochemical compatibility of ytterbia–(hafnia/silica) multilayers for environmental barrier coatings, Acta Materialia. 61 (2013) 6743–6755. https://doi.org/10.1016/j.actamat.2013.07.047.
[150] J.J.G. Chavez, R. Naraparaju, C. Mikulla, P. Mechnich, K. Kelm, C.V. Ramana, U. Schulz, Comparative study of EB-PVD gadolinium-zirconate and yttria-rich zirconia coatings performance against Fe-containing calcium-magnesium-aluminosilicate (CMAS) infiltration, Corrosion Science. 190 (2021) 109660. https://doi.org/10.1016/j.corsci.2021.109660.
[151] S. Duluard, E. Delon, J.-P. Bonino, A. Malié, A. Joulia, L. Bianchi, P. Gomez, F. Ansart, Transient and steady states of Gd2Zr2O7 and 2ZrO2·Y2O3 (ss) interactions with calcium magnesium aluminium silicates, Journal of the European Ceramic Society. 39 (2019) 1451–1462. https://doi.org/10.1016/j.jeurceramsoc.2018.12.016.
[152] R.I. Webster, E.J. Opila, Mixed phase ytterbium silicate environmental-barrier coating materials for improved calcium–magnesium–alumino-silicate resistance, Journal of Materials Research. 35 (2020) 2358–2372. https://doi.org/10.1557/jmr.2020.151.
[153] D.B. Wittry, N.C. Barbi, X-ray Crystal Spectrometers and Monochromators in Microanalysis, Microsc Microanal. 7 (2001) 124–141. https://doi.org/10.1007/S100050010080.
[154] A. Fluegel, Global Model for Calculating Room-Temperature Glass Density from the Composition, Journal of the American Ceramic Society. 90 (2007) 2622–2625. https://doi.org/10.1111/j.1551-2916.2007.01751.x.

[155] M. Newville, T. Stensitzki, D.B. Allen, A. Ingargiola, LMFIT: Non-Linear Least-Square Minimization and Curve-Fitting for Python¶, 2014. https://doi.org/10.5281/zenodo.11813.
[156] A. Dietzel, Strukturchemie des Glases, in: F. Süffert (Ed.), Die Naturwissenschaften, Springer, Berlin, Heidelberg, 1941: pp. 537–547. https://doi.org/10.1007/978-3-642-51845-4_57.
[157] S.Y. Kwon, I.-H. Jung, Critical evaluation and thermodynamic optimization of the CaO-ZrO2 and SiO2-ZrO2 systems, Journal of the European Ceramic Society. 37 (2017) 1105–1116. https://doi.org/10.1016/j.jeurceramsoc.2016.10.008.
[158] S.L. Dole, O. Hunter, F.W. Calderwood, D.J. Bray, Microcracking of Monoclinic HfO2, Journal of the American Ceramic Society. 61 (1978) 486–490. https://doi.org/10.1111/j.1151-2916.1978.tb16123.x.
[159] J.A. Krogstad, M. Lepple, Y. Gao, D.M. Lipkin, C.G. Levi, Effect of Yttria Content on the Zirconia Unit Cell Parameters, Journal of the American Ceramic Society. 94 (2011) 4548–4555. https://doi.org/10.1111/j.1551-2916.2011.04862.x.
[160] D.W. Stacy, D.R. Wilder, The Yttria-Hafnia System, Journal of the American Ceramic Society. 58 (1975) 285–288. https://doi.org/10.1111/j.1151-2916.1975.tb11476.x.
[161] K. Wu, Z. Jin, Thermodynamic assessment of the HfO2-YO1.5 quasibinary system, Calphad. 21 (1997) 421–431. https://doi.org/10.1016/S0364-5916(97)00042-4.
[162] F.F. Lange, Transformation toughening, J Mater Sci. 17 (1982) 240–246. https://doi.org/10.1007/BF00809059.
[163] U. Schulz, S.G. Terry, C.G. Levi, Microstructure and texture of EB-PVD TBCs grown under different rotation modes, Materials Science and Engineering: A. 360 (2003) 319–329. https://doi.org/10.1016/S0921-5093(03)00470-2.
[164] S. Sampath, U. Schulz, M.O. Jarligo, S. Kuroda, Processing science of advanced thermal-barrier systems, MRS Bulletin. 37 (2012) 903–910. https://doi.org/10.1557/mrs.2012.233.
[165] Wolfram Mathematica, Wolfram Research, Champaign, Illinois, n.d.
[166] COMSOL Multiphysics®, COMSOL AB, Stockholm, Sweden, n.d. www.comsol.com.
[167] A. Kucuk, A.G. Clare, L. Jones, An estimation of the surface tension for silicate glass melts at 1400°C using statistical analysis, Glass Technology. 40 (1999) 149–153.
[168] K.-H. Sun, Fundamental Condition of Glass Formation*, Journal of the American Ceramic Society. 30 (1947) 277–281. https://doi.org/10.1111/j.1151-2916.1947.tb19654.x.
[169] Thermo-Calc 2020b is Released, Thermo-Calc Software. (n.d.). https://thermocalc.com/blog/thermo-calc-2020b-is-released/ (accessed July 30, 2021).
[170] W. Braue, P. Mechnich, Recession of an EB-PVD YSZ Coated Turbine Blade by CaSO4 and Fe, Ti-Rich CMAS-Type Deposits, Journal of the American Ceramic Society. 94 (2011) 4483–4489. https://doi.org/10.1111/j.1551-2916.2011.04747.x.
[171] E. Osborn, A. Muan, The System CaO–Al2O3–SiO2, Phase Diagrams for Ceramists,. (1960) 219.
[172] B. Phillips, A. Muan, Phase Equilibria in the System CaO-Iron Oxide-SiO2, in Air, Journal of the American Ceramic Society. 42 (1959) 413–423. https://doi.org/10.1111/j.1151-2916.1959.tb12966.x.

[173] Phase Equilibria Diagrams Online Database (NIST Standard Reference Database 31), The American Ceramic Society and the National Institute of Standards and Technology, n.d.
[174] W.F. Foshag, New Mineral Names, American Mineralogist. 24 (1939) 278–280.
[175] N.C. George, K.A. Denault, R. Seshadri, Phosphors for Solid-State White Lighting, Annual Review of Materials Research. 43 (2013) 481–501. https://doi.org/10.1146/annurev-matsci-073012-125702.
[176] P.F. Smet, A.B. Parmentier, D. Poelman, Selecting Conversion Phosphors for White Light-Emitting Diodes, J. Electrochem. Soc. 158 (2011) R37. https://doi.org/10.1149/1.3568524.
[177] J.E. Geusic, H.M. Marcos, L.G. Van Uitert, LASER OSCILLATIONS IN Nd-DOPED YTTRIUM ALUMINUM, YTTRIUM GALLIUM AND GADOLINIUM GARNETS, Appl. Phys. Lett. 4 (1964) 182–184. https://doi.org/10.1063/1.1753928.
[178] S. Shionoya, W.M. Yen, H. Yamamoto, Phosphor Handbook, CRC Press, 2018. https://books.google.com/books?id=Il7LBQAAQBAJ.
[179] A. Talalaevskij, M. Decker, J. Stigloher, A. Mitra, H.S. Körner, O. Cespedes, C.H. Back, B.J. Hickey, Magnetic properties of spin waves in thin yttrium iron garnet films, Phys. Rev. B. 95 (2017) 064409. https://doi.org/10.1103/PhysRevB.95.064409.
[180] H.J.V. Hook, Phase Relations in the Garnet Region of the System Y2O3–Fe2O3–FeO–Al2O3, Journal of the American Ceramic Society. 46 (1963) 121–124. https://doi.org/10.1111/j.1151-2916.1963.tb11693.x.
[181] E.S. Grew, J.H. Marsh, M.G. Yates, B. Lazic, T. Armbruster, A. Locock, S.W. Bell, M.D. Dyar, H.-J. Bernhardt, O. Medenbach, MENZERITE-(Y), A NEW SPECIES, {(Y,REE)(Ca,Fe2+)2}[(Mg,Fe2+)(Fe3+,Al)](Si3)O12, FROM A FELSIC GRANULITE, PARRY SOUND, ONTARIO, AND A NEW GARNET END-MEMBER, {Y2Ca}[Mg2](Si3)O12, The Canadian Mineralogist. 48 (2010) 1171–1193. https://doi.org/10.3749/canmin.48.5.1171.
[182] L. Coes, High-pressure Minerals, Journal of the American Ceramic Society. 38 (1955) 298–298. https://doi.org/10.1111/j.1151-2916.1955.tb14949.x.
[183] E.S. Grew, A.J. Locock, S.J. Mills, I.O. Galuskina, E.V. Galuskin, U. Hålenius, Nomenclature of the garnet supergroup, American Mineralogist. 98 (2013) 785–811. https://doi.org/10.2138/am.2013.4201.
[184] B.J. Skinner, Physical properties of end-members of the garnet group, American Mineralogist. 41 (1956) 428–436.
[185] S. Geller, Crystal chemistry of the garnets, Zeitschrift für Kristallographie - Crystalline Materials. 125 (1967) 1–47. https://doi.org/10.1524/zkri.1967.125.16.1.
[186] S. Geller, H.J. Williams, R.C. Sherwood, G.P. Espinosa, Substitutions of divalent manganese, iron and nickel in yttrium iron garnet, Journal of Physics and Chemistry of Solids. 23 (1962) 1525–1540. https://doi.org/10.1016/0022-3697(62)90231-7.
[187] A.R. Ericks, F.W. Zok, D.L. Poerschke, C.G. Levi, Protocol for selecting exemplary silicate deposit compositions for evaluation of thermal and environmental barrier coatings, J Am Ceram Soc. (n.d.).
[188] G.A. Novak, G.V. Gibbs, The Crystal Chemistry of the Silicate Garnets, American Mineralogist. 56 (1971) 791–825.